

**Bauhaus-Universität Weimar**

# Nonlinear Analysis Models for the Static and Dynamic Behaviour of Structural Cables

## **DISSERTATION**

zur Erlangung des akademischen Grades  
Doktor-Ingenieur (Dr.-Ing.)

an der Fakultät Bauingenieurwesen  
der Bauhaus-Universität Weimar

vorgelegt von

**Abdulmagid Sedig Khalafallah Bendalla**

geboren am 22. Dezember 1993  
in Tripoli, Libyen

Mentor: Prof. Dr. Guido Morgenthal

Weimar, April 2024



# Abstract

Cables are integral to the structural stability of cable-supported structures, emphasising the need for improving assessment models in evaluating the structural condition of cable-supported structures. This work aims at enhancing the systematisation of cable models, and focuses on the analysis and system identification of cables with nonlinear geometry and complex physical–mechanical interactions. It employs a modelling framework approach, utilising inverse analyses and parametric application of the Finite Element Method to evaluate cable behaviour.

Following a discussion on assumptions, limitations, and applications of existing cable models, a categorised classification system is proposed. Two case studies are then presented, highlighting the influence of geometry, loading conditions, and bending stiffness on the cable contact point within supports.

The introduction of a novel saddled cable model employs an efficient Finite Element framework to explore the impact of changing contact points on suspended cables and external tendons with curved deviators. Comparisons with modal properties obtained from on–site vibration measurements of an external tendon result in accurate tension force identification. Detailed descriptions of the effects of curved deviators on dynamic behaviour follow.

Acknowledging that contact point identification significantly depends on bending stiffness and local interactions between cable wires, an investigation into the effects of inter–wire friction is conducted. The model, incorporating stored interlock cohesion between cable wires, demonstrates high accuracy compared to experimental data under varying tension forces.

Throughout the discussions, comparisons with experiments, previous studies, and analytical solutions are provided. This work suggests that Finite Element frameworks could be developed into a parametric toolbox for cable analyses, showcasing the adaptability of the models in practical applications.

**Keywords:** Cable analysis, model classification, FE modelling, system identification, curved supports, stick–slip, geometric stiffness, bending stiffness.



# Acknowledgements

I extend my gratitude to my mentor, *Prof. Dr. Guido Morgenthal*, whose unwavering guidance has illuminated my academic journey in Weimar. Over the past four years, his support has transformed this period into an enriching academic odyssey that will undoubtedly shape my future.

I am also profoundly grateful to *Prof. Charles Riley* of the Oregon Institute of Technology, whose insightful discussions and constructive critiques during his time in Weimar have been invaluable to the successful completion of this work.

My heartfelt thanks extend to my colleagues whose contributions have been instrumental: *Dr. Samir Chawdhury*, for his invaluable feedback and infectious wisdom in our shared workspace; *Gledson Tondo*, whose collaboration on our publication and expertise in surrogate models and Gaussian Process regression have been indispensable; *Sebastian Rau*, for his invaluable assistance in providing experimental data for model validation; and *Emadeddin Badi* for his assistance and linguistic suggestions.

I am indebted to *Ali Bani* for his encouragement and push to embark on this PhD journey at a tipping moment of uncertainty.

Above all, I extend my boundless gratitude to my family: *Sedig, Hamida, Marwan, Muhanned* and his family—*Noha, Mariam, Nour, and Sara*—as well as *Maha* and her family—*Zuhair, Amira, and Reem*. Their steadfast support, thoughtful counsel, love, kindness, joy, fun, and encouragement have been my pillars of strength throughout this journey. I dedicate this work to them.



# Ehrenwörtliche Erklärung

Ich erkläre hiermit ehrenwörtlich, dass ich die vorliegende Arbeit ohne unzulässige Hilfe Dritter und ohne Benutzung anderer als der angegebenen Hilfsmittel angefertigt habe. Die aus anderen Quellen direkt oder indirekt übernommenen Daten und Konzepte sind unter Angabe der Quelle gekennzeichnet.

Bei der Auswahl und Auswertung folgenden Materials haben mir die nachstehend aufgeführten Personen in der jeweils beschriebenen Weise unentgeltlich geholfen:

- *Gledson Rodrigo Tondo* - Aufbau und Programmierung des Gaussian Process regression model.

Weitere Personen waren an der inhaltlich-materiellen Erstellung der vorliegenden Arbeit nicht beteiligt. Insbesondere habe ich hierfür nicht die entgeltliche Hilfe von Vermittlungs- bzw. Beratungsdiensten (Promotionsberater oder anderer Personen) in Anspruch genommen. Niemand hat von mir unmittelbar oder mittelbar geldwerte Leistungen für Arbeiten erhalten, die im Zusammenhang mit dem Inhalt der vorgelegten Dissertation stehen.

Die Arbeit wurde bisher weder im In- noch im Ausland in gleicher oder ähnlicher Form einer anderen Prüfungsbehörde vorgelegt.

Ich versichere ehrenwörtlich, dass ich nach bestem Wissen die reine Wahrheit gesagt und nichts verschwiegen habe.

Weimar, 06.05.2024

Abdulmagid S. Kh. Bendalla



# Contents

<b>Abstract</b>	<b>ii</b>
<b>List of Figures</b>	<b>xi</b>
<b>List of Tables</b>	<b>xviii</b>
<b>Nomenclature</b>	<b>xxi</b>
<b>List of Acronyms</b>	<b>xxiv</b>
<b>1 Introduction</b>	<b>1</b>
<b>2 Structural cable systems</b>	<b>8</b>
2.1 Introduction . . . . .	8
2.2 Cable types . . . . .	8
2.2.1 Stranded ropes . . . . .	9
2.2.2 Locked-coil ropes . . . . .	10
2.2.3 Parallel strand systems . . . . .	10
2.2.4 Parallel wire systems . . . . .	11
2.2.5 Semi-parallel wire cables . . . . .	12
2.3 Cable anchorages . . . . .	13
2.3.1 Cable anchor . . . . .	13
2.3.2 Clevis connection . . . . .	15
2.3.3 Saddles and deviators . . . . .	16
2.4 Vibration control devices . . . . .	17
<b>3 Cable analysis models</b>	<b>20</b>
3.1 Introduction . . . . .	20
3.2 History of cable models . . . . .	20
3.3 Cable analysis models and system identification . . . . .	21
3.4 Fundamentals of Finite Element formulation for geometric nonlinear analyses	23
3.5 Cable models main assumptions . . . . .	27
3.5.1 Analysis type and sag effects . . . . .	28
3.5.2 Bending stiffness . . . . .	29

3.5.3	Boundary conditions . . . . .	30
3.5.4	Assumed self-weight . . . . .	31
3.5.5	Principles of model parameters . . . . .	33
3.5.6	Cable wire representation . . . . .	34
3.6	Advancements in cable analysis . . . . .	34
3.7	Categorisation of cable models . . . . .	37
3.7.1	The taut-string . . . . .	38
3.7.2	Modified taut-string . . . . .	38
3.7.3	The flat bar model . . . . .	39
3.7.4	Empirical models . . . . .	39
3.7.5	The sagged string model . . . . .	39
3.7.6	The sagged bar model . . . . .	39
3.7.7	Sagged bar with intermediate supports . . . . .	40
3.7.8	The saddled cable model . . . . .	40
3.7.9	Helically twisted cable models . . . . .	40
3.8	Classification table . . . . .	40
3.9	Summary . . . . .	43
<b>4</b>	<b>Identifying cable forces from vibration measurements</b>	<b>44</b>
4.1	Introduction . . . . .	44
4.2	Background . . . . .	44
4.3	A case study: The Øresund bridge . . . . .	46
4.3.1	Cable characteristics . . . . .	47
4.3.2	Vibration measurement . . . . .	48
4.3.3	Parameter Identification . . . . .	48
4.3.4	Parameter optimisation . . . . .	49
4.3.5	Cable force identification . . . . .	50
4.3.6	Model outputs . . . . .	55
4.4	A case study: Queensferry Crossing . . . . .	56
4.4.1	Cable characteristics . . . . .	58
4.4.2	Signal analysis . . . . .	58
4.4.3	Natural frequency identification . . . . .	61
4.4.4	Results . . . . .	64
4.5	Summary . . . . .	65
<b>5</b>	<b>Saddles and curved deviators as boundary conditions</b>	<b>67</b>
5.1	Cable models for form finding under self-weight . . . . .	67
5.1.1	Straight cable model . . . . .	68
5.1.2	Modified straight cable model . . . . .	69
5.1.3	Initially sagged cable model . . . . .	69

5.1.4	Extended cable model . . . . .	69
5.1.5	Assessment of model performance . . . . .	69
5.2	Modelling saddles and deviators . . . . .	72
5.3	Model application for form finding of suspended cables . . . . .	75
5.3.1	Profiles of cables without bending stiffness . . . . .	75
5.3.2	Profiles of cables with bending stiffness . . . . .	77
5.4	Model application for tension force identification of external tendons . . . . .	81
5.4.1	Test setup . . . . .	82
5.4.2	Identified tendon parameters . . . . .	85
5.4.3	Parametric study . . . . .	86
5.5	Dynamic behaviour of the saddled model for taut cables . . . . .	89
5.5.1	Static form finding and modal analysis . . . . .	90
5.5.2	Dynamic behaviour . . . . .	91
5.6	Summary and conclusions . . . . .	99
<b>6</b>	<b>Stick–slip behaviour of semi-parallel wire cables</b>	<b>100</b>
6.1	Introduction . . . . .	100
6.2	State-of-the-art helically twisted cable models . . . . .	102
6.3	Methodology . . . . .	104
6.3.1	FEM for modelling cable wire stick–slip . . . . .	104
6.3.1.1	Model construction . . . . .	105
6.3.1.2	Model 01: Constant residual . . . . .	109
6.3.1.3	Model 02: Varying residual . . . . .	109
6.3.2	Surrogate models using Gaussian processes . . . . .	110
6.4	Validation and results . . . . .	112
6.4.1	Model validation . . . . .	112
6.4.1.1	Model 01 . . . . .	113
6.4.1.2	Model 02 . . . . .	114
6.4.2	Parameter optimisation . . . . .	116
6.4.3	Parametric study and sensitivity analysis . . . . .	118
6.4.4	Response uncertainty in GP predictions . . . . .	120
6.4.5	Mechanics of the stick–slip of SPW cables . . . . .	123
6.4.6	Hysteresis behaviour . . . . .	129
6.5	Conclusion . . . . .	130
<b>7</b>	<b>Relevance of models for practical application</b>	<b>132</b>
7.1	Introduction . . . . .	132
7.2	Parametrisation of the inclined sagged bar model . . . . .	132
7.3	Parametrisation of the saddled cable model . . . . .	134
7.3.1	The saddled cable model for suspension bridges . . . . .	134

## CONTENTS

---

7.3.2	The saddled cable model for external tendons . . . . .	136
7.3.3	The saddled cable model for extradosed bridge cables . . . . .	140
7.4	Parametrisation of the SPW cable model . . . . .	143
<b>8</b>	<b>Summary, conclusions and outline</b>	<b>145</b>
8.1	Summary and conclusions . . . . .	145
8.2	Scope for further work . . . . .	148
<b>A</b>	<b>The Catenary Solution</b>	<b>A-1</b>
<b>B</b>	<b>Computational benchmarking</b>	<b>A-3</b>
B.1	Computations of the sagged bar model and the saddled cable model . . . . .	A-3
B.2	Computational costs for the SPW cable model . . . . .	A-5
	<b>Bibliography</b>	<b>A-7</b>
	<b>Publications by the Author</b>	<b>A-18</b>

# List of Figures

1.1	Rope making in ancient Egypt. ( <i>Courtesy of H. Hill's The Wonder Book of Knowledge 1921</i> ).	1
1.2	Using rope in construction and lifting of heavy object, utilising the lever arm concept in Assyrian civilisation about 1800 B.C. ( <i>Courtesy of A. H. Layard's Nineveh and Babylon 1859</i> ).	2
1.3	Examples of cable-supported bridges with cables as main load carrying elements.	3
1.4	Q'eswachaka bridge crossing the Apurimac canyon in Peru and a close-up of its main straw-woven suspension ropes.	4
1.5	Wadi el Kuf bridge near Al Bayda, Libya. <i>Courtesy of: Sanad Al-Ahlafi</i> .	5
2.1	An example cross section of a galvanised sprial strand rope.	9
2.2	An example cross section of a medium sized Locked-coil rope cable.	10
2.3	Examples of cross section types of a parallel multi-strands cable.	11
2.4	An example cross section of a parallel wire cable noting the wire spreading effect.	12
2.5	An example cross section of a Semi-Parallel Wire (SPW) cable with wires twisted concurrently with the same lay length.	13
2.6	Examples of clamping cable anchors. Cable anchor in a pylon (left) and anchor socket at bridge deck (right).	14
2.7	Cable anchorage tubes of a railway bridge in Istanbul, Turkey.	14
2.8	Examples of hinged connections.	16
2.9	Examples of deviating supports. A cable saddle used in suspension, cable-stayed and extradosed bridges (left), and a box-girder bridge deviator for external tendons.	17
2.10	Main types of damping devices: internal support damper (left), friction damper (middle), and external damper (right). <i>Courtesy to: Freyssinet (via Le Moniteur), DAMPTECH, and ravenelbridge.net &amp; Freyssinet (left to right)</i> .	18
2.11	Cross ties connected to stay-cables of the Normandy bridge in France. ( <i>Courtesy of David Henry - Getty Images</i> ).	19
3.1	Carrying a uniform load via bending stiffness (left) v.s. via axial and geometric stiffness i.e. tension and sag. It shows that for long span structures, cables achieve high material reduction in the cross section [5].	22

3.2	Relative differences between the natural frequencies of a linear taut-string (TS) model and the geometric nonlinear sagged string. Main differences are noted in natural frequencies for the asymmetric modes, predominantly for the first vibration mode. Comparison is made for different lengths. Model parameters used are as in Table 3.1. <i>Differences on the left side are small and might not be visible on the printed version.</i> . . . . .	29
3.3	Comparison between a linear flexible cable model (taut-string) and a modified taut-string model (mod. TS) accounting for the bending stiffness effects. Main differences increase significantly with higher mode numbers. The effects increases for short cables. Model parameters used are as in Table 3.1. . . . .	30
3.4	Effects of different boundary conditions on the natural frequencies employing three cases: the reference Modified taut-string (mod. TS) with both ends hinged), Flat bar (FB) with fixed ends, and Fixed-pinned (FPB). Comparison is done for two cases where the length is short $L = 50\text{m}$ and long $L = 200$ . Boundary condition effects decrease with longer lengths. Model parameters used are as in Table 3.1. . . . .	31
3.5	Self-weight distribution comparison: Uniform distribution along the chord length gives a parabolic cable form and a higher internal forces, while distribution along the cable axis gives a hyperbolic form and the minimum internal tension forces. A graphic statics example as taken from [13, 26]. Force diagrams are to scale. . . . .	33
3.6	Considerations and assumptions of most structural cable models. . . . .	41
3.7	A schematic showing a visual representations of the main cable models existing in the literature. . . . .	41
4.1	An overview of the Øresund bridge. . . . .	47
4.2	Errors $\Delta_i$ (left) and sum of absolute errors $\sum  \Delta_i $ (right) between the identified and the model-predicted frequencies for <b>cable ES1</b> compared with results from [56]. The sagged bar has lowest error and predicts fundamental frequency well due to inclusion of the axial, bending, and geometric stiffness effects. . . . .	52
4.3	Errors $\Delta_i$ (left) and sum of absolute errors $\sum  \Delta_i $ (right) between the identified and the model-predicted frequencies for <b>cable ES5</b> compared with results from [56]. The sagged bar has lowest error and predicts fundamental frequency well due to inclusion of the axial, bending, and geometric stiffness effects. . . . .	53
4.4	Errors $\Delta_i$ (left) and sum of absolute errors $\sum  \Delta_i $ (right) between the identified and the model-predicted frequencies for <b>cable EN1</b> compared with results from [56]. The sagged bar has lowest error and predicts fundamental frequency well due to inclusion of the axial, bending, and geometric stiffness effects. . . . .	54

4.5	Identified tension force for each cable using the three cable models. The uncertainty range shown in the plot refers to the tension force variation within 10% of the error between the identified and the model natural frequencies. . . . .	56
4.6	Queensferry crossing (left, cable-stayed), the Forth Road bridge (middle, suspension) and parts of the Forth bridge (right, red steel truss). Courtesy of: Scottish Construction Now. . . . .	57
4.7	Manual excitation (left) and sensing unit setup (right) of a cable of Queensferry Crossing. Sensing unit consists of: MEMS sensor (1), power supply (2) and RPi computer (3). Photos kindly provided by the authors of [75]. . . . .	59
4.8	Baseline corrected time history of in-plane acceleration signal for the available datasets. Time-history data kindly provided by [75]. . . . .	60
4.9	Interpolation and resampling: difference between main signal and the interpolated. (—base-corrected, —interpolated). Time-history data kindly provided by [75]. . . . .	61
4.10	Frequency spectrum for all four datasets derived after signal post-processing from C4 cable of the Queensferry Crossing. . . . .	62
5.1	Model schematic: load case and cable parameters. . . . .	68
5.2	Four types of the saddled cable model. Left: initial geometry, load and self-weight application. Right: system after deformation. . . . .	70
5.3	Difference in deformed shapes between straight, modified and extended models, and the sagged model. Straight and modified cable models overestimate cable length. Initially sagged model is virtually exacted compared with the analytic catenary solution. The extended cable agrees well with the latter. . . . .	72
5.4	Saddle springs alignment and spring gap calculation for the straight and modified straight cable models. . . . .	73
5.5	Model composition for the initially sagged cable model showing saddle springs and their gaps' calculation. $s_{\text{parb}}$ refers to the maximum sag of the parabola geometry only. . . . .	74
5.6	Saddle springs for the extended straight cable model and its gap calculation. Spring position before loading (left) and after loading (right). This model has vertical springs as to allow horizontal translation of the springs. . . . .	75
5.7	Contact point locations along the saddle for the four saddled cable models of different bending stiffness. . . . .	79
5.8	Effect of bending stiffness on saddle region and cable shape as per the extended cable model, which is used given its accuracy as a generalised saddled cable model. . . . .	80
5.9	Experimental direct and indirect tension force identification: Lift-off test jack in place at span anchor (left) and vibration signal acquisition setup near the deviation block (right). . . . .	82

5.10	Experimental tension force identification: a schematic showing the model setup at the anchor-deviator subsection and the saddled cable. . . . .	83
5.11	Experimental tension force identification: Acceleration time history for tendon under $T_1$ (left) and $T_2$ (right). . . . .	84
5.12	Experimental tension force identification: Frequency spectra for tendon under $T_1$ (left) and $T_2$ (right). . . . .	84
5.13	Frequency error for models with optimised parameters. . . . .	86
5.14	Tension force error values for models used in the tension force identification from vibration measurements. The saddled cable model shows lowest sum of absolute errors, while the taut-string tends to overestimate the tension force. . . . .	87
5.15	First order $S_1$ and total sensitivity index $S_{T_1}$ of parameters used in cable modelling: First natural frequency for tension force $T_1$ (top) and $T_2$ (bottom). . . . .	88
5.16	First order $S_1$ and total sensitivity index $S_{T_1}$ of parameters used in cable modelling: Sixth natural frequency for tension force $T_1$ (top) and $T_2$ (bottom). . . . .	88
5.17	Model setup for dynamic analysis. Harmonic load extends along the entire cable length with frequency excitation close to the first Eigenfrequency. . . . .	93
5.18	Time history comparison: in-plane free vibration at midspan for (—) pin-ended model and (—) straight saddled cable model. (- - -) the cable sag at midspan. Both models are subjected to the same harmonic load with the same timestep properties. Plot shows the first 30-second of the free vibration. . . . .	94
5.19	Frequency spectrum of a 100 second free vibration response at midspan: (—) the pin-ended cable model (—) straight saddled cable model. Vertical lines: (   ) the analytical natural frequencies, (   ) the frequencies obtained from the numerical model. Reference values: Table 5.13. . . . .	95
5.20	Free length time history ( $L - L_{c_{left}} - L_{c_{right}}$ ) during free vibration. (—) identified free length at static equilibrium, (- - -) average free length during free vibration. . . . .	95
5.21	Model setup for dynamic analysis. Harmonic load excites one quarter-length of the cable with two frequencies: first and second Eigenfrequency. . . . .	96
5.22	Time history for the vertical cable free vibration for multiple $q_0$ at midspan (coloured). (—) $q_0=0.4\text{kN}$ , (—) $q_0=0.8\text{kN}$ . (- - -) maximum sag at static equilibrium. . . . .	96
5.23	Time history of cable free length ( $L - L_{c_{left}} - L_{c_{right}}$ ) using free vibration response based on the identified contact lengths $L_c$ . (—) $q_0=0.4\text{kN}$ , (—) $q_0=0.8\text{kN}$ , (- - -) free length at static equilibrium. . . . .	97
5.24	Frequency spectrum of 100 second free vibration response of saddled cable model for multiple load amplitudes $q_0$ . Vertical dashed lines: the reference frequencies of Table 5.13. (—) $q_0=0.4\text{kN}$ , (—) $q_0=0.8\text{kN}$ . . . . .	98

6.1	Concurrent and reversed wire laying. The hexagonal wire arrangement of SPW cables allows to have a more compact cross section with inter and intrawire contact. .	103
6.2	Geometric parameters of a single SPW wire helically twisted along a cable laying length $l_{lay}$ . . . . .	106
6.3	Test setup [90] and model construction. Note: the load in the Finite Element (FE) model is placed on the top nodes at midspan similar to the actual test setup, which can lead to asymmetries in the load distribution and the yielding of springs. . . . .	107
6.4	Contact modelling using coupling springs with longitudinal and transverse components for a $61\phi 7\text{mm}$ SPW cable. . . . .	109
6.5	Comparison of residual contact between the model without circumferential contact Model02a (left) and the model with circumferential contact Model 02b (right). This cross section depicts the discretised slice at the midspan. While the cross section rotates at different slices, the springs maintain consistent wire coupling. . . . .	110
6.6	Validation of GP trained model (left) for and optimum bending curve (right) for shear springs with constant residual for $T_{tot} = 50\text{kN}$ . Within the physical upper and lower bounds, Model 01 is unable to adequately represent the experimental results. Optimum parameters with GP prediction = $[5.996^\circ, 0.8495, 12.68\text{kN}]$ . . . . .	114
6.7	Example of several FE simulations with different spring cohesion $c_k$ to determine the influence of the cohesion parameters on the $F - u$ curve and determine an appropriate upper and lower limits. For $[c_0, c_1, c_2, c_3, c_4]$ : Trial 1 = $[14, 11, 8, 5, 2]$ , Trial 2 = $[2, 5, 8, 11, 14]$ , Trial 3 = $[14, 11, 2, 1, 0]$ , Trial 4 = $[80, 30, 2, 1, 0]$ . For all trials: $[\beta_{max}, \mu] = [5^\circ, 0.5]$ . Trial 4 provided a similar curve to the experiment. Trial 3 has the most similar slope to the experiment under low $F$ load. .	115
6.8	Training validation for GP for inter-layer contact model (Model02a, left) and inter- and intra-layer contact model (Model02b, right) for $T_{tot} = 50\text{kN}$ . . . . .	116
6.9	Optimum bending curve for GP of inter-layer contact model (Model02a, left) and inter- and intra-layer contact model (Model02b, right) for $T_{tot} = 50\text{kN}$ . Upper and lower bounds are mentioned in Table 6.2. . . . .	117
6.10	$F - u$ curve comparison between FE Model 02b (inter- and intra-layer contact springs) with optimum parameters and the curve obtained from experiment for three tension forces $T_{tot} = 50, 80, 100\text{kN}$ (left to right). . . . .	118
6.11	Parameter first order $S_1$ and total $S_{T_1}$ Sobol' sensitivity for several bending loads for $T_{tot} = 50\text{kN}$ . . . . .	119
6.12	Parameter variation from the bending curve (other parameters kept as optimum values) for $T_{tot} = 50\text{kN}$ . . . . .	120
6.13	Normalised probabilistic deflection predictions for different load amplitudes. The cable parameters are taken as the optimal ones according to experimental data for Model 01 (left) and Model 02b (right). . . . .	121

6.14 Deflection mean and 95% confidence interval in Model 02b as predicted by GP, for different load magnitudes and varying model parameters for  $T_{tot} = 50\text{kN}$ . Parameters are normalised within their bound specified in Table 6.2. Experimental optimal values are shown by the black dot. . . . . 122

6.15 Failed (red circle) and active (white) springs in Model 02b at third and midspan for different loads and pretensioning values. Higher  $T_{tot}$  in (b) results in a greater radial normal force and an increase in friction between the wires, slightly enhancing the cable’s capacity to resist bending loads. Asymmetry in spring yielding associated with load  $F$  placement in the top wires. . . . . 125

6.16 Normal force distribution (top) within corner wires of the second wire layer (bottom) for four load phases  $F = 2, 8, 12,$  and  $18$  kN. It is noted that the force transfers from the midspan to the ends with an increasing load  $F$ .  $T_{tot.} = 50\text{kN}$ . Colours indicate the particular wires in the bottom figure.  $T_i$  (- - -). . . . . 126

6.17 Normal force distribution (top) within corner wires of the first wire layer (bottom) for four load phases  $F = 2, 8, 12,$  and  $18$  kN. Springs in the inner wires yield at high bending loads  $F$  and the wires take higher axial forces that in the other layers.  $T_{tot.} = 50$  kN. Colours indicate the particular wires in the bottom figure.  $T_i$  (- - -). 127

6.18 Comparison of the loss in bending stiffness for Model 02b and the calibrated bending stiffness of beam model for  $T_{tot} = 50$  kN. . . . . 127

6.19 Difference in deformed shape between Model 02b and calibrated beam for  $T_{tot} = 50$  kN. . . . . 128

6.20 The failed springs ratio for the FE Model 02 with optimised parameters for  $T_{tot} = 50$  kN. The colours indicate the failed springs ratio in a discretised node slice. . . . . 128

6.21 The failed springs ratio for the FE Model 02b for  $T_{tot} = 50$  kN with higher cohesion residual in the outer layers. Parameters:  $[\beta_{max}, \mu, c_0, c_1, c_2, c_3, c_4] = [4.5, 0.6, 180, 40, 2, 1.5, 0.5]$ . The colours indicate the failed springs ratio in a discretised node slice. . . . . 129

6.22 Hysteresis analysis of Model 02b for different bending loads and a tension force of  $T_{tot} = 50$  kN. Upon release of the load, the secondary effects of tension forces create a negative moment counteracting the deformation to restore the cable to the undeformed state, making the size of the hysteresis cycle small. The Loading sequence influences the residual displacement: Loading in the positive gravity direction tends to result in considerably higher residuals and has a smaller slope. . . . . 130

7.1 Actual case schematic and as modelled parametrised saddled cable. . . . . 135

7.2 An external prestressed tendon setup in a box-girder bridge. . . . . 137

---

7.3	Actual case schematic and as modelled parametrised saddled cable for a anchor-to-deviator section. . . . .	138
7.4	Actual case schematic and as modelled parametrised saddled cable for a deviator-to-deviator section. . . . .	139
7.5	Tendon profile embedded inside a box-girder and a corresponding FE model. .	140
7.6	Actual case schematic and as modelled parametrised inclined saddled cable in an extradosed bridge cable setting. . . . .	142
7.7	Parametrised cross section of a SPW cable. In the framework $n_{\text{layer}}$ specifies the number of layers of a given cross section, which assigns a compact cross section with a $n_{\text{layer}}$ . . . . .	144
A.1	Equilibrium of an infinitesimal element of a zero flexural stiffness member under its self weight. . . . .	A-1

# List of Tables

3.1	Parameters for a reference cable example. Example is used to examine the effects of several assumptions related to the cable. . . . .	28
3.2	Classification of common cable models used for cable force identification. . . .	42
4.1	Main cable characteristics of the Øresund bridge. . . . .	47
4.2	Identified frequencies and cable parameters for three stay-cables of the Øresund bridge (as taken from [56]). Parameters (bottom) are chosen within the predefined upper and lower bounds. . . . .	49
4.3	Prediction results: frequencies and optimum parameters of each cable model for <b>cable no. ES1</b> compared with results from [56]. Notably, is a difference of over 2% in the first fundamental frequency for most models compared to measured data, with the the sagged bar being the exception. Note: some values might be rounded and percentage difference show the difference from the actual value pre-rounding. The reference [56] used the taut-string theory for identification. . . . .	52
4.4	Prediction results: frequencies and optimum parameters of each cable model for <b>cable no. ES5</b> compared with results from [56]. Notably, there is a difference of over 1.5% in the first fundamental frequency for most models compared to the measured data, with the sagged bar being the exception. Note: some values might be rounded and percentage difference show the difference from the actual value pre-rounding. The reference [56] used the taut-string theory for identification. . . . .	53
4.5	Prediction results: frequencies and optimum parameters of each cable model for <b>cable no. EN1</b> compared with results from [56]. Notably, there is a difference of over 1.5% in the first fundamental frequency for most models compared to the measured data, with the sagged bar being the exception. Note: some values might be rounded and percentage difference show the difference from the actual value pre-rounding. The reference [56] used the taut-string theory for identification. . . . .	54
4.6	Main cable characteristics of the Queensferry bridge. . . . .	58
4.7	Identified frequencies and signal properties for cable C4 of the Queensferry Crossing for each dataset. . . . .	63

4.8	Identified averaged frequencies and prediction with optimum parameters computed with three cable models. Tension force prediction is compared with the reference value $T_{\text{ref.}} = 9630$ kN as taken from [75]. Note: some values might be rounded and percentage difference show the difference from the actual value pre-rounding. . . . .	65
5.1	Model parameters chosen for a benchmark case deploying the four proposed cable models. . . . .	68
5.2	Results comparison for several cable models under self-weight (beam elements with zero bending stiffness). . . . .	71
5.3	Results of four methods to model a saddled cable with $R = 8$ m and no cable bending stiffness. . . . .	76
5.4	Results comparison of the four saddled cable models with $0.5EI_{\text{ref.}}$ . Percentage differences correspond to tension forces in Table 5.3 of each model. . . . .	78
5.5	Results comparison of the four saddled cable models with $1.0EI_{\text{solid}}$ . Percentage differences correspond to tension forces in Table 5.3 of each model. . . . .	78
5.6	Experimental tension force identification: tendon properties and test setup parameters. . . . .	83
5.7	Identified natural frequencies for $T_1$ and $T_2$ . . . . .	84
5.8	Measurement system used in signal acquisition and digitisation. . . . .	85
5.9	Optimum parameters for frequencies identified at $T_1 = 2692$ kN (ref.). . . . .	86
5.10	Optimum parameters for frequencies identified at $T_2 = 1862$ kN (ref.). . . . .	87
5.11	Model parameters for the proposed cable models. . . . .	90
5.12	Comparison of static parameters for models with several $EI$ values. . . . .	90
5.13	Natural frequencies computed from modal analysis at static equilibrium. The difference values indicated are percentile deviations from analytical values. Anlt. Pin: analytical values of taut-string Equation (3.12) with total length $L$ . Anlt. Fixed: analytical values of Equation (3.14) with free length $L$ . Anlt. Fixed': Equation (3.14) with free length $L - 2L_c$ . Lengths as mentioned in Table 5.12 . . . . .	92
6.1	Upper and lower bounds for parameters used for sampling and training. . . . .	113
6.2	Upper and lower bounds for residual cohesion forces used for sampling and training. . . . .	115
6.3	Upper and lower bounds for residual cohesion forces used for sampling and training. $\beta_{\text{max}}$ and $\mu$ have the same parameter bounds as for Model 01. . . . .	116
7.1	Stay-cable analysis models for cable force identification. . . . .	133
B.1	Computational power of the device used for nonlinear FE analysis. . . . .	A-3

B.2 **Chapter 4**, computational cost for FE analysis of the cables for a single run and the optimisation requirements (opt.). *Mentioned details are collected along the following operations: geometry generation, a nonlinear form finding analysis, a subsequent Eigenvalue analysis, and results export in text formats.* . . . . . A-4

B.3 **Chapter 5**, Computational costs of FE analyses applied for self-weight comparison between models (without saddle springs). *The computational time involves: geometry generation, a nonlinear form finding analysis, and results export in text formats.* . . . . . A-4

B.4 **Chapter 5**, computational costs of FE analyses applied for determination of the contact point and the contact length (with saddle springs). *The computational time involves: geometry generation, a nonlinear form finding analysis, and results export in text formats.* . . . . . A-4

B.5 **Chapter 5**, computational cost of FE analyses applied for cable force identification from vibration measurement of an external tendon. *The computational time involves: geometry generation, a nonlinear form finding analysis, an Eigenvalue analysis, and results export in text formats.* . . . . . A-5

B.6 **Chapter 6**, computational cost of FE analyses applied for SPW detailed cable model. *The computational time involves: geometry generation, a nonlinear form finding analysis, and results export in text formats.* . . . . . A-6

# List of Symbols

<b>K</b>	Stiffness Matrix . . . . .	24
<b>U</b>	Displacement vector . . . . .	24
<b>R</b>	Applied Load Vector . . . . .	24
<b>F</b>	Internal Force Vector . . . . .	24
<i>A</i>	Cross sectional steel area . . . . .	28
<i>E</i>	Modulus of elasticity . . . . .	28
$\gamma$	Unit weight of cable material . . . . .	28
<i>EI</i>	Cable Bending Stiffness . . . . .	37
<i>v</i>	Lateral in-plane vibration displacement . . . . .	37
<i>u<sub>y</sub></i>	Lateral displacement due to self-weight . . . . .	37
<i>T<sub>h</sub></i>	Horizontal component of cable tension force . . . . .	38
<i>T</i>	Cable tension force . . . . .	38
<i>T<sub>d</sub></i>	Horizontal component of dynamic tension . . . . .	38
<i>k</i>	Spring stiffness . . . . .	38
<i>c'</i>	Viscous damping coefficient . . . . .	38
<i>m</i>	Mass per unit length . . . . .	38
<i>f<sub>n</sub></i>	Natural frequency of the <i>n</i> <sup>th</sup> . . . . .	38
<i>n</i>	Vibration mode number . . . . .	38
<i>L</i>	Cable chord length . . . . .	38
$\xi$	Non-dimensional bending stiffness . . . . .	39
$\lambda^2$	Irvin parameter . . . . .	39
<b>X</b>	Cable parameters vector considered for optimisation . . . . .	45
$\sum  \Delta_i $	Sum of the absolute minimum . . . . .	45
<i>f<sub>idn.</sub></i>	Identified natural frequencies . . . . .	45
<i>A<sub>steel</sub></i>	Area of steel . . . . .	47
$\phi$	Wire diameter of a multiwire cable . . . . .	48
<i>f<sub>idn.</sub></i>	Identified frequencies . . . . .	49
<i>f<sub>model</sub></i>	Model natural frequencies . . . . .	52
<i>L<sub>opt.</sub></i>	Optimum cable length . . . . .	52
<i>EI<sub>opt.</sub></i>	Optimum bending stiffness . . . . .	52
<i>T<sub>opt.</sub></i>	Optimum tension force . . . . .	52
$\xi$	Non-dimensional bending stiffness . . . . .	52
<i>E</i>	Modulus of Elasticity . . . . .	58

LIST OF SYMBOLS

---

$s_{\max}$	Maximum cable sag at midspan . . . . .	68
$\delta L$	total unstressed overlength . . . . .	68
$s_{\text{parb}}$	Maximum sag of the parabola . . . . .	69
$L_g$	Overall cable stressed length . . . . .	71
$R$	Saddle radius . . . . .	73
$x_i$	$x$ coordinate of a node numbered $i$ . . . . .	73
$z_i$	$z$ coordinate of a node numbered $i$ . . . . .	73
$\beta_i$	Radial angle at a saddle node numbered $i$ . . . . .	73
$r$	Radius of saddle springs for the initially sagged cable model . . . . .	74
$s_{\max.(\text{int.})}$	Initial maximum sagged for the initially sagged cable model . . . . .	74
$L_c$	Contact length of the cable with the saddle . . . . .	75
$M_y$	Midspan cable moment . . . . .	78
$q(t)$	Harmonic load function . . . . .	91
$q_0$	Harmonic load function . . . . .	91
$\zeta$	Damping coefficient . . . . .	93
$l_{\text{lay}}$	Laying length of a helix wire . . . . .	105
$\beta_j^k$	Laying angle of a helix wire $j$ in a layer $k$ . . . . .	105
$y_j^k$	$y$ coordinate of a helix wire $j$ in a layer $k$ . . . . .	105
$z_j^k$	$z$ coordinate of a helix wire $j$ in a layer $k$ . . . . .	105
$\theta_j^k$	Radial angle at $x_i = 0$ of a helix wire $j$ in a layer $k$ . . . . .	105
$F$	Transverse force at midspan of a cable under bending . . . . .	106
$\mu$	Friction coefficient . . . . .	107
$c_k$	Interlock cohesion force for wire layer $k$ (distributed along the length) . . . . .	107
$\beta_{\max}$	Maximum lay angle associated with the corner wire in the last layer . . . . .	108
$C_k$	Interlock cohesion force assigned for springs for wire layer $k$ (discretised at nodes) . . . . .	108
$u_z$	Cable displacement in $z$ direction . . . . .	111
$N_d$	Number of parameters in a cable model . . . . .	111
$\epsilon$	Uncertainty in surrogate model . . . . .	111
$\sigma_n^2$	Variance in surrogate model . . . . .	111
$\mathbf{k}$	Covariance kernel . . . . .	111
$\boldsymbol{\eta}$	Hyper-parameter vector used in the covariance kernel $k$ . . . . .	111
$\sigma_s$	Standard deviation of the covariance amplitude . . . . .	111
$\ell_i$	Length scales controlling the smoothness of each parameter dimension $i$ . . . . .	111
$\mathbf{K}_c$	Covariance matrix used in the GP surrogate model . . . . .	111
$\mathbf{m}^*$	Predictive mean of the GP surrogate model . . . . .	112
$L_{\text{sadd}}$	Length along which saddle springs are distributed . . . . .	134
$n_{\text{sadd}}$	Number of spring distributed along $L_{\text{sadd}}$ . . . . .	134
$L_{\text{cab}}$	Cable length without saddle springs . . . . .	135

$n_{\text{layer}}$       Number of layers in a helically twisted cable . . . . . 143

# List of Acronyms

Acronyms not listed in the following table will be explained in the text.

SPW	Semi-Parallel Wire . . . . .	xii
FE	Finite Element . . . . .	xvi
SHM	Structural Health Monitoring . . . . .	5
PE	Polyethylene . . . . .	9
FEM	Finite Element Method . . . . .	15
FD	Finite Difference . . . . .	35
CNN	Convolutional Neural Network . . . . .	37
SSI	Stochastic Subspace Identification . . . . .	37
PSO	Particle Swarm Optimisation . . . . .	49
GA	Genetic Algorithm . . . . .	50
ADC	Analogue to Digital Converter . . . . .	57
FFT	Fast Fourier Transform . . . . .	60
GP	Gaussian Process . . . . .	101
ARD	Automatic Relevance Determination . . . . .	111
MLE	Maximum Likelihood Estimation . . . . .	111
RMSE	Root Mean Squared Error . . . . .	113

# Chapter 1

## Introduction

Cables play a key role in creating the essential connections and bonds that nourish culture and advance economic progress. They serve as key structural members that connect rivers, valleys, and channels. Cables have a lineage that stretches to the the beginning of human civilisation. Their origins date back 28,000 years as one of humanity’s earliest hand-crafted structural members. This craft involved intertwining several thin fibres of natural materials such as hay and grass, yielding a single rope of great strength and flexibility. Cables have proven themselves indispensable, serving as reliable load carrying structural members, and as an invaluable aid during construction. Earliest known depictions of their use are found in ancient Egypt and Assyrian Mesopotamia showing the rope-making process and the use of ropes for lifting massive objects (Figures 1.1 and 1.2).

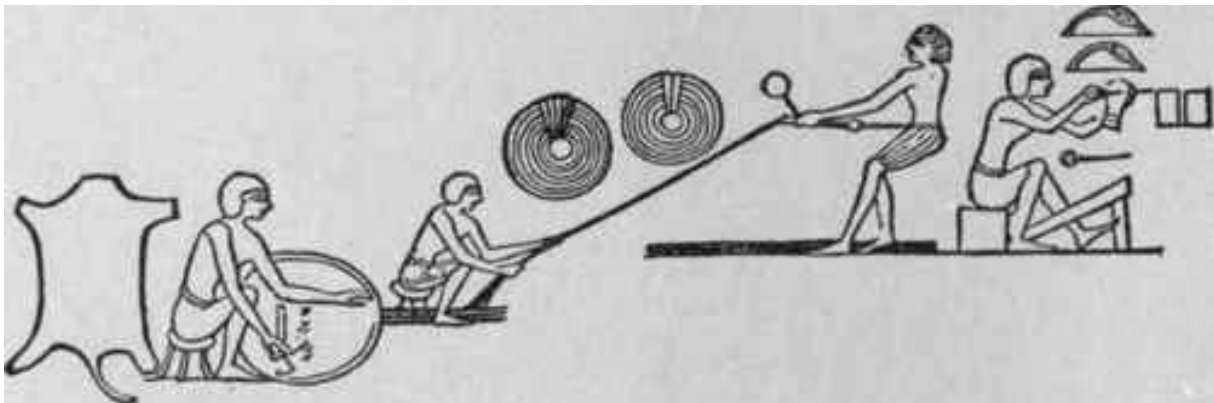


Figure 1.1: Rope making in ancient Egypt. (Courtesy of H. Hill's *The Wonder Book of Knowledge* 1921).



Figure 1.2: Using rope in construction and lifting of heavy object, utilising the lever arm concept in Assyrian civilisation about 1800 B.C. (Courtesy of A. H. Layard's *Nineveh and Babylon* 1859).

The use of ropes also laid the foundation for the development of essential mechanical and engineering principles. Through the application of static laws such as the lever arm and the resultant of forces, ropes helped construct massive monuments like the Great Pyramids of Giza and the Hanging Gardens of Babylon. They exhibit significant engineering advantages primarily due to their structural efficiency. Comprising flexible fibres or wires, cable members offer flexibility and manoeuvrability during construction. They can be fixed to structures with connections or navigated around geometric obstacles, facilitating easy replacement and reattachment. This has helped the development of more efficient and slender structures.

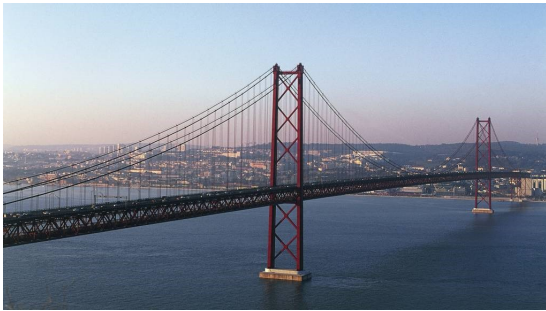
Moreover, cables stand out as environmentally sustainable structural members owing to their capacity to be manufactured from sustainable and recyclable materials. This has prompted a growing interest among engineers from various disciplines. Therefore, they serve as essential members in long-span structures such as cable-supported bridges (of which examples are shown in Figure 1.3), suspended roofs, guyed masts, and deployable aerospace structures. Their adaptability extends their use in electrical engineering as well, commonly serving as power transmission ropes or overhead transmission line conductors. Cables are also used in mechanical engineering applications e.g. elevators, cranes, and hauling devices. Additionally, they are used and in marine applications as tension legs for deep water platforms and buoyant structures.



(a) Airport bridge - Cable-stayed, Germany. (b) New Europe bridge - Extradosed, Romania.

*Photo by: Andreas Wiese.*

*Photo by: FCC group via Structuræ.*



(c) 25 of April bridge - Suspension, Portugal. (d) Geierlay bridge - Suspended foot bridge, Germany. *Photo from: mosel-zweinull.de).*

*Photo by: DeAgostini/Getty Images.*

*Photo from: mosel-zweinull.de).*

Figure 1.3: Examples of cable-supported bridges with cables as main load carrying elements.

Given that cables are long and slender, their integration within structures requires regular inspection and maintenance. This concept is far from novel, with various ancient civilisations recognising the significance of structural preservation and periodic maintenance. For example, the Q'eswachaka rope bridge, a 600-year-old bridge spanning the Apurimac canyon in Peru, serves as an illustrative case (Figure 1.4). In an annual ceremony, local Incan communities convened to replace the straw ropes of the bridge and undertake its reconstruction. This practice reflected an ingrained cultural awareness of the vital importance of periodic structural maintenance.



Figure 1.4: Q'eswachaka bridge crossing the Apurimac canyon in Peru and a close-up of its main straw-woven suspension ropes.

Despite the persistent efforts to implement rigorous structural health monitoring and maintenance practices, incidents of catastrophic structural failures continue to occur. A notable example is the 2018 collapse of the Polcevera viaduct, also known as the Ponte Morandi bridge, in Genoa, Italy. This collapse resulted in the tragic loss of over 60 lives and affected more than 650 people. Investigations revealed that the collapse was primarily due to the sudden failure of the stays comprised of steel cables encased in a prestressed concrete section. The bridge's support system had only  $2 \times 2$  cables per span, thereby having low structural redundancy and making it prone to collapse in the case of a stay failure [1]. Similar bridge designs, motivated by cost reduction but plagued by low redundancy issues, have been replicated in other regions, such as Wadi el-Kuf near Darna in Libya [2] as seen in Figure 1.5.



Figure 1.5: Wadi el Kuf bridge near Al Bayda, Libya. *Courtesy of: Sanad Al-Ahlafi.*

Such sudden failures can be prevented by increasing structural redundancy within a bridge span. However, adding more cables per span leads to an increase in the construction cost, in some instances accounting for up to 20-30% of the total expenditure. Consequently, accurately predicting cable behaviour before and during construction, as well as assessing their performance during in-service stages, becomes essential.

Throughout the phases of design, installation, and in-service health monitoring, various mechanical characteristics of cables come into play. These characteristics do not only facilitate cable installation but also offer insights into their long-term performance. Parameters such as cable form and sag, tension force, damping ratio, and indicators of corrosion or damage are of paramount importance.

Directly measuring these characteristics from the cables is feasible given the accessibility and visibility of cable members, and it can be further enhanced by the incorporation of Structural Health Monitoring (SHM) techniques and sensing units mounted on structural cables. Data collected from cables through e.g. vibration and displacement measurements, strain gauges, acoustic emission, remote laser scanning, and tension force measurement, enable proactive monitoring of cable-supported structures.

Furthermore, when processing measured data, it is essential to consider the inherent nonlinearities in cable behaviour. Validated cable models serve as indispensable tools in this regard, enabling comprehensive interpretation of measured quantities. These models

---

characterise both static and dynamic nonlinearities to establish correlations between the measurements and the cable structural state and health condition.

For instance, in the design phase and the pre-installation cable analysis, nonlinear cable models are used in predicting cable form and sag, aiding in determining the overall unstressed length required for cable installation. Furthermore, detailed cable models based on parameter calibration with experiments also help assessing the effects of inter-wire friction in multiwire cables, determining the nature of flexural rigidity and damping in cables, and predicting load redistribution in adjacent wires due to corrosion and loss in the cross section. Another common cable analysis method is the vibration-based monitoring. Facilitated by sensor installations such as accelerometers, this method offers an indirect mean of determining tension forces using cable models. The models are employed to correlate cable vibration properties with modal parameters, thus enabling efficient tension force identification through inverse analyses.

Despite the challenges associated with extracting relevant information from simplified cable models, advancements in computational machinery and data analysis have significantly improved computational efficiency. Standard personal computers can now handle the creation of intricate models, enhancing reliability and accuracy, particularly when calibrated with measured quantities from monitoring systems. This advancement offers promising solutions to challenges associated with complexity and insufficient instrumentation. However, it is important to acknowledge that a substantial portion of cable analysis is utilised in practical scenarios, such as during cable erection or in-service cable monitoring. Consequently, the formulation of advanced models should not only prioritise sophistication but also consider practicality and ease of application. Introducing parametric formulations for cable models ensures their widespread usability in various practical cases. To strike a balance between detailed modelling and numerical efficiency during design phases, Finite Element (FE) software solvers used for model development play a pivotal role in increasing the models' usability. This approach ensures that they perform detailed analysis while remaining practical and efficient for applications.

This thesis is motivated by the growing need for detailed yet practical models capable of detailed analyses using available Finite Element tools. Such models must strike a balance between sophistication and usability, enabling parameterisation of characteristics like tension force, boundary conditions, axial and bending stiffness, and vibration behaviour. By leveraging advancements in computational machinery, streamlined model formulations, and data analysis, this work seeks to develop parametrised models that not only enhance the understanding of cable behaviour but also provide reliable and efficient assessment frameworks. Ultimately, these models aim to address the critical demands of structural monitoring throughout design, erection, and in-service phases.

This thesis starts in Chapter 2 briefing on cable systems, including cable types, connections, and vibration control devices. In Chapter 3, the groundwork for the theoretical and numerical methodologies used for modelling cable systems is introduced. The state-of-the-art cable models are also examined based on their assumptions, applications, and limitations. This perspective of examining models is adopted further to propose a classification table of cable models aimed at systematically navigating their characteristics and components, and serve as a reference for selecting a cable model for application.

Then, Chapter 4 introduces two case studies conducted on cable force identification through vibration measurements on two bridges. It compares commonly used simplified methods and more intricate nonlinear numerical models. All throughout, a discussion on the mechanical representations for each model is made along with a comparison of the cable parameters e.g. tension force and bending stiffness. These discussions expand on clarifying the distinctions, respective applications, limitations, and the challenges encountered in the cable force identification process.

Further, Chapter 5 introduces a FE modelling framework to account for the mechanical effects of deviating supports such as saddles and block deviators. This modelling framework demonstrates high accuracy in predicting the contact point with geometric supports along with tension forces when compared to other existing models. The methodology presented in this chapter provides a practical FE approach for handling complex cable arrangements in system identification techniques, ensuring increased accuracy in force-response relationships.

Further, the focus continues in Chapter 6 to address the bending behaviour of structural cables, specifically the Semi-Parallel-Wire (SPW) cable. This study proposes a FE modelling of SPW cables, utilising Gaussian Process regression as a surrogate model to optimise computational efficiency. The study delves into the impact of inter-wire slip, bending curvature, and cyclic loading on cable behaviour, highlighting the necessity of considering wire slipping for precise predictions across diverse applications. Finally, Chapter 7 discusses the practical relevance of the presented models for applications by discussing the parametric formulations and their application cases.

This work ends with a summary and discussion on the scope for further work in Chapter 8.

# Chapter 2

## Structural cable systems

### 2.1 Introduction

To gain a comprehensive insight into how cable components affect model formulation in terms of their mathematical representation, it is important to understand the distinctions among various multiwire cable types and their anchoring systems. Each cable type is subjected to different loading and stiffness conditions that depends on its cross sectional composition and interactions at the cable connections with the structure. Therefore, their composition plays a pivotal role in understanding how each cable type transfers forces between its wires, and interacts with the supporting structures at the boundary. Equally important is understanding the tension force transfer mechanism into the structure using the different support types.

This chapter addresses these aspects by describing the main types of cables, anchoring devices, and external support types in use, and how each type of cable or support can be modelled as an assumption in the FE model.

### 2.2 Cable types

A multiwire structural cable is composed of individual wires coiled in strands or arranged in parallel configurations. Recent developments of cable types has focused on producing multiwire high strength cables with more compact cross sections. Structural cables are classified according to the Eurocode into four groups: group A for a single steel tension rods, group B for multiwire ropes, group C for parallel wire or parallel strand cable systems, and group D for prefabricated parallel wire systems [3]. The main multiwire cable types are included in the following categories:

- Stranded ropes (group B)
- Locked-coil ropes (group B)
- Parallel strand systems (group C)
- Parallel wire systems (group C)

- Prefabricate parallel wire systems (group D)

The selection of a specific cable type depends on the design criteria and mechanical properties such as ultimate strength, fatigue strength, modulus of elasticity, etc., and structural and practical considerations, such as cable erection methods, wind conditions, and the type of anchorage employed. A comprehensive understanding of these factors ensures the optimal choice of a cable type for a given application. Given that this work focuses on multiwire cables, the following are the main multiwire structural cable types.

### 2.2.1 Stranded ropes

The stranded rope is a type of cable that comprises a minimum of two layers of wires twisted around a straight centre wire, where each successive wire layer is twisted in the opposite direction to the previous one to improve the self-compacting properties under tension. This helps counteract nonlinear wire elongation caused by the radial component of tension and strand compaction. The strand can be enclosed in a Polyethylene (PE) pipe filled with grout to prevent corrosion. Alternatively, for enhanced protection against humidity and corrosion, galvanised wires, known as Galfan strands, can be utilised.

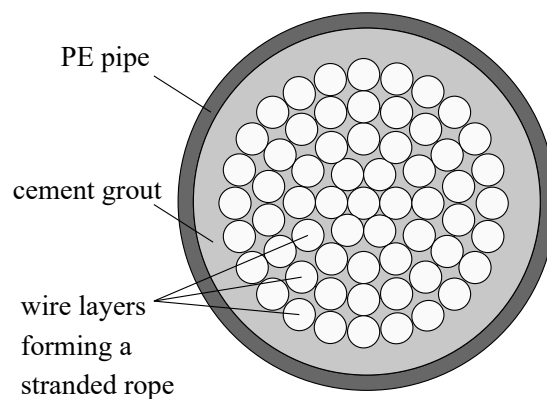


Figure 2.1: An example cross section of a galvanised spiral strand rope.

However, the twisting of the wires leads to a decrease in the modulus of elasticity to approximately 20-25% of that of straight wire, and the breaking strength of the individual wire is therewith reduced to 10% [4, 5].

The multistrand cable has a wide area of application, where medium to small size cables are used e.g. in lifting devices, towers and guyed masts, offshore anchoring systems and stay-cables. They are also used as cables for suspension bridges. However, parallel and semi-parallel wire cables prove more beneficial than when larger cables are required as they are not subjected to strength and stiffness reduction due to their geometry and would need less material, in addition to their more compact cross section.

### 2.2.2 Locked-coil ropes

This cable type comprises a stranded rope surrounded by an enveloping section. The central core consists of one or several layers of stranded round wires around a straight guide round wire. The wire layers are stranded in alternating directions, ensuring a twist-free rope configuration post tensioning. The enveloping section is usually made using Z-shaped wires. When the cable is stressed, the Z-shaped outer wires press against each other, creating a 'lock' that prevents water intrusion. This also results in a more compact cross section.

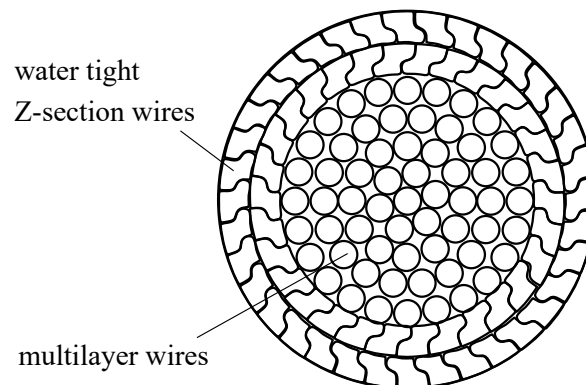


Figure 2.2: An example cross section of a medium sized Locked-coil rope cable.

The advantages of such cable types lie in their corrosion protection. This is achieved by the water-tight locked Z-shaped outer wires in addition to the galvanisation of wires. Corrosion indicators can also be checked with surface inspection [5]. However, there are known disadvantages to consider, such as reduced cable stiffness and strength due to the reverse laying of wires, susceptibility to creep, and reduced tensile and fatigue strength. The compact assembly of these cables increases also the friction between the wires. The increase in friction and the helical arrangement of wires leads to a longitudinal transfer of axial forces between the wires. When subjected to bending stresses from e.g. wind-induced vibrations, transverse loads, or flexural constraint at the cable end, the increase in cyclic wire stresses reduces the fatigue strength of individual wires.

### 2.2.3 Parallel strand systems

This type of cable consists of several high tensile strength strands, each comprising 7 wires. Multiple single layer strands are arranged in parallel and enclosed within a pipe casing along their free length. As they approach the anchorage point, they separate to allow each strand to be individually stressed.

Owing to their strand-per-strand installation inside the cable, parallel strand cables are renowned for their ease of stressing, replaceability, and cost-effective transportation. This

makes them a popular choice as a structural cable. It also asserts their leverage in recent specifications, when ease of cable replaceability, restressing, and assessment is required [6]. Additionally, given that the individual strands are laid in parallel and have a flexible material as a filler, there is less transfer of forces between the wires, and the effective bending stiffness of such a cable type is generally close to the minimum value.

Protection against corrosion for parallel strand cables is made by a hot extrusion of a PE layer over the strands. The gap between the strands and around the duct is usually filled by a flexible material such as wax or grease for an additional protection and ease of installation.

However, it's worth noting that for cables with larger diameters, parallel strand cables exhibit a high void ratio per cross section [4, 5], which does not make them favourable when large diameter cables are required.

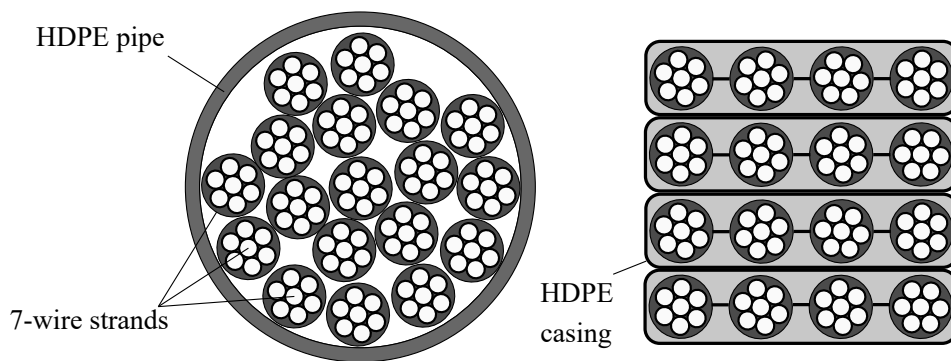


Figure 2.3: Examples of cross section types of a parallel multi-strands cable.

## 2.2.4 Parallel wire systems

Parallel wire systems were developed to avoid the strength and stiffness reduction originating from wire twisting [5]. The wires are laid in parallel in a more compact cross section giving a higher steel-per-void ratio. To ensure durability and resistance against corrosion, galvanised and zinc coated wires are employed. The cable is further protected by encasing it within a PE pipe and grouting it with a soft filler material.

In the current practice, suspension bridge main cables employing parallel wires typically consist of 5-5.5mm diameter wires, while stay-cables more commonly use 7mm wires. These can vary in size depending on the required tension force [5].

However, it's important to note that a change in geometry due to cable sag or support deviation can lead to wire spreading inside the cross section as shown Figure 2.4. This can lead to abrasion of the HDPE duct casing when cables are saddled or deviated over a support. It can also lead to higher frictional pressure on wire surfaces, therefore inflicting loss of Galvan

coating and a probable reduction of wire cross section. In response to this concern, a modified version of this cable, known as the SPW cable, was later introduced.

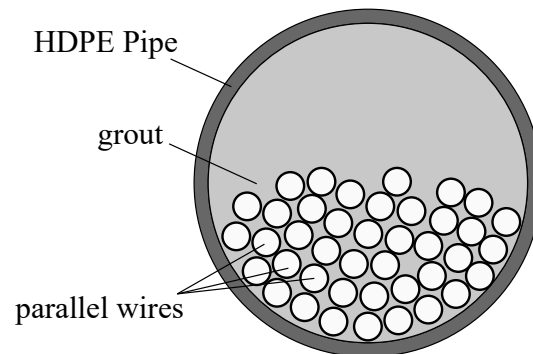


Figure 2.4: An example cross section of a parallel wire cable noting the wire spreading effect.

### 2.2.5 Semi-parallel wire cables

This cable system consists of a multiwire bundle intentionally twisted with a small lay angle to facilitate self-compaction when subjected to tension. This twisting mechanism effectively prevents the wires from spreading within the casing, and provides a compact cross section suitable for large diameter cables. Here, it is essential to ensure that all wires have the same lay length, and that the maximum lay angle does not exceed  $5^\circ$ , as exceeding this limit could adversely affect the wires' strength and stiffness.

Corrosion protection is achieved by applying an extruded PE cover directly onto the wire bundle. Moreover, eliminating the need for grout and spiral rope to secure the cross section of the cable allows a preferable reduction to the void ratio consistent along the cable length. This reduction is also advantageous for minimising wind-induced vibrations. The composition of this cable, its detailed modelling, and its mechanical characteristics under various loading are discussed in depth in Chapter 6.

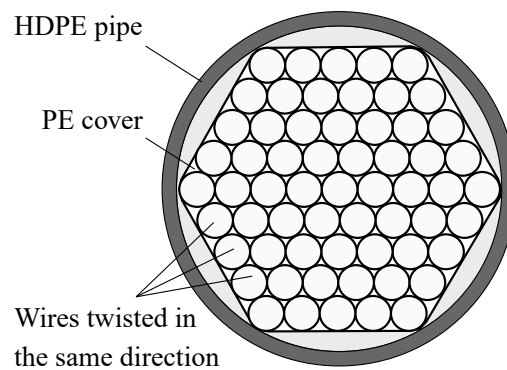


Figure 2.5: An example cross section of a SPW cable with wires twisted concurrently with the same lay length.

To gain insight into how the different cable types transfer their forces to the substructure, it is important now to delve into the types of connections and anchorages used.

## 2.3 Cable anchorages

The mechanism for force transfer between the cable and the structure depends on the specific type of anchorage employed at cable ends. The anchorage is a component used to transfer tension forces from the cable into the structure. Certain anchorages secure the cable firmly to the structure, thereby suppressing any rotations at the cable end. In contrast, other anchorages are engineered solely to transmit forces, consequently permitting the release of end rotations. Understanding the load transfer mechanism is important for determining appropriate assumptions for boundary conditions in cable models. In this context, anchorage types are categorised based on their respective load transfer mechanism, which include the transferring forces and moments, exclusive transfer of nodal forces at cable ends, and the use of deviator supports to transfer forces.

### 2.3.1 Cable anchor

The cable anchor serves as a terminal link employed to securely fasten the cable to the bridge deck as well as the pylon. This type of termination is generally used with group C type cables i.e. parallel strands and parallel wire cables. When situated within the deck, the implementation of bearing sockets or anchorage tubes, such as the HiAm anchorage, is prevalent.

This anchorage facilitates fixing the wires or single layer strands into the body of the anchor by secured fastening, where wire or strand passes through a tear-shaped hole in the anchor

end plate, then fixed in place using conical wedges. Minimum vacant spacing is required to the back to the anchor to facilitate placing the hydraulic jack on site used for tensioning the wires or single layer strands.

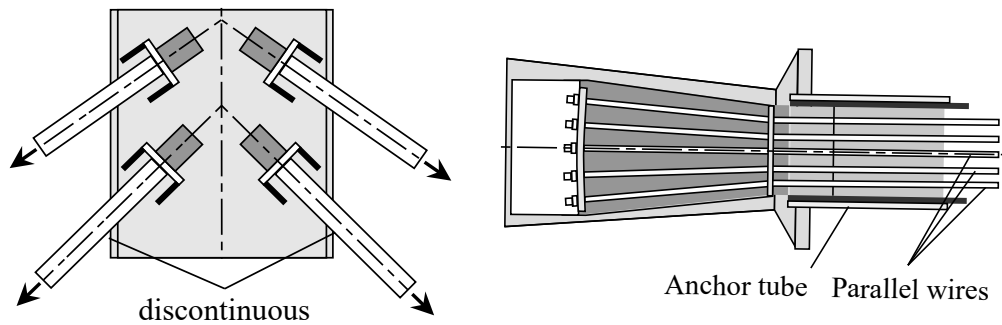


Figure 2.6: Examples of clamping cable anchors. Cable anchor in a pylon (left) and anchor socket at bridge deck (right).



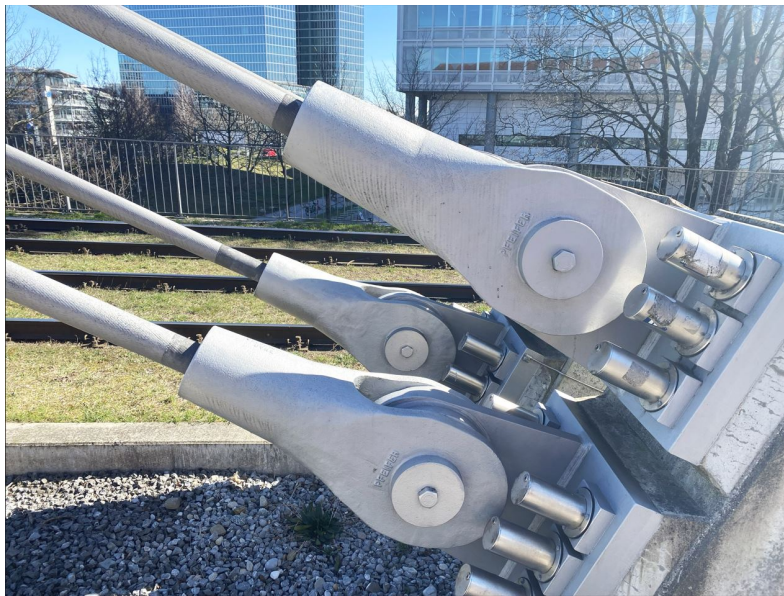
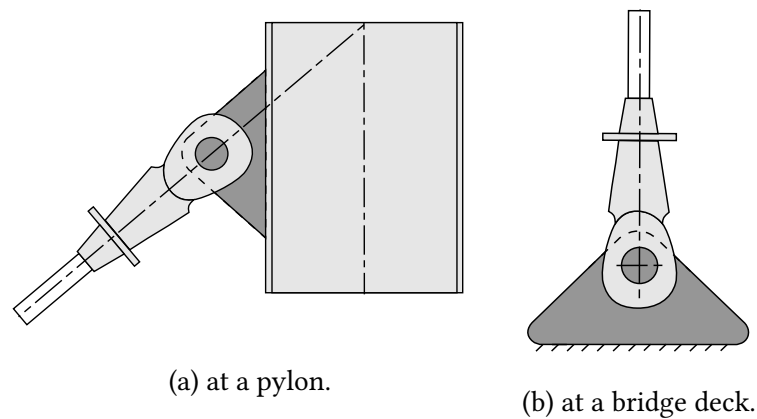
Figure 2.7: Cable anchorage tubes of a railway bridge in Istanbul, Turkey.

In order to minimise the impact of counter-curvature at the support and introduce flexibility, the cable section near the ends is either filled with a ductile substance, or the grouting material is removed to facilitate wire tensioning. As a result, both the bending stiffness and the rotational rigidity at the ends are reduced [7, 8]. Consequently, this rotational stiffness and reduced bending stiffness value at the ends should be accounted for.

### **2.3.2 Clevis connection**

For group B cables with small and medium diameters, a decoupling connection is implemented at the cable ends achieved by incorporating a hinge connection. The cable is affixed to a rigid plate that, in turn, connects to a clevis securely anchored to the structure.

This connection allows for angular changes between the cable and the substructure. Clevis and Spelter sockets connections are designed to accommodate bending and adapt to changes in rotations, enabling the transfer of nodal forces to the structure. Therefore, it might be intuitive to model these connections in Finite Element Method (FEM) as hinged nodes. However, under high tension forces, friction around the clevis resulting from bearing stresses on the connecting bolt may restrain rotations. To address this issue, it is advisable to consider the inclusion of calibrated rotational stiffness. This adjustment ensures accounting for the potential suppression of rotations, providing a more comprehensive representation of the system's behaviour.



(c) Spelter socket with pin at the Schenkendorf bridge in Munich, Germany.

Figure 2.8: Examples of hinged connections.

### 2.3.3 Saddles and deviators

Saddles and curved deviators are used to change the cable axis to transfer forces to the support. These members are frequently utilised in diverse bridge designs, such as externally prestressed box girders, suspension bridges, and extradosed bridges. In bridge pylons, the saddle comprises a pre-bent arc of steel guide tube with a saddle radius not less than 30 multiple of the cable diameter, either cast within the encompassing concrete or attached to a steel framework through stiffening plates [3].

Conversely, deviators in external tendons are typically fabricated using guide pipes and HDPE arc ducts, which are embedded into the concrete block anchorages or diaphragms

[9]. These ducts are designed to navigate the external tendon through the concrete block while facilitating load transmission through bearing. Consequently, the precise geometric configuration of the guiding duct takes a pivotal role in the mechanics of load transfer. The effective modelling of such support type remains an active area of research, and it is discussed in detail in Chapter 5. Figure 2.9 shows a schematic of such supports.

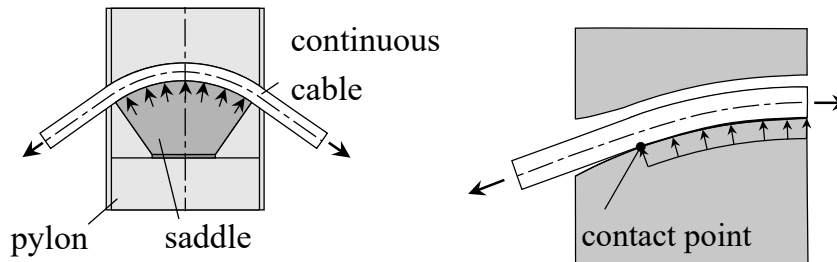


Figure 2.9: Examples of deviating supports. A cable saddle used in suspension, cable-stayed and extradosed bridges (left), and a box-girder bridge deviator for external tendons.

## 2.4 Vibration control devices

Cables represent long and flexible structural elements situated within areas with small surface friction with high wind speeds, e.g. rivers or valleys. Owing to their compact cross sectional configuration, material, and high tension forces, they also possess low inherent damping. Consequently, these cables become susceptible to oscillations prompted by the wind, such as instances of galloping induced by rainfall or ice accumulation. Their high-amplitude oscillatory motion leads to high stress cyclic loading that reduces their fatigue strength, particularly if the vibration frequencies from e.g. wind gusts match with the cable's natural frequencies. Additionally, high amplitude vibrations hold the potential to induce bridge vibrations and can cause instability to a bridge's overall structural integrity.

Several methods are used to control cable vibrations including the use of damping devices and intermediate connections to either reduce the vibration amplitude or increase the vibration frequency. Aerodynamic instabilities are commonly controlled using damping devices. The prevailing approach involves attaching dampers to a specific location on the cable, often in proximity to or directly connected to the anchorage on the deck. Dampers come in several types but can be categorised into: internal anchorage dampers, friction dampers, and external viscous dampers mounted in proximity to the support.

While internal dampers are placed at the installation or replacement of cables, external viscous dampers are usually mounted post-construction to reduce vibrations. On the other hand, friction-based dampers are placed when a bundle of cables, usually two or four, are in close proximity. The dampers then dissipate the vibrations energy and transform it into heat using friction discs placed inside the damper [4, 5]. Dampers are commonly modelled as damping elements or damping and spring elements. Figure 2.10 shows examples of dampers with common model representation of each type.

In addition to dampers, attaching supplementary ropes to the main stay-cables can also be effective in mitigating stay-cable vibrations. These ties significantly reduce low frequency oscillations through added fixation nodes along the cable, which leads to an increase in the natural frequencies of the cables as seen in Figure 2.11.

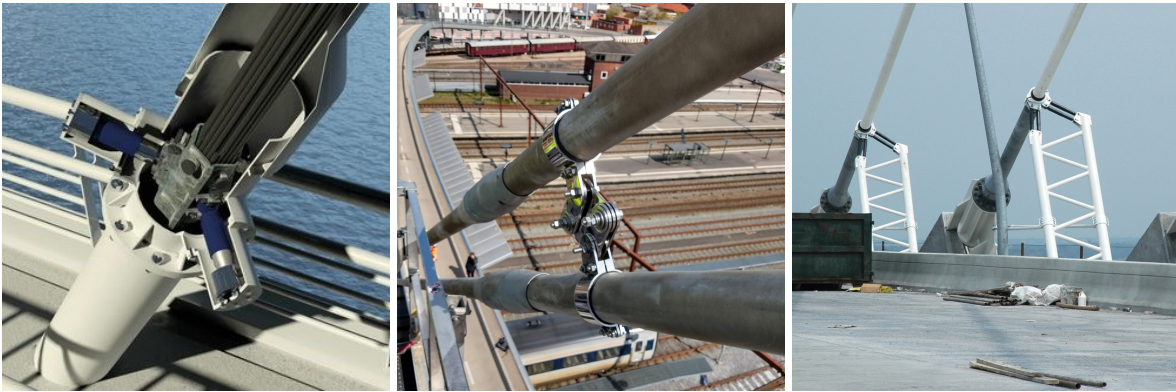


Figure 2.10: Main types of damping devices: internal support damper (left), friction damper (middle), and external damper (right). Courtesy to: Freyssinet (via Le Moniteur), DAMPTECH, and ravenelbridge.net & Freyssinet (left to right).



Figure 2.11: Cross ties connected to stay-cables of the Normandy bridge in France. (Courtesy of David Henry - Getty Images).

# Chapter 3

## Cable analysis models

### 3.1 Introduction

Having examined the technology of structural cables, various types of cross sections, and supports in the preceding chapter, the focus now shifts to a comprehensive exploration of cable modelling. This chapter begins with a brief historical background on the evolution of cable models, then it delves into exploring the modelling process for cables and cable supports with a detailed analysis of the underlying assumptions and their implications on cable dynamic properties. Furthermore, existing models in the literature are discussed, reviewed, and systematically classified and categorised based on their assumptions. This aims to provide a cohesive understanding of the diverse approaches employed in cable modelling for system identification and their corresponding limitations in practice.

### 3.2 History of cable models

The history of cable models can be traced back to Pythagoras, who discovered a mathematical relationship between the length and tension of a string, and the sound it produces [10]. This discovery hinted at the possibility of deducing a mathematical relationship between cable properties (i.e. mass, length, tension) and its vibration frequency.

Later in the 17th century, Marin Mersenne and Galileo Galilei were the first to formulate a validated mathematical equation explaining the relationship between length, tension and mass of a string and its natural frequencies [11]. This paved the way for the development of later cable models. Triantafyllou [12] summarised the previous research on the dynamics of a horizontal string until 1980.

### 3.3 Cable analysis models and system identification

Cables, as structural elements, demonstrate high efficiency in carrying both tension and transverse loads compared to other structural components. Their slenderness and flexibility make them primarily subject to tension forces, though they also experience some bending stresses. Unlike structural beams, cables rely on their axial stiffness and geometric form to carry transverse loading. This subjects the entire cross section to high normal stresses. Conversely, beams resist loading through bending stiffness, which often results in maximum stresses at the edges of a cross section and minimal stresses near the centre.

For example, when comparing the two structural members—both carrying the same uniformly distributed load of 24 kN/m (equivalent to 10 times the beam's self-weight) across a 30 m span, as shown in Figure 3.1—the steel beam requires a cross sectional area approximately 3.25 times larger than that of a solid section cable when designed for the same maximum stress of 320 MPa. To ensure a fair comparison, the cable's sag is kept within the vertical envelope of the beam's depth. Here, a linear elastic analysis is used, and the cable is assumed to be flexible, with no bending stiffness.

Unlike beams, which experience a linear stress distribution, cables adopt a sagging geometry that results in uniform axial stresses within the cross section, significantly improving material efficiency. Additionally, cables are made from high-strength materials, further reducing the required cross section and enhancing efficiency—making them a more favourable choice in long-span structures. In this regard, the cable achieves the same load-bearing capacity using 11 times less material, though it experiences a higher stress of 1015 MPa, which remains within typical ultimate stresses for cable materials.

However, their use introduces challenges in anchoring in comparison with beams, as the high tension forces generate substantial horizontal reactions at the supports. These forces require robust fixation solutions, such as saddles, backstays, or large supports, to effectively transfer loads. Additionally, in plastic analysis scenarios, the beam offers higher reserve capacity for plastic deformation.

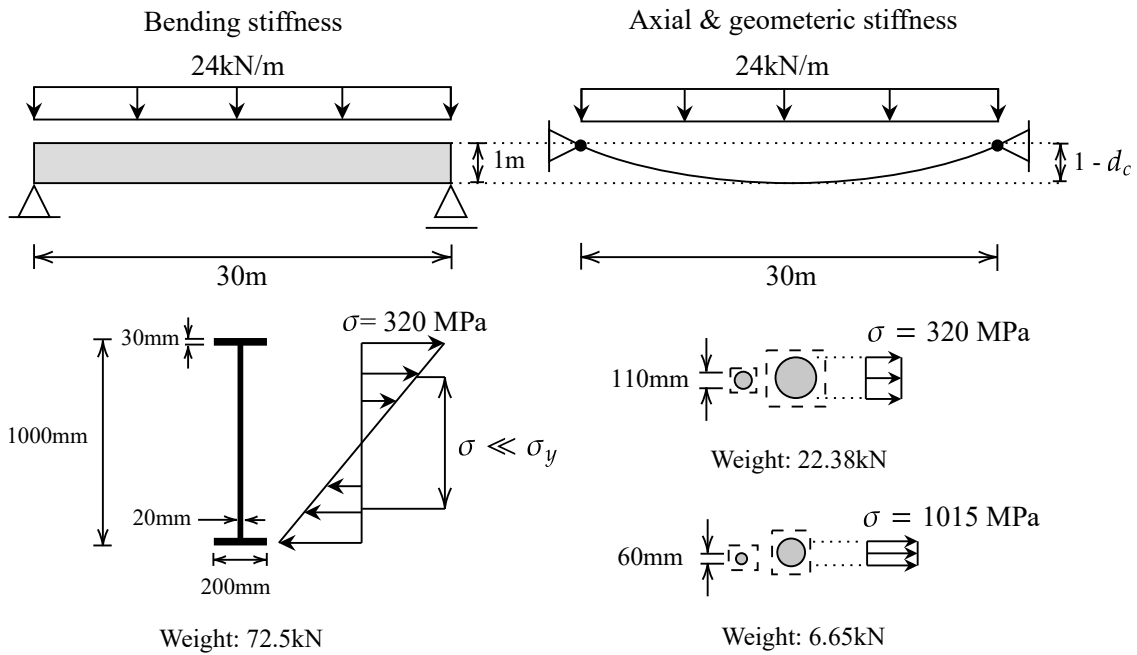


Figure 3.1: Carrying a uniform load via bending stiffness (left) v.s. via axial and geometric stiffness i.e. tension and sag. It shows that for long span structures, cables achieve high material reduction in the cross section [5].

The effectiveness of cables in bearing loads is closely tied to the form they take under loading [13, 14]. While cables are commonly associated with their hyperbolic catenary shape under self-weight, they possess a finite bending stiffness. This introduces an interaction between axial forces and bending moments, which considerably affects their internal stress distribution.

Due to the high slenderness, for any non-vertical cable, its internal stress state is closely linked to its geometry through the compatibility and equilibrium conditions. Considering the function of cables in engineering structures and specific aspects of structural design for strength, serviceability and fatigue, several types of analysis are of interest in relation to the mechanical behaviour:

- (1) the determination of the static equilibrium state under permanent loads,
- (2) the determination of modal properties of vibrations around the static equilibrium,
- (3) the computation of dynamic response under transient excitation.

Discussing the previous three types of cable analysis (1) (2) and (3), classical analytical solutions for the catenary shape under simple load and support conditions and neglecting bending stiffness exist for type (1) as included in [15–17], whilst numerical large-displacement geometrically nonlinear analysis are performed to determine the equilibrium state under

permanent loads and the pre-tension state in this condition. The analysis for (2) is directly based on (1) through a linearisation of the stiffness at static equilibrium as a tangent stiffness matrix and an Eigenvalue analysis. Such linearised properties are then representative of small amplitude vibrations around the static equilibrium. Dynamic analyses for (3) can be linearised by performing a time-domain analysis in mode space using the results of (2) or by nonlinearly integrating the system obtained in (1) to consider the transient load effects.

In addition to these direct analyses, inverse analysis techniques have attracted interest for system identification purposes. Specifically, measurements of cable vibrations can be a cost-effective way of determining cable forces from the extracted dynamic properties. Such methods are fundamentally based on (2) and highlight the importance of modal characteristics. As a linear concept, modes and modal superposition based analyses of the fundamentally nonlinear system of a cable are then defined in relation to the solution of (1) and only accurate for small-amplitude vibrations around this static equilibrium.

In the absence of any change in the loading or the surrounding conditions, the physical characteristics of the cable, including tension force, bending stiffness, and self-weight, remain constant. Therefore, discrepancies observed in the outcomes of cable models can be directly attributed to the assumptions made within these models. These assumptions encompass a spectrum of factors, ranging from geometric nonlinearity and axial and bending stiffness to tension force distribution along the cable and self-weight considerations. Thus, refining these assumptions represent essential steps in advancing the understanding of cable behaviour and enhancing the accuracy of cable models in practical applications. The implementation of these models for application is commonly made using the FEM for the flexibility and accuracy it provides for structural modelling. It is thus used here and the fundamentals for its implementation are detailed next.

### **3.4 Fundamentals of Finite Element formulation for geometric nonlinear analyses**

The contributions of this research and the studied cases are made using FEM. This section provides an insight into the mathematical formulation, delving into the details of the matrix-formed description of geometric nonlinear analyses.

In the context of linear FE analysis, certain foundational assumptions are made. Firstly, displacements are assumed infinitesimal and have no effect on the internal force distribution. Secondly, the material is assumed linearly elastic, and the boundary conditions remain

unchanged throughout the application of external loads. These assumptions collectively lead to the following fundamental equation [18]:

$$\mathbf{K}\mathbf{U} = \mathbf{R}. \quad (3.1)$$

Here,  $\mathbf{K}$  is the stiffness matrix,  $\mathbf{U}$  is displacement vector, and  $\mathbf{R}$  corresponds to the load vector. The assumption that the displacements remain infinitesimal influences the derivation of the matrix  $\mathbf{K}$  and the load vector  $\mathbf{R}$ . Additionally, this formulation also assumes that the relationship between strain and displacement remains consistent and unaffected by the displacements of the individual elements.

However, in cable FE modelling, it is necessary to consider the geometric change effects in the analysis, especially in the formulation of the stiffness matrix  $\mathbf{K}$ . This is because the displacements in cables are not infinitesimally small, and the relationship between strain and displacement can change as the cable deforms.

When loads are  $\delta\mathbf{R}$  instead of  $\mathbf{R}$  and the corresponding displacements are not  $\delta\mathbf{U}$  in Equation (3.1), it necessitates the use of a nonlinear analysis. Moreover, in cases where a boundary condition experiences changes under loading (e.g. a degree of freedom that transitions from being unconstrained to constrained at a specific load stage) the system's response remains linear only prior to the change in boundary condition. This scenario commonly arises in the examination of cable-support contact problem.

The fundamental problem in a general nonlinear analysis revolves around determining the equilibrium conditions of a body under applied loads undergoing large displacements. The loading can be applied incrementally, either as dynamic transient load accounting for inertia effects, or through an iterative stepwise loading in a static form-finding analysis. The equilibrium conditions of a FE system representing the member under consideration can be written as follows

$$\mathbf{R}^t - \mathbf{F}^t = 0, \quad (3.2)$$

where  $\mathbf{F}$  denotes the internal force vector corresponding to the stresses within the nodal points of the element, and  $\mathbf{R}^t$  is the nodal external force vector applied at time  $t$ . In the case of truss or cable elements,  $\mathbf{R}$  represents the concentrated nodal loads matrix. Also, in a dynamic analysis, the vector  $\mathbf{R}^t$  would include the inertia, damping and external stiffness (e.g. from springs).

Further, the equilibrium relationship presented in Equation (3.2) must remain fulfilled over the entire duration of load application. This encompasses the temporal domain, where the time variable, denoted as  $t$ , can span from zero to the maximum designated time. In static analysis, time serves solely as a convenient parameter signifying varying levels of load

application, and distinct structural configurations (e.g. change in a nodal restraint to represent displacement-based contact).

In some nonlinear static analyses, it is possible to compute the equilibrium conditions associated with incremental load levels without the necessity of also resolving other equilibrium states. Nonetheless, when the analysis incorporates nonlinear conditions dependent on geometry, material nonlinearity, or time-dependent phenomena, it is necessary to solve for the equilibrium relations outlined in Equation (3.2) across the entire time steps in a systematic, stepwise incremental solution. However, due to computational constraints, practical applications often necessitate an incremental solution, which is automatically executed, involving incremental load steps to ultimately attain the cumulative applied load in a given time step.

The basic approach in a stepwise incremental solution is to assume that the solution at a discrete time point  $t$  is already established, and seek the solution for the subsequent discrete time point  $t + \Delta t$ , where  $t + \Delta t$  signifies a suitably selected time increment. Consequently, when considering Equation (3.2) at the time  $t + \Delta t$ , the equation can be expressed as follows:

$$\mathbf{R}^{t+\Delta t} - \mathbf{F}^{t+\Delta t} = 0. \quad (3.3)$$

Assuming that  $\mathbf{R}^{t+\Delta t}$  is independent from the deformations and the solution is established at time  $t$ , we can write:

$$\mathbf{F}^{t+\Delta t} = \mathbf{F}^t + \mathbf{F}, \quad (3.4)$$

where  $\mathbf{F}$  represents the increment in nodal point forces corresponding to the increment in element displacements and stresses from time  $t$  to time  $t + \Delta t$ . This vector can be approximated using a tangent stiffness matrix  $\mathbf{K}^t$ , which corresponds to the geometric and material conditions at time  $t$ , as follows:

$$\mathbf{F} = \mathbf{K}^t \mathbf{U}, \quad (3.5)$$

where  $\mathbf{U}$  is a vector of incremental nodal point displacements and

$$\mathbf{K}^t = \partial \mathbf{F}^t / \partial \mathbf{U}^t. \quad (3.6)$$

Consequently, the derivative of the internal element nodal point forces  $\mathbf{F}^t$  concerning the nodal point displacements  $\mathbf{U}^t$  is represented by the tangent stiffness matrix. Upon incorporating Equation (3.5) and Equation (3.4) into Equation (3.3), the following is derived:

$$\mathbf{K}^t \mathbf{U} = \mathbf{R}^{t+\Delta t} - \mathbf{F}^t, \quad (3.7)$$

and solving for  $\mathbf{U}$ , we can calculate an approximation to the displacements at time  $t + \Delta t$

$$\mathbf{U}^{t+\Delta t} = \mathbf{U}^t + \mathbf{U}. \quad (3.8)$$

The exact displacements at the time  $t + \Delta t$  are determined by the applied loads  $\mathbf{R}^{t+\Delta t}$ . In this context, an approximation to these displacements is computed exclusively in Equation (3.8), primarily due to the utilisation of Equation (3.5). However, given the assumption used in Equation (3.5), this solution may be subject to considerable errors caused by an ill-chosen time or load step sizes. Therefore, practical application necessitates iterative procedures to attain a sufficiently accurate solution for Equation (3.3). One commonly employed iteration technique in FE analysis is based on the Newton-Raphson method.

This method extends the incremental approach outlined in Equation (3.7) and Equation (3.8). Following the calculation of an increment in nodal point displacements, which defines a new total displacement vector, the incremental solution presented earlier can be reiterated using the presently established total displacements instead of the displacements at time  $t$ .

For  $i$  iterations, the equations used in the Newton-Raphson iteration scheme are given as:

$$\mathbf{K}_{i-1}^{t+\Delta t} \Delta \mathbf{U}_i = \mathbf{R}^{t+\Delta t} - \mathbf{F}_{i-1}^{t+\Delta t} \quad (3.9)$$

$$\mathbf{U}_i^{t+\Delta t} = \mathbf{U}_{i-1}^{t+\Delta t} + \Delta \mathbf{U}_i, \quad (3.10)$$

with the following initial conditions:

$$\mathbf{U}_0^{t+\Delta t} = \mathbf{U}^t; \quad \mathbf{K}_0^{t+\Delta t} = \mathbf{K}^t; \quad \mathbf{F}_0^{t+\Delta t} = \mathbf{F}^t.$$

Subsequently, in successive iterations, the latest approximations for nodal point displacements are employed for the evaluation of the corresponding element stresses, as well as nodal point forces denoted as  $\mathbf{F}_{i-1}^{t+\Delta t}$ , and the tangent stiffness matrix represented by  $\mathbf{K}_{i-1}^{t+\Delta t}$ .

The load vector  $(\mathbf{R}^{t+\Delta t} - \mathbf{F}_{i-1}^{t+\Delta t})$  signifies an unbalanced load vector that is yet to be counteracted by the element stresses. Consequently, an increment in nodal point displacements becomes imperative. This iterative process of updating nodal point displacements persists until the out-of-balance loads fall below a predefined tolerance threshold. This threshold is usually set to a small value to reduce any residual forces and increase accuracy.

The generalised iteration scheme for nonlinear analysis has been adopted in several studies. In defining large-displacement analysis, both Lagrangian and updated Lagrangian formulations find frequent application [18]. Numerous other simplified formulations are rooted in the principles discussed in this section. For instance, in studies involving cable-struts structures, where structural stiffness and deformation are influenced by cable prestress and geometry, researchers have introduced the formulations for application [19–22]. Others also use a co-rotational iteration method for effective representation of the stiffness matrix in FE analysis [23, 24].

Additionally, recent advancements propose a two-step perturbation scheme for fully analytical solutions for equilibrium of inclined inextensible cables under gravitational loads aimed at enhancing the analytical and parametric study of cable structures [25].

Similarly, the numerical models developed in this research employ a formulation offered by SOFiSTiK Finite Element solver, which is also grounded in the FE formulation detailed in this section. In these models, cable elements are represented either as truss or cable elements (truss elements without compression), or as beam elements. The choice depends on the need to account for bending stiffness and boundary conditions, especially when cable action under significant displacements comes into play.

This formulation is termed as a geometric nonlinear analysis to denote the composite nature of the stiffness matrix. It encompasses the linear stiffness matrix, the finite large-displacement stiffness matrix, and the geometric stiffness matrix originating from the pre-stress component.

### **3.5 Cable models main assumptions**

In the literature, various cable models have been developed, with each having assumptions that reflect their levels of complexity. These assumptions span a range of factors, such as bending stiffness, boundary conditions, assumed self-weight, analysis order, and how cable cross section is presented.

These models serve different purposes in describing the static and dynamic behaviour of cables. In cable force identification from vibration measurements, models are employed for inverse analysis to estimate the tension force. Similarly, in vibration-based monitoring, the tension force is estimated by comparing identified natural frequencies from actual measurements with those predicted by the model. This estimation relies on inverse analysis, where the tension force is identified by minimising the difference between the identified natural frequencies and the ones provided by the model. However, the accuracy of the estimated tension force depends on the model's precision, making it evident that the model assumptions play a crucial role in influencing the estimation.

To gain a more comprehensive understanding of how these assumptions impact natural frequency outputs, a quantified example is presented. Specifically, a cable in a horizontal setup is considered with material and mechanical properties as outlined in Table 3.1.

Table 3.1: Parameters for a reference cable example. Example is used to examine the effects of several assumptions related to the cable.

Parameter	Symbol [Unit]	Value
Section area	$A$ [cm <sup>2</sup> ]	78.54
Modulus of elasticity	$E$ [GPa]	200
Bending stiffness	$EI_{ref}$ [kN.m <sup>2</sup> ]	1000
Unit weight	$\gamma$ [kN/m <sup>3</sup> ]	78.5

### 3.5.1 Analysis type and sag effects

When subjected to external forces, cables naturally adapt their shape to efficiently carry these axial loads. The form-finding at static equilibrium has significant implications on the dynamic behaviour.

Although linear analysis offers a quick and computationally efficient way to assess tension forces, it is limited in its ability to account for deformation and nonlinear cable form changes. To address these aspects and accurately represent the cable's deformation state and internal forces, a different type of analysis is necessary. This can be achieved by employing a geometrically nonlinear FE analysis. By accounting for geometric nonlinearity, the updated tangent stiffness can be integrated into the Eigenvalue analysis to determine natural frequencies as highlighted in Section 3.4.

The impact of geometric nonlinearity becomes especially evident in cables with high sag, low tension, or long length, or a combination thereof. These conditions lead to an increase in the natural frequencies of symmetrical vibration modes, most notably the first symmetrical mode. This analysis proves valuable when dynamically assessing cables under transient loads, as the stiffness matrix is continuously updated at each time step based on the cable's changing loading conditions.

To illustrate the effects of geometric nonlinearity on the dynamic properties, a comparison is made between a linear model (taut-string) and a geometrically nonlinear model solved using FEM, here called the sagged string. Figure 3.2 provides a visual example comparing the Eigenfrequencies of the linear taut-string theory and a flexible cable with geometric stiffness modelled with FEM.

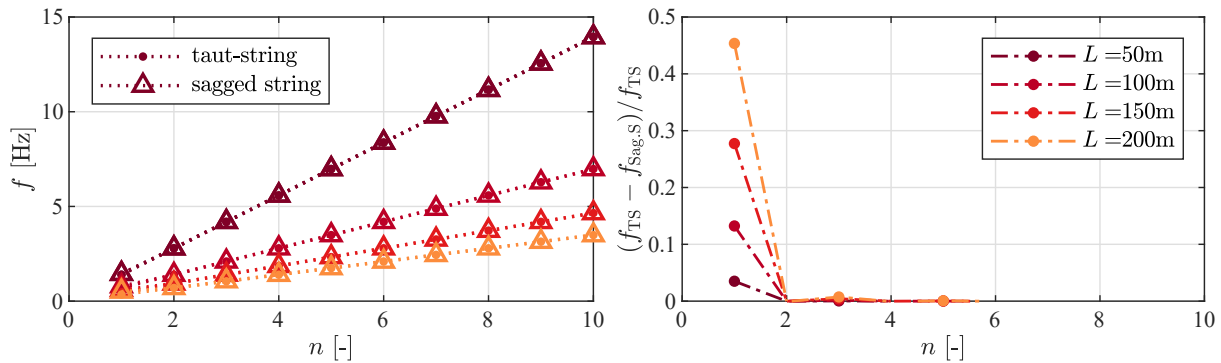


Figure 3.2: Relative differences between the natural frequencies of a linear taut-string (TS) model and the geometric nonlinear sagged string. Main differences are noted in natural frequencies for the asymmetric modes, predominantly for the first vibration mode. Comparison is made for different lengths. Model parameters used are as in Table 3.1. *Differences on the left side are small and might not be visible on the printed version.*

These results underscore the importance of incorporating nonlinear analysis, especially in the case of long structural cables. In the subsequent chapters, specific case studies present benchmarking quantified examples that emphasise the significance of this effect in practical applications.

### 3.5.2 Bending stiffness

Due to their sag and change in geometry, cables are often assumed as flexible members in analysis models. However, the assumption of a perfectly flexible cable with only axial and/or geometric stiffness does not accurately represent the behaviour. In fact, cables also have an additional bending stiffness given the composition of their cross section. Consequently, cable force identification assuming a flexible cable tends to overestimate the tension force to compensate for the neglected bending stiffness. As a result, increasing errors between measured and model natural frequencies are noticeable, particularly for higher vibration modes. The bending stiffness of the cable considerably impacts its overall stiffness and response to loading, behaving akin to a tensioned beam. This effect becomes clear for short and stiff cables.

Within cable force identification models, the influence of bending stiffness becomes more obvious as the vibration mode increases. To achieve more precise results, a constant value of  $EI$  is typically assumed along the cable. In our quantified example, a flexible cable model is compared with a cable assigned with an additional bending stiffness so that the results compare specific differences caused by the bending stiffness. Figure 3.3 highlights that the influence of bending stiffness becomes more significant with higher vibration modes.

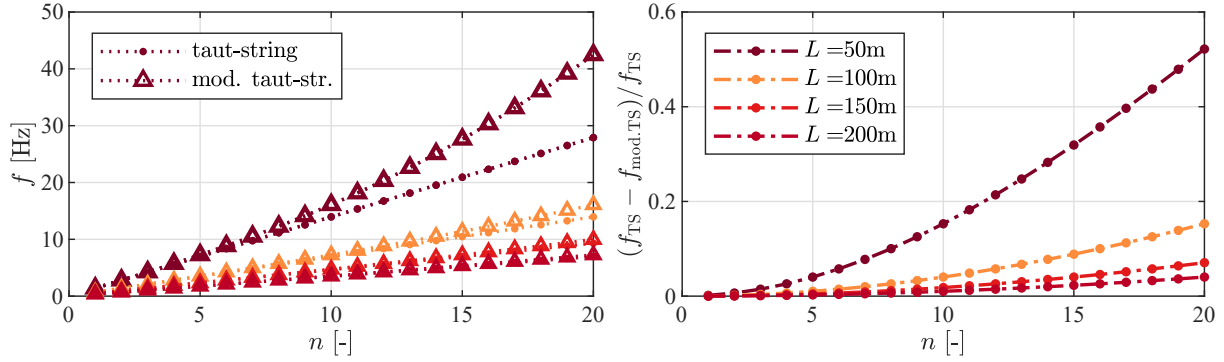


Figure 3.3: Comparison between a linear flexible cable model (taut-string) and a modified taut-string model (mod. TS) accounting for the bending stiffness effects. Main differences increase significantly with higher mode numbers. The effects increases for short cables. Model parameters used are as in Table 3.1.

For helically wired cables, the interlock between wires weakens under bending and inter-wire slippage occurs with increasing curvature. Therefore, specialised models are employed to accurately estimate the changing nature of the bending stiffness under varying loading conditions.

### 3.5.3 Boundary conditions

Similar to neglecting bending stiffness, overlooking the fixity effect of boundary conditions can lead to an overestimation of identified tension forces. For example, if cable ends are constrained from rotation but assumed to be hinged in the cable model, the estimation of tension force and bending stiffness tends to overestimate its value to compensate for the unaccounted rotational stiffness. Conversely, if cable ends are connected to a hinge condition but the model assumes fixed ends i.e. stiffer setup, the identification of the tension force and bending stiffness is likely to underestimate the actual value. The degree of under- or overestimation is proportionate to the overall impact of rotational stiffness on the cable's overall stiffness. Specifically, the rotational stiffness has a higher effect on shorter and stiffer cables, where the ends' condition plays a more pivotal role in accurate tension force estimation compared to longer cables.

The appropriate representation of boundary conditions depends therefore on the specific type of cable support or anchorage. For the ends of external tendons, a fixed end is typically selected. Pin-ends can be assumed for stay-cables employing clevis connections. However, even with the clevis support type chosen, friction effects generated by the axial force at the clevis might introduce additional rotational stiffness at that end. Consequently, it is more advantageous to calibrate the end fixity by employing rotational springs [8].

In our example, three models of a tensioned cable with bending stiffness are compared,

specifically considering hinged (pin) ends, fixed ends, and one fixed end and one hinged end model. The outcomes presented in Figure 3.4 show that increasing the rotational stiffness at the ends leads to a proportional increase in natural frequencies for all modes.

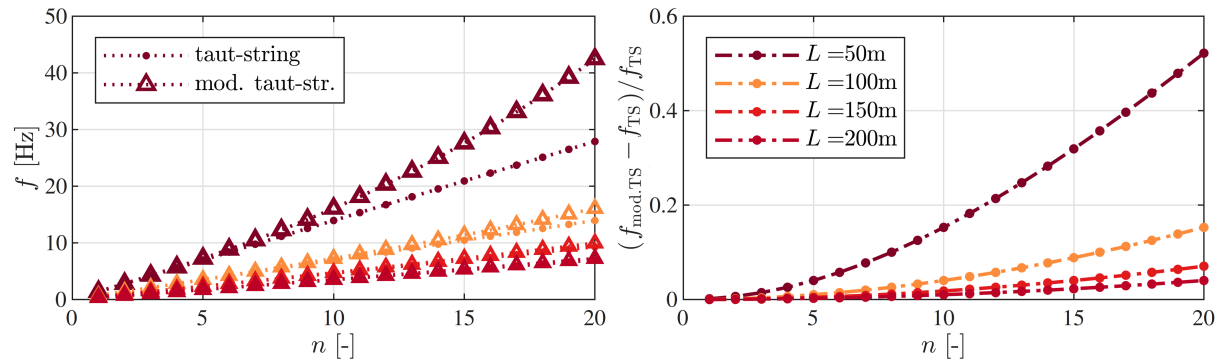


Figure 3.4: Effects of different boundary conditions on the natural frequencies employing three cases: the reference Modified taut-string (mod. TS) with both ends hinged), Flat bar (FB) with fixed ends, and Fixed-pinned (FPB). Comparison is done for two cases where the length is short  $L = 50\text{m}$  and long  $L = 200$ . Boundary condition effects decrease with longer lengths. Model parameters used are as in Table 3.1.

Furthermore, intermediate supports such as dampers or cross-ties are also used as elastic or viscous supports. Modelling damping devices requires understanding the energy dissipation mechanism, and quantifying the damping and added stiffness coefficients. In addition, the placement position and inclination of the damper/spring element is also important to determine for accurate prediction. Accurate representation of dampers hold particular significance when conducting nonlinear dynamic time history analyses.

Challenges arise in modelling geometric supports where the cable deviates over a contact length and not at a cut-off end, such as in curved saddles or deviators. Identifying the contact point is a primary concern as it assists in quantifying the load distribution on the deviator, estimating the contact point, and determining the overall free length.

### 3.5.4 Assumed self-weight

It is often reasonable to assume the cable's self-weight is linearly distributed along the chord length. This assumption holds when the sag-to-span ratio is low, and the difference between the chord length and the unstressed free length is negligible. However, for cables characterised by a high sag-to-span ratio in their unstressed state, the assumption of a linear weight distribution becomes insufficient.

Cables with high sag naturally adopt a catenary curve under their self-weight. This curve

results from the self-weight being distributed along the cable's axis, rather than uniformly along the chord. In such cases, a greater proportion of the weight is concentrated near the boundaries compared to the midspan. Consequently, there is more weight near the cable's boundaries.

To account for this, self-weight distribution in cable models is typically addressed using one of two approaches:

1. Parabolic: which assumes the weight is uniformly distributed along the chord length.
2. Hyperbolic or catenary: which reflects the true self-weight distribution along the cable's axis.

For cables with high sag-to-span ratios, such as suspended cables, accurately determining the unstressed length and tension force distribution along the length becomes important. If uniform distribution of the cable weight is assumed, this will in turn determine higher tension forces, especially at midspan.

A comparison between the two assumptions by using discretised nodal weight distribution highlights the variation in cable form and tension force distribution when modelling a parabolic form versus a catenary form as shown in the graphic statics example in Figure 3.5. A derivation of the catenary solution for an inclined flexible cable is also included in Appendix A. The implications of this assumption and the modelling methods adopted to address it are further addressed in Chapter 5.

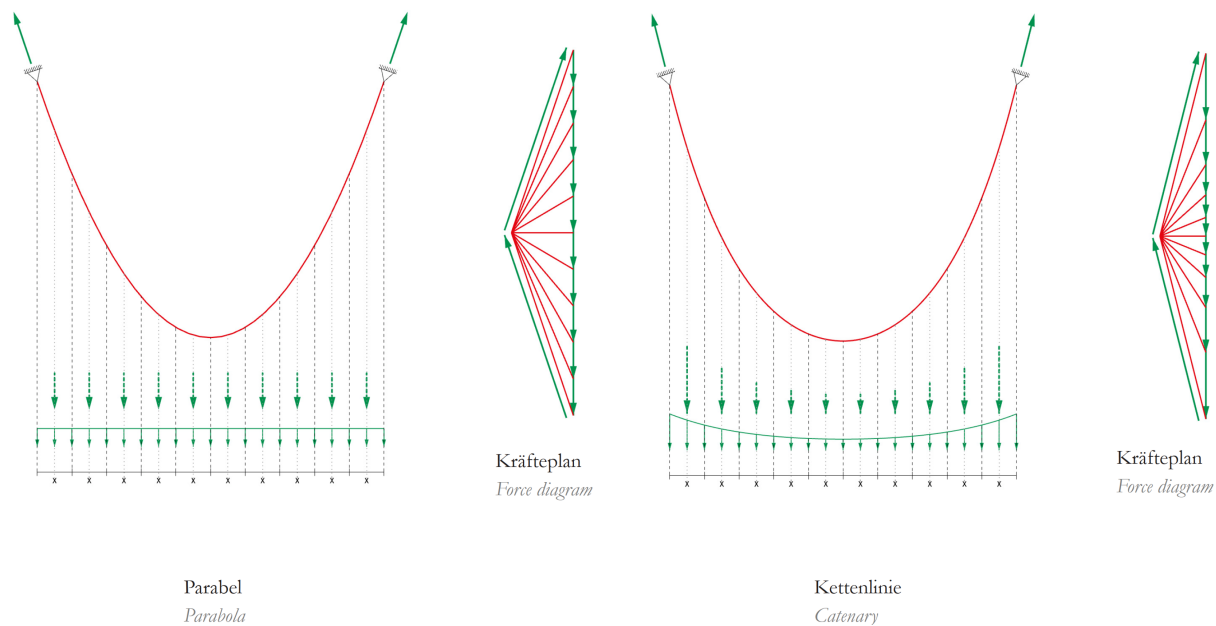


Figure 3.5: Self-weight distribution comparison: Uniform distribution along the chord length gives a parabolic cable form and a higher internal forces, while distribution along the cable axis gives a hyperbolic form and the minimum internal tension forces. A graphic statics example as taken from [13, 26]. Force diagrams are to scale.

### 3.5.5 Principles of model parameters

Constructing a cable model requires the identification of several parameters to accurately capture the physical characteristics of the cable, including its geometry, mass, material properties, and tension force. While cable force identification may be sufficient with these physical parameters, a more comprehensive understanding of the cable, such as studying stick/slip behaviour and detailed modelling, necessitates the inclusion of additional empirical and hyper-/meta parameters. For instance, when examining the stick/slip behaviour of cable wires, representing wire surface friction becomes crucial. In this context, theoretical formulas incorporating empirical and hyper-parameters are employed to refine and validate the model, capturing local effects that could otherwise be overlooked. In cable modelling, parameters can be categorised into three types: 1st order parameters, empirical parameters, and hyper-parameters.

First order parameters encompass the physical aspects of the cable, such as its geometry, mass, material properties, and tension force. Empirical parameters, derived from experimental research, serve to minimise uncertainty and enhance the usability of simplified formulas within predefined boundaries. For instance, Zui [27] provided non-dimensional stiffness ranges to constrain empirical formulations describing cable vibration behaviour. On the other hand, hyper-parameters deal with more theoretical concepts like rotational stiffness, friction

laws governing inter-wire behaviour, and spring/damper coefficients describing nonlinear interactions. These parameters are typically derived iteratively using optimisation methods, effectively reducing uncertainty and enhancing the model's descriptive capabilities.

### **3.5.6 Cable wire representation**

As explored in the preceding chapter, a cable is composed of several longitudinal wires arranged in specific geometries. The selection of a cross sectional assumption for the cable depends on the phenomenon under investigation and the intended application. In models designed for tension force identification, the multiple wires constituting the cable are simplified into a single truss or beam element discretised along the length, and characterised by a representative area and stiffness. The values assigned, particularly stiffness, may either remain constant or vary based on factors such as loading, geometry, stiffness loss, and changes in the internal structure of the cross section.

When delving into the study of high bending curvature and stick/slip behaviour, more detailed models are often used. One approach, offering a balance between detail and computational efficiency, involves modelling several cable layers as laminated beams stacked atop each other or as interconnected cylinders using contact algorithms to describe their interconnection. Nevertheless, these models are limited in their application due to their simplifications and are specifically tailored to certain cable arrangements. Consequently, they fall short when attempting to model more intricate aspects, such as wire cuts and local damages in wires.

In contrast, detailed multiwire models adopt a more granular approach by simulating individual wires within the cable. This enables them to capture intricate wire interactions, including the gradual loss in stiffness due to inter-wire slip and wire cuts. While these models demand a higher computational effort, recent advancements in computational power continually enhance efficiency and reduce the computational expense associated with such intricate models. Moreover, these models prove invaluable for exploring and gaining a deeper understanding of various mechanical aspects related to the cable, such as cable hysteresis behaviour and the mechanics of force redistribution under conditions like high curvature and wire cuts, as well as the effects of loss in cross section. In essence, detailed multiwire models offer profound insights into cable behaviour.

## **3.6 Advancements in cable analysis**

In light of the several assumptions a cable model has, its output can considerably vary depending on the application. Although these assumptions can be individually assessed, it is equally important to evaluate the state-of-the-art of cable models in this context, reviewing the often used combination of assumptions. This section provides a concise overview of the

key developments in this field by viewing the models and highlighting their strengths and limitations.

In the field of cable analysis, significant progress has been made, yielding a range of mathematical models and empirical approaches. Irvin and Caughey, in their work in 1974 [28], introduced the linear theory of vibration for flexible cables. Their mathematical model accounts for tension forces, cable sag, and the fundamental frequency, while it neglects the bending stiffness and boundary conditions. The taut-string theory is therewith one of the most used equations used for cable force identification, mostly owing to the simplicity in its formulation. However, in practical applications, it has become evident that the assumption of perfect cable flexibility is often too simplistic. To address this, several empirical models have been proposed, incorporating approximate bending stiffness [27, 29–31].

Expanding upon these foundational contributions, Mehrabi and Tabatabai [32] developed a numerical cable model using the Finite Difference (FD) method. Their model introduces assumptions like bending stiffness, geometric nonlinearity, and the inclusion of intermediate springs and dampers. However, it neglects the spatial variability of the tension force occurring from the change in geometry. It also assumes constant bending stiffness and complete fixity of cable ends, which may not accurately represent all scenarios.

Ni [33] conducted a study that further advanced cable modelling by considering cable flexural rigidity, varying tension forces depending on the sag, boundary conditions, and intermediate springs and/or dampers. This model achieves static equilibrium through a nonlinear stepwise iteration process, accommodating static profiles and their corresponding tension force. While this model serves as a baseline for accurately identifying cable parameters based on multimode measurements, it may not fully address scenarios involving short cables with variable bending stiffness or cables deviating along curved saddles.

Advancements have allowed for more precise modelling through fine-tuning and experimental calibration with hyper-parameters, coupled with adherence to first-order physical and material laws. For instance, Yan [34] introduced a local cable model with pin-ends and two zero amplitude points for each Eigenmode. This model efficiently utilises natural frequencies to calculate cable parameters within a linear, bending-stiff cable framework. This approach avoids the complexities and costs associated with constructing analytical models featuring multiple intermediate elastic supports and rotational constraints with unknown stiffness.

Ceballos and Prato [8] presented a geometrically nonlinear cable model with bending stiffness and rotational springs, allowing for partial fixity at cable ends. Their study revealed that cable forces can vary by more than 10% in some cases depending on the end fixity, underscoring the significance of considering boundary conditions, especially in the case of short cables.

Non-dimensional formulations have also proved effective in achieving low-error cable force

identification. Ricciardi [35] introduced a non-dimensional analytical model using the Irvine parameter representing sag ( $\lambda^2$ ), and non-dimensional bending stiffness ( $\xi$ ). The study highlighted that bending stiffness has a more pronounced effect on natural frequencies for cables with high sag.

In a recent study, the analytical catenary hyperbolic formulation was also exploited to determine tension forces in inclined sagged stay-cables using static measurements [36]. The method employs an approximation of the catenary curve involving perturbation-based low-order polynomial with tension-dependent coefficients inverted for tension identification using an inverse analysis model. Non-contact measurements, including laser scanner acquisition of point clouds, are applied successfully to a real-scale cable-stayed footbridge, with results validated through comparison with modal identification of frequencies using high-speed cameras. Another research employed digital image correlation techniques for non-contact remote vibration measurements [37]. The methodology involves extracting mode shapes using frequency domain decomposition and employing a tensioned pin-ended cable model for force estimation. Experimental validation on a laboratory-scale setup and hanger cables of a real-world arch bridge demonstrates the effectiveness of the proposed approach.

Another study employed a two-step approach for cable force identification based on cable force identification from vibration measurements by fitting the solution to cable responses at multiple points [38]. This method involves identifying tension force using a linear segment of the hinged-end cable and subsequently considering the geometric nonlinear static equilibrium.

Lacarbonara [39] presented an advanced cable model utilising FD and FEM to precisely model geometrically exact cable behaviour under axial strain and flexural curvature. This study further emphasised the impact of bending stiffness, particularly for high-sag cables, and demonstrated the model's suitability for extreme scenarios, such as cable loosening due to the relative displacement of the support. Further, researchers have explored iterative and efficient methods, including group theory and geometry updating, to enhance the computational efficiency and accuracy of static and dynamic analyses of symmetric cable structures [21, 22, 40, 41].

Furthermore, a recent study proposed a frequency-based method for cable force identification considering rotational and support constraint stiffness at the boundary [42]. The study established a nonlinear mathematical model of cable vibration, employing a FD method and a frequency-based sensitivity-updating algorithm to identify multiple system parameters, including tension, bending stiffness, and boundary conditions. The results emphasise the importance of considering cable boundary conditions in estimating cable tension.

In addition, applications of machine learning techniques in cable force identification have been reported. The taut-string theory was employed in a study as a training model, resulting in cable tension force predictions within a 10% error margin [43]. Furthermore,

a study presented a cable tension monitoring system employing Convolutional Neural Network (CNN) for automated peak-picking algorithm [44]. The aim of this study was to develop an automated tension identification system using a hinged end linear cable model with considerations also of the bending stiffness (modified taut-string model). Further developments to real-time monitoring of cable tension force using vibration signals, used Stochastic Subspace Identification (SSI) analysis to filter out and qualify cable natural frequencies and their corresponding mode numbers [45]. This study also used the modified taut-string theory for inverse analysis of the tension force. Recent investigations leveraged advancements to the FD model developed by Mehrabi and Tabatabai to include several end conditions, and used it as a training model for cable force estimation [46]. The FD model was further exploited to propose a universal damping curve for cables [47].

For all such methods, however, it is important to recognise that the effectiveness of machine learning models depends on the chosen training model and the assumptions the model adopts. For instance, if the model ignores the sag effects or fixity of boundary conditions, then the machine learning algorithm reciprocally ignores it too, in addition to the inherent prediction error of the method itself. Therefore, it's important to note the inherent limitations in machine learning predictions, stemming from the assumptions made by the mathematical models describing the cable's static and dynamic behaviour.

### 3.7 Categorisation of cable models

As reviewed, the state-of-the-art of cable analysis shows that the models cover a wide spectrum of assumptions and formulations, where each contribution takes assumptions into account based on a specific application case. Using these models for prediction of cable behaviour requires an overarching classification of the main components comprising these models. Serving as a main contribution to the community in this research, this section proposes a classification scheme of existing cable models.

Within the domain of SHM, these models are used in system identification and inverse analysis to indicate structural condition of cables, such as cable force identification. These models encompass various mathematical and numerical formulations, each differing in complexity. They are rooted in the dynamic equilibrium of an infinitesimal cable element, as originally presented in works such as [32, 48]. This dynamic equilibrium leads to the following differential equation:

$$\frac{\partial^2}{\partial x^2} \left( EI \frac{\partial^2 v}{\partial x^2} \right) - T_h \frac{\partial^2 v}{\partial x^2} - T_d \frac{\partial^2 u_y}{\partial x^2} + kv + c' \frac{\partial v}{\partial t} + m \frac{\partial^2 v}{\partial t^2} = 0, \quad (3.11)$$

where  $EI$  is the bending stiffness at point  $x$ ;  $v$  is the lateral in-plane vibration displacement,  $u_y$

is the lateral displacement due to self-weight,  $T_h$  is the horizontal component of cable tension force  $T$ ,  $T_d$  is the horizontal component of dynamic tension,  $k$ ,  $c$  and  $m$  are the additional spring constant, viscous damping factor and mass distribution (per unit length at point  $x$ ) respectively.

Given the many factors governing the dynamic behaviour of the cable, and the assumptions provided in each cable model, the models are studied for the main assumptions they take and a systematic classification scheme is proposed in the following sections.

### 3.7.1 The taut-string

One of the foundational cable models is the taut-string model, rooted in the linear theory of vibrations [28, 49]. This model assumes that the sag per span ratio is less than 1/8, making it a straightforward and widely employed choice in the literature. The taut-string model simplifies the cable as a flexible linear horizontal string, with evenly spaced frequencies based on the fundamental frequency. It finds application in structural cables, particularly in medium to long-length cables, such as those in cable-stayed bridges. Solving the differential equation for this model as given in [49] yields the taut-string equation:

$$\left(\frac{f_n}{n}\right)^2 = \frac{T}{4m \cdot L^2}, \quad (3.12)$$

where  $f_n$  is the natural frequency of the  $n^{\text{th}}$  mode and  $L$  is the chord length of the cable.

### 3.7.2 Modified taut-string

When considering the cases of short and stiff cables, such as external tendons or extradosed bridges, the assumption of a flexible cable as in the taut-string model can lead to significant errors due to the neglect of boundary conditions and bending stiffness.

To address this limitation, modifications to the linear taut-string theory include the inclusion of beam-like bending stiffness effects, resulting in the modified taut-string model. This model considers hinged boundary conditions and is widely utilised in the literature, with examples found in [22, 34, 44, 45, 48, 50–53]. The equation for the modified taut-string model is as follows:

$$\left(\frac{f_n}{n}\right)^2 = \frac{1}{4L^2 \cdot m} \cdot \left(T + \frac{n^2 \pi^2 EI}{L^2}\right). \quad (3.13)$$

### 3.7.3 The flat bar model

It's important to note that assuming hinged ends may not be representative in cases where clamping ends are present in the cable. In such instances, a highly applicable model is the flat bar model, as described by Morse [29] and utilised in various research studies [29, 54–57]. The equation for the flat bar model is given as:

$$f_n = \frac{n}{2L} \cdot \sqrt{\frac{T}{m}} \cdot \left( 1 + 2 \cdot \sqrt{\frac{EI}{T \cdot L^2}} + \left( 4 + \frac{n^2 \pi^2}{2} \right) \cdot \frac{EI}{T \cdot L^2} \right). \quad (3.14)$$

### 3.7.4 Empirical models

Empirical and practical formulas have also been developed to approximate cable tension forces using measured natural frequencies of low-order modes as in [27, 30, 31]. These formulas are applicable depending on the rigidity of the cable, as characterised by the non-dimensional bending stiffness value  $\xi$ .

### 3.7.5 The sagged string model

An extension of the linear taut-string model takes into account the effects of sag and geometric nonlinearity, resulting in the sagged string model. This model treats the cable as a flexible member and neglects bending behaviour. It can be formulated mathematically based on the  $\lambda^2$  mentioned in [28] describing cable flexibility, or using FEM.

Applying this model with FEM involves discretising truss or cable elements connected by nodes with defined degrees of freedom. It calculates the tangent stiffness matrix at static equilibrium and solves the Eigenvalue problem using the updated stiffness at static equilibrium to determine vibration modes and natural frequencies. The sagged string model is particularly useful for high sag cables, such as those found in suspension bridges, with examples of its application in [49, 58–61].

### 3.7.6 The sagged bar model

Adding the effects of bending stiffness to the sagged string model results in the sagged bar model with boundary conditions that could be either fixed or hinged. This model can be formulated using mathematical or numerical equations, or by utilising the FEM with discretised beam elements. This model has been used in various research studies [32, 35], with the possibility of introducing intermediate supports as springs or dampers, as mentioned in [62]. Additionally, numerically-solved mathematical extensions of this model, accounting for dynamic tension variability, are discussed in [33, 39].

### 3.7.7 Sagged bar with intermediate supports

Further extending the sagged bar with intermediate supports, Ceballos and Prato 2008 studied the effect of bending stresses and their effects in proximity to the ends of a parallel wire cable [7]. In [8], the paper introduced an extension that includes assigning rotational springs to the ends of the cable, termed the partially released-end sagged bar model. A recent development of this model also accounts for the effects of inclination angle effect as detailed in [63].

For practical purposes, this model is one of the most advanced models in terms of accounting for the factors affecting the cable behaviour. However, it is also computationally demanding. For the sake of comparison with simpler models, it is adopted in this research for tension force identification in Chapter 4.

### 3.7.8 The saddled cable model

The saddled cable model accounts for the change in contact point in geometric supports such as saddles or deviators, where the contact with the support depends on the cable sag, tension force and stiffness, as well as the support geometry. This model is designed to obtain the contact point with the support and capture the local interactions between the cable and the geometric support. A detailed study on the behaviour of cable structures supported by geometry using this model is presented in Chapter 5.

### 3.7.9 Helically twisted cable models

The aforementioned models are often used in cable force identification and assume a homogeneous cross section for the cable. Another critical application of cable models is the investigation of stick/slip behaviour between wires. This is particularly relevant for understanding cable bending behaviour, especially near supports, and the load transfer mechanism between wires. Individual wires within the cable are modelled as individual beam elements, and a contact algorithm is employed to describe interactions between wires, often involving hyper-parameters. Examples of such models are found in [64–70], with a comprehensive discussion of these helically twisted cable models can in Chapter 6.

## 3.8 Classification table

To facilitate the assumptions for these cable models, a systematic categorisation of existing models based on the discussed assumptions is presented in Table 3.2. These assumptions encompass the discussed considerations related to bending stiffness, boundary conditions, applied loads, cross sectional properties, types of parameters involved, and the nature of

both static and dynamic analyses conducted. The constituent components of these models are illustrated in Figure 3.6.

bending stiffness	boundary conditions	assumed self-weight	analysis type	parameters' principles	cross-section representation
n.a. $EI = 0$	pin fixed rotational spring	linear	linear	physical/material	single
constant $EI = cons.$	coupling damper spring/damper intermediate springs	linear	geo. nonlinear	empirical	equivalent
varying $EI = f(\kappa)$	radial springs with gaps	nonlinear	geo. nonlinear + pretension update	hyperparameters	multiwire

Figure 3.6: Considerations and assumptions of most structural cable models.

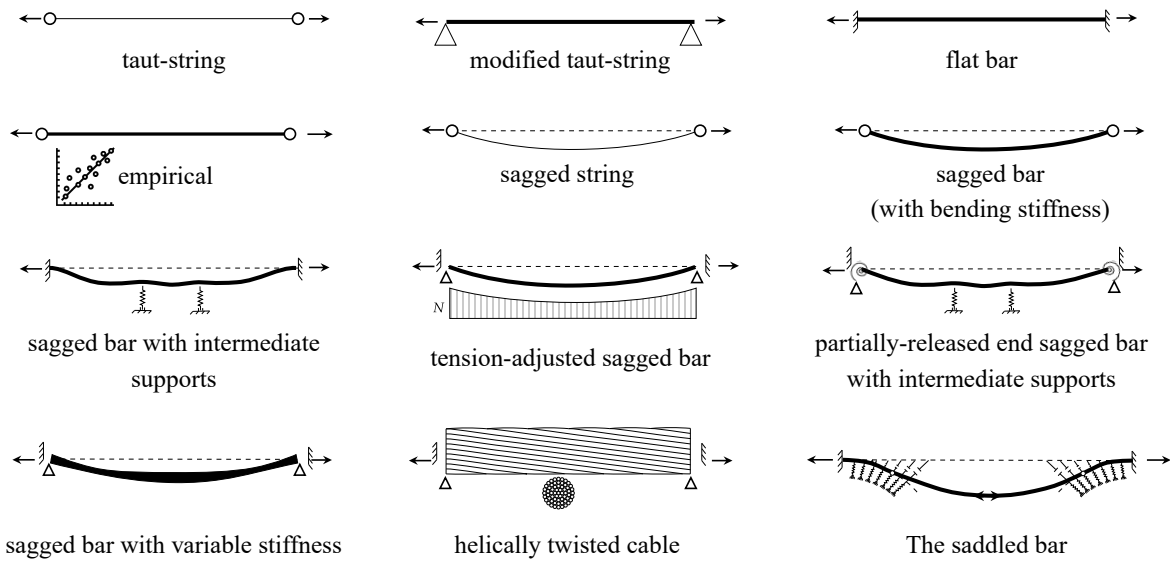



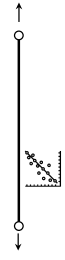



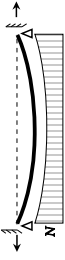
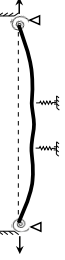





Figure 3.7: A schematic showing a visual representations of the main cable models existing in the literature.

This contribution aims to provide a guide for researchers and practitioners to systematically navigate through the assumptions and limitations in these models. Acknowledging the continuous developments of computational machines, artificial intelligence, and the understanding of cable behaviour, these models are expected to develop further. Therefore, this classification table represents an initial step to laying the groundwork for categorical expansion in cable model development.

Table 3.2: Classification of common cable models used for cable force identification.

Model name	bending stiffness	boundary condition	assumed self-weight	analysis type	parameters' principles	cross section	model schematic
Taut-string	n.a.	pin-ended	linear	linear	physical	solid	
Modified taut-string	constant	pin-ended	constant	linear	physical	solid	
The flat bar	constant	fixed	linear	linear	physical	solid	
Empirical	constant	pin-ended/fixed	linear	linear	empirical	solid	
The sagged string	n.a.	pin-ended	linear	geo. nonlinear	physical	solid	
The sagged bar	constant	pin	linear	geo. nonlinear	physical	solid	
Sagged bar with intermediate supports	constant	fixed	constant	geo. nonlinear	physical+hyper.	solid	
Tension-adjusted, (pin-ended) sagged bar	constant	pin-ended/fixed	constant	geo. nonlinear + pretension update	physical	solid	
Partially released-end sagged bar with intermediate supports	constant	rot. spring	constant	geo. nonlinear	physical+hyper.	solid	
Helicallly twisted cable	varying	pin-ended/fixed	linear	geo. nonlinear	physical+hyper.	multiwire	
Sagged bar with variable stiffness [38]	varying	pin-ended/fixed	constant	geo. nonlinear	physical	solid	
<b>The saddled cable</b> [71]	constant	geo. aligned springs	nonlinear	geo. nonlinear + pretension update	physical	solid	

## 3.9 Summary

This chapter lays the groundwork for the theoretical and numerical methodologies used in this thesis. It begins by categorising the engineering analysis for cable models encompassing the static equilibrium under permanent loads, modal analysis around the equilibrium, and the dynamic analysis under transient excitations—each grounded in considerations of geometrical stiffness and cable form. The chapter delves further into discussing the tools and methodologies utilised for such type of analyses. The FEM is adopted in this thesis, and the fundamentals of the nonlinear FE formulations are detailed.

Then, the state-of-the-art cable models are discussed based on the main assumption they take i.e. large displacement sag effects, bending stiffness, boundary conditions and intermediate supports, self-weight, principles of model parameters, and cross section representation. This perspective of examining models is adopted to propose a classification of cable models aimed at systematically navigating their characteristics, assumptions, applications, and limitations. The classification table additionally serves as a reference for selecting a cable model for application.

In the next chapter, a sample of these models are selected for cable force identification from vibration measurements to highlight their advantages and disadvantages in application.

# Chapter 4

## Identifying cable forces from vibration measurements

### 4.1 Introduction

The previous chapter described the most common models and modelling methods in the literature used for analysing cable behaviour. This chapter takes a quantitative approach to compare between commonly used simplified methods and more intricate nonlinear numerical models. It does so by presenting two case studies involving relatively long stay-cables from highly cited scientific articles and serve as a good benchmark. Through these cases, a comprehensive comparison of the outputs is made, clarifying the models' distinctions, respective applications, limitations, and the challenges encountered in the cable force identification process.

### 4.2 Background

Cable models are instrumental in identifying tension forces through the analysis of vibration data, as previously mentioned. This process involves the collection of vibration data, often obtained directly from the cable using specialised sensing units or indirectly through advanced techniques like laser scanning and image analysis. Subsequently, the collected signals undergo transformation into the frequency domain to extract dynamic characteristics including natural frequencies and mode shapes. An in-depth dissertation focusing on the vibration characteristics of inclined cables employs system identification and inverse analysis to identify cable forces. The research underscores the importance of examining aerodynamic and traffic-related excitation mechanisms by assessing cable vibrations [72].

A central component of the analysis of cable vibrations lies in determining the cable tension force, a fundamental parameter that directly influences the cable's integrity into the structural system and safety. This determination unfolds through an iterative process, closely involving a cable model. At its core, this process revolves around comparing the natural frequencies predicted by the model with those identified with field tests. To fine-tune the model and

derive optimal parameters, including cable length, tension force, and bending stiffness, an iterative approach is adopted. This iterative refinement aims to minimise the discrepancies between the model-predicted natural frequencies and the natural frequencies identified through experiments or field tests. Typically, error functions like the sum of absolute errors are used for this purpose.

Minimising these errors necessitates the application of optimisation algorithms, where cable parameters are systematically adjusted to best-fit an objective function. This objective function often compares the outputs of the model with the outputs for the target (e.g. experimental results), and then calculates the difference between them in a defined error equation. Then, the algorithm searches for the optimum parameters that give the lowest error. For cable models, the parameters often have a measured physical reference and are therefore constrained within specified upper and lower bounds (e.g. length, mass, force, etc). Therefore, constrained optimisation methods are often used in this context. A common optimisation task is defined as follows:

$$\min \quad \sum |\Delta_i| = \sum \left| \frac{f_{\text{model}}^i(\mathbf{X}) - f_{\text{idn.}}^i}{f_{\text{idn.}}^i} \right| \quad (4.1)$$

$$\text{subject to:} \quad \mathbf{X} \geq [T_{\text{min}}, EI_{\text{min}}, L_{\text{min}}, \dots] \quad (4.2)$$

$$\mathbf{X} \leq [T_{\text{max}}, EI_{\text{max}}, L_{\text{max}}, \dots], \quad (4.3)$$

where  $\mathbf{X}$  represents the vector of cable parameters under consideration, constrained within predefined minimum and maximum values,  $\sum |\Delta_i|$  is the sum of absolute errors between the identified frequencies from the experiment and from the cable model, and  $f_{\text{idn.}}^i$  is the identified natural frequency of a vibration mode  $i$ .

Ensuring the accurate determination of cable parameters requires addressing two key challenges. First, selecting an appropriate optimisation method becomes crucial given the nonlinear nature of cable models. This scheme should ensure that the algorithm converges to a global minimum of error while adhering to the prescribed parameter bounds.

Secondly, cable models are built upon certain assumptions that may or may not accurately represent the physical reality. These differing assumptions among cable models, whether they account for factors like bending stiffness, fixed or pin-ended conditions, or sagged versus straight profiles, often lead to distinct sets of optimally fitted parameters. For example, the taut-string theory assumes only axial cable stiffness, potentially overestimating tension force or underestimating length due to unaccounted bending and geometric stiffness. Therefore, the choice of the most appropriate model directly impacts the precision of parameter identification. To shed light on the effects of different cable models in practice, it is essential to highlight the variations between these models within an existing structure, emphasising their

impact on tension force determination.

In this chapter, a cable force identification scheme involves signal analysis, parameter optimisation, uncertainty quantification and results interpretation. However, it is not to be confused with the main aim which is studying the effects of the different models on the tension force identification through inverse analysis. Following every case study, a detailed discussion on the effects of each model is discussed to best-interpret the results and study how models behave in a multi-parametric identification scheme.

### **4.3 A case study: The Øresund bridge**

The Øresund Bridge is a cable-stayed structure that connects Denmark and Sweden. Spanning an 8 km distance across the Øresund strait, it establishes a vital link between Malmo and Copenhagen. The bridge consists of 49 approach spans and features a cable-stayed section with a free span of 490m (see Figure 4.1). The bridge's superstructure adopts a dual-level design, accommodating both a highway and a railway deck. This superstructure is supported by 10 pairs of cables on each side, connecting to the two H-shaped towers located at the ends of the maximum span.

A comprehensive investigation, as detailed in [56], was conducted to address significant deformations observed in the bridge during heavy traffic loads and substantial cable oscillations occurring under strong winds. This investigation involved a thorough vibration analysis to determine the natural frequencies of the bridge components, including cables. The analysis also included a methodology for identifying cable forces.

Given that the previously conducted study followed a similar scheme for tension force identification using the taut-string theory, it is now beneficial to compare their results with more advanced models such as the sagged bar model. This highlights the effect of cable form on the geometric and bending stiffness even for taut cables. In addition, uncertainty in the results between the models is also compared to better understand the effect of increasing the number of parameters and model complexity on the overall accuracy of the identification.



Figure 4.1: An overview of the Øresund bridge.

### 4.3.1 Cable characteristics

The bridge employs parallel strand cables, with each cable comprising 70 strands, and each strand consists of 7 wires laid in a helix, each measuring 5mm in diameter. Anchorage to the bridge deck is achieved through a guiding tube that leads to an anchor plate. Detailed specifications for the measured bridge cable can be found in Table 4.1.

Table 4.1: Main cable characteristics of the Øresund bridge.

Cable type	Parallel strand cable
No. strands	70 strands of 5mm wires
Anchor type	guiding tube, anchorage plate
$A_{\text{steel}}$	96.31cm <sup>2</sup>
Main span	490m
Inclination angle $\alpha$	30°
Outside cable diameter	25cm

### 4.3.2 Vibration measurement

In the referenced study, ambient vibrations caused by wind and traffic loading were recorded, and natural frequencies were determined using operational modal analysis. The recorded signals had a duration of 5 minutes and were sampled at a rate of 100 Hz, enabling the identification of frequencies below the Nyquist frequency of 50 Hz. For a more comprehensive understanding of the sensing units, sensor placement, and signal analysis methodologies, kindly refer to [56]. In this context, the focus is on three selected cables: two located in the East-South (ES) pylon leading to the main span (cables ES-1 and ES-5), and one from the East-North pylon (EN-1). The natural frequencies obtained for these cables, along with other relevant cable parameters, are presented in the Table 4.2.

### 4.3.3 Parameter Identification

As noted in Equation (4.1), upper and lower limits of each parameter need to be defined for constrained optimisation. These limits often rely on actual site measurements, specifications, or theoretical models. For instance, the free vibrating length of a cable may vary due to its integration within guiding tubes or deviators and anchors. Consequently, an increase in length beyond the design specifications is usually factored into the upper limit of the optimisation problem. Regarding bending stiffness, a parameter often associated with higher uncertainty, the lower bound is determined under the assumption that cable wires translate independently without friction. This assumes that the  $70\phi7$  wire strands bend without any axial force transmission between them. Conversely, the upper limit for bending stiffness is influenced by factors such as inter-wire friction and bonding with filler grout. As such, the upper bound assumes that strands within a cable are in a perfect monolithic bond with each other.

For this particular set of bridge cables, the tension force values from the published study serve as a reference point for establishing the upper and lower bounds (referred to as taut-string from [56]). It's important to acknowledge that the analysis method employed (taut-string) may introduce inaccuracies of up to 15%. To accommodate this potential variation, an enveloping range of  $\pm 20\%$  of the tension force identified in the study is chosen as upper and lower bounds. Table 4.2 provides insight into the natural frequencies identified, along with the corresponding upper and lower bounds for the cable parameters utilised in the optimisation. For the mass per unit length  $m$  and modulus of elasticity  $E$ , the values used are 91.2kg/m and 2.05E5 MPa respectively.

Defining these upper and lower bounds is crucial to ensure that the fitted parameters remain within the relevant constraints, keeping in mind the nonlinear relationships between them. This process can be initiated during measurements, involving factors such as cable length, mass per unit length, inclination angle, and cable type, all of which contribute to a more accurate approximation. By establishing these boundaries, the precision and reliability of our parameter

optimisation is enhanced.

Table 4.2: Identified frequencies and cable parameters for three stay-cables of the Øresund bridge (as taken from [56]). Parameters (bottom) are chosen within the predefined upper and lower bounds.

$n$	$f_{\text{idn.}} [\text{Hz}]$		
	ES-1	ES-5	EN-1
1	0.473	0.728	0.457
2	0.929	1.445	0.894
3	1.386	2.166	1.35
4	1.851	2.878	1.789
5	2.323	3.583	2.261
6	2.779	4.302	2.712
7	3.242	5.005	3.126
8	3.706	5.727	3.586
9	4.171	-	4.069
10	4.621	-	-
$L$ [m]	[262, 265]	[169, 172]	[262, 265]
$T$ [kN]	[4200, 6200]	[4200, 6200]	[4200, 6200]
$EI$ [kN.m <sup>2</sup> ]	[3, 9000]	[3, 9000]	[3, 9000]

### 4.3.4 Parameter optimisation

Conventional constrained optimisation approaches rely on gradient descent optimisers which start from an initial point and follow the gradient of an error function defined by Equation (4.1) to reach a local minimum. However, their effectiveness heavily depends on the choice of initial parameters and the algorithm can get trapped in local minima when the exploration space has numerous local minima. In this case, it is expected to occur given that the parameters have nonlinear interactions. For instance, the increase in tension force could be interpreted as a decrease in length. This is expected to happen in simple models where the assumptions are too simplistic to account for such small differences. To mitigate this challenge, multiple optimisation trials with various initial points can be made. Nonetheless, this strategy does not guarantee convergence to a global minimum unless a large number of trials are performed, incurring significant accumulated computational costs.

To address these issues, Particle Swarm Optimisation (PSO) emerges as a promising solution. PSO is a population-based optimisation algorithm that distributes a swarm of particles throughout the parameter space boundaries. Each particle within a swarm explores its

individual range, and unlike gradient-based approaches, PSO operates independently of gradients. The PSO algorithm begins by evaluating the objective function for all particles within the swarms. These particles then adjust their positions based on their best-known individual positions and the best-known positions within the entire swarm. This iterative process allows particles to explore and exploit the parameter space effectively [73]. A comparative study of PSO and Genetic Algorithm (GA) for tension force identification using a sagged cable model reveals that PSO surpasses GA in uncertainty reduction [74]. The optimisation method is effectively employed on experimental data, showcasing its proficiency in cable force identification. Emphasising the significance of precision, the study underscores the need for incorporating a number of natural frequencies in estimations, including high-order vibration modes.

By exploring various local minima from different swarms, PSO guides the optimisation process toward promising regions of the exploration space. Although PSO may take longer than the standard gradient descent optimisation, its primary goal is to efficiently and systematically navigate the exploration space and ultimately discover the global minimum of the objective function. It is therefore used in this case and all other cases involving parameter calibration with experiments.

### **4.3.5 Cable force identification**

The cables under consideration in this study are notably long, and their length affects their dynamic behaviour. Therefore, it is important to consider the geometric nonlinearity given the sag of the cable, which is expected to have a notable impact on the first symmetrical natural frequency. Additionally, it is reasonable to assume that the influence of bending stiffness would be relatively minimal given the long length of the cables. However, the bending stiffness is still important to consider in the analysis given that it might affect the higher modes of vibration. Similarly, the effect of boundary conditions may not be particularly significant in this context. To better understand the interplay of these parameters on tension force identification, three primary cable models are selected. These models include the taut-string theory, the flat bar model, and the sagged bar model.

The taut-string theory model is widely used for cable force identification. Here, it also serves as a comparison benchmark, since it was also used in the study [56]. Additionally, the flat bar model is used because the cable ends are anchored in the pylon and the deck using anchoring tubes and plates. This anchoring suggests fixed boundary conditions, which may indeed slightly influence the natural frequency. Moreover, the cable cross section comprises 70 strands, making it relevant to consider the effects of bending stiffness.

The accurate prediction of cable natural frequencies necessitates the consideration of the cable form, and the precise computation of the static equilibrium of the cables, particularly when

dealing with long cables that have a considerable sag. The effect of geometrical nonlinearity on the modal properties is considered by utilising the effective linearised stiffness around that static equilibrium condition and performing an Eigenvalue analysis. The sagged bar model includes both the geometric nonlinearity and the effects of bending stiffness and thus it is used in as a cable model to provide a comprehensive analysis of cable behaviour. Here, nonlinear FEM is used with the assumptions of this model for modal analysis as described in Section 3.4. The cable is modelled as discretised Bernoulli beam elements with lengths of 0.5m. Using the cable parameters outlined in Table 4.2, the optimisation scheme discussed in Section 4.3.4 is applied to all three cable models for the purpose of identifying the cable parameters.

The results show that the identified natural frequencies from sagged bar model consistently yield the lowest sum of errors for the three cables. The outcomes, including the calculated frequencies and optimal parameters for cables ES-1, ES-5, and EN-1, are presented in detail in Tables 4.3 to 4.5. Visualising these findings through comparison plots for the calculated frequencies (Figures 4.2 to 4.4), a distinct pattern emerges. The most significant disparity among the models becomes evident in the fundamental frequency. The sagged bar model consistently outperforms the others in this prediction, emphasising its advantage in including the axial, bending, and geometric stiffness on the prediction accuracy. However, given that this is a nonlinear FE analysis, the computational cost for this model is highest between all other models. Information about the computational cost is mentioned in the Appendix B. Additionally, given that the cables are long and flexible, and the identified modes are not of a high order, the bending stiffness is less sensitive to the modal properties and therefore the outputs might not be reliable. Accurately identifying the bending stiffness requires identifying and including higher vibration modes in the analysis.

Table 4.3: Prediction results: frequencies and optimum parameters of each cable model for **cable no. ES1** compared with results from [56]. Notably, is a difference of over 2% in the first fundamental frequency for most models compared to measured data, with the the sagged bar being the exception. Note: some values might be rounded and percentage difference show the difference from the actual value pre-rounding. The reference [56] used the taut-string theory for identification.

$n$	$f_{\text{idn.}} [\text{Hz}]$ (ref.)	$f_{\text{model}} [\text{Hz}]$			
		from [56]	taut-string	flat bar	sagged bar
1	<b>0.473</b>	<b>0.463 (-2.11%)</b>	<b>0.463 (-2.08%)</b>	<b>0.463 (-2.08%)</b>	<b>0.473 (+0.00%)</b>
2	0.929	0.926 (-0.32%)	0.926 (-0.29%)	0.926 (-0.29%)	0.926 (-0.36%)
3	1.386	1.389 (+0.22%)	1.389 (+0.25%)	1.389 (+0.25%)	1.389 (0.22%)
4	1.851	1.852 (+0.05%)	1.853 (+0.09%)	1.853 (+0.09%)	1.852 (0.04%)
5	2.323	2.315 (-0.35%)	2.316 (-0.31%)	2.316 (-0.31%)	2.315 (-0.34%)
6	2.779	2.778 (-0.04%)	2.779 (+0.00%)	2.779 (+0.00%)	2.778 (-0.02%)
7	3.242	3.241 (-0.03%)	3.242 (+0.01%)	3.242 (+0.01%)	3.242 (+0.00%)
8	3.706	3.704 (-0.05%)	3.705 (-0.02%)	3.705 (-0.02%)	3.706 (-0.00%)
9	4.171	4.167 (-0.10%)	4.169 (-0.06%)	4.169 (-0.06%)	4.170 (-0.02%)
10	4.621	4.630 (+0.19%)	4.632 (+0.23%)	4.632 (+0.24%)	4.635 (+0.30%)
$L_{\text{opt.}} [\text{m}]$		<b>262.00 (ref.)</b>	262.87 (+0.33%)	262.79 (+0.30%)	263.93 (+0.73%)
$EI_{\text{opt.}} [\text{kN.m}^2]$		-	-	51.525	1036.656
$T_{\text{opt.}} [\text{kN}]$		<b>5368.0 (ref.)</b>	<b>5407.6 (+0.74%)</b>	<b>5402.3 (+0.64%)</b>	<b>5278.7 (-1.66%)</b>
$\xi [-]$		-	-	2747.86	602.95

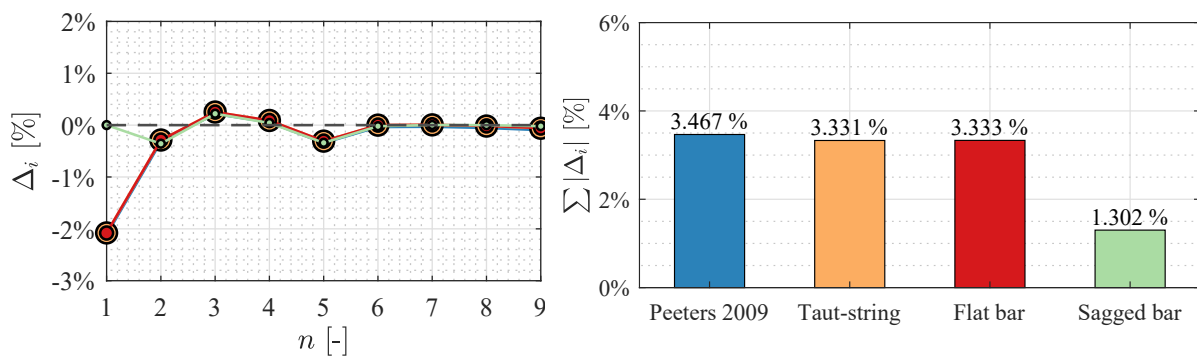


Figure 4.2: Errors  $\Delta_i$  (left) and sum of absolute errors  $\sum |\Delta_i|$  (right) between the identified and the model-predicted frequencies for **cable ES1** compared with results from [56]. The sagged bar has lowest error and predicts fundamental frequency well due to inclusion of the axial, bending, and geometric stiffness effects.

Table 4.4: Prediction results: frequencies and optimum parameters of each cable model for **cable no. ES5** compared with results from [56]. Notably, there is a difference of over 1.5% in the first fundamental frequency for most models compared to the measured data, with the sagged bar being the exception. Note: some values might be rounded and percentage difference show the difference from the actual value pre-rounding. The reference [56] used the taut-string theory for identification.

$n$	$f_{\text{idn.}} [\text{Hz}]$ ( <b>ref.</b> )	$f_{\text{model}} [\text{Hz}]$			
		from [56]	taut-string	flat bar	sagged bar
1	<b>0.728</b>	<b>0.717 (-1.55%)</b>	<b>0.717 (-1.51%)</b>	<b>0.717 (-1.51%)</b>	<b>0.724 (-0.62%)</b>
2	1.445	1.433 (-0.80%)	1.434 (-0.76%)	1.434 (-0.76%)	1.433 (-0.80%)
3	2.166	2.150 (-0.73%)	2.151 (-0.69%)	2.151 (-0.69%)	2.151 (-0.71%)
4	2.878	2.867 (-0.39%)	2.868 (-0.35%)	2.868 (-0.35%)	2.867 (-0.37%)
5	3.583	3.584 (+0.02%)	3.585 (+0.06%)	3.585 (+0.06%)	3.584 (+0.04%)
6	4.302	4.300 (-0.04%)	4.302 (+0.00%)	4.302 (+0.00%)	4.302 (-0.01%)
7	5.005	5.017 (+0.24%)	5.019 (+0.28%)	5.019 (+0.28%)	5.019 (+0.28%)
8	5.727	5.734 (+0.12%)	5.736 (+0.16%)	5.736 (+0.16%)	5.737 (+0.17%)
$L_{\text{opt.}} [\text{m}]$		<b>169.00 (ref.)</b>	172.13 (+1.85%)	173.48 (+2.65%)	170.22 (+0.72%)
$EI_{\text{opt.}} [\text{kN.m}^2]$		-	-	7.540	250
$T_{\text{opt.}} [\text{kN}]$		<b>5352.0 (ref.)</b>	5556.6 (+3.82%)	5640.8 (+5.40%)	5349.7 (-0.04%)
$\xi [-]$		-	-	2690.80	580.76

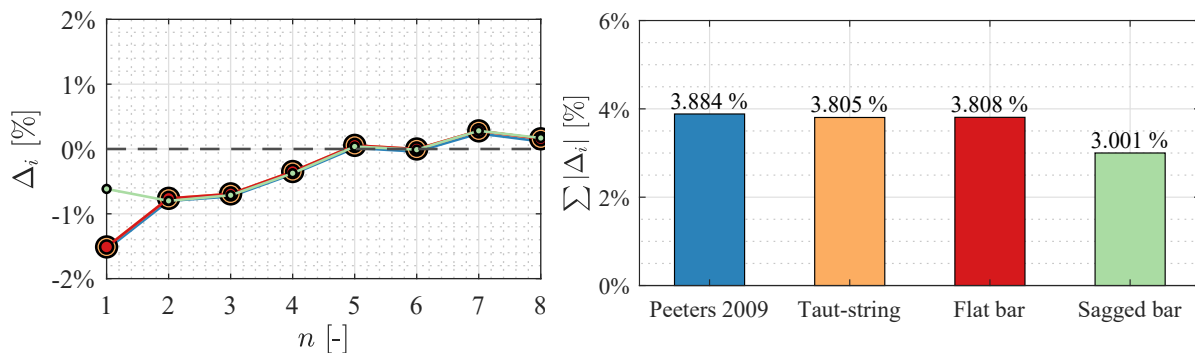


Figure 4.3: Errors  $\Delta_i$  (left) and sum of absolute errors  $\sum |\Delta_i|$  (right) between the identified and the model-predicted frequencies for **cable ES5** compared with results from [56]. The sagged bar has lowest error and predicts fundamental frequency well due to inclusion of the axial, bending, and geometric stiffness effects.

Table 4.5: Prediction results: frequencies and optimum parameters of each cable model for **cable no. EN1** compared with results from [56]. Notably, there is a difference of over 1.5% in the first fundamental frequency for most models compared to the measured data, with the sagged bar being the exception. Note: some values might be rounded and percentage difference show the difference from the actual value pre-rounding. The reference [56] used the taut-string theory for identification.

$n$	$f_{\text{idn.}}$	$f_{\text{model}}$			
		from [56]	Taut-string	Flat bar	Sagged bar
1	<b>0.457</b>	<b>0.450 (-1.55%)</b>	<b>0.450 (-1.53%)</b>	<b>0.450 (-1.58%)</b>	<b>0.459 (+0.47%)</b>
2	0.894	0.890 (+0.65%)	0.900 (+0.67%)	0.900 (+0.64%)	0.894 (-0.04%)
3	1.350	1.350 (-0.02%)	1.350 (+0.00%)	1.350 (+0.00%)	1.341 (-0.64%)
4	1.789	1.800 (+0.60%)	1.800 (+0.61%)	1.801 (+0.66%)	1.789 (-0.01%)
5	2.261	2.250 (-0.50%)	2.250 (-0.49%)	2.252 (-0.38%)	2.238 (-1.04%)
6	2.712	2.700 (-0.46%)	2.700 (-0.44%)	2.705 (-0.27%)	2.687 (-0.92%)
7	3.126	3.149 (+0.75%)	3.150 (+0.77%)	3.158 (+1.02%)	3.138 (+0.38%)
8	3.586	3.599 (+0.37%)	3.600 (+0.39%)	3.613 (0.74%)	3.590 (+0.11%)
9	4.069	4.049 (-0.49%)	4.050 (-0.47%)	4.069 (-0.01%)	4.044 (-0.63%)
$L_{\text{opt.}}$ [m]		<b>262.00 (ref.)</b>	263.52 (+0.58%)	264.01 (+0.77%)	263.90 ( <b>0.72%</b> )
$EI_{\text{opt.}}$ [kN.m <sup>2</sup> ]		-	-	4956.73	4987.17
$T_{\text{opt.}}$ [kN]		<b>5352.0 (ref.)</b>	5130.0 (-4.15%)	5068.7 (-5.29%)	4849.8 (-9.38%)
$\xi$ [-]		-	-	266.98	260.24

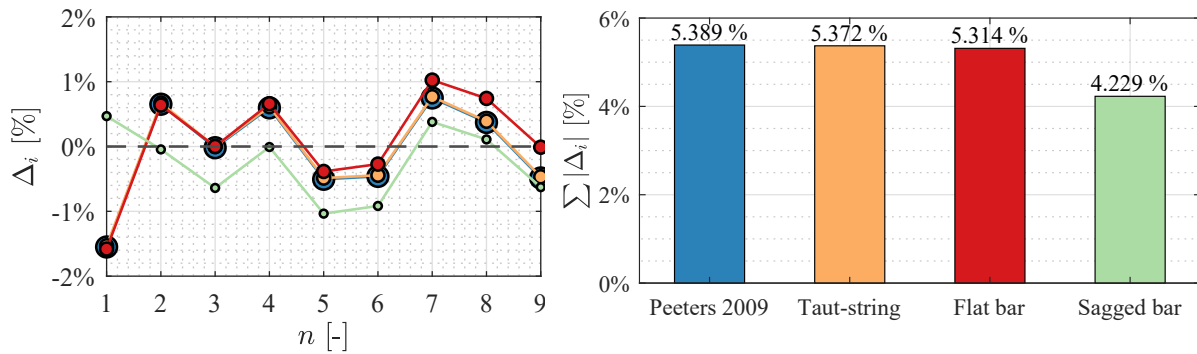


Figure 4.4: Errors  $\Delta_i$  (left) and sum of absolute errors  $\sum |\Delta_i|$  (right) between the identified and the model-predicted frequencies for **cable EN1** compared with results from [56]. The sagged bar has lowest error and predicts fundamental frequency well due to inclusion of the axial, bending, and geometric stiffness effects.

Further, examining the predictions for bending stiffness show considerable variations in the identified values across different cables. Given that only 10 vibration modes are identified, the model sensitivity to the bending stiffness is reduced, addressing both the flexibility and the long length of the cable. This observation underscores the challenge of accurately predicting bending stiffness, especially in long cables, as it is influenced by various physical factors such as wire slip and loading history, which can vary significantly from one cable to another. Additionally, the prediction accuracy of the bending stiffness would considerably increase if more modes are identified. The optimal cable length has also shown to differ from the chord length specified in the designs and reported in the study. For cables ES1, ES5 and EN1, the optimum cable lengths for the taut-string theory and flat bar model differ in their variation by up to 2%. While for the sagged bar model, the difference from the reference value is a consistent 0.73%. This consistent difference hints at the fact that free vibrating length of the cable extends inside the support until it reaches a contact point with the supporting structure. Therefore, accounting for these differences in length is important to increase the accuracy in the analysis.

### 4.3.6 Model outputs

Central to parameter identification is the determination of cable tension forces. A comparison between the identified values for the tension force of the three models is found in Tables 4.3 to 4.5. It is clear after comparison that the taut-string theory gives the highest value predictions for tension forces. The flat bar model gives a slightly lesser value due to the inclusion of the end fixity and bending stiffness. On the other hand, the sagged bar model is found to consistently yield the lowest tension force values. The inclusion of geometric stiffness, alongside bending and axial stiffness, allows this model to balance its reliance on tension force to simulate cable behaviour by including other stiffness effects.

The uncertainty in the predicted values is also accounted for to explore the optimisation space. Here, an enveloping value for the error of 10% is taken to assess the variation of the tension force around the optimum value. The variation in the error is caused not only by the tension force, but also by the different parameters included in the optimisation (i.e. length, bending stiffness). By examining the optimisation search space for the multiple local errors that exist below 10%, an accurate enveloping range for the tension force, thereby accounting for a more reliable identification of the tension force.

As previously discussed, the taut-string theory tends to predict higher tension force values. However, it has the lowest deviation bounds ranging between -4.97% and 4.20% of the predicted  $T_{opt.}$  value. Compared with the flat bar model and the sagged bar model, the deviation from the optimum value amount to -8.52% and 3.78%, and -6.64% and 4.65% for both models respectively. Here it can be concluded that the precision decreases when models having more parameters. The taut-string theory requires less parameters for prediction,

which also means less accumulated uncertainty in prediction. The flat bar model and the sagged bar model both show higher uncertainty due to their more complex formation and additional parameters. The prediction and uncertainty are plotted in Figure 4.5.

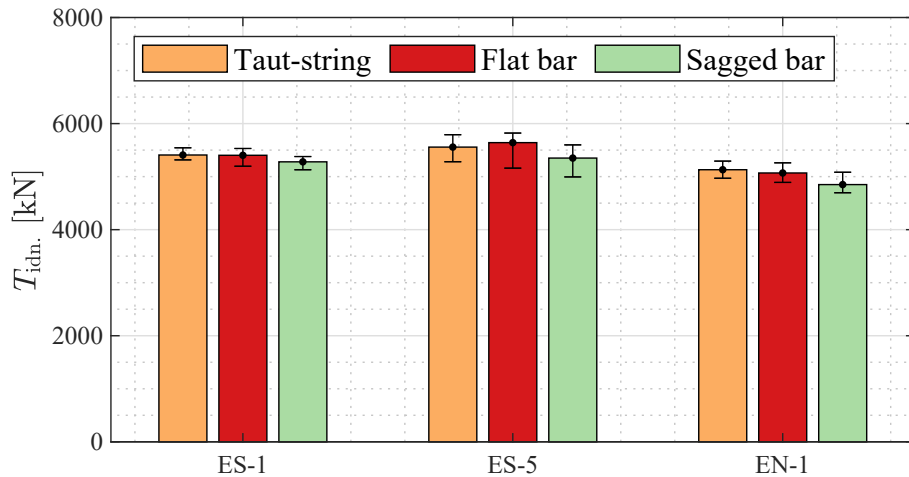


Figure 4.5: Identified tension force for each cable using the three cable models. The uncertainty range shown in the plot refers to the tension force variation within 10% of the error between the identified and the model natural frequencies.

It is important to emphasise that while these findings provide valuable insights to each model, a more thorough evaluation necessitates direct tension force readings from (e.g. lift-off tests) to assess the quality of the prediction. The next case study examines the three models with the existence of actual tension force values obtained from the site to assess the methodology, assumptions and determine accuracy of models.

## 4.4 A case study: Queensferry Crossing

The Queensferry Crossing (QFC) is a bridge located in the north eastern region of Edinburgh, Scotland over the river Forth. It is a cable-stayed bridge with three towers, comprising two main spans, each measuring 650 meters in length. In each of the two cable planes, a total of 144 stay-cables are present. Figure 4.6 shows an aerial view of the bridge.



Figure 4.6: Queensferry crossing (left, cable-stayed), the Forth Road bridge (middle, suspension) and parts of the Forth bridge (right, red steel truss). Courtesy of: Scottish Construction Now.

Following cable installations, vibration readings were recorded using a low-cost, highly mobile sensing set-up. This sensing unit incorporates a MEMS accelerometer sensor equipped with an integrated Analogue to Digital Converter (ADC), a Raspberry Pi single-board computer for signal recording, and a low-voltage power supply. Additional details regarding the sensing unit can be found in the reference [75].

In previous research, cable force determination for the stays was also undertaken employing smartphones [76, 77]. However, in the work presented in [75], the bridge deck was in the erection process in 2016 and the tested cable was undergoing tensioning. Consequently, it was feasible to directly obtain the cable force reading from the lift-off test. This affords the opportunity to identify the tension force through vibration measurements and compare it with the one acquired by the lift-off test. Moreover, this enables a comparative assessment of the identification accuracy between each of the used models, and uncertainty associated with parameters identification.

### 4.4.1 Cable characteristics

In light of the measured cables, this study is directed towards the longest cable, denoted as C4. This cable comprises 85 individual strands placed within a duct. Notably, at the time of measurement, neither dampers nor guiding tubes were installed, facilitating the straightforward measurement of the length between the anchors  $L$  at the bridge deck and the pylon with minimal uncertainty ( $\pm 0.0013\%$ ). Furthermore, the cable's mass per unit length  $m$  could be precisely determined. These two parameters are taken as constants in this case. Therefore, the tension force and the bending stiffness are the parameters to be identified from the optimisation. Table 4.6 presents the acquired cable parameters alongside the reference tension force  $T_{\text{ref}}$ , obtained from the lift-off test.

Table 4.6: Main cable characteristics of the Queensferry bridge.

Cable number	C4
Cable type	Parallel strand cable
No. strands	85 strands of 5.22mm wires
$A_{\text{steel}}$ [cm <sup>2</sup> ]	127.50
$\alpha$ [°]	22.893
Outside diameter [cm]	25
$E$ [MPa]	2.05E5
$L$ [m]	342.98
$m$ [kg/m]	116.4
$T_{\text{ref}}$ [kN]	<b>9630</b>
$EI_{\text{min}}$ [kN.m <sup>2</sup> ]	49

### 4.4.2 Signal analysis

The cable was tested by attaching the sensor in close proximity to the lower end of the cable, positioned at a distance of 7 metres from the anchorage. To initiate the experiment, the cable was manually excited as depicted in Figure 4.7.

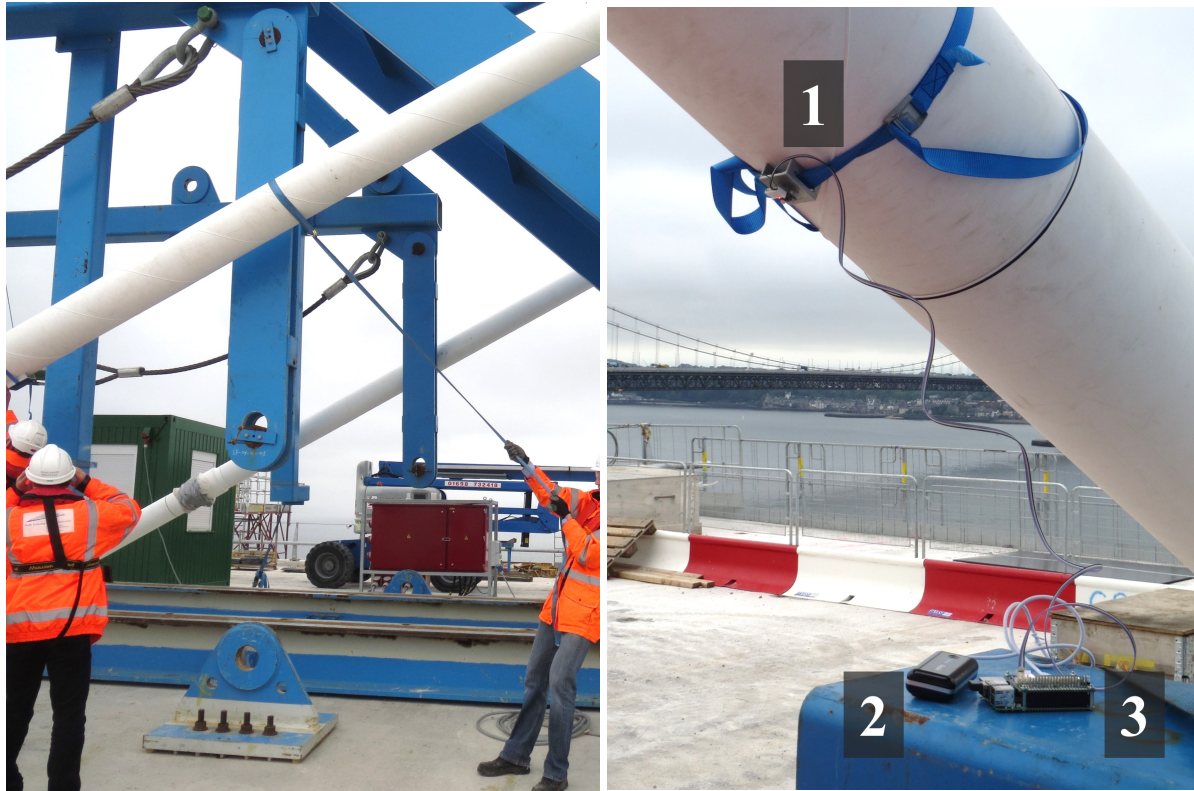


Figure 4.7: Manual excitation (left) and sensing unit setup (right) of a cable of Queensferry Crossing. Sensing unit consists of: MEMS sensor (1), power supply (2) and RPi computer (3). Photos kindly provided by the authors of [75].

Four datasets were collected, consisting of two with a duration of 30 seconds and two with a duration of 60 seconds. Consequently, this results in frequency resolutions of 0.033 Hz and 0.017 Hz respectively, leading to variations in the obtained frequencies across the datasets. These varying resolutions have implications for the frequencies identified within the datasets and necessitate post-processing and subsequent averaging to determine the precise natural frequency corresponding to a given vibration mode.

The acceleration time history data in the in-place direction for all four datasets was sourced from the study. Visual representations of these time histories can be seen in Figure 4.8.

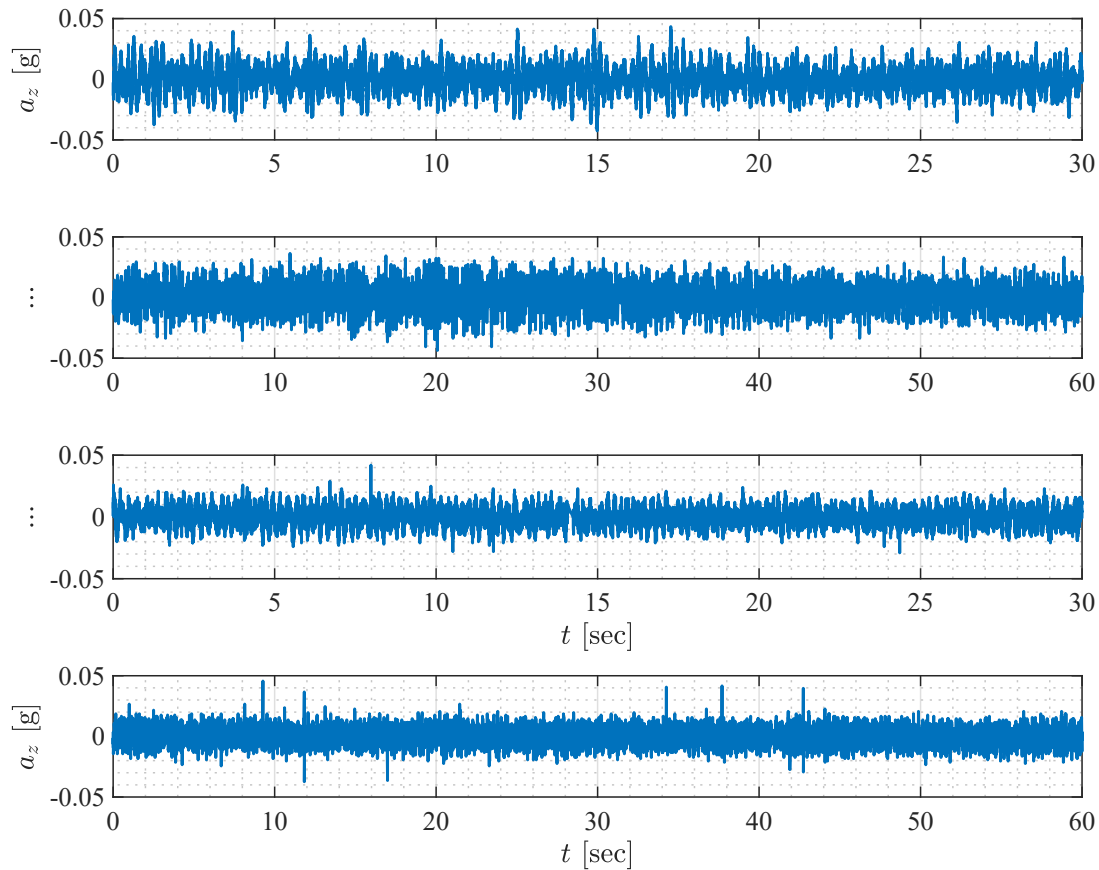


Figure 4.8: Baseline corrected time history of in-plane acceleration signal for the available datasets. Time-history data kindly provided by [75].

First, the acceleration time history is post-processed to extract the signal's frequency content. The post-processing includes standard baseline correction. Additionally, irregularities in the time intervals are observed, indicating non-uniform sampling rates within the signal. These time interval discrepancies range from 0.0017 to 0.0092 seconds, with a single instance where the time interval increases by approximately 0.13 seconds. These discrepancies can be attributed to the utilisation of a low-cost ADC in the MEMS sensor, which clearly affects the digitisation quality of the recorded signal. To adjust this, the signal is re-sampled based on the average time step and signal interpolation. More importantly, these discrepancies are found to be relatively minor and they would have negligible effect on the frequency content, as shown in Figure 4.9. The signal can therefore be transferred into the frequency domain via a Fast Fourier Transform (FFT), and natural frequency could be identified.

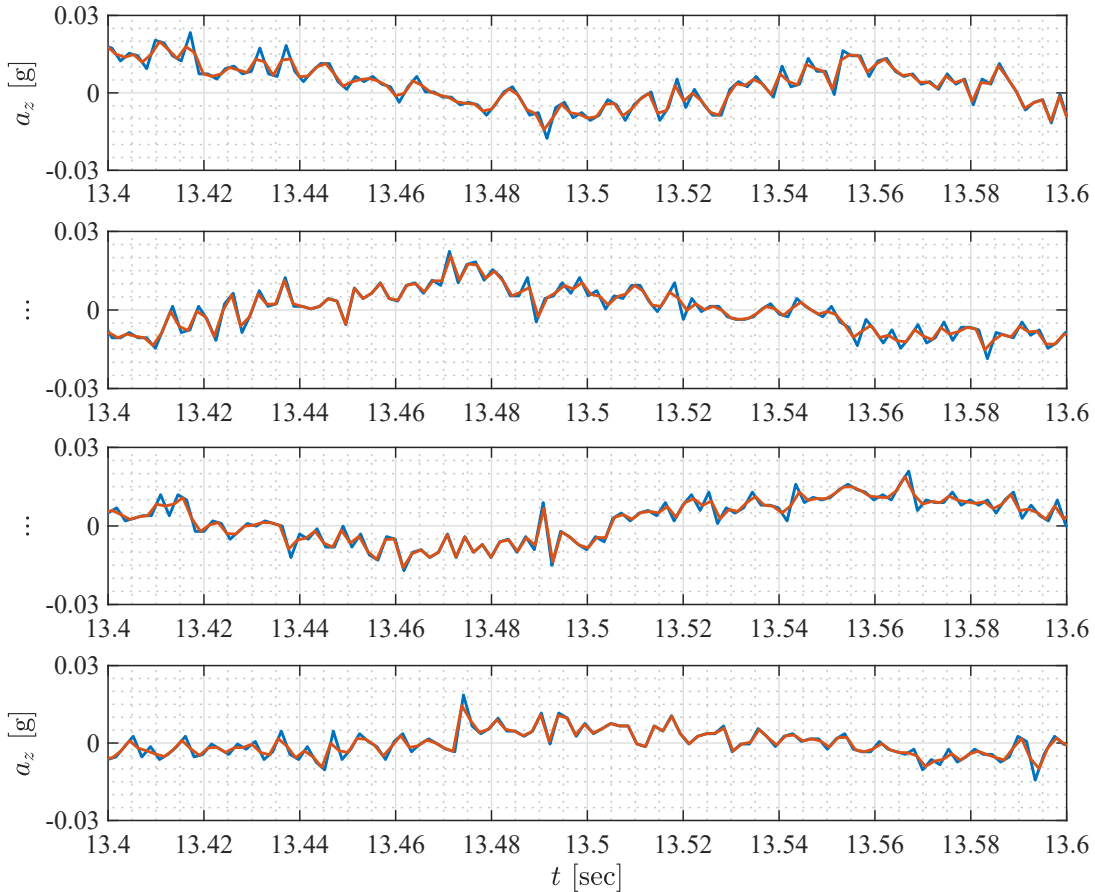


Figure 4.9: Interpolation and resampling: difference between main signal and the interpolated. (—base-corrected, —interpolated). Time-history data kindly provided by [75].

### 4.4.3 Natural frequency identification

Given that this cable is a long stay-cable with a fundamental frequency of less than 0.5 Hz, attempts at ambient and manual excitations to initiate the first symmetrical vibration mode prove to be unsuccessful [75]. Therefore, it is important to note that the accurate identification of the tension force should encompass not only the fundamental frequency but also higher vibration modes.

In addition to natural frequency considerations, several other factors require attention to maintain a precise prediction. Vibration amplitude, sampling rate, and frequency resolution are all pivotal determinants of signal quality, each exerting influence on the accuracy of predictions. In situations involving a wide frequency spectrum—such as having more than 20 vibration modes spanning the 1 to 10 Hz range—the use of a cable model requires the assignment of the correct vibration mode to each identified frequency, as included in Equations (3.12) to (3.14).

For the case of this cable, it becomes evident that the frequency content in the signal concentrates between 1 and 9 Hz, as illustrated in Figure 4.10.

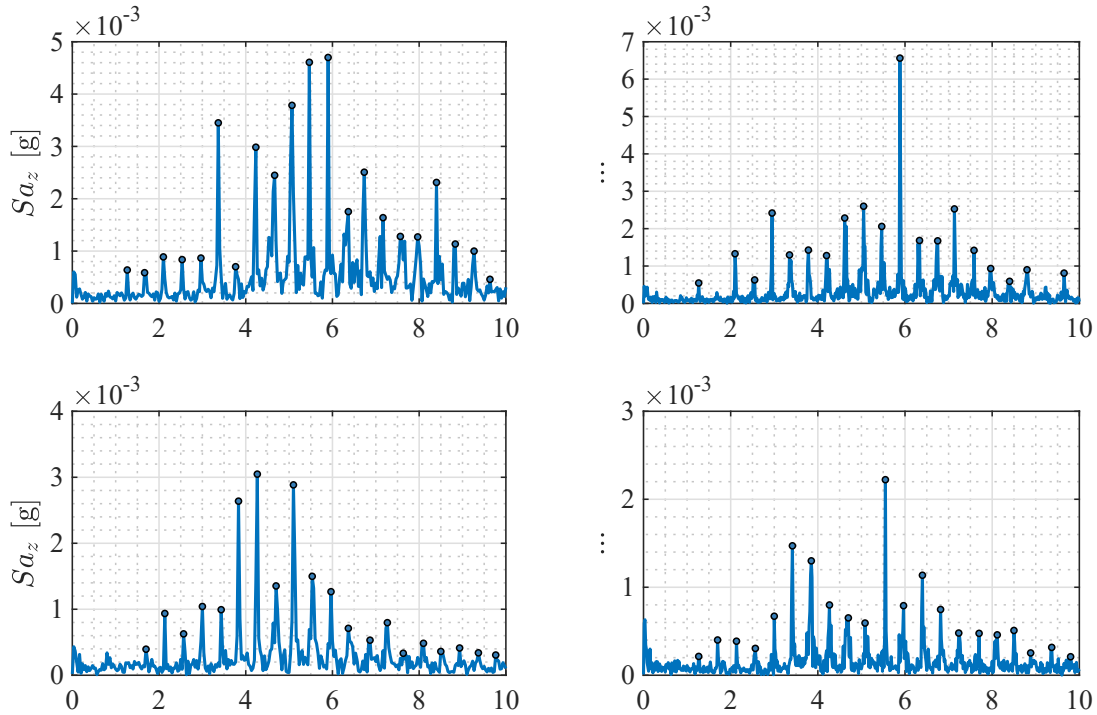


Figure 4.10: Frequency spectrum for all four datasets derived after signal post-processing from C4 cable of the Queensferry Crossing.

Given the presence of multiple datasets and variations in excitation conditions, it becomes apparent that not all frequencies identified in one dataset necessarily exist in another. To address this effectively, a pragmatic approach is made involving clustering the natural frequencies found within a range of  $\pm$  the highest frequency resolution (here 0.033 Hz). This clustering process allows grouping frequencies and assigning mode numbers  $n$  as arranged in Table 4.7. These mode numbers are determined using the taut-string theory, along with the measured cable parameters ( $m$ ,  $L$ ) from Table 4.6, which enables calculating a tension force within a consistent range for all frequencies.

It is essential to clarify that this process does not aim to precisely identify the tension force itself but rather focuses on iteratively deriving the actual mode number for each natural frequency. The calculation of a steady tension force serves as a mere reference point.

Table 4.7: Identified frequencies and signal properties for cable C4 of the Queensferry Crossing for each dataset.

Property	Dataset 1	Dataset 2	Dataset 3	Dataset 4
$f_{\text{idn.}}$ [Hz]	1.267	1.267	n.a.	1.267
	1.667	n.a.	1.700	1.700
	2.100	2.100	2.133	2.133
	2.533	2.550	2.567	2.567
	2.967	2.950	3.000	3.000
	3.367	3.350	3.433	3.417
	3.767	3.783	3.833	3.850
	4.233	4.200	4.267	4.267
	4.667	4.617	4.700	4.700
	5.067	5.050	5.100	5.083
	5.467	5.467	5.533	5.550
	5.900	5.883	5.967	5.967
	6.367	6.333	6.367	6.400
	6.733	6.75	6.867	6.817
	7.167	7.133	7.266	7.233
	7.567	7.583	7.633	7.700
	7.967	7.967	8.100	8.116
	8.400	8.400	8.500	8.500
	8.833	8.800	8.933	8.883
9.267	n.a.	9.366	9.366	
9.633	9.650	9.766	9.800	
Sampling rate [Hz]	548.62	547.47	544.25	547.97
Signal duration [sec]	30	60	30	60
Frequency resolution [Hz]	0.033	0.017	0.033	0.017

The identified frequencies for each vibration mode up to the 20<sup>th</sup> are unified through the calculation of a weighted average between each frequency and its corresponding amplitude. This process allows harmonising the diverse frequencies identified from the datasets, where each dataset might have a small variation within its frequency resolution. A similar optimisation scheme to Section 4.3.4 is conducted for the three cable models: the taut-string, the flat bar, and the sagged bar models.

#### 4.4.4 Results

Given unidentified fundamental frequency from the data, it is anticipated that the error values might not show significant variations between the models. Interestingly, this scenario provides an opportunity to compare models with similar frequency errors in terms of their predictions for tension forces. As previously mentioned, this case study is distinguished by the simultaneous measurement of the tension force during a direct lift-off test. This allows the cable force to serve as a reference accuracy evaluation of each model, ultimately identifying the model aligning closest to the reference values.

Consistent with the previous case study, the sagged bar model again provides accurate prediction of tension force, mostly due to the accounting of geometric stiffness. Nonetheless, it is worth noting that the other two models also perform well, predicting tension forces with a discrepancy of less than 2% compared to the reference tension force. It is important to highlight that these models tend to slightly overestimate the tension force, which is likely attributed to the omission of geometric stiffness effects.

The prediction uncertainty is also accounted for to quantify uncertainty in the identified values. Again, an enveloping value for the natural frequency variation error of  $\sum |\Delta_i|$  10% is taken to assess the tension force variation. The variation in the error is caused by the tension force and by the bending stiffness. Examining  $T_{opt.}$  values within an enveloping value of  $\leq 10\%$ , the taut-string model showed a deviation from the identified value between -1.0% and 1.2%, while for the flat bar and the sagged bar models, the deviation is within -2.2% and 1.1%, and -2.3% and 1.2% respectively. Again, the few parameters required for the taut-string accumulate lesser deviation from the optimum value. However, the accurate measurement of the length considerably reduced the deviation.

Moreover, bending stiffness for long cables is a property entailing substantial uncertainties and is challenging to quantify accurately due to the involvement of numerous physical factors. Nevertheless, given the use of parallel strand cables, the identified bending stiffness is found to slightly exceed the value of  $EI_{min.}$  The averaged frequencies, error values and optimum tension forces for the three models that have been used are listed in Table 4.8.

Table 4.8: Identified averaged frequencies and prediction with optimum parameters computed with three cable models. Tension force prediction is compared with the reference value  $T_{\text{ref.}} = 9630$  kN as taken from [75]. Note: some values might be rounded and percentage difference show the difference from the actual value pre-rounding.

$n$	$f_{\text{idn.}}$ [Hz] (ref.)	$f_{\text{model}}$ [Hz]		
		Taut-string	Flat bar	Sagged bar
3	1.267	1.268 (+0.09%)	1.268 (+0.09%)	1.268 (+0.11%)
4	1.686	1.690 (+0.28%)	1.690 (+0.28%)	1.690 (+0.28%)
5	2.112	2.113 (+0.03%)	2.113 (+0.03%)	2.113 (+0.03%)
6	2.551	2.536 (-0.59%)	2.536 (-0.59%)	2.536 (-0.59%)
7	2.970	2.958 (-0.39%)	2.958 (-0.39%)	2.958 (-0.39%)
8	3.383	3.381 (-0.07%)	3.381 (-0.07%)	3.381 (-0.07%)
9	3.817	3.803 (-0.37%)	3.803 (-0.37%)	3.803 (-0.37%)
10	4.244	4.226 (-0.41%)	4.226 (-0.41%)	4.226 (-0.41%)
11	4.660	4.649 (-0.24%)	4.649 (-0.24%)	4.649 (-0.24%)
12	5.073	5.071 (-0.03%)	5.071 (-0.04%)	5.071 (-0.03%)
13	5.494	5.494 (+0.00%)	5.494 (+0.00%)	5.494 (+0.00%)
14	5.902	5.916 (+0.24%)	5.916 (+0.24%)	5.916 (+0.24%)
15	6.363	6.339 (-0.37%)	6.339 (-0.37%)	6.339 (-0.37%)
16	6.762	6.762 (+0.00%)	6.762 (+0.00%)	6.762 (+0.00%)
17	7.172	7.184 (+0.17%)	7.184 (+0.17%)	7.184 (+0.17%)
18	7.595	7.607 (+0.16%)	7.607 (+0.16%)	7.607 (+0.16%)
19	8.011	8.029 (+0.23%)	8.029 (+0.23%)	8.029 (+0.23%)
20	8.415	8.452 (+0.45%)	8.452 (+0.45%)	8.452 (+0.44%)
$\sum  \Delta_i $ [%]		4.140%	4.141%	4.154%
$T_{\text{opt.}}$ [kN]		<b>9781.5</b> (+1.57%)	<b>9772.4</b> (+1.48%)	<b>9614.0</b> (-0.17%)

## 4.5 Summary

This chapter presented two case studies involving indirect cable force identification through vibration measurements. The selected cables are from two cable-stayed bridges; the Øresund bridge in Denmark and the Queensferry Crossing in Scotland. These examples are made to compare between common cable models, where each model takes assumptions related to the physical, mechanical, and geometrical characteristics of cables. These case studies serve as a good benchmark for comparing and examining the effects of the axial, bending, rotational stiffness and effects of large displacement on the cable stiffness. The selected cable models used

for identification are namely the taut-string theory (axial stiffness only), the flat bar model (axial, bending, and end-rotational), and the sagged bar model (axial, bending, end-rotational, and geometrical).

In comparison, the results indicated that the sagged bar model exhibited the least uncertainty in identifying natural frequencies in both cases, with a mean absolute error (MAE) of 1.3%, compared to 3.3% for the taut-string theory and 3.3% for the flat bar model. The sagged cable model also demonstrated enhanced accuracy in tension force identification, with an MAE error of 0.17%, compared to 1.6% and 1.5% for the models respectively.

The prediction for the taut-string theory tends to overestimate the tension force because it relies on the axial stiffness only. It compensates for the neglect of other types of stiffness by increasing the axial stiffness (i.e. overestimation of tension force). Given that this theory relies on fewer parameters, the uncertainty in the prediction shows to be lower than the other two models. On the other hand, the flat bar model also tends to overestimate the tension force. Long taut-cables tend to have large displacement, which increases the effects of the geometric nonlinearity on the overall stiffness. However, the flat bar and the sagged bar models also show that they have a higher uncertainty envelope due to the increase of cable parameters and complexity of the models.

In this chapter, it is shown that models that represent the physical effects by taking adequate assumptions tend to balance the prediction by providing a wider range for the tension force to be closer to the actual value. Therefore, selecting an adequate model should be based on the physical nature of the cable under study.

Additionally, including the length in the optimisation shows that the prediction tends to consistently overestimate its value from the chord length. This suggests that these cables are in fact longer than the distance from each support. It indicates that, for certain support types, there is an interaction between the support and the cable, and that the cable extends inside the support until it reaches a contact point. The next chapter discusses this contact point problem for cables with large displacement and deviating saddle supports.

# Chapter 5

## Saddles and curved deviators as boundary conditions

This chapter delves into the form-finding and static equilibrium in large sag cables influenced by self-weight. The focus is set first to introduce and compare four numerical modelling techniques based on a nonlinear FE formulation. Further, a novel approach, the saddled cable model, is introduced to account for the contact problem and the mechanical effects of cable-deviating supports.

The chapter transitions from static analysis to cable force identification from vibration measurements, showcasing the accuracy of the saddled cable model in identifying cable forces from on-site vibration measurements. A parametric study reveals insights into natural frequencies and the effects of various parameters.

Expanding the analysis to dynamic responses, the chapter explores the impact of saddles on effective free length throughout vibration cycles, affecting the frequency spectrum. Notably, the models presented here are parametrised and offer high accuracy, making them valuable for system identification in scenarios demanding precision for complex cable arrangements.

The findings of this section have been published by the author in a journal article [71]. Thus it serves as a key contribution to this research.

### 5.1 Cable models for form finding under self-weight

Numerical approaches based on the Finite Element Method model cable behaviour through a discretisation by truss or beam elements with boundary conditions as either fixed or hinged. Such models are generated based on an assumed unstressed initial geometry and subjected to a large-displacement geometrically nonlinear analysis to determine the cable state under self weight.

The modelling assumption of an initially straight cable may be sufficiently accurate for cables

with low sag to span ratios (taut cables) but might be unacceptable for cables where the ratio is high. Analytical models for catenary shapes may be used to estimate the cable profile either as a parabola, which is a result of self weight distribution assumed along the chord length, or as a hyperbolic function, taking into account that the self-weight of the cable is actually distributed along its axis [5]. The basis of an accurate cable modelling is an accurate representation of the self-weight state and this section investigates four different modelling strategies with respect to the accuracy of predicting the static cable behaviour. Herein, it is assumed that the cable characteristics in the static condition are defined by chord length  $L$ , maximum sag  $s_{\max}$  and unit weight  $w$  to be input parameters and the cable to have zero bending stiffness but a certain finite axial stiffness. The assumed model parameters used for benchmarking are shown in Table 5.1.

Table 5.1: Model parameters chosen for a benchmark case deploying the four proposed cable models.

Parameter	Symbol [Unit]	Value
Section area	$A$ [cm <sup>2</sup> ]	78.54
Modulus of elasticity	$E$ [GPa]	200
Span length	$L$ [m]	100
Max. sag at midspan	$s_{\max}$ [m]	10.000
Bending stiffness	$EI_{\text{ref.}}$ [kN.m <sup>2</sup> ]	400
Unit weight	$\gamma$ [kN/m <sup>3</sup> ]	78.5

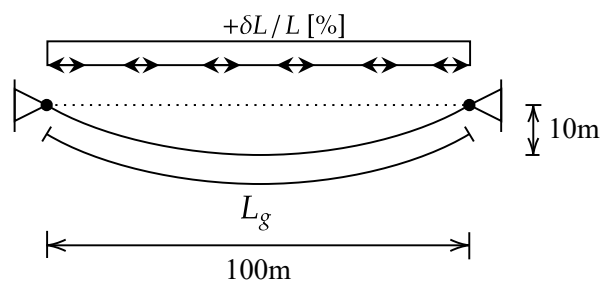


Figure 5.1: Model schematic: load case and cable parameters.

### 5.1.1 Straight cable model

The straight cable model consists of an initially linear geometry of length  $L$  along which the self-weight  $w$  is distributed. The maximum sag required  $s_{\max}$  is obtained by increasing the element length by a total unstressed overlength  $\delta L$  through the application of a positive pre-strain in the analysis, i.e. providing an overlength as a load case. The cable is modelled

as zero-bending-stiffness beam elements suspended between two end points. The large displacement and the tensile force generate transverse geometric stiffness and a respective internal force state [14], which for all models described in this chapter are obtained using a large-displacement geometrically nonlinear analysis. A model outline is shown in Figure 5.2a.

### 5.1.2 Modified straight cable model

The modified straight model uses the same initial geometry, load case and analysis of the straight cable model, however the self weight generated with respect to the unstressed cable length is corrected by increasing the self weight as follows

$$w' = w \cdot \left( \frac{L + \delta L}{L} \right) \quad (5.1)$$

in order to account for the weight of the overlength in the unstressed cable compared to the chord length modelled. The model is depicted in Figure 5.2b.

### 5.1.3 Initially sagged cable model

This cable model uses an initial parabolic cable profile to estimate the initial geometry of the cable before deformation (see Figure 5.2c) and the self weight is distributed and computed with respect to this curved cable axis. The sag of the parabola  $s_{\text{parb}}$  is determined to lead to the prescribed  $s_{\text{max}}$  after loading. This model leads to more realistic distribution of the self-weight along the cable axis.

### 5.1.4 Extended cable model

The extended cable model uses an initially straight cable geometry with a total length of  $L + \delta L$ . Here however, the horizontal fixity of cable ends is replaced by sliding support and a gap element. This allows the cable model to extend by the gap length of  $\delta L/2$  at each side when loaded and thus models the required extension while generating the correct self-weight according to the extended length. Generating a curved initial geometry is not necessary and, upon analysing the model with geometric nonlinear analysis, results in accurate cable form-finding and a final sag of  $s_{\text{max}}$ . See Figure 5.2d for the model outline.

### 5.1.5 Assessment of model performance

Analysis results for each model are shown in Table 5.2. For the problem at hand, where hinge supports and zero bending stiffness have been assumed, the analytical catenary solution of the target span and sag can be used as reference, giving a total length of 102.6187 m and a corresponding weight of 63.2682 kN. It should be noted that this length represents the stressed cable length, whereas the weight relates to the unstressed length (prior to elastic elongation).

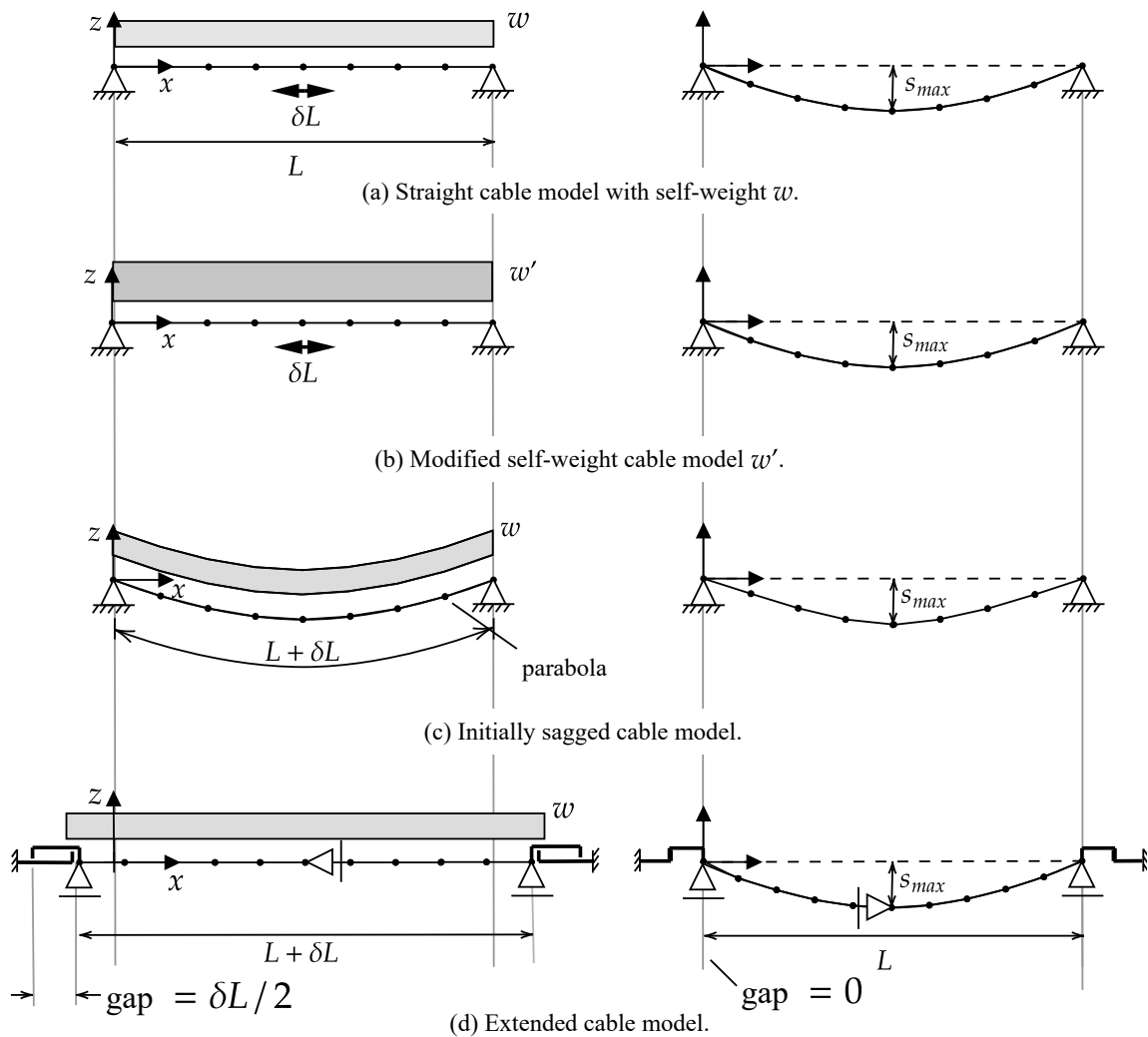


Figure 5.2: Four types of the saddled cable model. Left: initial geometry, load and self-weight application. Right: system after deformation.

The mean strain is approximately  $5E-5$ , i.e. the unstressed cable is about  $5E-3\%$  shorter and the above mentioned weight must be reduced accordingly to 63.2649 kN.

In relation to these results, the obtained support forces serve as a useful reference regarding accuracy of the total self-weight present in each FE model. The total weight of the sagged model is virtually exact compared with the analytical solution within the accuracy of the discretisation and numerical solution because it had to deform only to account for the elastic elongation.

Upon comparing the two models, it is observed that the unstressed overlength value introduced as a load case is slightly higher for the straight model than for the modified one. However, the final cable form and stressed length exhibit negligible differences. This implies

that the difference in self-weight magnitude has a more significant effect on the tension force in the cable for the case at hand. While the total weight of the modified model is close to correct, the weight distribution along the cable is not accurate, which has an impact on the cable's form. In reality, due to the cable curved sag the projected self-weight is closer near the support than at the centre, whereas the modification was applied as a constant line load. This results in differences in the determined shape of the two simpler models, essentially being the difference between the catenary and a parabola as the sagged geometry of a cable subjected to a constant line load with respect to the projected length (see Figure 5.3).

The total weight of the extended model lays within 0.01% from the analytical value. This is an excellent result considering the significant vertical as well as longitudinal displacements which the model needs to accommodate to deform from a straight shape into the equilibrium state. Thus the extended model is a versatile model that can account for the correct self-weight even without prior knowledge of the final shape of the cable. In interpreting the results, it is important to remember that here the cable length is adjusted in all models to have the same midspan sag of  $s_{\max}$ . The straight and modified models therefore overestimate the cable length.

Table 5.2: Results comparison for several cable models under self-weight (beam elements with zero bending stiffness).

Parameter	Symbol [Unit]	Straight	Modified	Sagged	Extended
Unstressed length	$L + \delta L$ [m]	102.6238 (+0.0101%)	102.6237 (+0.010%)	102.6134 (ref.)	102.6132 (-0.0002%)
Max. sag	$s_{\max}$ [m]	10.000	10.000	10.000	10.000
Stressed length	$L_g$ [m]	102.6288 (+0.010%)	102.6288 (+0.010%)	102.6186 (ref.)	102.6188 (+0.0002%)
Tension at midspan	$T_h$ [kN]	76.8691 (-1.499%)	78.8802 (+1.078%)	78.0389 (ref.)	78.056 (+0.022%)
Sum of vertical support forces	- [kN]	61.6527 (-2.549%)	63.2571 (-0.0125%)	63.2649 (ref.)	63.2711 (+0.010%)

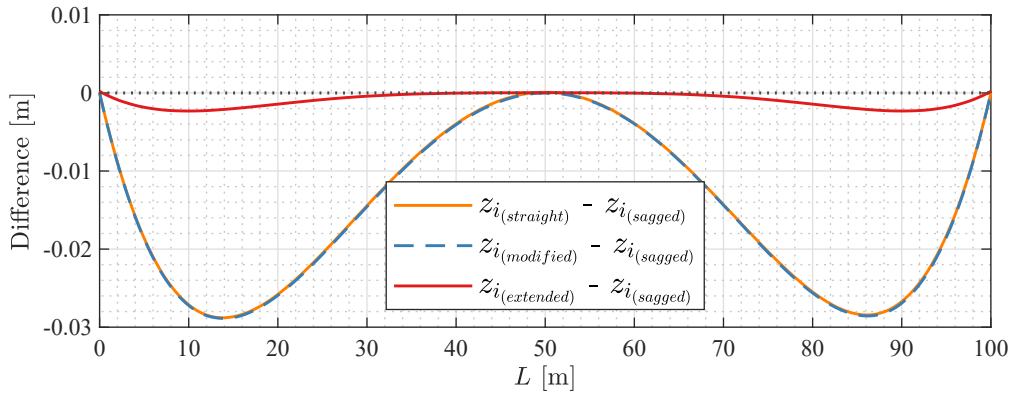


Figure 5.3: Difference in deformed shapes between straight, modified and extended models, and the sagged model. Straight and modified cable models overestimate cable length. Initially sagged model is virtually exacted compared with the analytic catenary solution. The extended cable agrees well with the latter.

## 5.2 Modelling saddles and deviators

Cable models typically assume support conditions to be non-translatable and either hinged, fixed or with a certain rotational stiffness. Either of these are based on a point-supported cable as can be assumed for a typical anchorage.

For curved supports and deviators, however, the cable remains in contact with the curved surface of the support element up to a point where it detaches and then sags freely under its self-weight. This last contact point arises naturally from the combined equilibrium conditions and the deformation behaviour of cable and deviator, and its determination requires the analysis of a nonlinear contact problem with consideration of the aforementioned cable characteristics. The properties that will affect the length of the contact region and the distribution of contact pressures are: cable tension force, bending stiffness, and length as well as saddle geometry. This section presents a numerical modelling method to account for the effect of geometric supports on structural cables using nonlinear Finite Element formulations that can be used for suspension bridge cables as well as for external post-tensioning tendons and extradosed cables.

Modelling the contact region requires developing a contact formulation. While many generalised contact formulations exist [78, 79], they can be computationally expensive and inefficient for specific and complex applications. Other approaches address variations in the length and uncertainties associated with boundary conditions by determining the effective vibration length independently from mode shape ratios [45, 80–83]. However, such

methods heavily rely on adequate sensor placements and draws comparisons with a simplified modified taut-string model, indicating avenues for future research to address these limitations. Furthermore, this technique considers the impact of uncertainties at the boundary (i.e. curved saddle) using statistical methods and optimisation. These approaches generalise over the uncertainties arising from localised interactions at the boundary and do not directly represent mechanical interactions.

Utilising nonlinear springs in FE cable modelling is a more efficient approach that assures higher versatility and adaptability to other cases. Research has explored the use of nonlinear springs to model the contact between cable wires [66, 84–87]. However, the novel method presented in this study models the contact between the deviating support and the cable by employing stiff radial springs assigned with a gap. This gap represents the distance between the support surface and the cable's undeformed state. The spring will only activate its longitudinal stiffness when the cable deflects down onto the actual deviator surface location, thus ensuring accurate modelling of the contact region. Saddle springs are added to the models presented in section 5.1 and can be easily generated algorithmically when the deviator geometry and the intended spring spacing (spatial discretisation) is defined. The spring stiffness can account for deviator deformability but is here assumed to be rigid.

Since the initial cable geometry for the straight and modified straight models is the same, the spring gap for both models is given as per the saddle radius  $R$  and location of the node  $(x_i, z_i)$  (shown in Figure 5.4). The gap at point  $i$  is given from trigonometry as

$$\text{gap}_i = R \left( \frac{1 - \cos \beta_i}{\cos \beta_i} \right), \quad (5.2)$$

where  $\beta_i = \arctan x_i / (R + z_i)$ .

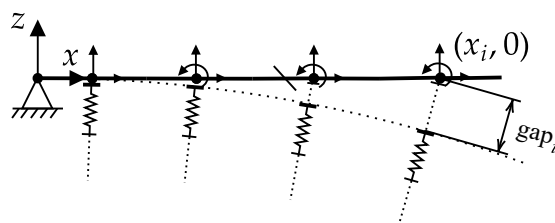


Figure 5.4: Saddle springs alignment and spring gap calculation for the straight and modified straight cable models.

For the initially sagged cable model a geometry is generated that connects the circular shape in the saddle region with the free cable parabolic profile. This is done using piecewise continuous functions which fulfil  $C^1$  continuity at the interface.

Therefore, the support region of horizontal length  $l_1$  is analytically determined depending on the radius  $r$  where that is chosen slightly larger than  $R$  (here  $r = R + 0.01\text{m}$ ) so that an initial spacing is formed between the initial cable geometry and the modelled deviator. The spring gaps calculated in this case are

$$\text{gap}_i = \frac{R(1 - \cos \beta_i) + z_i}{\cos \beta_i} \quad (5.3)$$

where  $z_i$  here is determined according to  $r$ . The loading allows the cable to find the form and contact point based on the self-weight. The remaining geometry is assigned as a second order parabola with an initial maximum sag  $s_{\text{max.}(int.)}$ . Figure 5.5 depicts the geometry and the saddle springs arrangement for the initially sagged model.

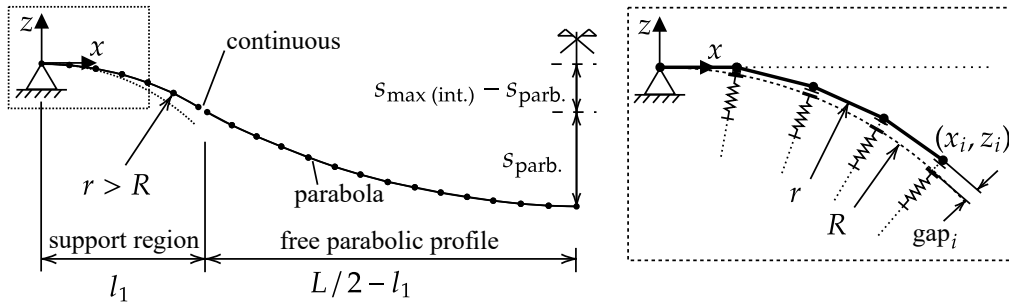


Figure 5.5: Model composition for the initially sagged cable model showing saddle springs and their gaps' calculation.  $s_{\text{parb}}$  refers to the maximum sag of the parabola geometry only.

In the above models the springs are aligned in the radial direction of the saddle, which effectively approximates the direction of the nodal displacements during the contact finding process. The extended straight model, however, uses vertical springs which can slide longitudinally and whose spring gap corresponds to the distance to the saddle as shown in Figure 5.6. Since the cable is initially extended beyond the span length to model the overlength (see section 5.1.4), the cable nodes move substantially in the span direction during the form-finding process. As the correct spring gap is dependent upon the final position of the node according to the saddle geometry, the spring gaps need to be calculated here in an iterative process. The initial spring gap is assigned according the nodes' undisplaced positions. These are corrected after the first form-finding analysis with updated longitudinal node positions and the analysis is repeated until geometry compatibility is achieved. Typically no more than two iterations are needed for a sufficiently accurate model.

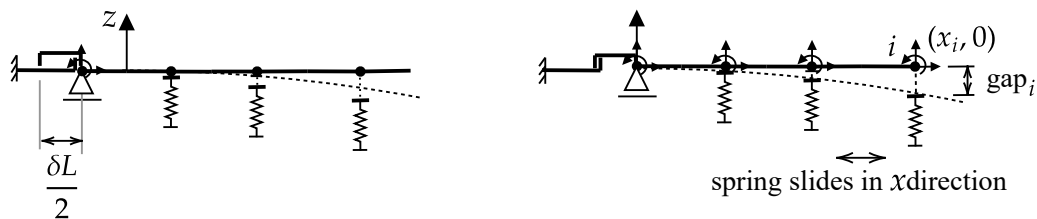


Figure 5.6: Saddle springs for the extended straight cable model and its gap calculation. Spring position before loading (left) and after loading (right). This model has vertical springs as to allow horizontal translation of the springs.

## 5.3 Model application for form finding of suspended cables

In all described saddle models, the cable finds its form under its self-weight using large-displacement geometric nonlinear analysis mentioned in Section 5.1.1, which also accounts for the nonlinear spring elements being activated if the node's displacement reaches the corresponding spring gap length. The contact length of the cable is obtained from the last contact point being the last node that activates its respective spring.

The analysis was performed here with saddles discretised by 400 springs along a total provided saddle perimeter length of 5m on a typical saddle radius  $R = 8\text{m}$  otherwise using the same model parameters as in Table 5.1.

### 5.3.1 Profiles of cables without bending stiffness

In this section the cable is analysed assuming zero bending stiffness, such that cable curvature can only originate from loads perpendicular to the axis. The saddle has a positive curvature with net contact pressures directed upwards and the cable catenary a negative curvature due to self-weight directed downwards. The last contact point must thus naturally constitute an inflection point of the cable profile and is located where the tangent of a hinge-supported catenary (hyperbolic function) matches the tangent of the saddle curvature. This can hence be analytically computed and is in this case at a length of  $L_c = 3.0725\text{m}$  measured along the perimeter of the saddle.

The results of the analysis using the four models and assuming no cable bending stiffness are shown in Table 5.3, comparing the respective results in terms of cable length, length of saddle contact region (measured along the saddle perimeter) and tension force at midspan.

Generally, all models perform reasonably well and are able to represent the saddle contact

problem effectively. However, the performance of the models would differ when bending stiffness is considered. It is noted that due to the contact length the effective span length is substantially reduced, resulting in a difference of some 6% for the tension force compared to the results of Table 5.2 without saddle and highlighting the importance of accurate contact modelling for cables of substantial sag. The initially straight model underestimates the cable force by 1.1% compared to the initially sagged model, whilst the modified straight model overestimates it by almost 2%. The extended model's tension force is within 0.5% difference from the reference value.

The initially sagged model is found to be the most accurate compared with the catenary solution with the computed contact length having an error of only 13.1mm compared to the analytical solution, which is close to the spring spacing (saddle discretisation) of 12.5mm. It shall thus serve as reference model for the validation and indicates that the extended straight model is also highly accurate. The very large displacements that this model undergoes are accurately accommodated, providing good prediction of the cable shape in terms of contact length and catenary shape, which are a result of the accurate representation of the self-weight due to the extension length. The need to iterate the spring gap spacings is a result of the large longitudinal node displacements of well over one meter at each model end, but results in an accurate and versatile model which can represent the complex geometrical and mechanical conditions through a systematic modelling approach that does not require prior assumptions to be made regarding the final cable shape.

The errors of the simpler straight and modified straight models might still be acceptable for some engineering applications, yet these models require more attention in terms of the sensitivity of the model to certain model parameters, especially when considering bending stiffness.

Table 5.3: Results of four methods to model a saddled cable with  $R = 8\text{m}$  and no cable bending stiffness.

Parameter	Symbol [Unit]	Straight	Modified	Sagged	Extended
Unstressed length	$L + \delta L$ [m]	102.6255 (+0.013%)	102.6254 (+0.013%)	102.6117 (ref.)	102.6148 (+0.003%)
Stressed length	$L_g$ [m]	102.6302 (+0.013%)	102.6302 (+0.013%)	102.6167 (ref.)	102.6198 (+0.003%)
Contact length	$L_c$ [m]	3.1431 (+1.863%)	3.1431 (+1.863%)	3.0856 (ref.)	3.1127 (+0.878%)
Tension at midspan	$T_h$ [kN]	72.1396 (-1.094%)	74.0365 (+1.506%)	72.9378 (ref.)	73.243 (+0.418%)

### 5.3.2 Profiles of cables with bending stiffness

In the previous section the cable is analysed assuming the simplifying case of zero bending stiffness. Now the analyses are repeated with cable bending stiffness added to illustrate its effect on the contact problem and the tension force and show the performance of the models. It is already indicated in the research that the effects of the bending stiffness increases for cables with high sag [35, 39].

When bending stiffness is increased, curvatures of the cable will be associated with bending moments, which in turn will affect the equilibrium condition of the cable. In the specific case of the saddled cable, the contact length is supported by the saddle springs. When the cable reaches the final contact point, it is allowed to sag freely and its ability to remain in a positive curvature beyond the contact region depends on its bending stiffness. This generates a fixing effect at the contact point, causing the cable to maintain its positive curvature until it reaches the inflection point where the curvature changes from positive to negative along the remaining free length (point of zero moment). Therefore, beam Finite Element formulations are required to model this behaviour and the inflection points indicate locations where the bending moment becomes zero. The four cable models with saddle saddle springs can be used otherwise unchanged and shall be studied here.

Naturally, no analytical solution can be derived for this problem. In Tables 5.4 and 5.5 the results of the models for two  $EI$  values are given. These correspond to 0.5 and 1.0 of the reference bending stiffness value, selected within the typical range for cables of this size as given in Table 5.1.

Firstly, it is noticeable that the midspan moment value for the initially sagged model significantly differs from the other models. This is due to the initial geometry, which already imposes a substantial curvature as an unstressed geometry and hence requires much smaller moment-inducing curvature to be induced during form finding. This highlights the importance of erection of a cable when bending stiffness is present in the model and the sag is large. In a suspension bridge, for example, the main cable is installed wire-by-wire and hence obtains its geometry without appreciable moments. Therefore, the sagged model would be highly accurate because the bending stiffness of an individual wire can be neglected.

For cables erected as a single component that is initially straight in its unstressed condition, the other models are more representative. Such cables often do not have a very large sag, but still the bending moments induced due to the sagging effect might not be negligible. In the present example, the straight and modified models replicate the bending moment effect well. It is noteworthy that the bending stiffness effect activated from an initially straight model appreciably reduces the equilibrium tension force. This effect is much less pronounced in the initially sagged model.

All models successfully reproduce the fixing effect of the saddle contact area that the bending stiffness activates and that leads to a substantially different curvature distribution as compared to an infinitely flexible cable, as discussed above. The higher the bending stiffness becomes, the less contact length required to produce the fixing effect, as can be seen in the table. Further, Figure 5.7 visualise the contact point locations between the models with different bending stiffness, and Figure 5.8 shows the effect of bending stiffness on the contact point and the cable profile as computed with the extended cable model.

Table 5.4: Results comparison of the four saddled cable models with  $0.5EI_{ref.}$ . Percentage differences correspond to tension forces in Table 5.3 of each model.

Parameter	Symbol [Unit]	Straight	Modified	Extended	Sagged
Unstressed length	$L + \delta L$ [m]	102.5926	102.5932	102.5851	102.6094
Stressed length	$L_g$ [m]	102.5972	102.5979	102.5900	102.6143
Contact length	$L_c$ [m]	1.5518	1.577	1.5876	1.5775
Tension force (ref.)	$T$ [kN]	70.6887 (2.01%)	72.5676 (1.98%)	71.8583 (+1.89%)	72.7577 (0.25%)
Midspan moment	$M_y$ [kN.m]	1.743	1.742	1.716	-0.211

Table 5.5: Results comparison of the four saddled cable models with  $1.0EI_{solid.}$ . Percentage differences correspond to tension forces in Table 5.3 of each model.

Parameter	Symbol [Unit]	Straight	Modified	Extended	Sagged
Unstressed length	$L + \delta L$ [m]	102.5616	102.5624	102.5640	102.6119
Stressed length	$L_g$ [m]	102.5661	102.5670	102.5688	102.6168
Contact length	$L_c$ [m]	0.8718	0.9103	0.9626	0.9751
Tension force (ref.)	$T_h$ [kN]	68.4740 (5.08%)	70.3071 (5.04%)	70.4570 (3.80%)	72.5136 (0.58%)
Midspan moment	$M_y$ [kN.m]	3.5681	3.5943	3.4974	-0.4118

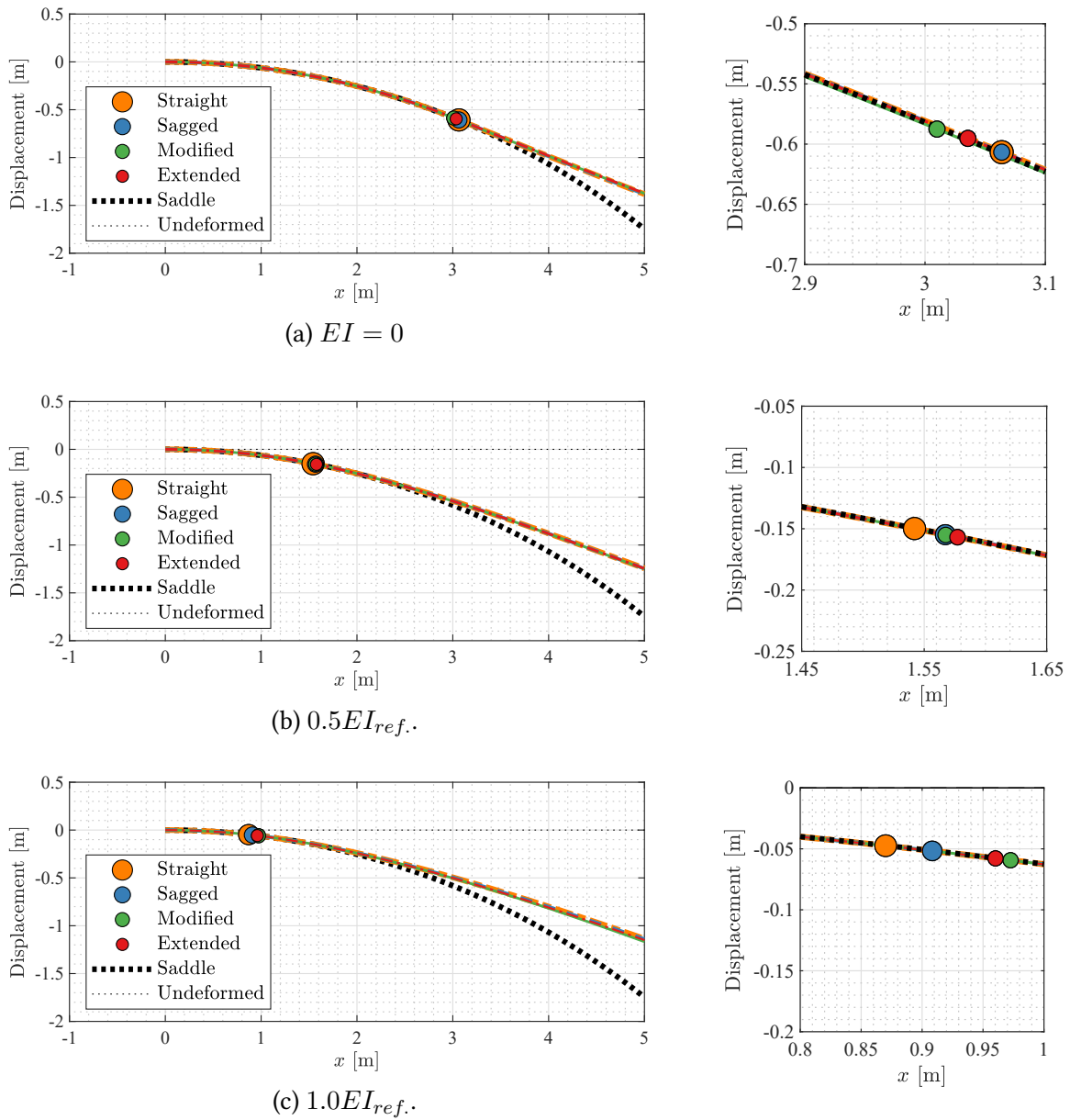
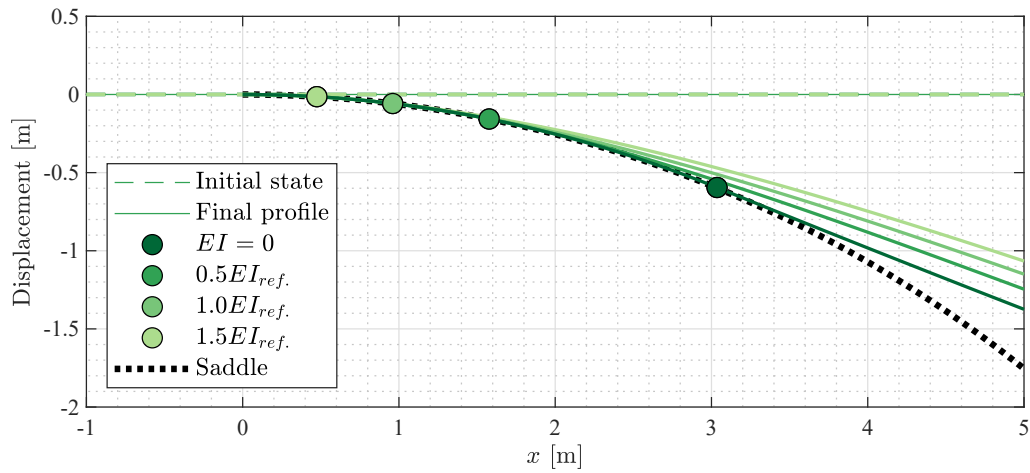
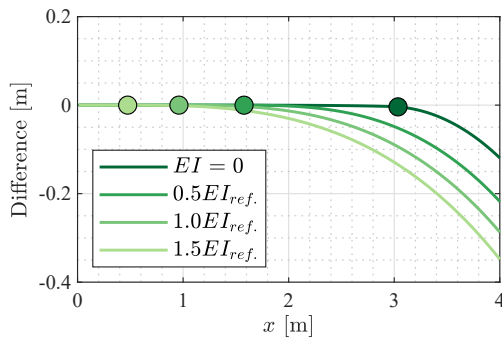


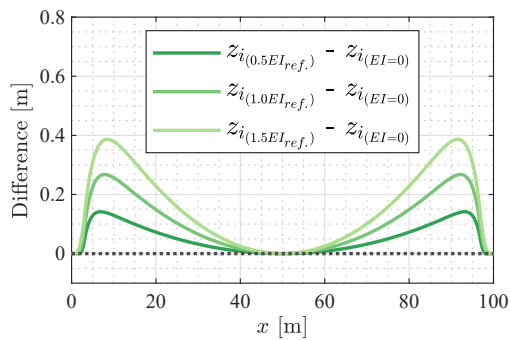
Figure 5.7: Contact point locations along the saddle for the four saddled cable models of different bending stiffness.



(a) Cable profile showing the contact point. Aspect ratio is 1:1.



(b) Difference between the saddle geometry and cable profile.



(c) Difference between cable profiles in reference to cable without bending stiffness.

Figure 5.8: Effect of bending stiffness on saddle region and cable shape as per the extended cable model, which is used given its accuracy as a generalised saddled cable model.

Considering the distinct assumptions governing the models, various advantages and some drawbacks emerge for each. The straight and modified cable models present a straight linear initial geometry that proves applicable in diverse cases. Notably, this geometry ensures precise gap values between the cable and the saddle to be assigned to the radial spring. Despite its simplicity, challenges arise with the linear assumption of self-weight distribution along the cable, particularly as inaccuracies increase with higher sag. This results in a potential overestimation of the contact point, especially when including the bending stiffness. Additionally, performing a large displacement geometrically nonlinear analysis becomes computationally expensive. Nevertheless, given its simplicity, this model remains practical for analysing small sag taut cables.

The initially sagged model offers a notable advantage in terms of reduced computational

costs, as it leverages the initial parabolic cable profile, limiting the load case to self-weight only. Its avoidance of large displacements enhances efficiency, making it particularly suitable for suspension bridges or scenarios where cables are installed wire by wire. Furthermore, the model is virtually exact compared with the analytical catenary solution regarding the stressed length and contact point when bending stiffness is neglected. Nevertheless, requiring user-defined small gaps in the radial spring elements and the inability to determine moments induced by high curvature during large displacements with bending stiffness consideration pose limitations.

The extended model possesses a standalone advantage, as it can be applied in any setup and delivers highly accurate results. Its initial straight geometry enhances the model's versatility, eliminating the need for making assumptions about the final cable shape beforehand. The resulting cable geometry closely approximates the analytical solution. Nevertheless, the considerable horizontal and vertical displacement experienced by this model results in an augmented computational cost.

The next section deals with applying on of these modelling methods for on-site cable parameter identification using vibration measurements.

## **5.4 Model application for tension force identification of external tendons**

When external post-tensioning tendons are guided over deviator saddles, the contact length along the deviator changes according to the cable tension force, sag and bending stiffness. The change in the free length of the cable is reflected as a nonlinear change in the system stiffness. From the perspective of practical measurement techniques used to determine cable tension forces from identified natural frequencies, a model able to compute this complex response can be used to identify system parameters more accurately.

This section focuses on adapting the straight saddled cable model to calculate tension force from on-site vibration measurements. The model, referred to here as the saddled model, enables direct determination of the cable form (as described in Section 5.1.1). Instead of using an unstressed overlength of  $L + \delta L$ , a pre-tensioning force  $T_h$  and self-weight are employed as a load case. Once the cable form is obtained, modal properties (i.e. natural frequencies and modal numbers) are iteratively calculated by conducting an Eigenvalue analysis, utilising the obtained tangent stiffness matrix.

### 5.4.1 Test setup

A 10-span motorway bridge in Thuringia Germany was undergoing maintenance works. The bridge superstructure is a concrete box girder prestressed with external tendons, and a new deviation shell was to be replaced on a deviation block. This required the tendon to be gradually destressed and removed to allow installation. During destressing, tension forces were directly measured with a lift-off test as seen in Figure 5.9. In addition, accelerometers were placed on the tendon to identify the natural frequencies at each off-loading step. The tension force is then indirectly derived using the saddled model and the results are compared with the values from the lift-off test.



Figure 5.9: Experimental direct and indirect tension force identification: Lift-off test jack in place at span anchor (left) and vibration signal acquisition setup near the deviation block (right).

The tested tendon is a parallel wire SUSPA Draht EX-66 cable encased in a PE duct [88]. The duct is filled with a flexible filler material to prevent wire corrosion and allow wire re-tensioning and replacement.

Tension forces selected for comparison are taken from the lift-off test as  $T_1 = 2692\text{kN}$ , and  $T_2 = 1862\text{kN}$  and cable properties and geometry measurements on-site are mentioned in Table 5.6. The span selected for the vibration test is located between the span anchor and the first deviation point. When tension force decreases, the corresponding increase in sag changes the contact point with the deviator and increases the free length  $L - L_c$ . This effect could be simulated using the saddled model as the model geometry is independent from the free length and only requires the prior knowledge of the inclination angle  $\alpha$ , the distance between the two anchored points  $L_x$ , and the deviator radius  $R$  as depicted in Figure 5.10.

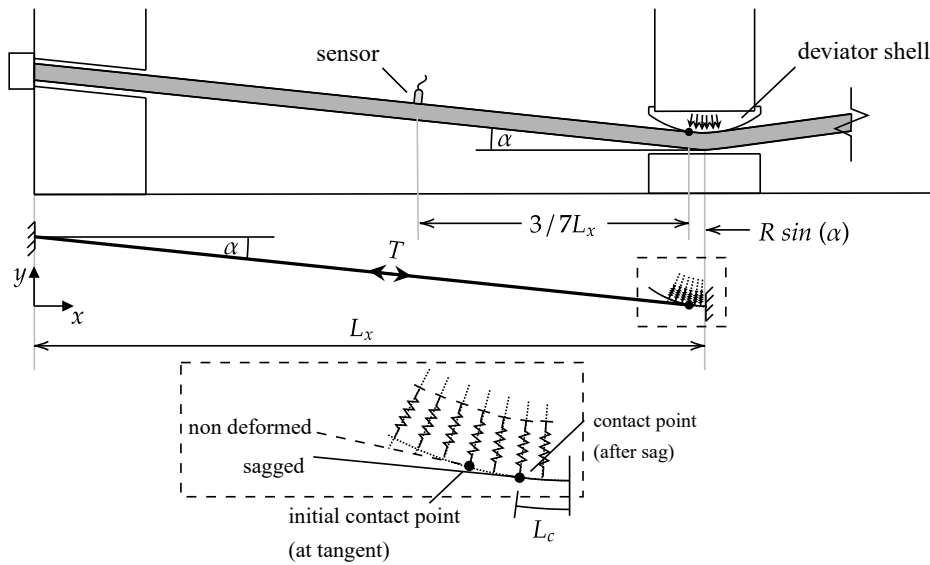


Figure 5.10: Experimental tension force identification: a schematic showing the model setup at the anchor-deviator subsection and the saddled cable.

Table 5.6: Experimental tension force identification: tendon properties and test setup parameters.

Parameter	Symbol [Unit]	value
Wire diameter	$D$ [mm]	7
No. of wires	-	66
Duct outer diameter	- [mm]	90
Duct thickness	- [mm]	5.1
Total mass per length	$m$ [kg/m]	23.85
Measured free length of cable (at $T_1$ )	$L - L_c$ [m]	$17.460 \pm 5\text{cm}$
Total length horizontal projection	$L_x$ [m]	[17.822-17.925]
Inclination angle	$\alpha$ [deg]	5.74
Deviator shell radius	$R$ [m]	5
Bending stiffness	$EI$ [kN.m <sup>2</sup> ]	[0-120]

The in-plane acceleration time history for  $T_1$  and  $T_2$  are obtained from an ambient vibration test under active traffic (Figure 5.11). The signals are then analysed using a Fast Fourier transform (FFT) to obtain the frequency spectrum and identify natural frequencies as shown in Figure 5.12 and Table 5.7. The measurement and digitisation system data are mentioned in Table 5.8.

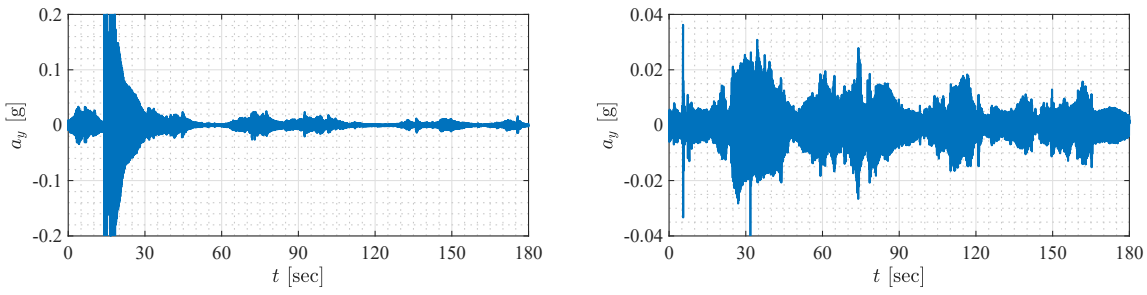


Figure 5.11: Experimental tension force identification: Acceleration time history for tendon under  $T_1$  (left) and  $T_2$  (right).

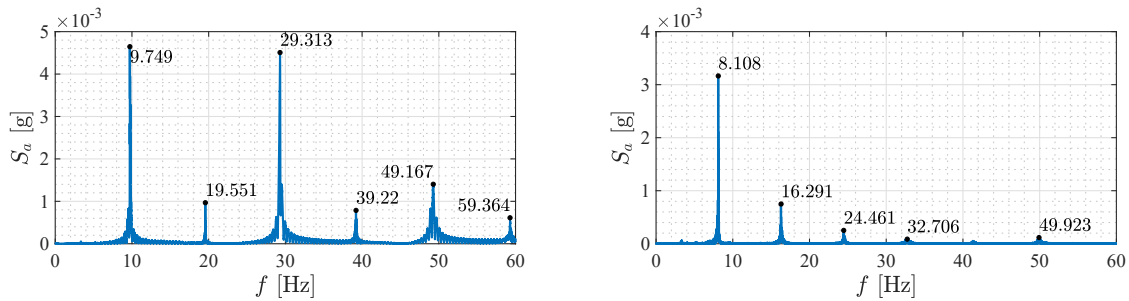


Figure 5.12: Experimental tension force identification: Frequency spectra for tendon under  $T_1$  (left) and  $T_2$  (right).

Table 5.7: Identified natural frequencies for  $T_1$  and  $T_2$ .

Mode number	1	2	3	4	5	6
$f_{idn.}^{T_1}$ [Hz]	9.749	19.551	29.313	39.220	49.167	59.364
$f_{idn.}^{T_2}$ [Hz]	8.108	16.291	24.461	32.706	–	42.923

Using the natural frequencies, common cable models are used to identify the tension force and compare results with the saddled cable model. Selected models are the taut string theory (Equation (3.12)), the modified taut string model (Equation (3.13)), and the Flat Bar model Equation (3.14).

The cable parameters used in all models lie within a range of uncertainty, which requires the use of optimisation methods to give the most accurate prediction of natural frequencies. Given the multivariable nature of the models, it is most appropriate to use the PSO method to assure converging to a global error minimum in the search space. This algorithm generates a set of swarms across the entire search space, where each swarm is comprised of uniformly

Table 5.8: Measurement system used in signal acquisition and digitisation.

Sensor type	PCB (ICP) Accelerometer 326A03
Sensitivity	1000 mV/g
Range	$\pm 5$ g
Resolution	0.000005
Data logger	HBM MX410
Sampling rate	1200 Hz
Measurement duration	180 s

distributed data points (particles). This assures guiding the optimiser to the lowest error minimum in the search space [73, 89].

The cost function used for optimisation for a given  $T$  is the mean of absolute errors ( $MAE$ ) between natural frequencies from the models and those from the test. The natural frequencies used in optimisation for each tension force  $T$  are those listed in Table 5.7. The parameters used in the optimisation are tension force  $T$ , free length  $L - L_c$  or  $L_x$  for the saddled model, and bending stiffness  $EI$ . Lower and upper parameter limits are as given in Table 5.6. For the tension force, the lower and upper limits are chosen to be  $\pm 200$  kN for each  $T_1$  and  $T_2$  to ensure obtaining the lowest error in the search space. The optimal solution is reached when the difference between  $MAE$  values remains less than  $1E-6$  for 40 iterations in a row. The number of swarms used is 400 swarms with 30 particles each.

## 5.4.2 Identified tendon parameters

The results show that the models gave very low absolute error with their optimum values, with mean error ranging between 0.61% and 0.08%. The error values for frequencies are shown in Figure 5.13 for  $T_1$  and  $T_2$  respectively. Given the low  $MAE$  values, it is found nonetheless that the taut string model and the modified TS overestimate the tension force by 3.606% and 2.584% for  $T_1$  and 3.892% and 2.127% for  $T_2$  respectively. The former overestimates the tension force to compensate the neglected bending stiffness, therefore also giving the highest  $MAE$  value of all models. Similarly, the hinged end linear beam assumption for modified TS underestimate the boundary condition effects, which leads to an overestimation of the tension force.

Contrarily, the flat bar model underestimates the tension force ( $-0.570\%$  for  $T_1$  and  $-2.518\%$  for  $T_2$ ). The assumption of a fixed end linear beam model deems this model too stiff for an accurate prediction, especially as the sag increases when tension is decreased. The saddled cable model gave the most accurate tension force results with errors of  $-0.047\%$  for  $T_1$  and  $-1.343\%$  for  $T_2$ . The ability to determine the free length based on the interaction between the geometry and the tension force, and including the additional effects of the geometric stiffness

positively contributed to increasing the accuracy of the prediction. Table 5.9 and Table 5.10 mention the optimum parameters for  $T_1$  and  $T_2$  respectively.

In addition, all models predicted similar values for the bending stiffness, with a clear increase in its value as the tension force decreased. This may be attributed to two phenomena. First, decreasing the tension force by releasing the wires at the anchor end leads to an increase in stored inter-wire friction, especially as wires compress against one another as the cable axis changes at the deviator. The increase in inter-wire friction increases the bending stiffness. Second, it might also be due to the nature of the bending stiffness itself; the cable in all models is represented as a solid section. Therefore, the bending stiffness is assumed constant along the entire length. In reality, the flexible filler between the cable wires leads to an elastic longitudinal connection between wires, and their bond would differ along the length depending on the curvature of the cable. This phenomenon is previously observed in other cable types as in [65, 66, 90, 91] and could therefore lead to considerable errors.

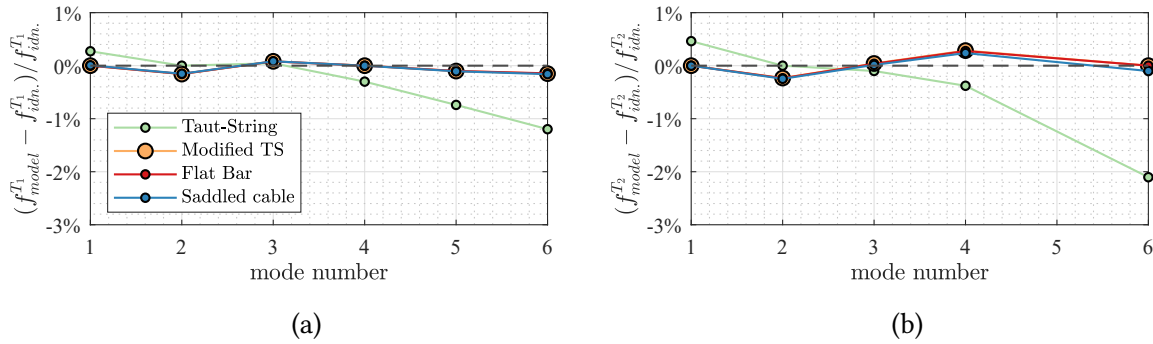


Figure 5.13: Frequency error for models with optimised parameters.

Table 5.9: Optimum parameters for frequencies identified at  $T_1 = 2692$  kN (ref.).

Model	$T$ [kN]	$L - L_c$ [m]	$EI$ [kN.m <sup>2</sup> ]	min. MAE
Taut String	2789.07 (+3.606%)	17.491	-	0.426 %
Modified TS	2761.55 (+2.584%)	17.459	65.56	0.098%
Flat Bar	2676.66 (-0.570%)	17.499	64.78	0.080%
Saddled	2690.73 (-0.047%)	$L_x=17.923$	63.43	0.085%

### 5.4.3 Parametric study

A sensitivity study is made to infer the parameters' influence on the natural frequencies. The contribution of each parameter differs as per the modal number. For the first natural frequencies, the effect of the tension force is much higher than e.g. bending stiffness, whereas the latter plays a more important role with higher vibration modes. Sensitivity indices are

Table 5.10: Optimum parameters for frequencies identified at  $T_2 = 1862$  kN (ref.).

Model	$T$ [kN]	$L - L_c$ [m]	$EI$ [kN.m <sup>2</sup> ]	min. $MAE$
Taut String	1934.47 (3.892%)	17.482	-	0.609%
Modified TS	1901.61 (2.127%)	17.426	88.91	0.112%
Flat Bar	1815.11 (-2.518%)	17.461	86.18	0.110%
Saddled	1837.00 (-1.343%)	$L_x=17.925$	80.00	0.120%

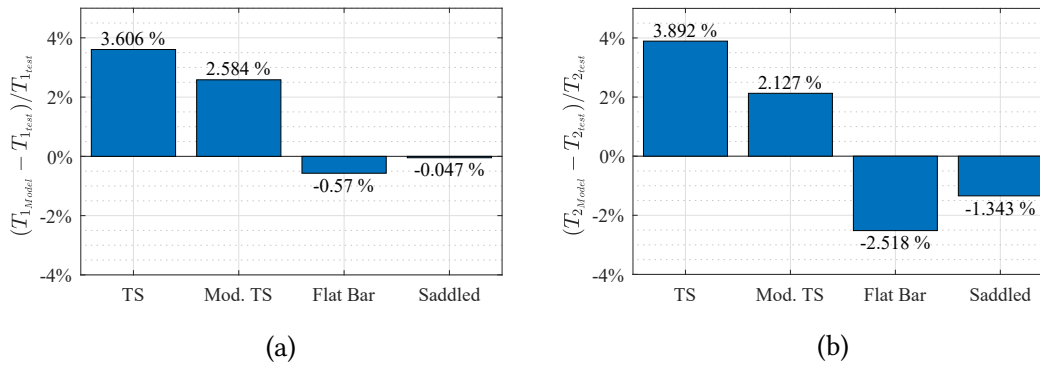


Figure 5.14: Tension force error values for models used in the tension force identification from vibration measurements. The saddled cable model shows lowest sum of absolute errors, while the taut-string tends to overestimate the tension force.

calculated to identify the contributions of each parameter on the output of the first  $f_{model}^1$  and the sixth  $f_{model}^6$  natural frequency.

To determine the parameter influence on the natural frequencies of each model Sobol sensitivity indices are used. First order indices  $S_1$  determine the influence of a parameter while maintaining all other parameters constant and neglects the interaction between the parameters. The total indices  $S_{T_1}$  additionally include the overall sensitivity and interaction effects between the parameters. Details and equations for calculating the indices are found in [92]. The parameters are uniformly sampled within their uncertainty range as aforementioned to calculate the indices. The number of sampling size for parameters is 100,000.

The results show that there are negligible differences between the first order and total sensitivity indices, hinting at the low interaction effects. The first frequency has the highest sensitivity to the tension force for all models under  $T_1$  and  $T_2$ , especially the taut string and modified taut string models. The effect of bending stiffness is more pronounced in the other two models. Additionally, the effect of varying the length by only 10 cm shows to have a very low effect on the model output. For the sixth natural frequency, the bending stiffness effect is much more noticeable, especially for the flat bar model and the saddled model.

#### 5.4. Model application for tension force identification of external tendons

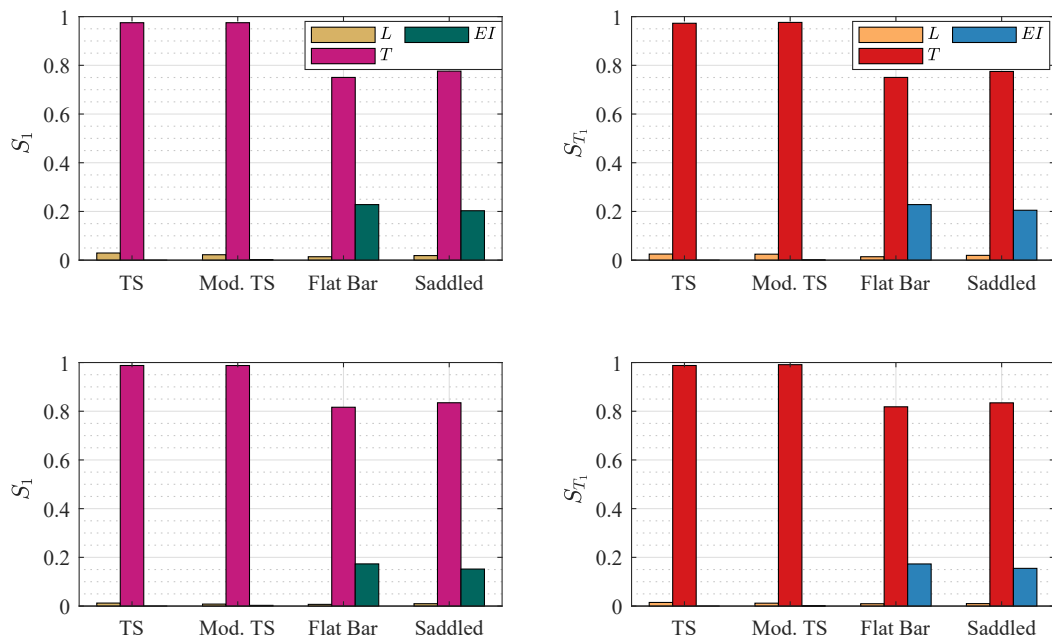


Figure 5.15: First order  $S_1$  and total sensitivity index  $S_{T_1}$  of parameters used in cable modelling: First natural frequency for tension force  $T_1$  (top) and  $T_2$  (bottom).

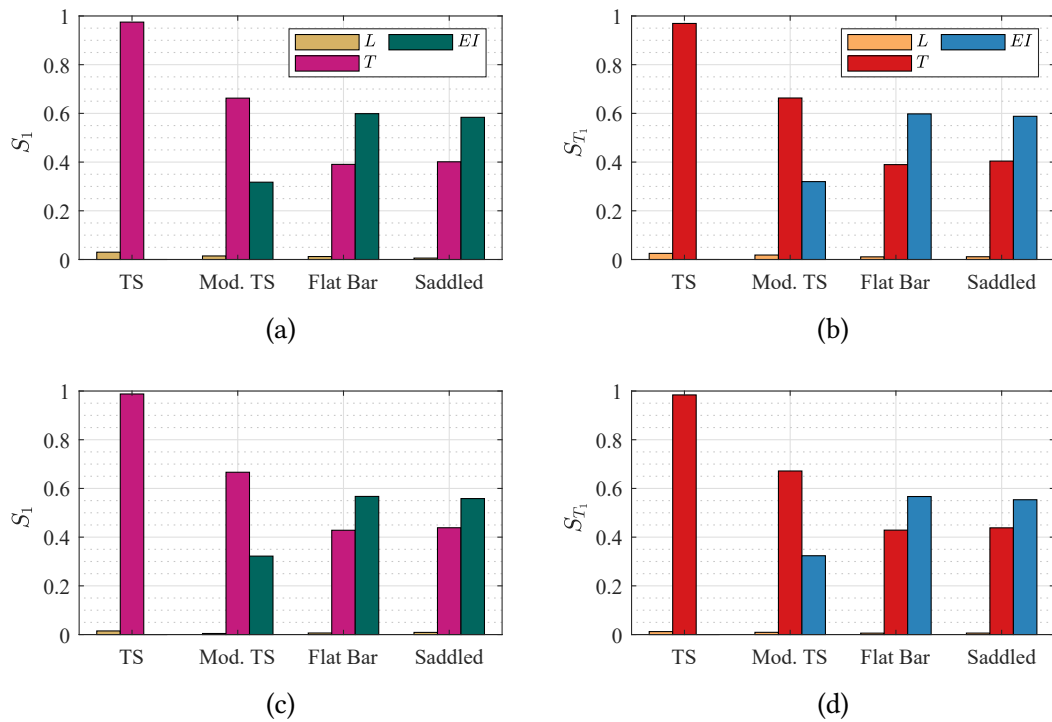


Figure 5.16: First order  $S_1$  and total sensitivity index  $S_{T_1}$  of parameters used in cable modelling: Sixth natural frequency for tension force  $T_1$  (top) and  $T_2$  (bottom).

In summarising this test setup, the straight saddled cable model not only demonstrated its proficiency in tension force identification, but also showcased its high accuracy by closely aligning with reference values. The model's noteworthy feature lies in its ability to maintain its geometry almost independently from the tension force. As tension decreased, so did the contact length, resulting in an longer free length. This elongation is attributed solely to the interplay between geometry and stiffness.

However, delving into the dynamic behaviour under transient loads introduces a new perspective. The change in free length can occur during vibration cycles under the same tension force e.g. the the dynamic variability of tension force, intensity of the vibration, geometric stiffness reduction during upward and downward motion and the subsequent variation in contact length, all collectively influence parameter identification and dynamic properties.

The following section discusses the the dynamic behaviour of the saddled cable model.

## **5.5 Dynamic behaviour of the saddled model for taut cables**

In this section, the saddled cable model is used to compute dynamic cable response in order to investigate the nonlinear effects arising from the contact-type support conditions and to assess the ability of the model to replicate such effects. The Eurocode also advises to investigate the dynamic interactions between the cable and the surrounding structure, and that nonlinear effects should be analysed with the FE method [3].

When external post-tensioning tendons are guided over deviator saddles, the contact length along the deviator will change over time as the cable moves up and down during a dynamic response. This results in a change of the free length of the cable, which represents a stiffness change that causes highly nonlinear effects in the system response.

From the perspective of practical measurement techniques that aim to determine cable tension forces from measured natural frequencies, such effects introduce a fundamental complication. Whilst for pin-ended cables the effective length of the cable remains constant and nonlinearity arising from cable sag remains limited, the effective stiffness change in the deviated cable will render the linear concept of a modal representation inapplicable. However, if a nonlinear model is able to compute such a system's response in time accurately, it can be used to identify system parameters.

The models discussed before can be readily used to perform such dynamic analysis by first obtaining the cable form and then integrating the dynamic equation of motion forward in

time by a nonlinear time-domain analysis. The element formulation used here for incremental analysis to update the geometric stiffness at every time step is the Updated Lagrangian method typically used for large displacement analysis [18]. A frequency spectrum of the dynamic response is then computed from the free vibration response of the cable using a Fast Fourier Transform (FFT) to study the degree of nonlinearity and determine frequency bands of the response.

As a reference object, a mildly taut cable with parameters listed in Table 5.11 is studied at a cable force of 1500 kN in the static case under self-weight. The cable is modelled with beam elements. In the saddle region, the cable is discretised into 320 elements stretching along 1.6m from each end. At each node in the saddle region, a rigid radial spring with a respective gap is assigned. In the free span region, the cable is discretised into 284 elements.

Table 5.11: Model parameters for the proposed cable models.

Parameter	Symbol [Unit]	Value
Section area	$A$ [cm <sup>2</sup> ]	78.54
Modulus of elasticity	$E$ [GPa]	200
Span length	$L$ [m]	60
Reference tension force at midspan	$T_h$ [kN]	1500
self-weight	$w$ [kN/m]	0.6165
Saddle radius	$R$ [m]	30

### 5.5.1 Static form finding and modal analysis

First, a static analysis is conducted for the cable in order to establish its equilibrium condition as discussed earlier. Since the sag is relatively small for taut cables, the initially straight cable model is employed. In order to obtain the target cable force  $T_h$  of 1500 kN under self-weight, the static analysis is performed iteratively until the required unstressed length is found. The results of the cable shape for the pin-ended and the saddled cable are compared in Table 5.12 for different bending stiffnesses. As discussed before, the bending stiffness significantly affects the contact length along one saddle perimeter  $L_c$  and thus also the resulting free cable span length ( $L - 2L_c$ ).

Table 5.12: Comparison of static parameters for models with several  $EI$  values.

Parameter [unit]	$EI = 0$		$EI = 0.125EI_{ref.}$		$EI = 0.25EI_{ref.}$	
	Pin-ended	Saddled	Pin-ended	Saddled	Pin-ended	Saddled
$s_{max}$ [mm]	184.867	182.839 (-1.097%)	182.834	182.311 (-0.286%)	181.965	181.785 (-0.099%)
$L_c$ [m]	-	0.360	-	0.200	-	0.160
$L - 2L_c$ [m]	60.000	59.280	60.000	59.580	60.000	59.700
$L_g$ [m]	60.00152	60.00149	60.00148	60.00147	60.00147	60.00146

Using the results of the static analysis, the natural frequencies and modes of vibration can be determined through an Eigenvalue analysis. This assumes a linear system behaviour and is thus representative of a vibration with infinitely small amplitudes around the static equilibrium only. These properties can be computed using the tangent stiffness matrix as obtained from the geometrically nonlinear static analysis and the results are shown in Table 5.13. Therein, the natural frequencies obtained from the numerical models are compared with approximating analytical models. The analytical model of the taut string of Equation (3.12) serves as reference for the pin-ended cable. Here, the numerical model obtains a fundamental frequency that is about 2.54% higher than that of the analytical model, highlighting the limitations of the analytical model in the first mode due to the cable sag. The frequencies of the higher modes are however within 0.08% for the cable with  $EI = 0$ . The analytical model of a fixed-end flat bar according to Equation (3.14) can be used as reference with the free length of  $L - 2L_c$  used as cable length for the cases with bending stiffness. This increased stiffness leads to higher frequencies which compare well with the ones obtained from the saddled cable model. Only the fundamental frequency is again significantly underestimated by the analytical model, but higher modes' frequencies are in good agreement.

## 5.5.2 Dynamic behaviour

The vibration of the saddled cable is investigated using a nonlinear time-history analysis with an initial transient excitation through a harmonic loading. During the time integration procedure using a standard Newmark scheme the stiffness of the dynamic system is updated at each time step to account for the large-displacement geometric nonlinearity and the nonlinear spring effects on the saddle in an iterative process until the convergence criteria of a residual force limit of 0.001 kN in that time step is fulfilled.

Here, the cable is modelled with zero bending stiffness in order to maximise the nonlinear saddle effect. The excitation is firstly applied as a distributed harmonic load  $q(t)$  along the length of the cable with a load amplitude  $q_0$  and a sinusoidal frequency of 1.340 Hz. This excitation frequency is chosen to be close (within  $\pm 10\%$ ) to the first Eigenfrequency of the cable. The time step used for the simulations is 0.02 seconds. A schematic showing the model setup is shown in Figure 5.17.



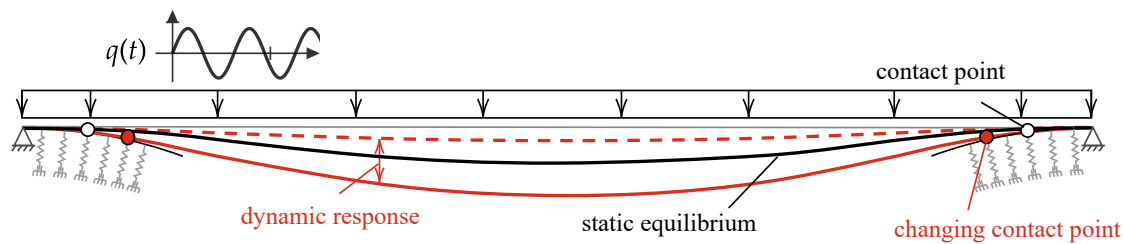
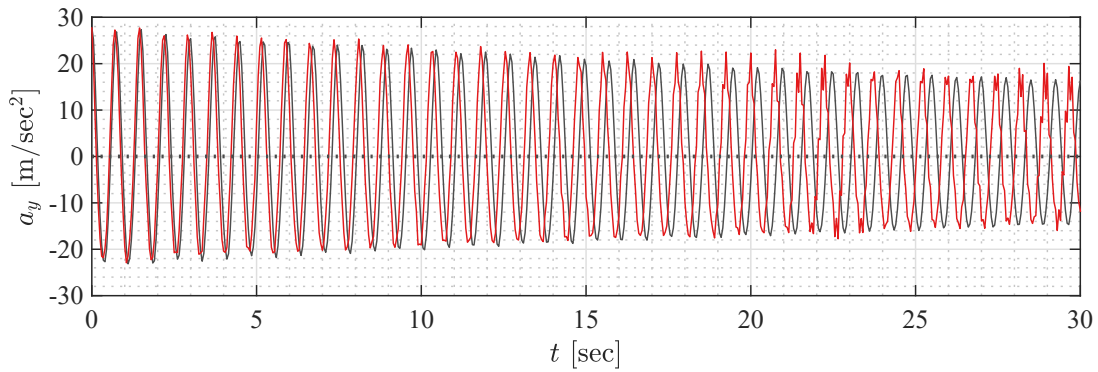


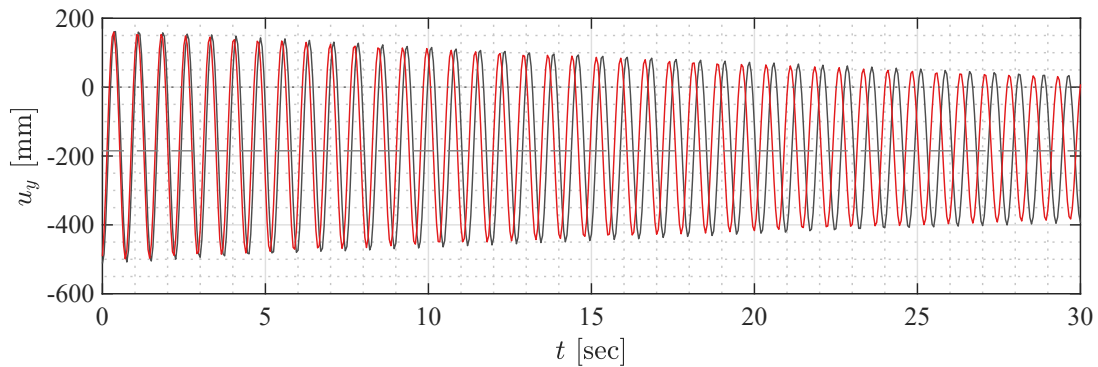
Figure 5.17: Model setup for dynamic analysis. Harmonic load extends along the entire cable length with frequency excitation close to the first Eigenfrequency.

Due to the low intrinsic damping ratios of structural cables and the varying effective stiffness, a mass and stiffness proportional damping matrix is used in the dynamic analysis. Usually, the stiffness proportional coefficient is assumed zero. However, given the relatively low mass of the cable and the dependence of the stiffness on the loading and tension force, the stiffness component of the damping is equally important to be accounted for. The damping coefficient  $\zeta$  used was 0.2% for the first and second vibration modes.

Initially, a small amplitude for the harmonic load is chosen to compare the saddled model with the sagged string model (here referred to as the pin-ended model). A choice of a small load amplitude is made equalling one sixth of the self-weight of the cable  $q_0 = w/6$ . This shall provide insight into the small amplitude vibration behaviour of both models. After exciting the cable for 4 seconds, the cable is left free to vibrate for 100 seconds. Analysing the free vibration gives a frequency resolution of 0.01 Hz. To this end, the in-plane vertical acceleration and displacement are obtained at midspan and the acceleration time history of the free vibration is transformed into a power spectrum using a FFT. The fundamental frequency is then obtained to interpret characteristic vibration frequencies that correspond to natural frequencies of a linearised system. The vertical displacement and acceleration time history for free cable vibration are shown in Figure 5.18.



(a) In-plane vertical acceleration.



(b) In-plane vertical displacement.

Figure 5.18: Time history comparison: in-plane free vibration at midspan for (—) pin-ended model and (—) straight saddled cable model. (- - -) the cable sag at midspan. Both models are subjected to the same harmonic load with the same timestep properties. Plot shows the first 30-second of the free vibration.

The spectral peaks are found to compare well with the analytical and modal results reported in (Table 5.13), cf. Figure 5.19. This highlights that response measurements on pin-ended cables can be readily used to determine cable forces using identified frequencies and such analytical relationships. However, the dynamic analysis determines the natural frequency of a cable vibrating with cycles of upwards and downwards motion. In contrast with the modal analysis, it is noticed that the identified frequencies have a reduced reliance on the maximum sag at the static equilibrium by identifying a lower fundamental frequency. The response spectrum shows that the fundamental frequency for the pin-ended model is slightly less than the one determined from the modal analysis, with a reduction of around -1%. A similar outcome is determined in the saddled cable model with a reduction in the determined frequency of around 0.6%. Figure 5.19 shows the response spectrum for both the pin-ended model and the saddled cable model.

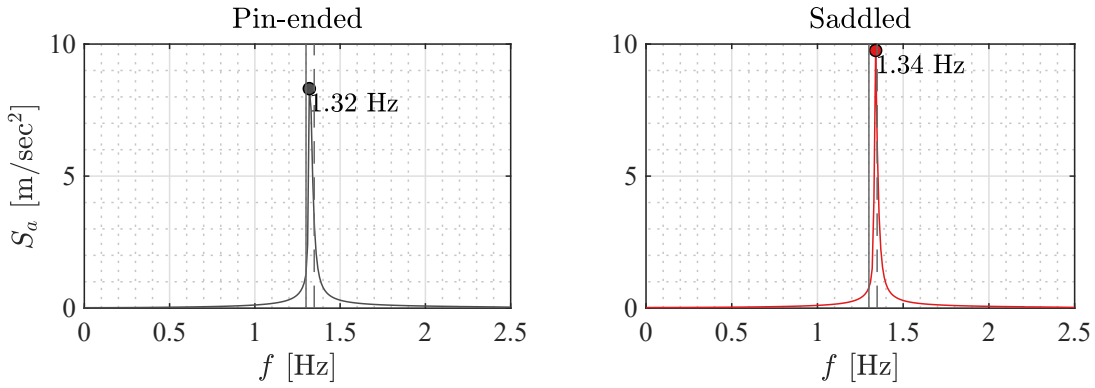


Figure 5.19: Frequency spectrum of a 100 second free vibration response at midspan: (—) the pin-ended cable model (—) straight saddled cable model. Vertical lines: (|) the analytical natural frequencies, (:) the frequencies obtained from the numerical model. Reference values: Table 5.13.

Moreover, the free cable length changes significantly in time due to the instantaneous contact points moving on the saddle throughout the vibration cycles. When the cable translates downwards, the contact length increases and the free length reduces, effectively stiffening the cable – and vice versa. Figure 5.20 plots the time history of the free length.

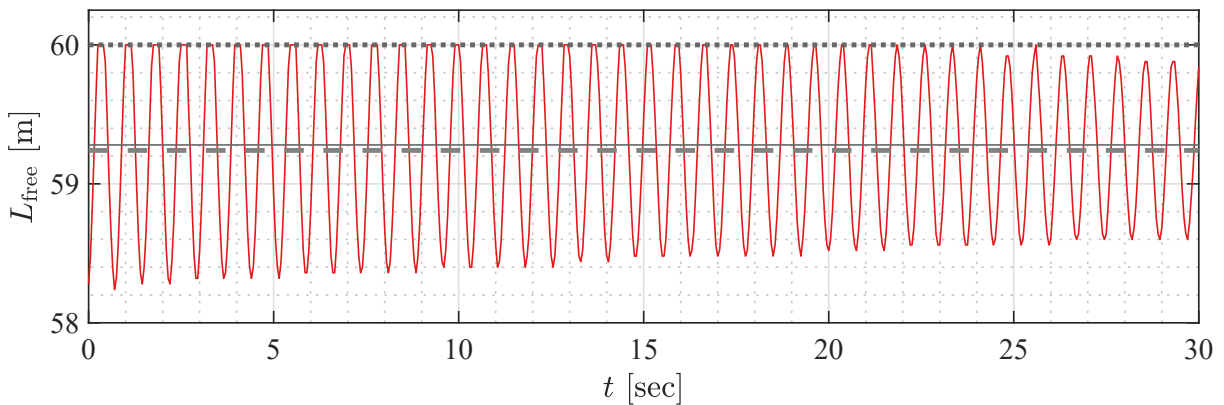


Figure 5.20: Free length time history ( $L - L_{c_{left}} - L_{c_{right}}$ ) during free vibration. (—) identified free length at static equilibrium, (- - -) average free length during free vibration.

The degree to which this nonlinear saddle effect is present depends on the amplitude of vibration and can subsequently affect the values of the Eigenfrequencies as well as the spectral peak shape. To investigate this, multiple harmonic load amplitudes are applied eccentrically along one quarter the length from the end. This can ensure that several modes be excited. For this case, two amplitudes are chosen for excitation ( $q_0 = 0.65w$  and  $q_0 = 1.3w$ ). Similarly, the cable is then left free to vibrate for 100 seconds. A schematic showing the excitation is made in Figure 5.21.

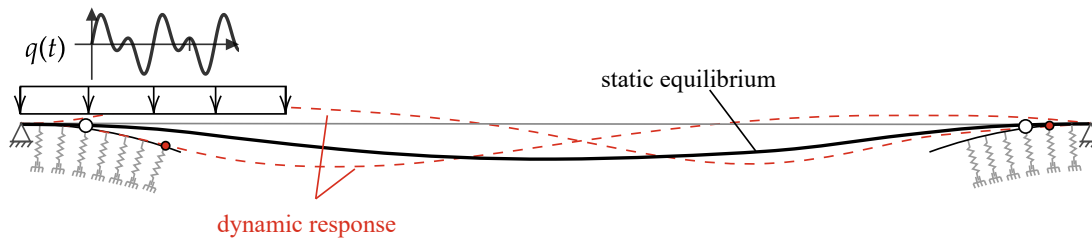


Figure 5.21: Model setup for dynamic analysis. Harmonic load excites one quarter-length of the cable with two frequencies: first and second Eigenfrequency.

The vertical displacement and acceleration time history at midspan for free cable vibration are shown in Figure 5.22. Whilst accelerations are dominated by the response of higher modes, the displacements are largely due to the fundamental mode. These displacements are the main source of nonlinearity arising from the cable saddle effect.

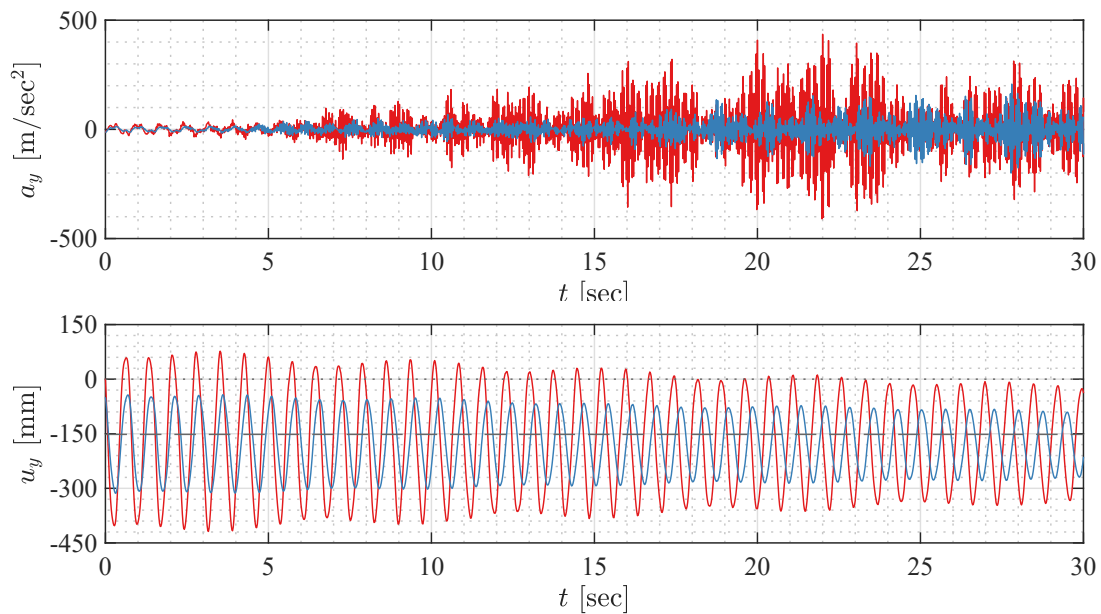


Figure 5.22: Time history for the vertical cable free vibration for multiple  $q_0$  at midspan (coloured). (—)  $q_0=0.4\text{kN}$ , (—)  $q_0=0.8\text{kN}$ . (---) maximum sag at static equilibrium.

The free length is also obtained by identifying the activate springs at every time step. The results show that the free cable length changes significantly in time due to the instantaneous contact points moving on the saddle throughout the vibration cycles. Given that the harmonic load excites the cable in several vibration modes, the free length also shows significant variation. Figure 5.23 plots the time history of the free length, highlighting that the degree

to which this nonlinear saddle effect is present depending on the amplitude of vibration and excitation frequency.

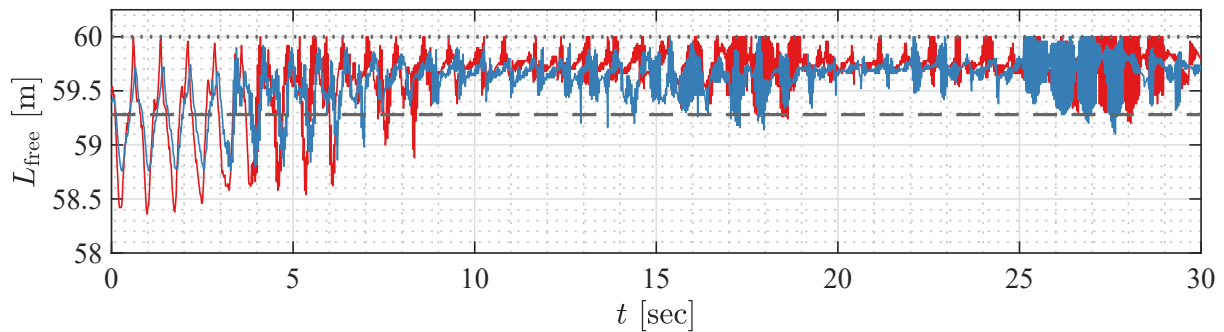


Figure 5.23: Time history of cable free length ( $L - L_{c_{left}} - L_{c_{right}}$ ) using free vibration response based on the identified contact lengths  $L_c$ . (—)  $q_0=0.4\text{kN}$ , (—)  $q_0=0.8\text{kN}$ , (---) free length at static equilibrium.

The FFT analyses shows that the change in free length and corresponding variations in effective stiffness result in a spreading of the mode-related frequency peaks, cf. Figure 5.24. What are very narrow-banded responses for the small amplitude vibration become successively broader responses for increasing amplitudes because of the increase in contact length variation. Additionally, the frequency of the peaks picked for each response band successively increase as the load amplitude increases, because the free length reduction increases.

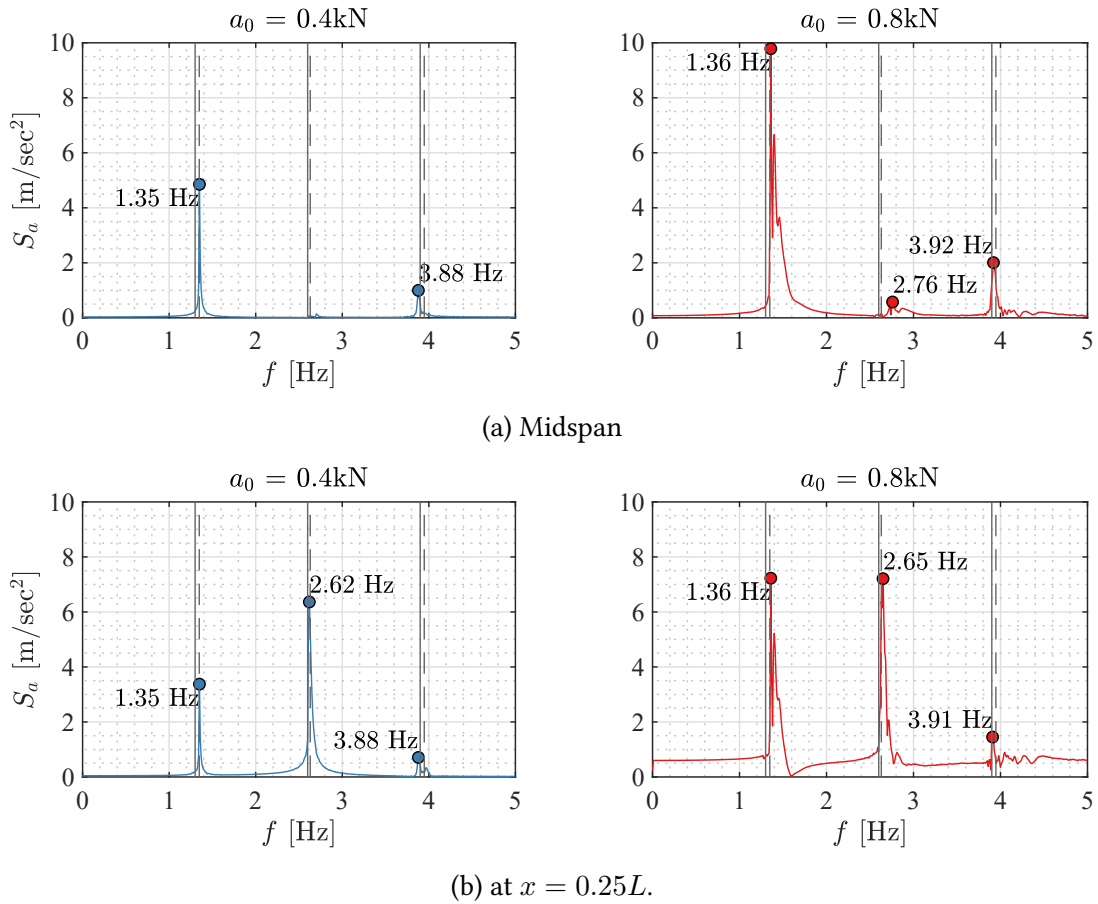


Figure 5.24: Frequency spectrum of 100 second free vibration response of saddled cable model for multiple load amplitudes  $q_0$ . Vertical dashed lines: the reference frequencies of Table 5.13. (—)  $q_0=0.4\text{kN}$ , (—)  $q_0=0.8\text{kN}$ .

The results clearly show, that the effect of saddles and deviators on cable vibration can considerably affect the dynamic properties and should be carefully considered when attempting system identification based on vibration measurements. On the other hand, the nonlinear modelling approach presented here accounting for saddle effects, can be used to derive relationships between cable parameters including cable force, saddle geometry, excitation amplitudes and the frequency bands of the dynamic response. Such relationships can be used in an inverse analysis to identify e.g. tension forces from measured response data. Further, if the numerical model is used in a parameterised fashion, unknown parameters such as cable force can be determined through standard model updating procedures.

## 5.6 Summary and conclusions

Given that the dynamic response characteristics of a cable fundamentally depend on the static equilibrium condition, the chapter compares four numerical modelling techniques for determining the equilibrium condition in a geometrically nonlinear analysis with application of the cable self-weight for large sag cables. One model, the initially sagged cable model, is identified as highly accurate.

Additionally, this section proposes a novel numerical modelling approach that accounts for the mechanical effects of cable-deviating supports. The proposed saddled cable model is based on a nonlinear FE formulation that uses nonlinear radial springs to represent local geometric contact conditions efficiently. The model considers the effect of bending stiffness and shows the fixing effect of the saddle contact area, resulting in a different curvature distribution than that of an infinitely flexible cable.

Modal properties obtained from the static analysis are used for cable force identification of an external tendon on site. The actual tension forces are provided using a lift-off test, and commonly-used cable models are used for referenced comparison. Results show that error values for the tension force identification of the saddled cable model are notably lower e.g. 1.3% in comparison to 3.9% for the taut-string theory, 2.1% for the modified taut-string model, and 2.5% for the flat bar model. The saddled cable model predicts the tension force most accurately because it represents the change in stiffness by adopting to the change in geometry and the decrease in contact length as the tension force decreases, and a parametric study shows the effect of parameters on natural frequencies.

The static analysis is then used to determine linearised modal properties and as a basis for nonlinear time history analyses of a cable's dynamic response. The effect of saddles is confirmed to be a change of effective free length throughout vibration cycles which leads to considerable effects on the frequency spectrum. Specifically, wide frequency bands are found during strong saddle interaction and the effect of vibration amplitude and cable stiffness is highlighted.

The numerical models presented in this section are highly accurate and can be used for determining force-response relationships in system identification techniques, especially when increased accuracy for complex cable arrangements is required.

# Chapter 6

## Stick—slip behaviour of semi-parallel wire cables

### 6.1 Introduction

In the preceding chapters, the impact of bending stiffness on both static and dynamic behaviour of cables has been explored. In Chapter 4, the identification of bending stiffness encountered notable uncertainties for long cables, where the vibration behaviour was predominantly influenced by axial and geometric stiffness. Achieving accurate identification of the bending stiffness value required the inclusion of high mode numbers. Despite these efforts, a significant degree of uncertainty persisted in the identified value, evident in the considerable differences between the model outputs.

Expanding on this in Chapter 5, the cable's bending stiffness played a major role in determining the contact point between the saddle and the cable. Moreover, it was established that the determination of tension force for a short cables exhibited higher dependence on the bending stiffness. The identified values showed increased consistency due to the high sensitivity of the bending stiffness to the Eigenfrequencies. However, anomalies were observed in the values under a change in loading, thus hinting at a possible dependency of the bending stiffness on the loading history.

While bending stiffness was treated as a constant parameter in previous sections, it's imperative to acknowledge that in reality, the bending stiffness of cables is not a constant numeral. This overarching variable is a composite outcome of mechanical interactions between cable wires. It encompasses factors such as cross section composition, friction, tension force, loading history, and end conditions. The stick—slip behaviour of helically twisted cables, a broad research field, is dependent upon factors like cable type, geometry, inter-wire friction assumptions, loading conditions, etc.

As discussed in Chapter 3, prediction models often simplify cables as flexible strings or tensioned beams [8, 27, 49, 50, 55, 93, 94]. In the case of modelling cables as tensioned beams, the flexural rigidity is typically calculated using either theoretical estimates, experimental

calibrations, or optimisation methods. However, when subjected to high bending curvature, the frictional bond between the wires starts to decrease by displacing the wires relative to each other in the longitudinal direction, and the bond between the wires is lost [95]. This relative longitudinal displacement contributes to the loss of flexural rigidity, leading to a nonlinear moment-curvature relationship that affects the hysteresis behaviour and cable dynamic properties [79, 96]. Therefore, it is essential to account for wire slipping in analysis models to accurately predict bending stiffness, hysteresis behaviour, cable self-damping, and wear effects [97].

Nonlinear FE modelling is a valuable tool used for the prediction of the stick—slip interaction between cable wires and yields detailed insights about cable behaviour under different load cases. Nevertheless, FE models require careful selection of representative parameters and are computationally expensive. Surrogate models, such as Gaussian Process (GP), can accurately predict the output of a high-fidelity nonlinear FE model at a much-reduced computational cost. GPs are a valuable tool for efficient and accurate prediction, as they can learn the mapping between input parameters and output response using limited training data from FE simulations. The use of GPs for surrogate modelling is becoming increasingly popular in engineering applications due to their flexibility, scalability, and ability to quantify prediction uncertainty [98, 99].

This chapter introduces a FE modelling framework that relies on experimental calibration and parameter fitting to predict the stick—slip behaviour of large diameter pretensioned SPW cables. The proposed model considers important factors such as cable geometry, friction, and residual interlock between the wires. Gaussian Processes are utilised to optimise the model parameters and quantify their uncertainty. Focusing specifically on helically twisted cables, this chapter initiates with an extensive literature review on cable bending models, emphasising the unique properties of SPW cables that necessitate precise prediction models for wire interactions. Subsequently, a novel FE modelling framework is introduced. The framework is augmented by a surrogate GP model to address computational challenges. Application of this model on an experiment highlight the impact of residual interlock on bending behaviour. A detailed parametric study examines the force-deflection ( $F - u$ ) curve sensitivity to the model parameters and reveals the considerable impact on the residual interlock between wires.

The main objective of this chapter is to provide a comprehensive model of the internal mechanics governing the bending behaviour of large diameter SPW cables. This model aims to contribute to the scientific community and practitioners alike in making well-informed decisions by offering efficient and validated FE models.

It is noteworthy that the author published the findings of this chapter in a journal article [70], establishing it as a significant contribution to this research.

## 6.2 State-of-the-art helically twisted cable models

Several studies are found in the literature addressing the stick–slip behaviour of multi-strand conductors and locked-coil ropes. Raj and Parthasarathy 2007 [100] conducted a comprehensive review of mathematical models, with a focus on addressing friction and damping effects in multi layered stranded cables under different loads. The study critically evaluated previous models for predicting the mechanical behaviour of helical wire strands and conductors, considering experimental data when available. The ultimate aim of this review study was to identify mathematical models that accommodate to complex situations like inter-wire friction effects under different load cases. It underscored the need for future research to develop more realistic models considering friction, damping, and inter-wire contact deformations, especially for multi-layered cables facing complex situations.

One prominent model presented by Papailiou for multi wire cables modelled the wire slip as a multilinear moment-curvature law assigned to beam elements and concluded that the cable bending stiffness is directly affected by the curvature and tension force applied [65]. A later study built on Papailiou's model to study the response of short span conductors [68], and developments additionally included delayed slippage effects [91]. Others derived analytical and numerical models to study the effects of wire slip and multilayer helical assemblies on the static and dynamic behaviour of cables [93, 101–113] some using efficient nonlinear spring laws to couple wires within a cross section [67, 84, 85, 87, 114] as used for modelling partial bond of composite materials [86, 115].

In most studies, inter-wire friction is represented by the Amontons-Coulomb dry friction theory, which depends only on the tension force component normal to the contact surface, and the friction coefficient. Research showed that the nature of surface micro-structure lead to a residual interlock and an amplification of dry friction between wires in the form of a stored resistance to relative displacement [116]. This physical phenomenon rose to media attention with the enigmatic two interleaved phone books experiment [117]. The additional cohesive bond is related to the manufacturing and wire laying process, which has a significant effect on the relative wire slip of slack cables and cables with low radial friction. A numerical study on Gaflan strand cables concludes that the residual inter-wire contact significantly affects the moment-curvature diagram of taut cables [66]. However, there are only few available studies addressing the bending behaviour of widely used SPW cable despite the existence of experimental results [90].

SPW cables are composed of several wires concurrently twisted about a straight core wire with diameters between 5–7mm and small lay angles typically between 2–6°. The radial component

of the tension force generates friction that holds the wires together, preventing individual spreading inside the duct. However, the pressure imposed in manufacturing helical layers and the surface micro-structure roughness generates a residual contact between the wires, increasing the overall interlocking force.

Further, twisting wire layers in the same direction with the same lay length as in SPW cables leads to a compact hexagonal wire arrangement and a high fill factor of around 0.91. Comparing with other cable types, multi-strand cables with reversed laying e.g. Galfan strands or locked coil ropes are less compact due to the circular layer arrangement with fill factors in the range between 0.7–0.82, as seen in Figure 6.1. In this case, each wire layer is in contact with the layer that precedes it only at specific, discrete contact points defined explicitly by geometry and laying angles. Therefore, the interaction between wires is not distributed along the entire length of the cable but occurs selectively at these defined contact points. Additionally, the reversed laying of each layer and the use of steep lay angles results in an increase in torsion dominated response [109, 118]. Furthermore, the circumferential contact friction is often neglected due to micro inter-layer gaps between wires of most cable types with helical arrangement [64, 96, 119]. However, the more compact cross section of SPW cables increases the effect of circumferential contact and should be considered for accurate bending prediction.

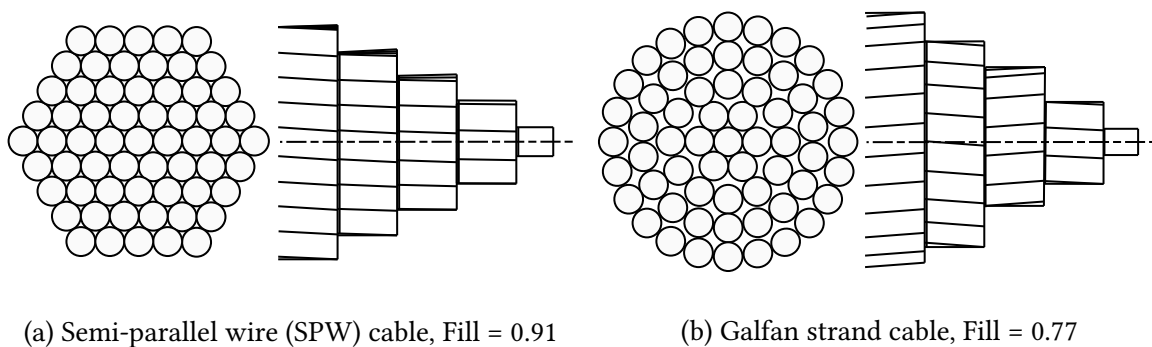


Figure 6.1: Concurrent and reversed wire laying. The hexagonal wire arrangement of SPW cables allows to have a more compact cross section with inter and intrawire contact.

Prediction models of SPW cables are important not only for high curvature loading e.g. near anchorage or at cross-tie connections [120, 121], but also for prediction of dynamic behaviour of short or large diameter cables. To the knowledge of the authors, the stick–slip behaviour of SPW cables has not been modelled outside of these studies [67, 87, 114, 122–125]. The internal contact mechanics of a 61 Aluminium SPW cable were investigated under cable clamp loads for suspension bridges [124]. The investigation included a FE model calibrated with laboratory experiments and proved successful in determining the effects of cable clamp loading and micro-surface differences on the cable stiffness. Furthermore, a

study on contact friction among inner steel wires in the bending process of  $37\phi 7$  SPW cables employed a refined FE model with a 3D mesh to analyse contact friction variations under different boundary conditions [125]. The study assumed a uniform load on outer wires and demonstrated enhanced accuracy in calculating bending and mechanical properties, revealing nonlinear relationships between the contact pressure and the displacement. However, the study neglected the effect of stored cohesion force between wires, relying solely on dry friction to assume the extrusion stress at the contact point. Additionally, the computational demands are high due to the use of 3D meshed elements for each wire along the length. In modelling larger diameter cables, the computational is expected to significantly increase along with increased numerical convergence challenges. Moreover, few researches modelled cable wires as laminated beams with analytical formulation describing inter-facial connection [122, 123]. The results showed efficient prediction when compared with experiments, but the simplification of laminated beams did not explain the physical nature of inter-wire slipping nor the specifics of wire slip propagation. Other researches modelled the bending behaviour of SPW cables [114] to be used for prediction of wire cuts behaviour and load redistribution [67, 87]. However, residual interlock was not considered and therefore resulted in clear accuracy shortcomings when compared with experiments.

## 6.3 Methodology

### 6.3.1 FEM for modelling cable wire stick–slip

The tightly twisted, helical configuration in which semi-parallel wire cables are laid results in a compact cross section, which enhances overall structural aesthetics and reduces wind-induced cable vibration. However, this compactness also generates frictional forces between cable wires, making it important to consider when predicting the bending and hysteresis behaviour of these cables. Previous research has emphasised the significance of considering the impact of cable wire friction in cable design and analysis [66, 79].

In contrast to other locked-coil types, where the wire layers are laid in a reverse pattern [65, 126, 127], the wires of SPW cables are twisted in the same direction, forming a hexagonal wire arrangement [90, 114]. As a result, each inner wire has six contact surfaces continuous along the length, which is a significant difference from other multistrand types where they have discrete contact points defined by their helix geometry.

Given the limited research on SPW cables, detailed models are necessary to investigate the frictional interaction and its impact on the bending and hysteresis behaviour. In this study, the FEM is utilised to model a  $61\phi 7$ mm diameter SPW cable, for which experimental results are available from bending tests with different pretensioning values [90].

Refined FE modelling with 3D elements offer an accurate prediction, but can be computationally demanding. To overcome this limitation, more efficient modelling approaches are used. In this chapter, cable wires are simplified as Bernoulli beams with a 3D helical geometry, and inter-wire connections are assumed to occur at discretised points along the length. Although the effect of the PE sheathing is not explicitly accounted for, this simplification allows for more streamlined parametrised modelling.

At each contact point, the two adjacent beams are coupled using a friction shear spring with an elastic-perfectly plastic law. This is a similar modelling scheme to that used in [114]. However, due to the interlocking nature of the wire micro-structure, resistance to relative longitudinal displacements between wires can occur even in the absence of normal forces on the contact surface. To simplify the model, an additional cohesion spring force is introduced. This spring yields when the transverse force surpasses the friction ratio of the normal force plus an added cohesion  $C$ . Such simplifications have been reported in validated literature results [66].

### 6.3.1.1 Model construction

The geometry of SPW cables is characterised by having a constant laying length  $l_{\text{lay}}$  and a hexagonal arrangement of wires. Each wire in a given layer has its own distance to the centre wire and lay angle, as follows

$$\beta_j^k = \tan^{-1} \left( \frac{2\pi r_j^k}{l_{\text{lay}}} \right), \quad (6.1)$$

where  $j$  is the wire number in a layer  $k$ ,  $r_j^k$  is its radial distance to the centre and  $\beta_j^k$  being its lay angle. The nodal positions  $y_j^k$  and  $z_j^k$  for each beam node for a given  $x_i$  are as follows

$$y_j^k(x) = r_j^k \cos(\theta_j^k + \gamma_i), \quad (6.2)$$

$$z_j^k(x) = r_j^k \sin(\theta_j^k + \gamma_i), \quad (6.3)$$

where  $\theta_j^k$  is the angle the wire makes with  $y$  axis at  $x = 0$  and  $\gamma_i$  is the twist angle after  $x_i$ , given as

$$\gamma_i = \frac{2\pi x_i}{l_{\text{lay}}}, \quad (6.4)$$

where  $i$  is the discretisation number of along the  $x$  axis starting at  $x = 0$ . Figure 6.2 displays a schematic of wire laying parameters.

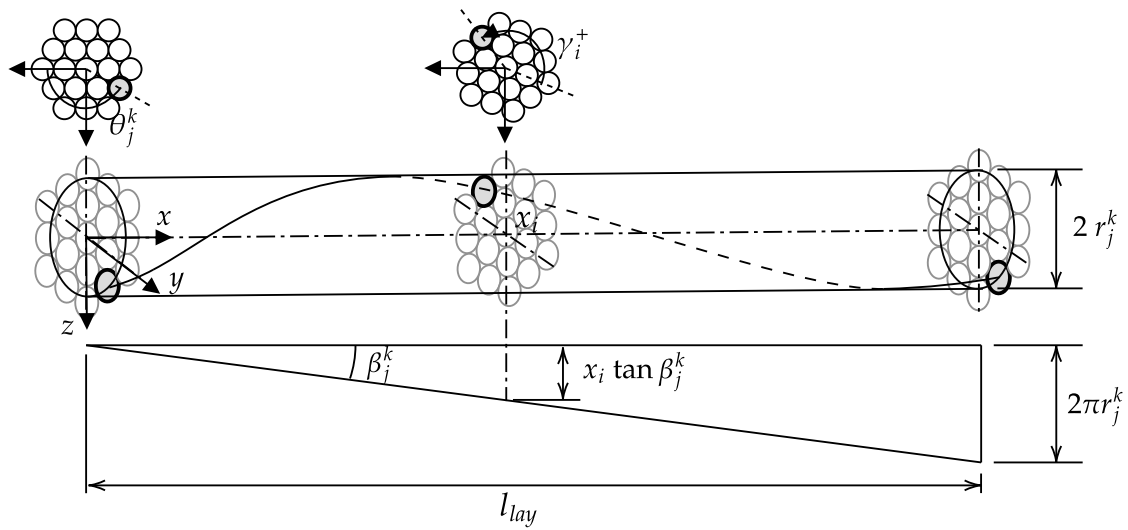


Figure 6.2: Geometric parameters of a single SPW wire helically twisted along a cable laying length  $l_{lay}$ .

Validation of the model consists of a comparison with an experimental bending test conducted on a 0.82m bending span  $61\phi 7\text{mm}$  SPW cable specimen pretensioned from both ends and subjected at midspan to a transverse load  $F$  [90]. To simulate the experimental test, the FE model is assumed hinged from both ends with a horizontal displacement release, and the load case applied includes a tension force  $T_i$  at each beam end node and a transverse load  $F$  distributed at the top wires in midspan, which corresponds to the loading conditions in the experiment. The FE model includes second order effects of the tension force and a commercial FE solver is used for the analysis. A schematic of the test setup and the FE model is shown in Figure 6.3.

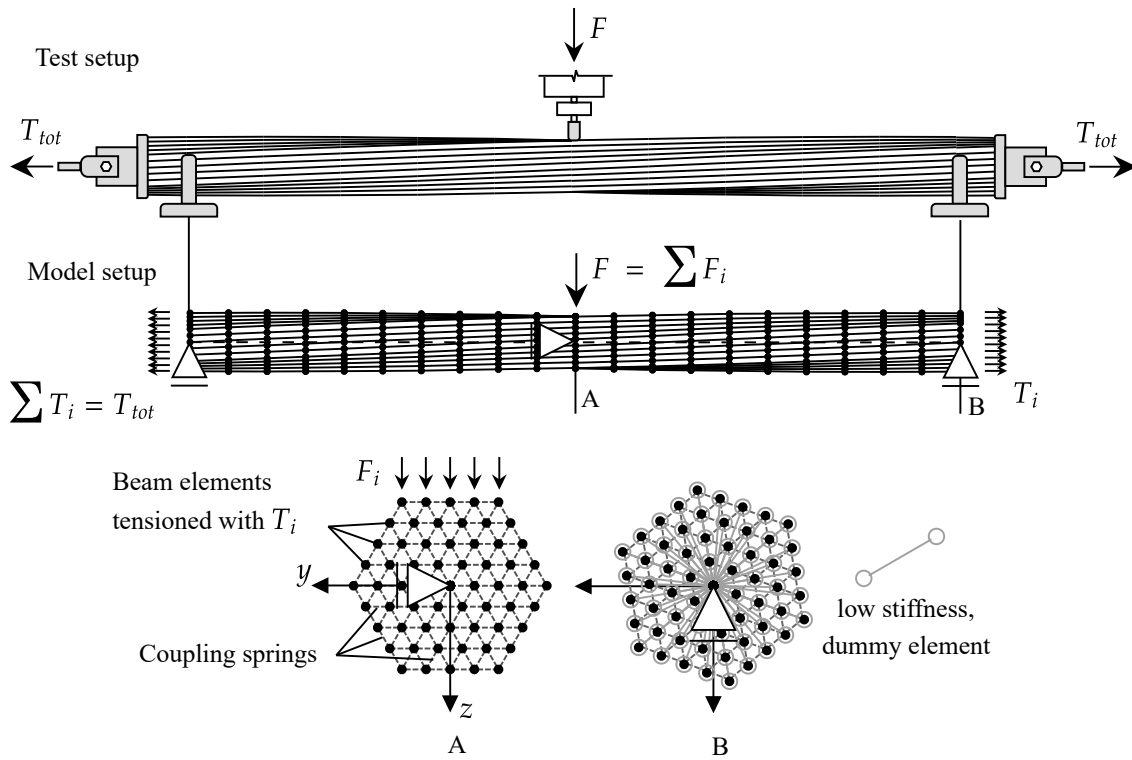


Figure 6.3: Test setup [90] and model construction. Note: the load in the FE model is placed on the top nodes at midspan similar to the actual test setup, which can lead to asymmetries in the load distribution and the yielding of springs.

In the context of bending, there are two primary forces that resist the relative axial displacement between wires and maintain inter-wire bond. The first force is associated with the cable’s geometry and tension force. When tension forces are applied to the cable, the helical configuration of a wire  $j$  in a layer  $k$  generates radial pressure along the length, directed towards the centre of gravity of the cross section. This radial pressure resists relative displacement between the wires and is proportional to both the tangent of the lay angle  $\tan(\beta_j^k)$  and the friction coefficient  $\mu$ . The second force, on the other hand, is not influenced by the arrangement of the wires or the loading but rather depends on the interlocking of the wires themselves. To account for this force, a cohesion force is introduced, designated as  $c_k$ , which operates in parallel to the contact surface. This cohesion force remains present even when non-helical, parallel wire surfaces come into direct contact. It is a result of the material’s micro-structure roughness and the pressure applied during the wire manufacturing and coiling processes. As such, it is independent of the cable’s geometric configuration.

Further, SPW cables undergo twisting with small lay angles, usually ranging from 2 to 6°[90]. Consequently, the radial normal force exerted on the contact surface, which opposes

differential axial forces in the wires, remains minimal due to the shallow lay angle. The limited effects on the geometric arrangement on wire slipping resistance emphasises the significance of the stored inter-wire cohesion in wire-to-wire contact. A distinctive characteristic of SPW cables is that all the wires are twisted together, ensuring continuous contact along their entire length. This unique feature guarantees the preservation of their hexagonal cross section throughout the cable length. In the case of 4-layer SPW cables, the typical lengths for an evolution period fall within the range of 1.67 meters to 5.04 meters. This range represents a physical constraint in the optimisation problem, particularly regarding the maximum lay angle  $\beta_{\max}$  associated with the corner wire in the last layer. In this model, each contact point is represented as two rigid elements coupled with a two-way spring acting longitudinally and transversely, as depicted in Figure 6.4. The longitudinal stiffness of the springs is here assigned a high value in this study, assuming rigid interactions on the surface and no wire spreading effect.

The transverse component of the spring yields when the spring surpasses a ratio  $\mu$  of the radial component of the tension force plus a cohesion force  $C_k$  assigned to the spring. This added force corresponds to the residual cohesion along the length  $c_k$  by multiplying it with the element length. The wires are discretised along the length with elements' nodes located at a plane slice perpendicular to the  $x$  axis. Each slice has a rotated cross section depending on the helix geometry and lay angle. Therefore, the springs at any given discrete slice have the same coupling pattern and connect the same wires, but their orientation differs with rotation of the helix geometry.

There are several ways to account for the inter-wire cohesion force, either assuming it as constant in all layers, or by assigning each layer with a different value. Here, both assumptions are considered and investigated.

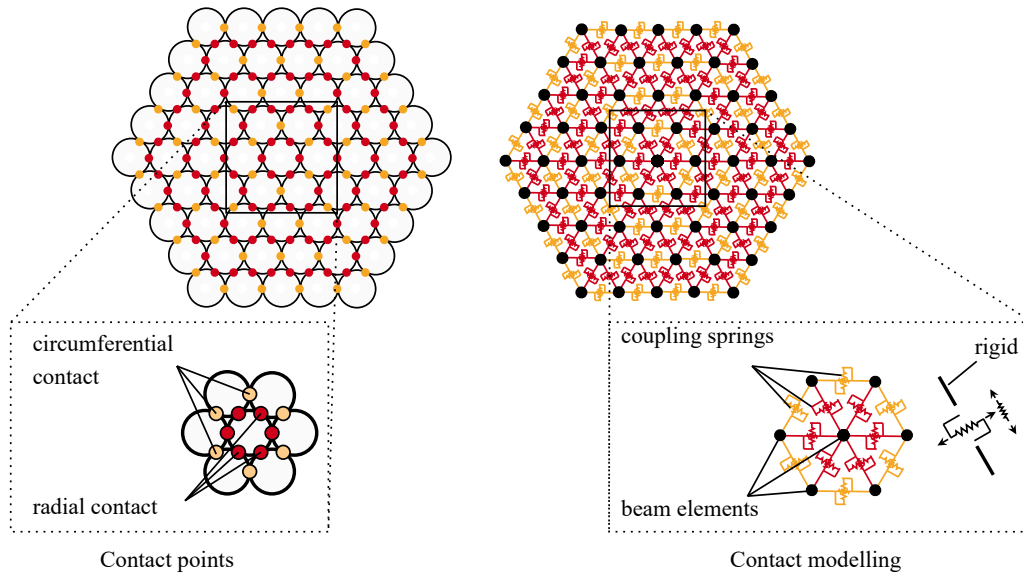


Figure 6.4: Contact modelling using coupling springs with longitudinal and transverse components for a  $61\phi 7\text{mm}$  SPW cable.

### 6.3.1.2 Model 01: Constant residual

This model assumes equal residual force ( $C_0$ ) for all coupling shear springs, neglecting any possible variations in inter-layer residual cohesion between different layers. This assumption can help elucidate the effects of maintaining a constant value. The interlocking behaviour of wires is also influenced by the maximum lay angle  $\beta_{\max}$  and friction coefficient  $\mu$ , which are additional parameters considered in this model.

### 6.3.1.3 Model 02: Varying residual

As the bending curvature increases, loss in its bending stiffness is observed to progress from the outer layers inwards. This is supported by the experimental force-displacement curve, which shows a gradual decrease in slope with increasing loads, indicating a variation in stored interlock residual forces between layers. In order to investigate this phenomenon, additional models have been considered: one with only inter-layer contact (Model 02a) springs and another with combined inter- and intra-layer i.e. circumferential contact (Model 02b). In these models, coupling springs in a given layer  $k$  are assigned with an interlock cohesion  $C_k$  that differs from that in the next layer. A schematic of the residual interlock consideration for both models is shown in Figure 6.5.

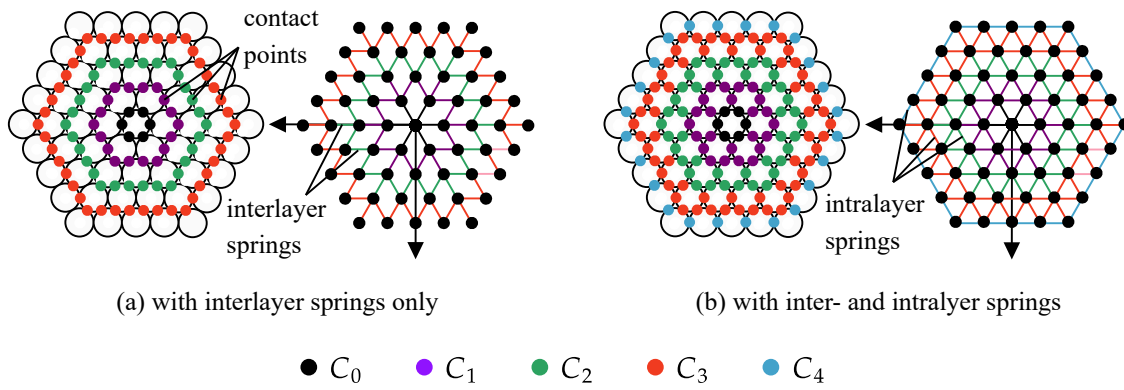


Figure 6.5: Comparison of residual contact between the model without circumferential contact Model02a (left) and the model with circumferential contact Model 02b (right). This cross section depicts the discretised slice at the midspan. While the cross section rotates at different slices, the springs maintain consistent wire coupling.

For a  $61\phi 7\text{mm}$  cable, inter-layer contact sums to 96 contact points per cross section, where including the intra-layer (circumferential) contact totals the coupling springs to 156. Whereas finer discretisation leads to more accurate results, a large number of simulations makes computational cost of the FE model a significant challenge. For example, simulating a 0.82m long cable using an element length of 0.01m as selected throughout this chapter generates 12948 nonlinear coupling springs with 5002 discretised beam elements. Therefore, employing the FE model for multivariable optimisation or assessing uncertainty and sensitivity is significantly inefficient given the considerable number of simulations needed. Therefore, utilising surrogate models e.g. Gaussian processes is advisable to enhance computational efficiency.

### 6.3.2 Surrogate models using Gaussian processes

GP regression is a non-parametric probabilistic machine learning model with a powerful training scheme that includes regularisation by construction [128]. Based on Bayesian theory, GPs define a flexible prior over functions and use noisy observations to derive a predictive posterior distribution. They can be viewed as equivalent priors for single-layer neural networks with an infinite number of neurons [129].

In this research, GP regression is employed within a surrogate modelling framework as a cost-effective alternative to expensive FEM simulations. The goal is therefore to learn a transfer function

$$u_z = f(\mathbf{x}) + \epsilon, \quad (6.5)$$

where the target displacement  $u_z \in \mathbb{R}$  is a non-linear combination of the  $N_d$  parameters contained in  $\mathbf{x} \in \mathbb{R}^{N_d}$ , and  $\epsilon \sim \mathcal{N}(0, \sigma_n^2)$  is a term that accounts for model uncertainty, with a total variance  $\sigma_n^2$ . The parameters in  $\mathbf{x}$  are defined according to the specific FE model, and in this work, considering Model 01 (cf. Section 6.3.1.2) would be  $\mathbf{x} = (\beta_{\max}, \mu, c_0)$  with  $N_d = 3$ , Model 02 (cf. Section 6.3.1.3) without intra-layer springs, would be  $\mathbf{x} = (\beta_{\max}, \mu, c_0, c_1, c_2, c_3)$  with  $N_d = 6$ , and for Model 2 with intra-layer springs, the addition of  $c_4$  to  $\mathbf{x}$  results in  $N_d = 7$ . The selected parameters are normalised between 0 and 1. Placing a zero-mean Gaussian process prior on the true values  $f(\mathbf{x})$  yields

$$f(\mathbf{x}) \sim \mathcal{GP}(0, k(\mathbf{x}, \mathbf{x}'; \boldsymbol{\eta})), \quad (6.6)$$

with a covariance kernel  $\mathbf{k} = k(\mathbf{x}, \mathbf{x}; \boldsymbol{\eta})$  that is a function of the hyperparameters contained in  $\boldsymbol{\eta}$ . The covariance kernel encodes prior statistical properties of  $f(\mathbf{x})$ , and its choice is generally case-dependent. For this work the squared exponential kernel is selected, reflecting the assumptions that  $f(\mathbf{x})$  is stationary and continuous. Automatic Relevance Determination (ARD) is employed to reflect anisotropy in the  $N_d$  dimensions of  $\mathbf{x}$  [129, 130], such that

$$k(\mathbf{x}, \mathbf{x}; \boldsymbol{\eta}) = \sigma_s^2 \exp \left( -\frac{1}{2} \sum_{i=1}^{N_d} \frac{(x_i - x'_i)^2}{\ell_i^2} \right), \quad (6.7)$$

where  $\boldsymbol{\eta} = (\sigma_s, \ell_1, \ell_2, \dots, \ell_{N_d})$  is the vector containing the kernel hyper-parameters. This vector includes the standard deviation  $\sigma_s$  that controls the covariance amplitude, and the length scales  $\{\ell_i\}_{i=1}^{N_d}$  that control the smoothness of each dimension  $N_d$ . For discrete uncertain measurements  $\mathbf{u}_z \in \mathbb{R}^N$  made using cable parameters  $\mathbf{X} \in \mathbb{R}^{N_d \times N_d}$ , the prior can be interpreted as a collection of random variables, which based on (6.5) and (6.6) results in a multivariate normal distribution:

$$\mathbf{u}_z \sim p(\mathbf{u}_z | \mathbf{X}, \boldsymbol{\eta}^e) = \mathcal{N}(\mathbf{0}, \mathbf{K}_c + \mathbf{I}\sigma_n^2), \quad (6.8)$$

where the entries of the covariance matrix  $\mathbf{K}_c \in \mathbb{R}^{N \times N}$  are calculated using (6.7) as  $\mathbf{K}_{c_{ij}} = k(\mathbf{x}_i, \mathbf{x}_j; \boldsymbol{\eta})$ ,  $\mathbf{I}$  is an identity matrix and the extended parameter vector is  $\boldsymbol{\eta}^e = (\boldsymbol{\eta}, \sigma_n)$ .

The optimal parameters  $\boldsymbol{\eta}_{\text{opt}}^e$  are identified via Maximum Likelihood Estimation (MLE), by solving the optimisation [128]

$$\boldsymbol{\eta}_{\text{opt}}^e = \underset{\boldsymbol{\eta}}{\operatorname{argmax}} \log p(\mathbf{u}_z | \mathbf{X}, \boldsymbol{\eta}^e) = \underset{\boldsymbol{\eta}}{\operatorname{argmax}} \left( -\frac{1}{2} \mathbf{u}_z^T (\mathbf{K}_c + \mathbf{I}\sigma_n^2)^{-1} \mathbf{u}_z - \frac{1}{2} \log |\mathbf{K}_c + \mathbf{I}\sigma_n^2| - \frac{N_d}{2} \log 2\pi \right), \quad (6.9)$$

which is carried out using gradient ascent, by supplying the partial derivatives

$$\frac{\partial}{\partial \eta_i^e} \log p(\mathbf{u}_z | \mathbf{X}, \boldsymbol{\eta}^e) = \frac{1}{2} \text{tr} \left( \boldsymbol{\lambda} \boldsymbol{\lambda}^T \frac{\partial (\mathbf{K}_c + \mathbf{I} \sigma_n^2)}{\partial \eta_i^e} - (\mathbf{K}_c + \mathbf{I} \sigma_n^2)^{-1} \frac{\partial (\mathbf{K}_c + \mathbf{I} \sigma_n^2)}{\partial \eta_i^e} \right) \quad (6.10)$$

where  $\boldsymbol{\lambda} = (\mathbf{K}_c + \mathbf{I} \sigma_n^2)^{-1} \mathbf{u}_z$  and  $\text{tr}(\cdot)$  is the trace.

Predictions for a different combination of cable parameters  $\mathbf{X}_* \in \mathbb{R}^{N_* \times N_d}$  that were not used during training can be made after the optimal parameters are identified. For that purpose, a joint distribution between the measurements  $\mathbf{u}_z$  and the true function values  $f(\mathbf{X}_*)$  is created:

$$\begin{bmatrix} \mathbf{u}_z \\ f(\mathbf{X}_*) \end{bmatrix} \sim \mathcal{N} \left( \mathbf{0}, \begin{bmatrix} \mathbf{K}_c + \mathbf{I} \sigma_n^2 & \mathbf{K}_{c_*} \\ \mathbf{K}_{c_*}^T & \mathbf{K}_{c_{**}} \end{bmatrix} \right), \quad (6.11)$$

where the covariance matrices depending on  $\mathbf{X}_*$  are calculated as:  $\mathbf{K}_{c_*} = k(\mathbf{X}, \mathbf{X}_*) \in \mathbb{R}^{N \times N_*}$  and  $\mathbf{K}_{c_{**}} = k(\mathbf{X}_*, \mathbf{X}_*) \in \mathbb{R}^{N_* \times N_*}$ . Conditioning the joint distribution (Equation (6.11)) on the measurements  $\mathbf{u}_z$ , and noting the fact that both models are Gaussian processes, the predictive posterior has the analytically tractable form [131]:

$$p(f(\mathbf{X}_*) | \mathbf{X}_*, \mathbf{u}_z, \mathbf{X}, \boldsymbol{\eta}_{\text{opt}}^e) = \mathcal{N}(\mathbf{m}^*, \mathbf{K}_c^*), \quad (6.12)$$

with the predictive mean  $\mathbf{m}^* \in \mathbb{R}^{N_*}$  and covariance  $\mathbf{K}_c^* \in \mathbb{R}^{N_* \times N_*}$  calculated as

$$\mathbf{m}^* = \mathbf{K}_{c_*}^T (\mathbf{K}_c + \mathbf{I} \sigma_n^2)^{-1} \mathbf{u}_z, \quad (6.13)$$

$$\mathbf{K}_c^* = \mathbf{K}_{c_{**}} - \mathbf{K}_{c_*}^T (\mathbf{K}_c + \mathbf{I} \sigma_n^2)^{-1} \mathbf{K}_{c_*}. \quad (6.14)$$

## 6.4 Validation and results

### 6.4.1 Model validation

To train a GP, reference data from the FE model are required. In the referenced experiment, the cable is tested under three tension forces; 50, 80, and 100 kN. The pretension value selected for training is at  $T_{\text{tot}} = 50$  kN, where maximum displacements at midspan are higher and more sensitive to the effects of inputs. The parameters used to for sampling of all models are the maximum lay angle  $\beta_{\text{max}}$ , the friction coefficient  $\mu$ , the residual cohesion  $c_k$ , and the transverse load  $F$ . Other parameters such as the modulus of elasticity ( $E = 2.05 \times 10^5$  MPa) are assumed constant.

Once trained, the GP is used to replace the FE simulations. The objective is to determine optimal parameters  $(\beta_{\max}, \mu, c_k)$  that best-fit the experimental data from [90]. For this end, the PSO is used. This algorithm generates a set of uniformly distributed data points (particles) to guide the optimiser towards the lowest error minimum [73]. The cost function is selected as the mean squared error (MSE) between the predicted  $u_z^{\text{pred.}}$  and the experimental maximum deflection  $u_z^{\text{exp.}}$  for different  $F$ . The optimisation process ends when the difference in the cost function does not exceed a threshold of  $10^{-6}$  for 40 consecutive trials.

#### 6.4.1.1 Model 01

The parameter bounds for the lay angle  $\beta_{\max}$  and friction coefficient  $\mu$  in this study are assumed to be typical for SPW cables, but determining appropriate bounds for the residual cohesion  $c_0$  is more challenging. Several FE simulations within the bounds for  $\beta_{\max}$  and  $\mu$  and different values of  $c_0$  are conducted until the upper and lower bound for  $c_0$  enveloping the  $F - u$  experimental curve are reached.

Once the bounds are established for Model 01 (listed in Table 6.1) a GP model is trained using 600 data points randomly sampled from within the parameter bounds, and another 1500 data points are used for validation of training. The validation results, depicted in Figure 6.6a, indicate a satisfactory Root Mean Squared Error (RMSE) between the FE max. deflection  $u_z^{\text{FE}}$  and the GP-predicted  $u_z^{\text{pred.}}$  of 0.1654 mm.

Table 6.1: Upper and lower bounds for parameters used for sampling and training.

Parameter	$\beta_{\max}$ [°]	$\mu$ [-]	$c_0$ [kN/m]
Bounds	2 – 6	0.3 – 0.85	5 – 15

Next, the GP model is utilised in optimising model parameters to best-fit the experimental force-deflection curve using the PSO method. The optimised values show that the prediction for the  $F - u$  curve approximates the experimental results with considerable discrepancies. As can be seen in Figure 6.6b, yielding pattern of the curve is not compatible with the experimental curve. Under low bending loads ( $F < 8\text{kN}$ ), the FE curve shows a much higher slope than the experimental results. By increasing  $F$ , the slope is abruptly reduced to a constant value lower than the experiment curve. This hints that all the shear springs in the cross section have yielded and the wire bond is lost. Moreover, the optimum lay angle and friction coefficient are at the upper bounds of the angle physical parameter ranges, with optimum parameters being  $\beta_{\max} = 5.996^\circ$ ,  $\mu = 0.8495$ , and  $c_0 = 12.68$  kN/m. Since the lay angle and friction coefficient are at the upper bound specified by SPW cables and material properties, these results show that in order for Model 01 to best-fit the experimental curve, the parameters might be outside of the upper limit specified by the material properties and SPW geometry. This, thereby, deems

Model 01 inadequate for a reliable prediction. Leading to the conclusion that the  $c_k$  values would have variations from one layer to another.

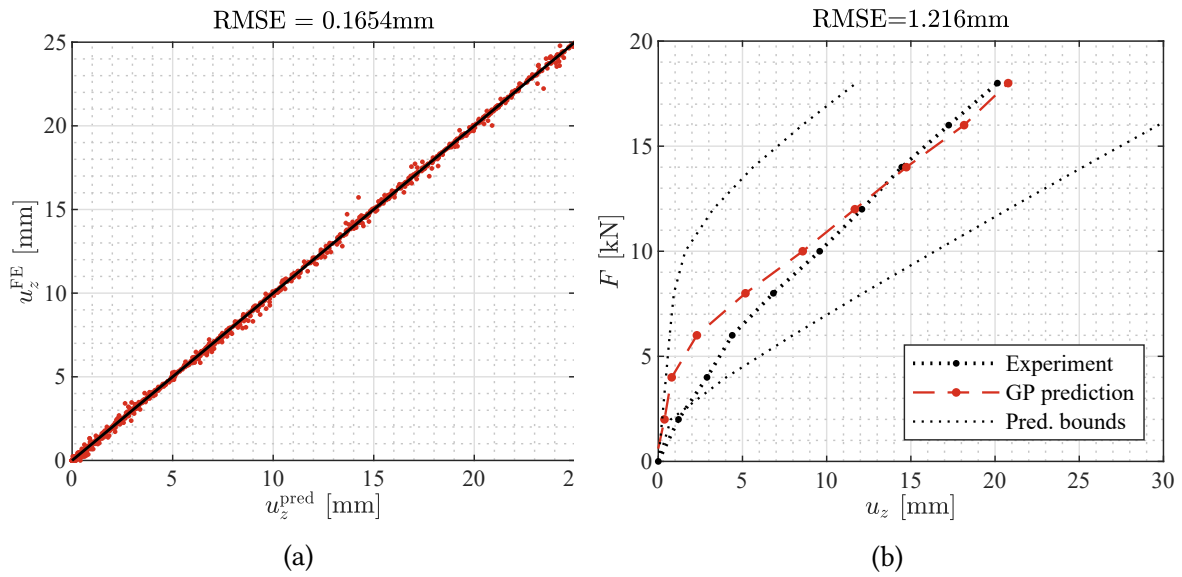


Figure 6.6: Validation of GP trained model (left) for and optimum bending curve (right) for shear springs with constant residual for  $T_{tot} = 50\text{kN}$ . Within the physical upper and lower bounds, Model 01 is unable to adequately represent the experimental results. Optimum parameters with GP prediction =  $[5.996^\circ, 0.8495, 12.68\text{kN}]$ .

### 6.4.1.2 Model 02

Based on the observations of Model 01's behaviour, it is evident that assigning a uniform cohesion value to all springs is inadequate to give an accurate  $F - u$  curve prediction. Therefore, it was hypothesised that the inner wires possess a stronger interlock force due to the pressure endured during the laying process. Conversely, the coiling of these cables onto reels subjected the outermost wire layer to substantial curvatures and hysteresis loading during reeling and unreeling, resulting in comparatively weaker interlock forces for these outer layers.

In order to address this discrepancy, several FE trials are conducted to explore the search space and determine estimates for the behaviour of each  $c_k$  value. Trials assuming higher cohesion values for the inner springs and lower values for the outer ones provided better resemblance with the experimental curve. Notably, the yielding pattern of the  $F - u$  curve confirmed that the springs in the outermost layers yielded under small bending loads, as they are positioned furthest from the neutral axis. Conversely, under heavier bending loads, the slope of the experimental curve is evidently higher than the FE prediction. This discrepancy underscored the fact that the inner wires possessed a greater stored interlock force and yielded

only under more substantial bending loads.

Through numerous iterations involving various parameters, suitable upper and lower bounds for the cohesion force  $c_k$  are determined to envelop the bending curve. These bounds serve as the basis for establishing the optimisation limits, as detailed in Table 6.2.

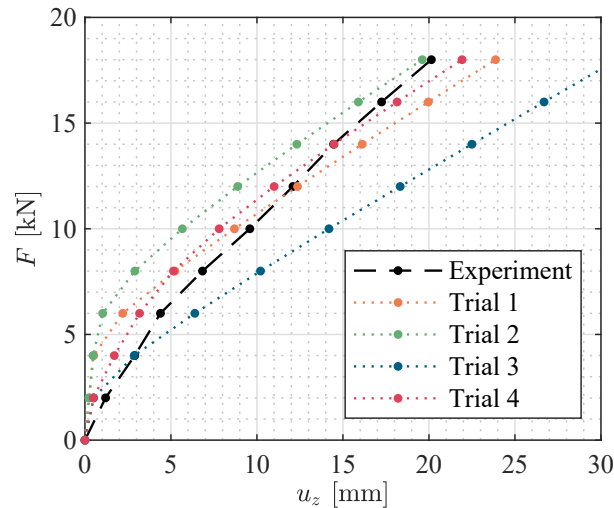


Figure 6.7: Example of several FE simulations with different spring cohesion  $c_k$  to determine the influence of the cohesion parameters on the  $F - u$  curve and determine an appropriate upper and lower limits. For  $[c_0, c_1, c_2, c_3, c_4]$ : Trial 1 = [14, 11, 8, 5, 2], Trial 2 = [2, 5, 8, 11, 14], Trial 3 = [14, 11, 2, 1, 0], Trial 4 = [80, 30, 2, 1, 0]. For all trials:  $[\beta_{\max}, \mu] = [5^\circ, 0.5]$ . Trial 4 provided a similar curve to the experiment. Trial 3 has the most similar slope to the experiment under low  $F$  load.

Table 6.2: Upper and lower bounds for residual cohesion forces used for sampling and training.

Distributed cohesion [kN/m]	$c_0$	$c_1$	$c_2$	$c_3$	$c_4$
Bounds	50 – 200	15 – 60	0 – 2	0 – 2	0 – 2

Next, a GP model is trained for each FE model for  $T_{tot} = 50\text{kN}$ , using 800 data points sampled from the FE data. The GP validation accuracies for Model 02a and 02b are shown in Figure 6.8, with a satisfactory root mean square error (RMSE) of less than 0.13 mm for both models.

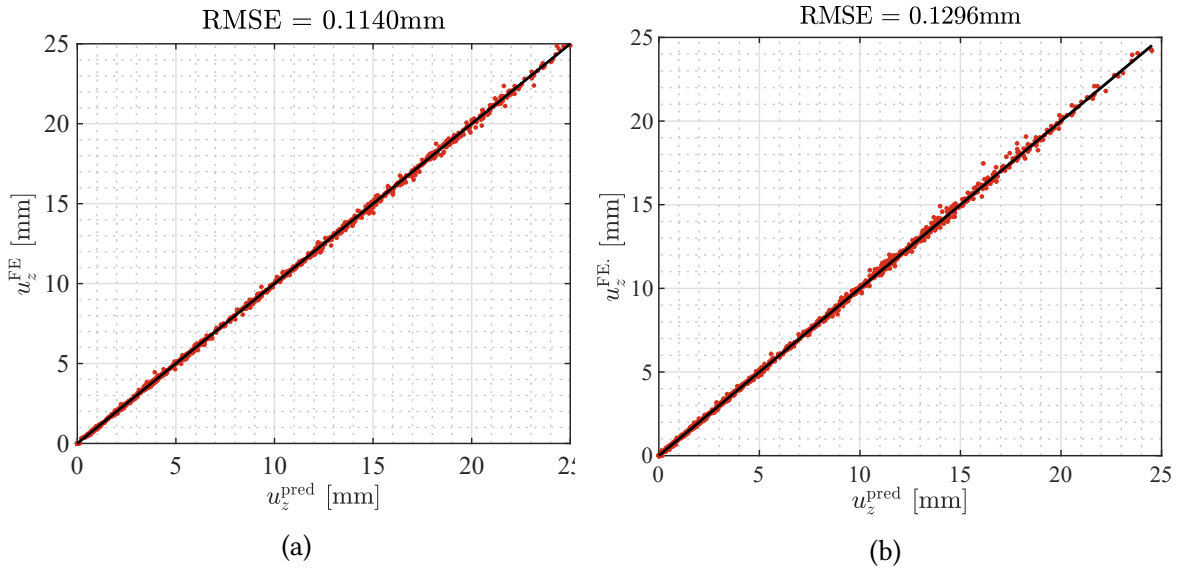


Figure 6.8: Training validation for GP for inter-layer contact model (Model02a, left) and inter- and intra-layer contact model (Model02b, right) for  $T_{tot} = 50\text{kN}$ .

## 6.4.2 Parameter optimisation

The PSO method is employed for parameter optimisation to best fit the force-deflection curve. The optimum parameters are found within the predetermined bounds, as mentioned in Table 6.3. It is noteworthy that the residual interlock in the outer layers is found to be close to zero, while in the inner layer, it increases significantly. This finding shows that the residual interlock is much higher in the inner layers. Additionally, the comparison between the GP model and the experimental data yields satisfactorily low RMSE values. Figure 6.9 shows a comparison between the experiment and the GP prediction, along with the range of prediction for both models.

Table 6.3: Upper and lower bounds for residual cohesion forces used for sampling and training.

$\beta_{\max}$  and  $\mu$  have the same parameter bounds as for Model 01.

Model type	$\beta_{\max}$ [°]	$\mu$ [-]	$c_0$ [kN/m']	$c_1$ [kN/m']	$c_2$ [kN/m']	$c_3$ [kN/m']	$c_4$ [kN/m']
inter-layer only	4.42	0.312	199.85	35.475	0.002	0.002	n.a.
Inter- and intra-layer	4.15	0.305	169.82	29.68	0.002	0.002	0.002

The models are able to accurately predict the experimental curve and achieve low discrepancy.

The lowest RMSE found is that for Model 02b with inter-/intra-layer coupling springs. This model is more generic since it accounts for the intra-layer contact between wires, whose effect is more pronounced in more compact cross sections as in SPW cables.

As previously noted, the GP training is made for a tension force of  $T_{tot} = 50\text{kN}$ . Therefore it is important to verify that the FE models show similarly low uncertainty for the other higher tension forces i.e. 80 and 100 kN.

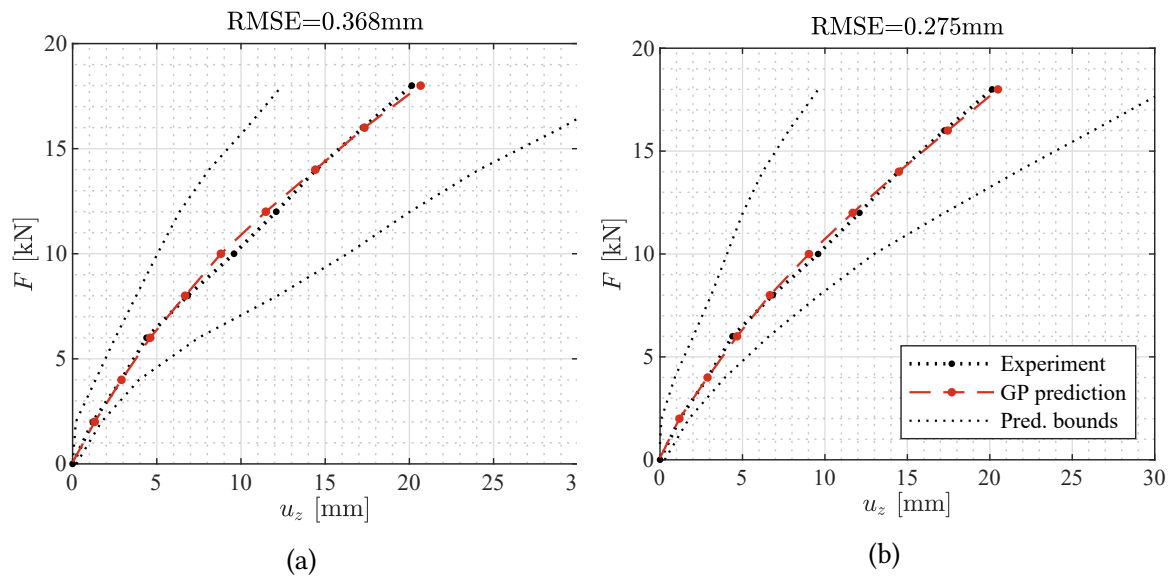


Figure 6.9: Optimum bending curve for GP of inter-layer contact model (Model02a, left) and inter- and intra-layer contact model (Model02b, right) for  $T_{tot} = 50\text{kN}$ . Upper and lower bounds are mentioned in Table 6.2.

Given the numerical efficiency and the lower RMSE achieved by Model 02b, it is selected for further analysis. The optimum parameters are assigned in the FE model to compare the RMSE for  $T_{tot}$  values of 50, 80, and 100 kN. The results shown in Figure 6.10 indicate that the discrepancy decreases with higher tension forces, suggesting that the optimum parameters accurately represent the experiment.

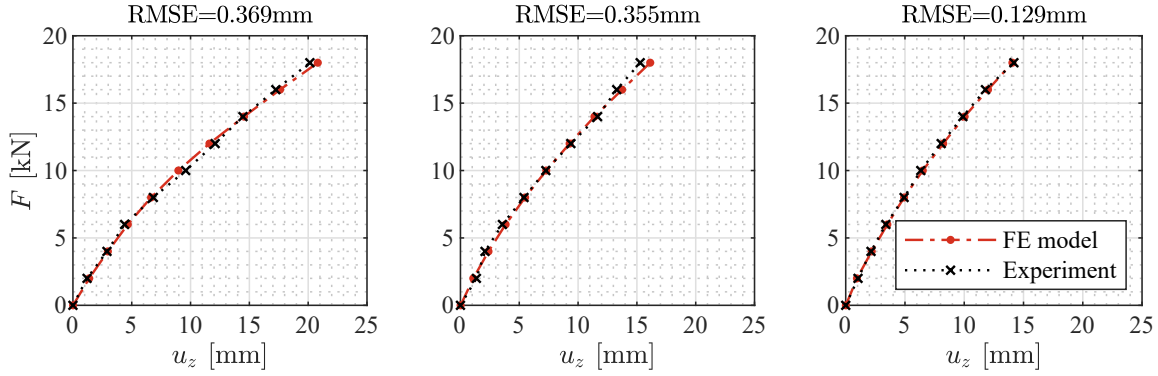


Figure 6.10:  $F - u$  curve comparison between FE Model 02b (inter- and intra-layer contact springs) with optimum parameters and the curve obtained from experiment for three tension forces  $T_{tot} = 50, 80, 100\text{kN}$  (left to right).

### 6.4.3 Parametric study and sensitivity analysis

To examine the impact of various parameters on the cable bending load, it is crucial to consider the nonlinear relationship between the load and displacement of Model 02b. This nonlinearity implies that the influence of each parameter is likely to fluctuate at different levels of applied load. For example, the effect of residual interlock in a specific layer may decrease significantly once the springs in that layer yield, necessitating a sensitivity analysis across different  $F$  load levels.

To evaluate the influence of individual parameters on the cable bending load, the Sobol sensitivity indices are employed. The first-order sensitivity, denoted as  $S_1$ , quantifies the effect of a particular parameter while keeping all other parameters constant, without accounting for interaction effects. In contrast, the total indices, represented as  $S_{T_1}$ , consider the nonlinearity and interaction between parameters, providing a comprehensive measure of sensitivity. The comparison between first-order and total indices allows us to assess nonlinear interactions. The steps for computing these sensitivity indices are outlined in [92]. To obtain these indices, the model parameters are uniformly sampled within their specified lower and upper bounds, as listed in Table 6.2, using a total of  $10^5$  sampling points. Subsequently, a GP model is utilised for the sensitivity analysis.

The results highlight that the sensitivity of parameters is contingent on the applied bending load. Specifically, the Sobol sensitivity indices for the lay angle  $\beta_{max}$  and friction coefficient  $\mu$  exhibit minimal variations across different values of  $F$ , with the total sensitivity index  $S_{T_1}$  surpassing  $S_1$ . This suggests considerable nonlinear interactions between these parameters.

The interaction between  $\beta_{max}$  and  $\mu$  can be attributed to the geometric arrangement of the cable cross section. Radial pressure propagates from the outer wires towards the inner ones until reaching the core wire at the centre of gravity. The inner wires accumulate these

radial forces from the outer wire layers, resulting in resisting higher longitudinal forces. This enhanced capacity of the inner wires to resist differential shear force strengthens the bond within the wires of the inner layer, particularly with an increase in the coefficient  $\mu$ . Consequently, both  $\beta_{\max}$  and  $\mu$  consistently influence the bending behaviour across all load levels, despite the helical wire laying of SPW cables, and both exhibit relatively low sensitivity.

In contrast, cohesion forces display different yield patterns and sensitivities depending on the loading conditions. Springs assigned to outer layer wires yield early in the bending load process and have limited impact in higher loads. However, in the inner layers, springs contribute significantly to higher bending loads due to the small frictional contribution of the radial components of the tension forces. The sensitivity indices for cohesion assigned to the second layer  $C_2$  are highest during the initial loading phases, gradually decreasing to nearly negligible levels in later stages, similar to  $C_3$ . Conversely, the sensitivity of  $C_1$  is relatively low in the early loading phase due to its high value. Nevertheless, as the load increases and the inner layers begin to lose bond, the sensitivity indices for  $C_1$  increase substantially. The influence of intra-layer cohesion  $C_4$  in the outer layer appears to be minimal, suggesting a limited impact of intra-layer contact on the overall bending stiffness in the present case.

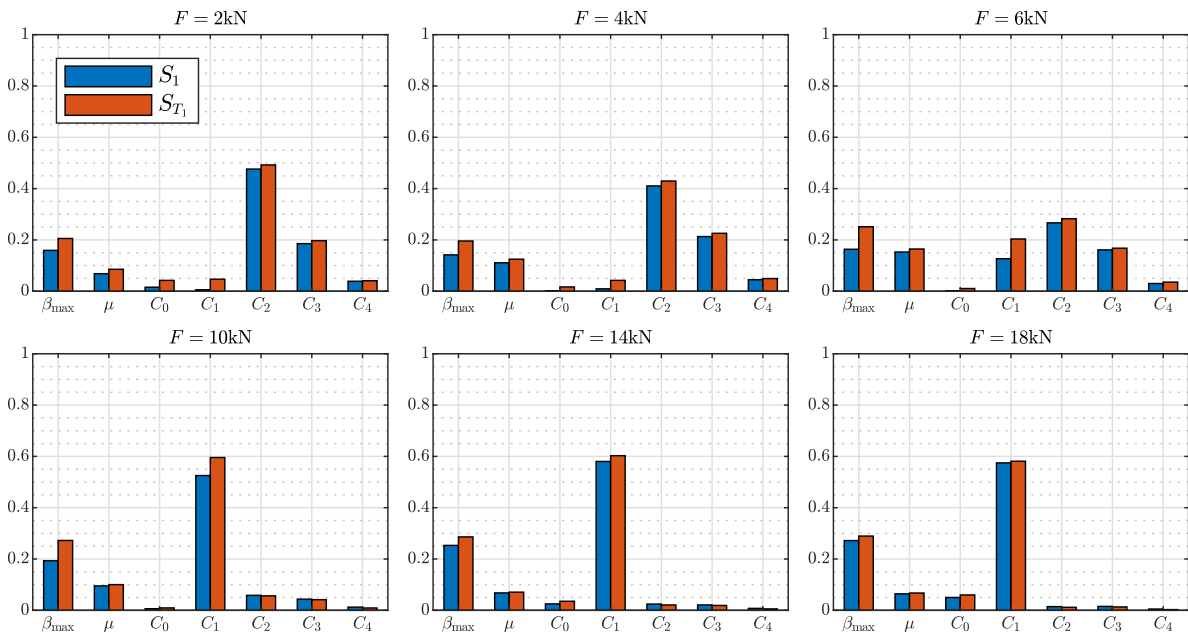


Figure 6.11: Parameter first order  $S_1$  and total  $S_{T_1}$  Sobol' sensitivity for several bending loads for  $T_{tot} = 50\text{kN}$ .

The influence of each parameter on the force-deflection curve is seen in Figure 6.12. In this figure, optimal parameters are fixed and a selected variable is changed between its upper and lower bounds. Similarly, the effects of  $\beta_{\max}$  and  $\mu$  are steady across the bending loads, where for  $C_0$  and  $C_1$ , the effect is most pronounced in higher loads.

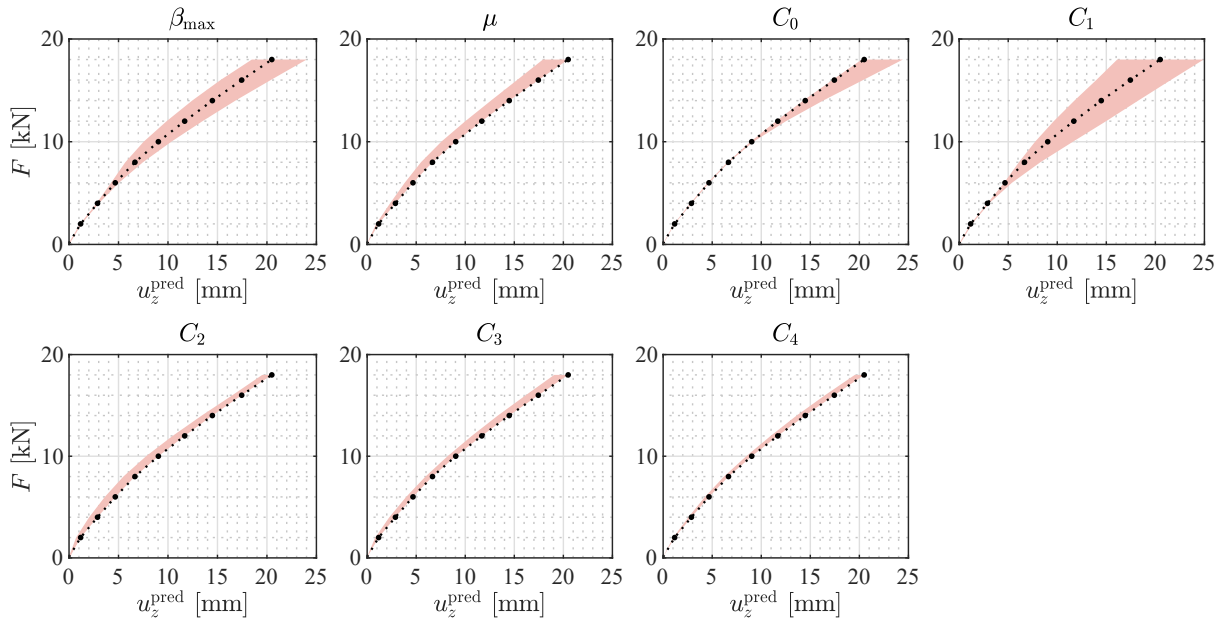


Figure 6.12: Parameter variation from the bending curve (other parameters kept as optimum values) for  $T_{tot} = 50\text{kN}$ .

#### 6.4.4 Response uncertainty in GP predictions

In the previous sections, the trained GP model was used to approximate the deflection response for different cable models, effectively replacing expensive FE simulations. The prediction mean was defined as the approximation for the cable response, given a set of parameters governing the model. Gaussian process models are, however, probabilistic by nature and provide confidence intervals on their predictions. To illustrate this aspect, Figure 6.13 displays the normalised deflection prediction for Models 01 and 02b, for different load amplitudes, using the optimal parameters that fit experimental data.

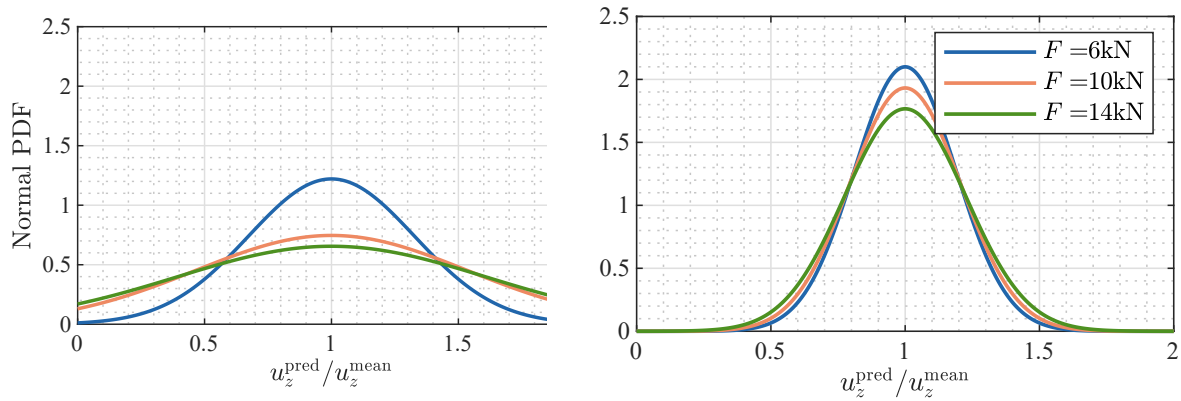


Figure 6.13: Normalised probabilistic deflection predictions for different load amplitudes. The cable parameters are taken as the optimal ones according to experimental data for Model 01 (left) and Model 02b (right).

Results for both models demonstrate that the magnitude of the applied loads is proportional to the uncertainty in the GP predictions. This behaviour is explained by the increasing nonlinear response in high load regimes, which although partially captured by the GP mean value (see e.g. Figure 6.9), also renders it less certain about its predictions. The variance in deflection predictions varies also for different modelling assumptions. A significant increase in variance is observed when constant cohesion is assumed (Figure 6.13, left), when compared to the refined model with variation in inter- and intra-layer cohesion (Figure 6.13, right). This indicates that the provision of different cohesion values is beneficial to explain the nonlinear deflection response, especially for varying load levels, as indicated Figure 6.11. This is supported in the GP model through the kernel choice, which allows for anisotropy across parameters via its automatic relevance determination (ARD) property.

Results for both models demonstrate that the magnitude of the applied loads is proportional to the uncertainty in the GP predictions. This behaviour is explained by the increasing nonlinear response in high load regimes, which although partially captured by the GP mean value (see e.g. Figure 6.9), also renders it less certain about its predictions. The variance in deflection predictions varies also for different modelling assumptions. A significant increase in variance is observed when constant cohesion is assumed (Figure 6.13, left), when compared to the refined model with variation in inter- and intra-layer cohesion (Figure 6.13, right). This indicates that the provision of different cohesion values is beneficial to explain the nonlinear deflection response, especially for varying load levels, as indicated Figure 6.11. This is supported in the GP model through the kernel choice, which allows for anisotropy across parameters via its Automatic Relevance Determination (ARD) property.

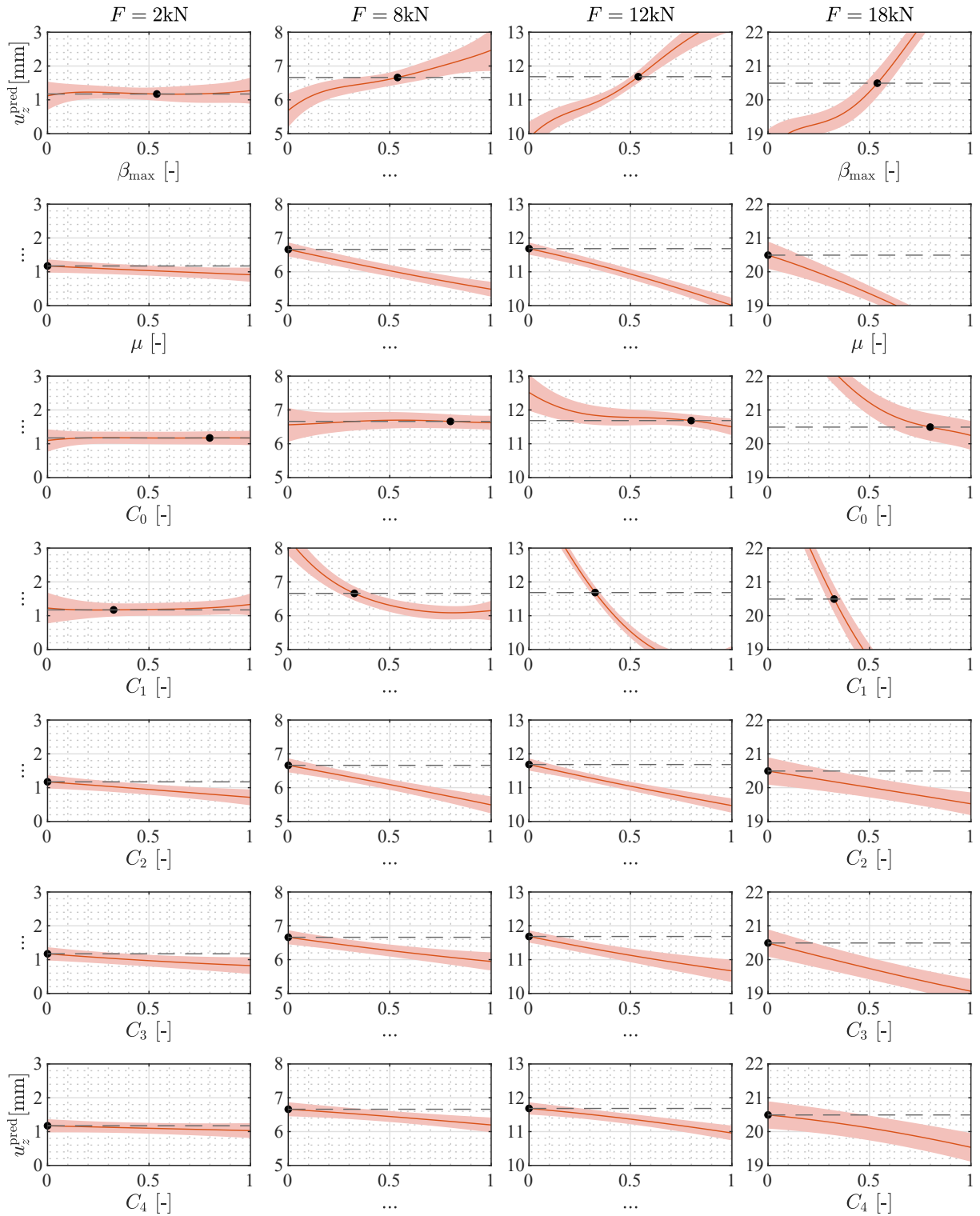


Figure 6.14: Deflection mean and 95% confidence interval in Model 02b as predicted by GP, for different load magnitudes and varying model parameters for  $T_{\text{tot}} = 50\text{kN}$ . Parameters are normalised within their bound specified in Table 6.2. Experimental optimal values are shown by the black dot.

### 6.4.5 Mechanics of the stick–slip of SPW cables

Upon optimising the relevant parameters, the Finite Element (FE) model is employed to analyse and predict the spread of wire slippage. Post-analysis, the shear springs are evaluated to determine whether or not they yielded. Their nonlinear state is taken as an indication of the occurrence of slippage between each two adjacent wires. To gain a more profound insight into the mechanism by which loads are transferred between wires, it is crucial to delve into their internal force distribution and the behaviour of the shear springs.

A coupling shear spring transfers the differential axial force caused by bending between each two interconnected wires. When this differential force reaches the maximum capacity of the spring, it undergoes perfect yielding and no longer resists the excess differential force. The yielding of these springs hinges on two key factors: the predefined properties of the spring  $\mu$  and  $C_i$  as previously discussed, and the magnitude of the differential axial forces within adjacent wires.

The magnitude of axial force within a specific wire depends on both the bending load  $F$ , and the helical geometry i.e. the distance of the wire from the neutral axis. Consequently, when a shear spring yields, any excess differential force is redirected to the wires in the underlying layer where the springs have not yet yielded. This results in a gradual reduction in the overall bending stiffness of the cable.

In the case of the model at hand, the results clearly demonstrate that the wires located in the outer layers of the loaded structure undergo slippage during the early stages of loading. This is attributed to the higher axial forces generated by the bending moment, and the much lower residual interlock. Wire slip subsequently propagates from the outer to the inner layers as the applied load increases. At  $F = 18\text{kN}$ , almost all wires in the midspan lose their bond, resulting in a reduction in the bending stiffness. Figure 6.15 depicts the different states of spring yielding for several bending loads at third and midspan for  $T_{\text{tot}} = 50$  and  $100$  kN. Additionally, a slight asymmetry in the spring yielding pattern is evident, with the springs at the top yielding last. This phenomenon is linked to the placement of the transverse load  $F$ , as depicted in the model sketch in Figure 6.3. In the experiment, the load is applied from the top of the cable by an actuator, leading to an uneven distribution of the load among the wires. While it might be possible to model this symmetrically and achieve a more uniform load distribution among the wires and springs, it's important to acknowledge that the model may not perfectly replicate the experimental setup.

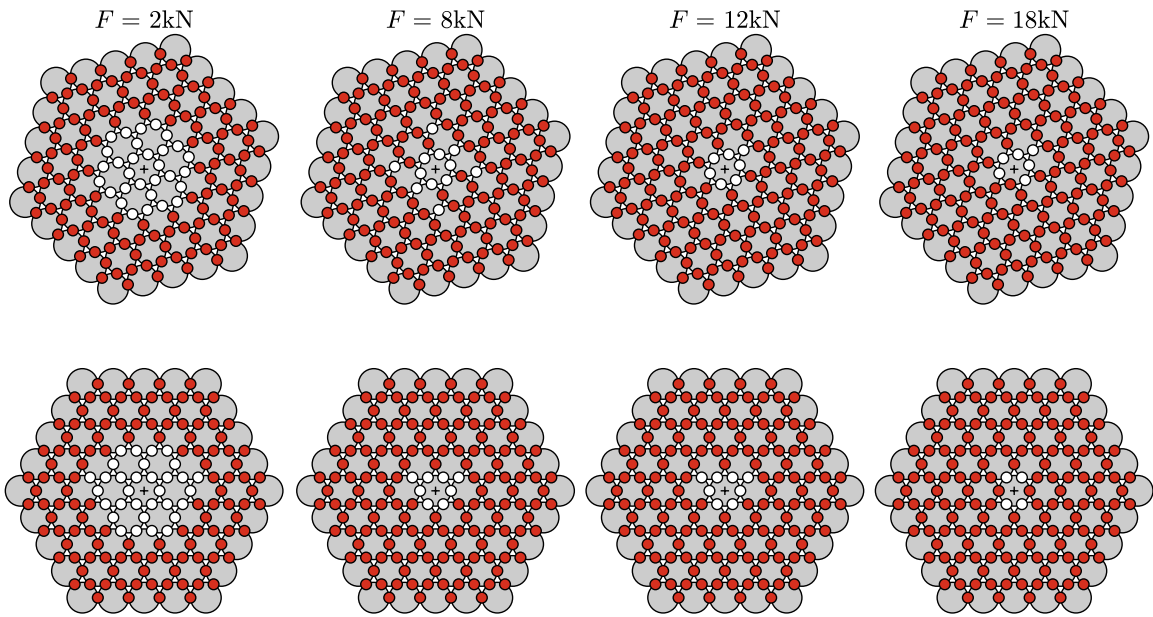
Further, when examining the wires along their length, the magnitude of axial force varies depending on their proximity to the wire's neutral axis. Under an applied load, a wire may undergo tension in one segment and compression in another, thereby influencing the uniformity of its bending stiffness along its length. Given that the two outermost wire layers

yield even under the smallest applied force  $F$ , the focus shifts to investigating the distribution of normal forces in the inner two layers.

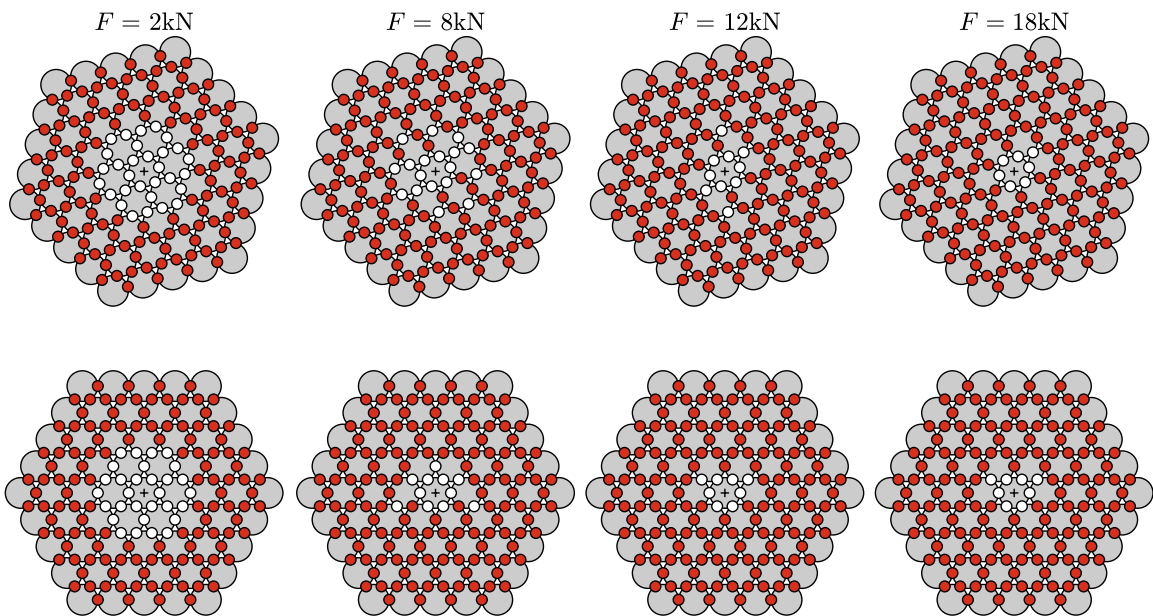
From Figure 6.15, it is apparent that the springs connecting the wires of the second layer at midspan begin to yield at a load of  $F = 12\text{kN}$ . Consequently, the normal force in the wires reaches a maximum with higher loading. However, more towards the span's end, not all springs have yielded, resulting in an increase in the magnitude of normal forces in the wires. This can be observed in the normal force distribution of the corner wires of the second layer, as shown in Figure 6.16, and is even clearer in the wires of the first layer as seen in Figure 6.17. The springs coupling the wires in the first layer do not yield with an increasing load  $F$ . Thus, the wires can carry higher normal forces due to the high identified  $C_0, C_1$  values.

The extent of wire slippage is significantly influenced by the bending curvature and cross sectional orientation along the cable length. In particular, the slippage in the region with the highest curvature (midspan) is more pronounced than that in regions with lower curvature. This results in a non-uniform bending stiffness along the length of the cable ( $EI_{\text{eff}}$ ). To demonstrate these effects, a comparison is made between a calibrated beam model assigned with  $EI_{\text{eff}}$  and the FE cable model. The bending stiffness of the beam model is calibrated until the maximum displacement corresponds to that of the FE cable model. Then, the curvature of the FE cable model is determined by dividing the difference between the beams giving maximum and minimum axial strain by the distance between them, and the corresponding bending stiffness is calculated by dividing the moment by the curvature, yielding  $EI_{\text{eff}} = M_{\text{tot}}/\kappa$ .

The results indicate that the two models exhibit similar behaviour. However, in the FE cable model, the slip occurs initially in the region with the high curvature and subsequently propagates to regions with low curvature. This results in abrupt changes in  $EI_{\text{eff}}$  occurring with each wire slip. This effect is more prominent in comparing the deformed shapes of the two models. Figures 6.18 and 6.19 compare the bending stiffness and deformed shapes of the calibrated beam model and the FE cable model.



(a)  $T_{tot} = 50\text{kN}$ . At  $x = L/3$  (top) and  $x = L/2$  (bottom).



(b)  $T_{tot} = 100\text{kN}$ . At  $x = L/3$  (top) and  $x = L/2$  (bottom).

Figure 6.15: Failed (red circle) and active (white) springs in Model 02b at third and midspan for different loads and pretensioning values. Higher  $T_{tot}$  in (b) results in a greater radial normal force and an increase in friction between the wires, slightly enhancing the cable's capacity to resist bending loads. Asymmetry in spring yielding associated with load  $F$  placement in the top wires.

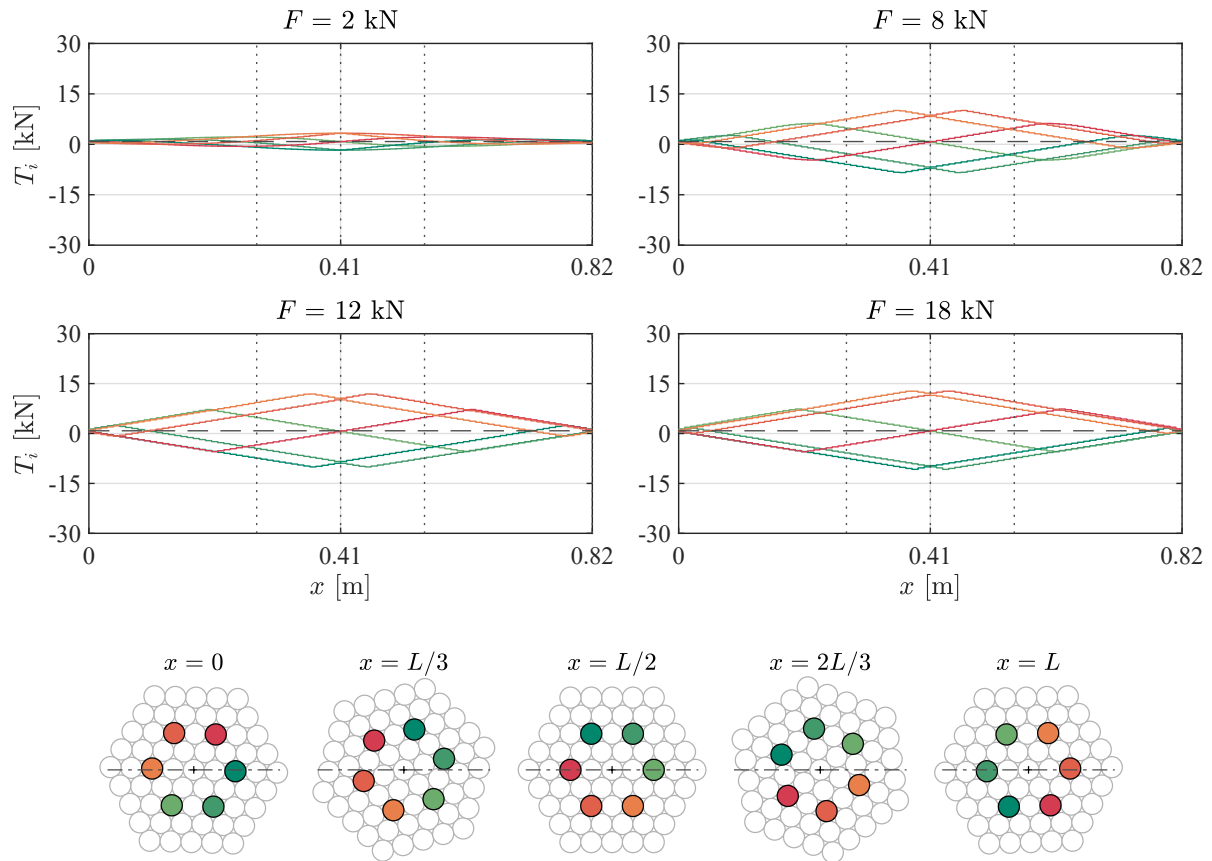


Figure 6.16: Normal force distribution (top) within corner wires of the second wire layer (bottom) for four load phases  $F = 2, 8, 12,$  and  $18$  kN. It is noted that the force transfers from the midspan to the ends with an increasing load  $F$ .  $T_{\text{tot.}} = 50$  kN. Colours indicate the particular wires in the bottom figure.  $T_i$  (---).

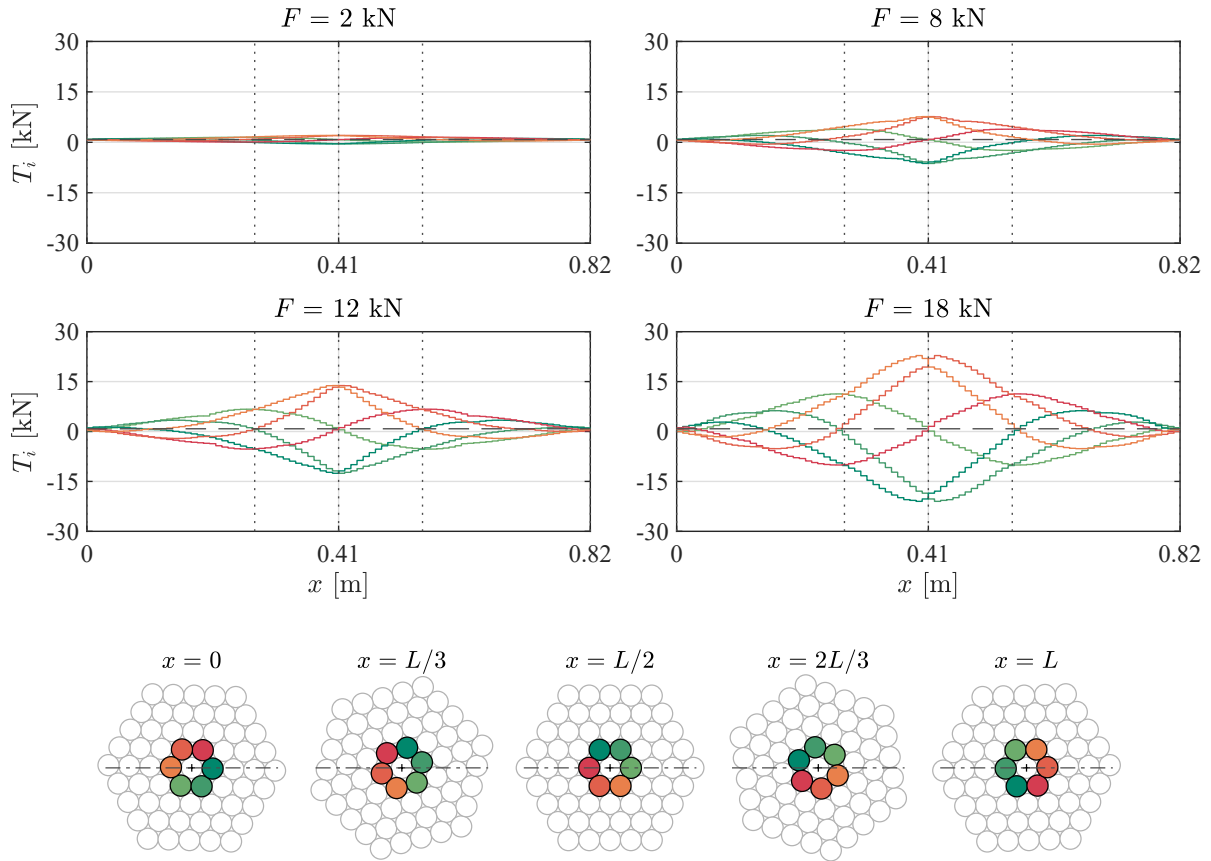


Figure 6.17: Normal force distribution (top) within corner wires of the first wire layer (bottom) for four load phases  $F = 2, 8, 12,$  and  $18$  kN. Springs in the inner wires yield at high bending loads  $F$  and the wires take higher axial forces than in the other layers.  $T_{tot.} = 50$  kN. Colours indicate the particular wires in the bottom figure.  $T_i$  (---).

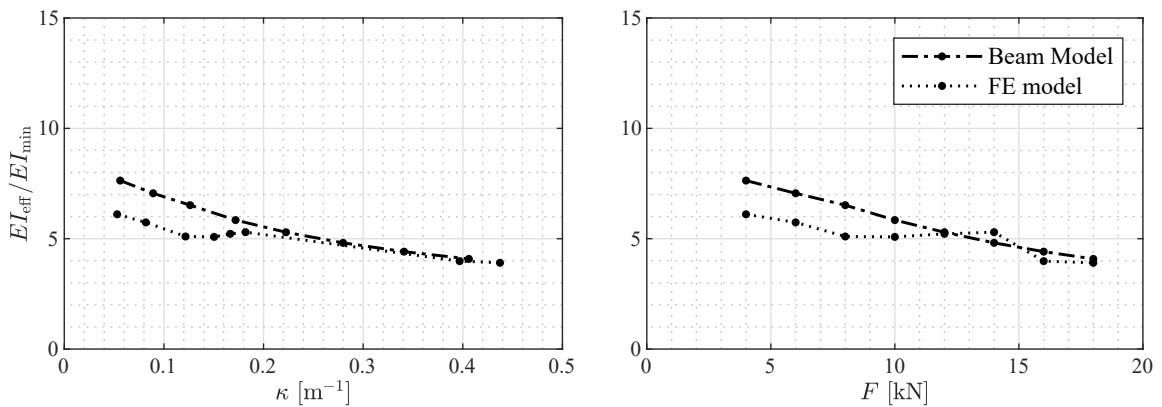


Figure 6.18: Comparison of the loss in bending stiffness for Model 02b and the calibrated bending stiffness of beam model for  $T_{tot} = 50$  kN.

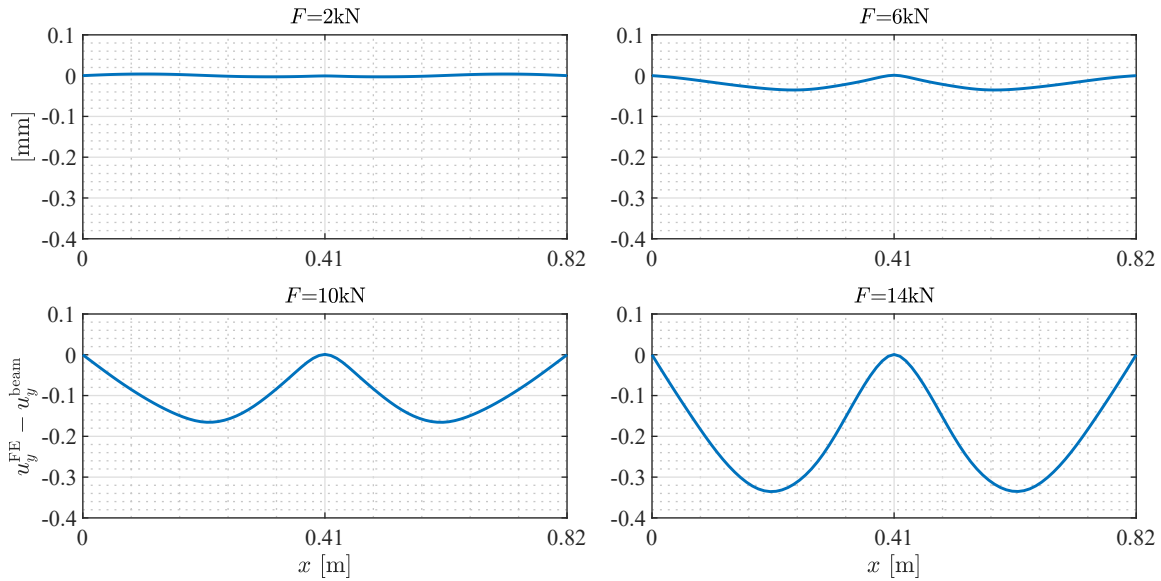


Figure 6.19: Difference in deformed shape between Model 02b and calibrated beam for  $T_{tot} = 50$  kN.

A ratio between the number of failed springs and the total number of springs is computed to demonstrate the impact of varying wire slip along the modelled cable length. The results reveal the difference in yielding shear springs along the length. The springs start to fail where curvature is maximum and extend towards the supports.

In addition, it is noted that for a model with a higher interlock cohesion forces in the outer layers, the effect of spring failure propagation is clearer, especially in the outer layers. Figures 6.20 and 6.21 show the failed spring ratio and its spread along the length of the modelled cable.

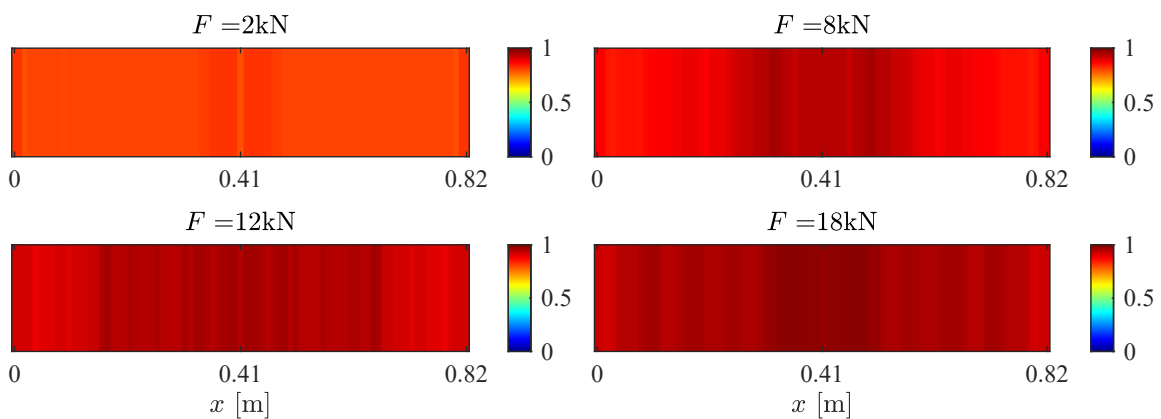


Figure 6.20: The failed springs ratio for the FE Model 02 with optimised parameters for  $T_{tot} = 50$  kN. The colours indicate the failed springs ratio in a discretised node slice.

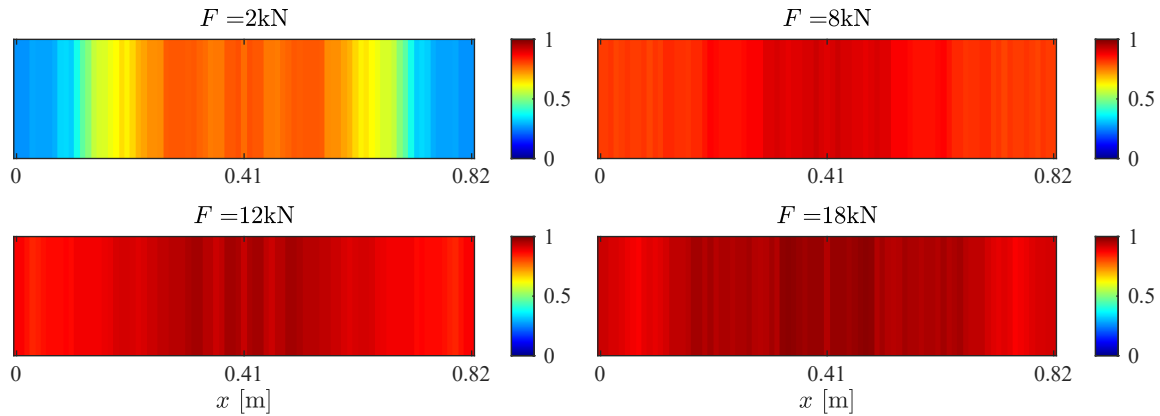


Figure 6.21: The failed springs ratio for the FE Model 02b for  $T_{tot} = 50$  kN with higher cohesion residual in the outer layers. Parameters:  $[\beta_{\max}, \mu, c_0, c_1, c_2, c_3, c_4] = [4.5, 0.6, 180, 40, 2, 1.5, 0.5]$ . The colours indicate the failed springs ratio in a discretised node slice.

### 6.4.6 Hysteresis behaviour

The hysteresis behaviour is also investigated using the FE model by applying a step-wise cyclic load and measuring the maximum deflection at each load-step. Geometric nonlinear analysis is used as a realistic representation, whereby the stiffness matrix is updated at each load step, incorporating material and spring stiffness, update in geometric stiffness after deflection, and geometric stiffness resulting from pre-tensioning. The hysteresis analysis iteration scheme is implemented using a FE solver, which utilises the Newton-Raphson iteration method to consider the global stiffness matrix. Further information of a comparable FE methodology is detailed in [19, 21, 71].

The  $F - u$  curve reveals some interesting observations. Loading with high values of force  $F$  results in only a small residual displacement, whereas loading in the negative direction generates an even smaller (negligible) residual, as illustrated in Figure 6.22.

Results show that although the springs yield and inter-wire bonding decreases during high-load cycles, the hysteresis loop's size remains small, limiting the dissipation of energy from inter-wire slipping. Pretension applied to SPW cables introduces a counteracting moment that aids in restoring the cable to its original position. When subjected to a bending load, the cable wires lose their bond, subsequently reducing the cable's overall bending stiffness. However, upon release of the load, the secondary effects of tension forces create a negative moment that counteracts the residual displacement, ultimately restoring the cable to its original, undeformed state.

The FE analysis yields two main findings. Firstly, the loading sequence plays a crucial role in residual displacement, with loading in the positive gravity direction resulting in considerably

higher residuals compared to loading in the negative direction. This underscores the influence of the loading history and sequence on wire bonding and, consequently, bending stiffness. Secondly, depending on the applied pretension force, the residual displacement resulting from the loading cycles remains relatively small. This observation indicates that high pretension forces lead to a reduction in the energy dissipation.

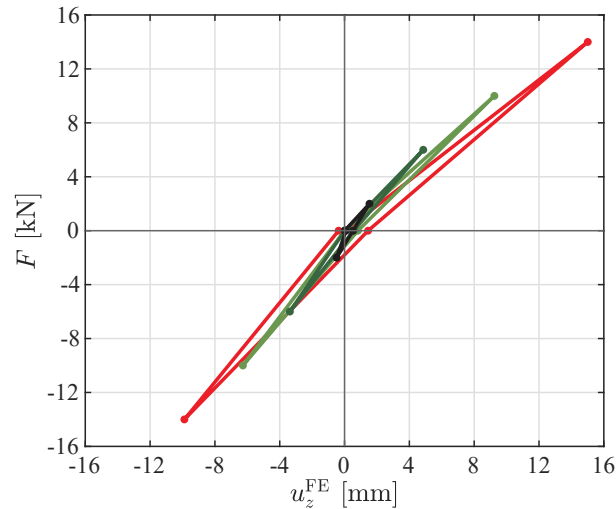


Figure 6.22: Hysteresis analysis of Model 02b for different bending loads and a tension force of  $T_{tot} = 50$  kN. Upon release of the load, the secondary effects of tension forces create a negative moment counteracting the deformation to restore the cable to the undeformed state, making the size of the hysteresis cycle small. The Loading sequence influences the residual displacement: Loading in the positive gravity direction tends to result in considerably higher residuals and has a smaller slope.

## 6.5 Conclusion

While the majority of studies focused on examining the bending behaviour of electric conductors, there is a noticeable lack of attention given to the bending of structural cables, specifically SPW cables. The SPW cable comprises several layers of wires that are twisted simultaneously around a straight core wire with small lay angles. The development of efficient models to predict their mechanical behaviour (e.g. bending and hysteresis behaviour) becomes important.

To simulate an experimental bending test performed on a large-scale  $61\phi 7$  SPW cable, a novel modelling framework is presented. As creating FE models demands careful selection of suitable parameters and requires a significant amount of computational resources, surrogate GP models are employed to predict the FE model at significantly lower costs.

The results reveal that the residual interlock among the wire layers has a noteworthy impact on the bending behaviour. Experimental validation indicates that there is a clear variation in the residual interlock between the wire layers. As a result, a model that incorporates interlock cohesion with varying values for each wire layer exhibits high accuracy when compared with experimental data under varying tension forces. To further investigate this phenomenon, a comprehensive parametric study is conducted to assess the impact of different parameters on the force-deflection ( $F - u$ ) curve obtained from the experimental test.

Further, the FE model, incorporating optimised parameters, is utilised to investigate the inter-wire slip. The latter is found to be markedly influenced by the bending curvature and cross sectional orientation along the cable length. A comparison with a calibrated bending stiffness  $EI_{\text{eff}}$  beam model reveals that wire slipping arises in the region with the largest curvature and spreads to areas with lower curvature.

Finally, a study on the effect of cyclic loading shows that the size of hysteresis loops is small, due to the second-order effects of cable pretensioning. However, the inter-wire friction leads to residual displacement resulting in the dependence of wire slip and bending stiffness on the loading history.

The proposed models presented in this chapter accurately predict the stick–slip behaviour of SPW cables, while accounting for the main factors that affect wire slipping. They make use of physical parameters like the lay angle and hyper/meta-parameters that describe the inter-wire friction such as the friction coefficient and the cohesion. This approach enables better calibration of the model to match experimental measurements, where these parameters essentially capture local effects that are might be overlooked in cable analysis. The findings of this chapter highlight the importance of considering proper wire slip modelling in cable analysis to ensure precise predictions of cable behaviour across a wide range of applications.

# Chapter 7

## Relevance of models for practical application

### 7.1 Introduction

The preceding chapters explored the development, validation, and application of cable models used in system identification. By employing inverse analysis techniques, these models enable the identification of global static and dynamic behaviour, in addition to the local mechanical interactions such as wire stick–slip phenomena in simplified FE formulations. Beyond extracting parameters like tension force, free cable length, and bending stiffness, the models can also be used to investigate additional physical phenomena, including inter-wire friction through experimental deformation measurements.

Utilising FEM, the numerical formulations incorporate nonlinear analysis, often facilitated by material and geometric nonlinearity in FE solvers. This modelling approach ensures the applicability of the models in scenarios demanding increased accuracy. The key feature of these models is their parametric nature and computational efficiency, enabling broad application within a FEM framework.

The primary objective of this final chapter is to provide the details necessary to construct the models through discussing their range of application, considerations for parametrisation, and the geometric and mechanical relationships used in their formulations.

### 7.2 Parametrisation of the inclined sagged bar model

In Chapter 4, the sagged bar model was shown to be highly accurate for tension force identification in stay-cable analysis. This model demonstrated several advantages in its formulation as it adopts a linear input geometry of discretised beam elements, allowing for the calculation of sag effects and corresponding nonlinear geometry without a predefinition

of the sagged profile. Therefore, the final sagged geometry can be derived as an output of the analysis.

Another notable feature is the flexibility to adopt various elements and intermediate supports for realistic modelling e.g. springs or dampers, and the adaptation of changes in bending stiffness at the cable ends by changing  $EI_i$  at the beam elements close to the ends. Moreover, the model allows for the consideration for partial release in the rotation fixity. Additionally, the model takes into account the inclination effects of the cable, which affect the tangent stiffness at static equilibrium and further enhances its capacity for realistic representation of cable behaviour. Table 7.1 highlights the main characteristics of common stay-cable models used for cable force identification.

Table 7.1: Stay-cable analysis models for cable force identification.

Model name	Formulation	Tension force	Inclination effects	Bending stiffness	Geometric nonlinearity effects	Boundary conditions	Intermediate supports
Taut-string	eq. (3.12)	constant	-	-	-	pin	-
Modified taut-string	eq. (3.13)	constant	-	included	-	pin	-
Flat bar	eq. (3.14)	constant	-	included	-	fixed	-
Sagged bar	numerical	constant or varying	included	included	included	pin/rot./fixed/spring	included

The parametric formulation of this model in FE solvers gives the chance to adopt most cases for stay-cable analysis. The initial geometry for each  $x_i$  and  $z_i$  can be assigned based on the inclination angle  $\alpha$ , where for  $x_1$  and  $z_1$  the first node condition is assigned (fixed/hinged/rotational spring) and the same for  $x_{\text{end}}$  and  $z_{\text{end}}$ . For internal support dampers, an additional spring/damper element can be assigned at the end node with a corresponding stiffness and damping ratio to model the damping effects on the cable vibration.

Additionally, steel guide tubes are used to protect the cable from impact accidents, vandalism, and explosion at the lower anchorage using a steel guide tube. When the cable vibration surpasses the gap distance between the tube's internal surface and the cable's outside diameter, impact can occur. This phenomenon is especially relevant for cables without internal dampers. A nonlinear spring at the node corresponding to the guide tube's end position can be employed to investigate the cable impact. Herein, the spring engages once the gap distance is exceeded, with spring stiffness derived based on the bending stiffness of the guiding tube.

Factors influencing this scenario encompass the stiffness of the guide tube, gap distance, excitation frequency and amplitude, guide tube length, cable mass, and the cable inclination angle  $\alpha$ . A comprehensive exploration of cable impact against the guide tube, utilising a horizontal sagged bar model, is detailed in [132], where a bridge response time history at the stay-cable anchorage serves as input for the cable model.

## 7.3 Parametrisation of the saddled cable model

In Chapter 5, the introduction of the saddled cable geometry is accompanied by a comprehensive exploration of its formulation and behaviour under static and dynamic loading. A distinctive feature of this model lies in its adaptation to the cable interaction with the saddle geometry, achieved through efficient modelling techniques. The saddle geometry is defined by employing nonlinear, very-stiff springs. These springs resist compression forces only and become active after a predetermined displacement, effectively representing the geometric boundary constraints imposed by the saddle.

While alternative solutions involving contact algorithms and volume FE elements could address similar issues, their computational expense and reported convergence problems often present challenges. Practical applications necessitate the efficiency of commercial solvers to estimate the effects of such phenomena on design and construction phases. This underscores the rationale for adapting the simplified FEM approach, emphasising the provision of validated results using streamlined models. The saddled cable model can therefore be applied to analyse cases where curved deviators are used. Here, its formulation and application are discussed within the context of suspension bridges, external tendons and extradosed bridges.

### 7.3.1 The saddled cable model for suspension bridges

In the construction of suspension bridge cables, a cable overlength  $L + \delta L$  value is often targeted to achieve the desired cable form and maximum sag value at midspan. The calculation of this overlength relies on models assuming a perfectly flexible cable with a parabolic shape and a symmetric setup. However, assuming a perfectly flexible cable becomes increasingly inaccurate with larger cable diameters due to the growing influence of bending stiffness on the overall cable behaviour. The contact point deviates from the flexible cable assumption as bending stiffness increases, as discussed in Chapter 5.

Creating a parameterised framework for modelling such cable setups require parameters representative of the support geometry, cable mechanical properties, the free span, and the required maximum sag. Using these parameters, the saddle springs of each end are then distributed along a predefined length  $L_{\text{sadd}}$  with  $n_{\text{sadd}}$  number of springs. The choice of an adequate  $L_{\text{sadd}}$  depends on the maximum sag  $s_{\text{max}}$ , the distance between supports  $L$ , and the

cable weight  $w$ . For large spans or cable diameters,  $L_{\text{sadd}}$  should be appropriately increased. Furthermore, the accuracy of the contact point prediction is dependent on spring discretisation and the chosen value of  $n_{\text{sadd}}$ . Gaps assigned for the saddle springs depend on the saddle radius  $R$ , which can differ between the supports. The remaining length of the cable along the span  $L_{\text{cab}}$  is then assigned as the distance between the supports minus the distance on which the saddle springs are distributed from both sides.

Given these parameters, the model finds the optimum overlength value for the required sag  $s_{\text{max}}$  and the estimate of the contact point. The loadcase involves a positive strain assigned to each beam element. The model is then solved iteratively using a geometric nonlinear analysis until reaching a strain giving a sag of  $s_{\text{max}}$ . Here, the computational time required for solving one iteration depends on the targeted final sag, as the number of numerical steps increase with larger  $s_{\text{max}}$ . Figure 7.1 shows a schematic for the actual cable setup and the representative model.

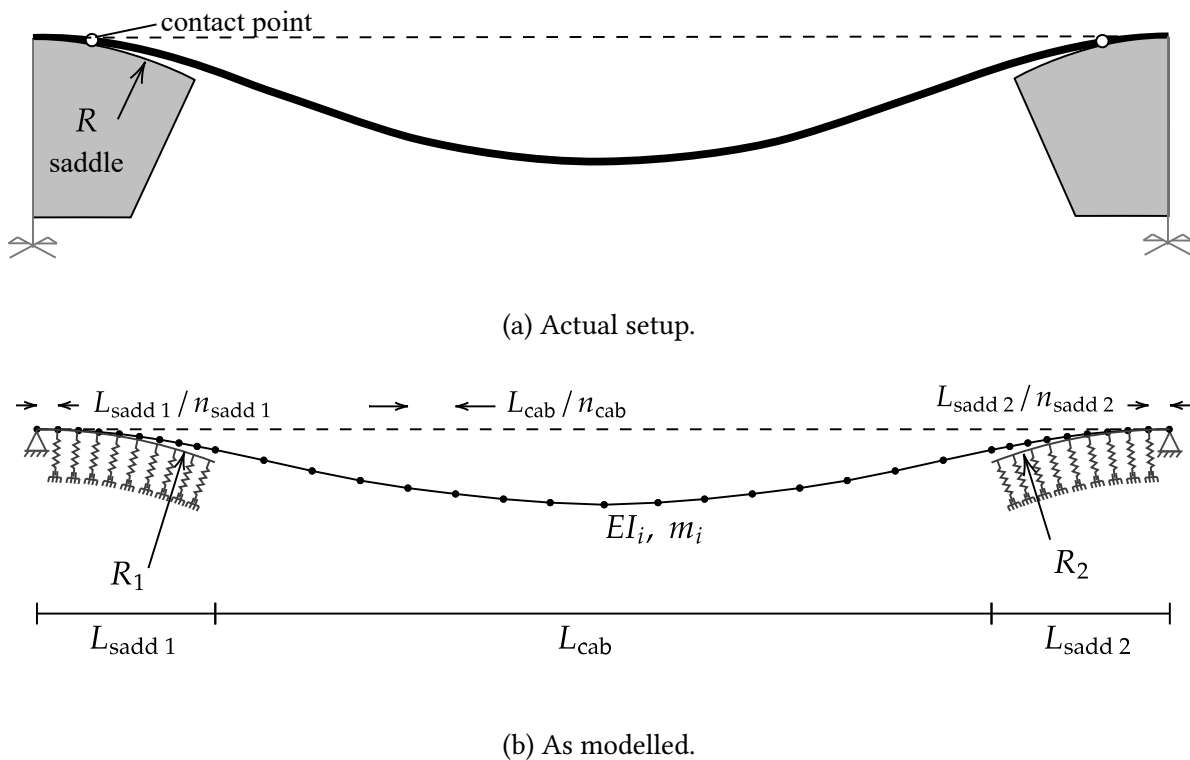


Figure 7.1: Actual case schematic and as modelled parametrised saddled cable.

Comparing different models used for saddled cable analysis, the straight and modified straight saddled cable models offer a simplified linear geometry as input and moderate computational time. However, they slightly deviate from accurately accounting for the self weight distribution along the length and the corresponding tension force at midspan. More

accurate representation of the self-weight can be made by assuming a parabolic cable profile in the initial stage. This is represented in the initially sagged saddled cable model, as it provides a high computational efficiency given its preliminary sagged profile. When accounting for the bending stiffness, the model is found most suitable for a construction method where cables are laid wire by wire. The extended saddled cable model offers a generalised formulation with the most accurate representation of self-weight, tension force and bending moments distribution. However, the large displacements the model undergoes and the moving boundaries require high computational time.

In conclusion, these models present a parametrised toolbox suitable for practical applications in suspended cable analysis. In scenarios involving asymmetric loading e.g. during the stepwise erection of the bridge deck from one end, determining the contact point and cable internal forces becomes crucial. This process accounts for the changing asymmetric pressure on the saddle and the consequential change in the internal forces it generates. By providing a versatile framework, these models ensure accurate and efficient analyses also in such construction stages.

### **7.3.2 The saddled cable model for external tendons**

In box-girder concrete bridges, external prestressed tendons introduce a negative moment at the girder's midspan to minimise deformation and achieve the desired decompression condition within the structure. The deployment of tendons externally inside the box-girder not only enhances adaptability in design but also facilitates the flexibility of replacing or introducing new tendons in later stages.

To induce the negative moment in the girder from prestress, a common practice involves deviating the tendons under block deviators and prestressing them to generate an uplift force. The block deviation shells feature a negative curvature, ensuring that the cable maintains contact with the circular shape along a specified contact length. This circular shape proves crucial in deviating the cable without introducing kinks or corner edges that could damage the cable. The deviation shell adopts a circular shape to accommodate different inclination angles and variations in the tendon profile [9]. At the ends, the tendon passes through the block section to be securely anchored. It's worth noting that the design tolerance distance between the tendon and the internal surface of the deviator block may decrease based on tendon vibration and prestress levels. Consequently, updating the distance-dependent boundaries might be necessary to assess the implications of cable contact with the block's edge.

The schematic representation in Figure 7.2 provides an overview of the different sections comprising a typical external tendon. This illustration captures the intricacies involved in the design and implementation of these tendons in box-girder bridges.

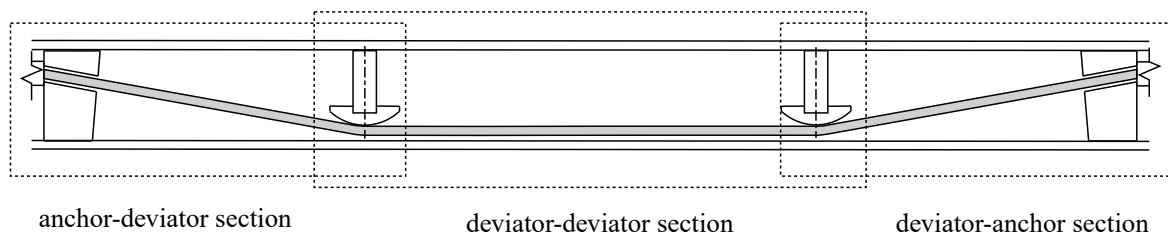


Figure 7.2: An external prestressed tendon setup in a box-girder bridge.

Subdividing the cable model into specific subsections, partial models of the tendon arrangement offer valuable insights into its behaviour. The initial segment, termed as the anchor-deviator section, has been used for system identification discussed in Chapter 5. This partial model effectively demonstrates the model's adaptability to decreasing tension forces through a corresponding adjustment in the contact point, all while maintaining the structure's geometry unchanged.

The definition of the geometric contact point pre-analysis is a key aspect of this partial model. It is determined as the tangent at the deviator from inclination with angle  $\alpha$ . This contact point serves as the basis for establishing gaps in the saddle springs. The number of saddle springs for the deviator section is determined by factors such as sag, cable inclination angle, and amplitude of vibration. For inclined cables, an additional tolerance angle  $\gamma$  between  $2-5^\circ$  is assumed and incorporated when assigning saddle springs.

Upon solving the model, the actual contact point is defined by the updated cable geometry and the last activated spring. In utilising this partial model for tension force identification from vibration measurements, it consistently yielded the lowest error when compared with other established models. Furthermore, the results obtained from the saddle springs facilitate determining the pressure on the deviator shell and the overall uplift force provided by the external tendons.

On the anchor side, where the cable is embedded in the anchor block and can potentially impact the edge, the impact effect can be modelled as a very stiff spring assigned with a gap distance corresponding to the distance between the edge and the outside diameter of the cable. Figure 7.3 provides a visual representation of the partial anchor-deviator tendon setup and the schematic of the model.

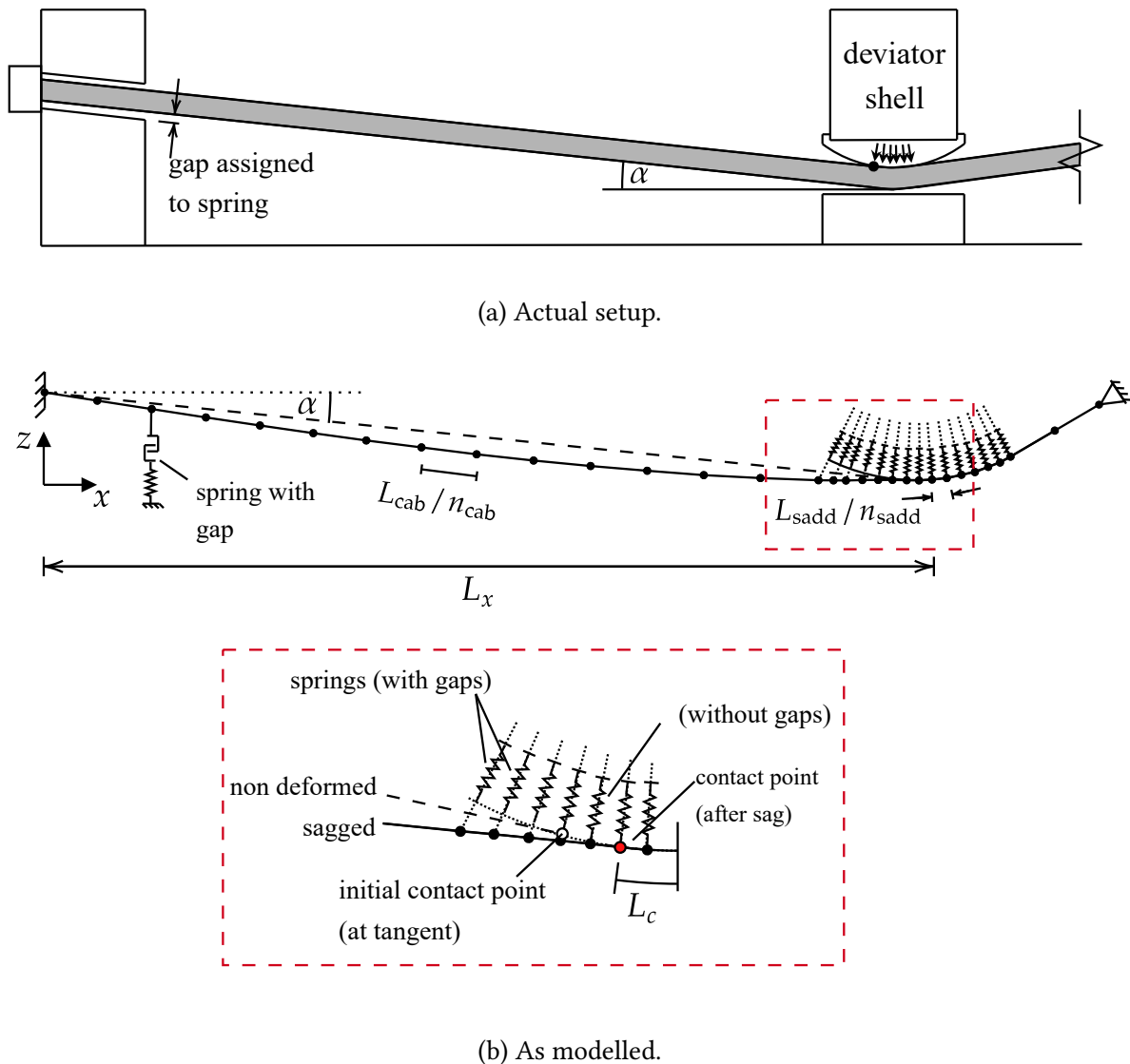


Figure 7.3: Actual case schematic and as modelled parametrised saddled cable for an anchor-to-deviator section.

The second subsection of an external tendon is between the two deviators. This tendon section is located in the the midspan region in the girder. The in-plane inclination between the two deviators can be assumed as zero which means that the geometric contact points are at the tip of the deviator as seen in Figure 7.4. The tendon length in this section is long and can be affected by the sag, which affects the actual contact point and the cable shape under self-weight.

By having the self-weight and prestressing force as a loadcase, solving the model determines the actual contact points, from which the free length is determined as well as the uplift pressure on the deviator. Here, the free length tends to be longer than the distance between the centre

lines of the deviators.

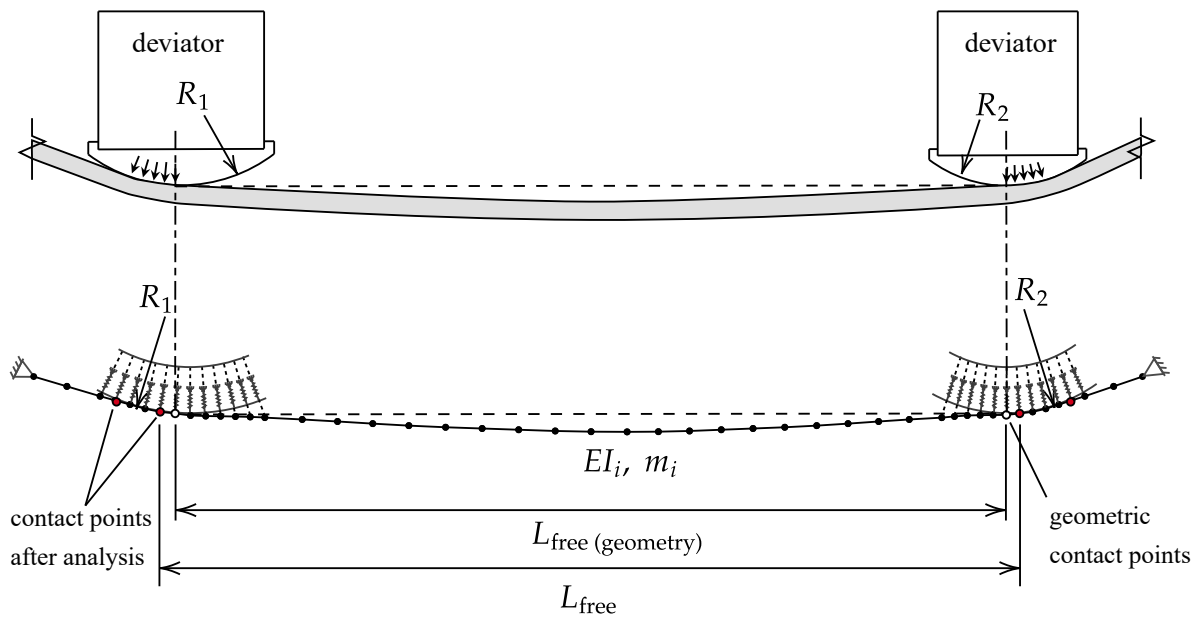


Figure 7.4: Actual case schematic and as modelled parametrised saddled cable for a deviator-to-deviator section.

A more comprehensive approach is to model the entire tendon profile over the deviators and into the anchors. The model formulation is parametrised based on the distances between the anchors and deviators, the inclination angles from each end, radius of each deviator, and saddle springs' discretisation. Figure 7.5 shows the parametrised model outline corresponding to the actual tendon setup.

At the expense of increased computational time, the comprehensive modelling of the entire tendon setup proves invaluable for various types of analyses related to external tendons. Firstly, employing static analysis enables the study of the effects of cable tensioning from different ends. It provides insights into how tension force distribution varies when the tendon is tensioned from one end versus both ends. The incorporation of friction at the deviators, and its impact on the PE duct, is explored by assigning springs with nonlinear transverse stiffness with friction law nonlinearity. Slip resistance at the deviators and in-service fretting fatigue can be further investigated based on model calibration, aligning with studies conducted using 3D FE at suspension cable saddles discussed in [133, 134]. The static analysis aids in determining uplift pressure on the deviator and induced bending moments on the deviator block due to cable inclination and friction resisting cable slipping at the deviator blocks.

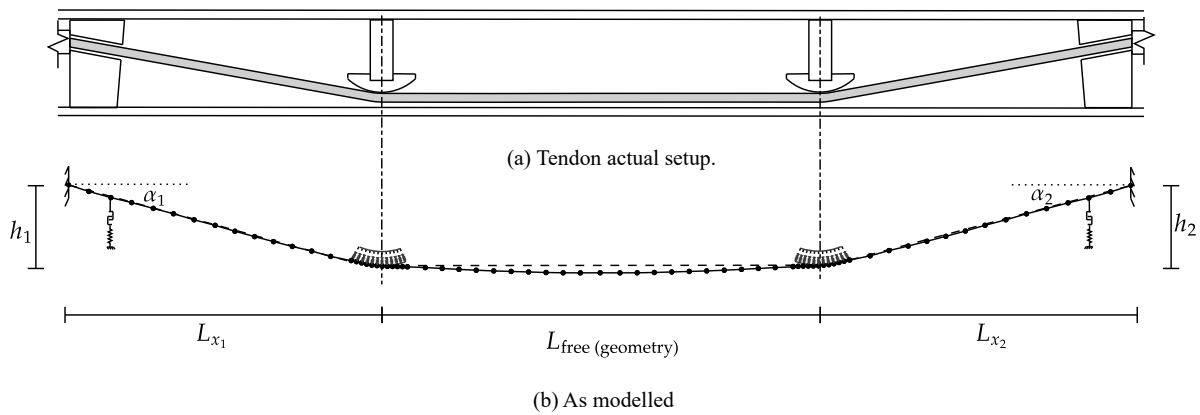


Figure 7.5: Tendon profile embedded inside a box-girder and a corresponding FE model.

Secondly, modal analyses under this cable setup can identify natural frequencies and corresponding mode shapes for each subsection between two supports. This is particularly valuable in practical applications, aiding in the identification of tension forces when measurements are taken from multiple sections of the tendon.

Thirdly, while tendons embedded inside box girders typically aren't subjected to large amplitude vibrations, conducting a nonlinear time history analysis proves useful for investigating specific phenomena occurring on the tendon. This analysis delves into the effects of tension force distribution along the tendon, the relaxation of tension along the length due to friction with the deviators under vibrations, and the cable's impact with the anchor and the resulting changes in contact length.

### 7.3.3 The saddled cable model for extradosed bridge cables

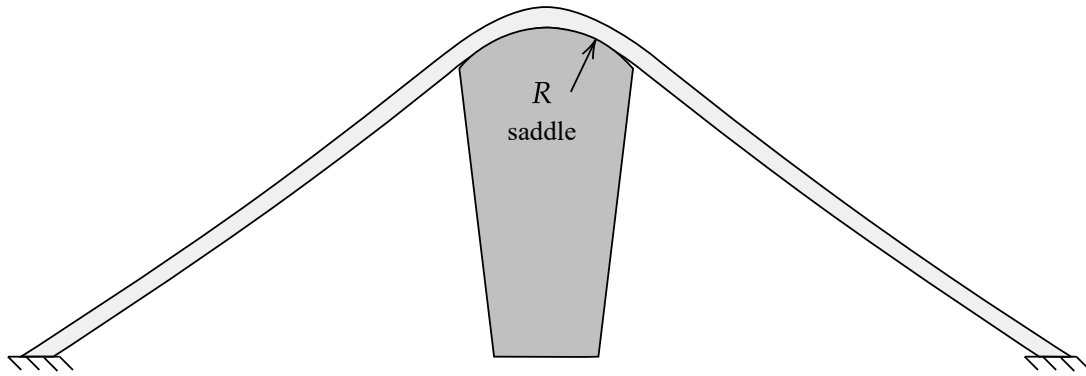
After discussing model application for suspension bridges and box-girder external tendons, this subsection explains its application on extradosed bridges. This type of bridges is renowned as the most suitable structural system for spans ranging from 100 to 200m, featuring stays serving as external prestressing tendons that extend beyond the deck and deviate over the pier via a short pylon. Saddles, employed as deviators, offer advantages in terms of saving anchorages at the pylon, streamlining pylon design and construction, and contributing to the achievement of a slender pylon head.

Similar to the modelling approach for suspension bridge cables and external tendons, the cable model for extradosed bridges can be effectively implemented using FEM. This model entails the division of the cable into two sections: the saddle section and the free cable section.

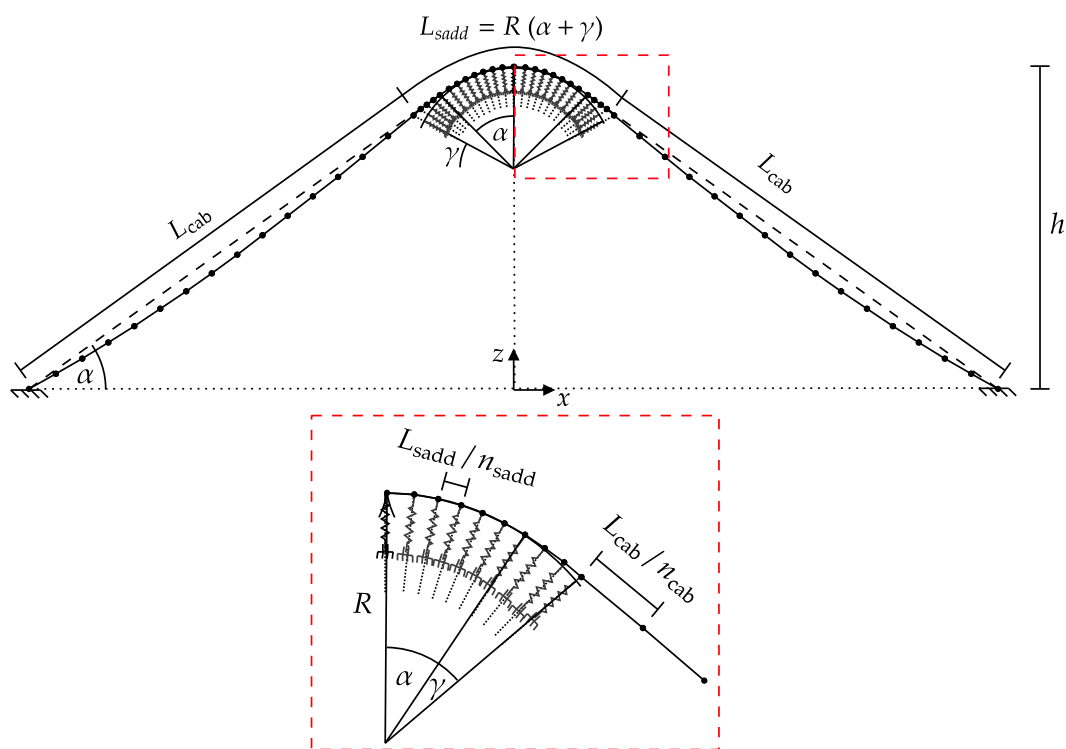
In the saddle region, the determination of node positions ( $x_i$  and  $z_i$ ) follows the circular

shape of the saddle. This continues until the radial angle equals the inclination angle  $\alpha$ . The geometric contact point is then identified at this node. Along a tolerance angle  $\gamma$ , elements with the same length as those in the saddle region are linearly discretised to identify the contact point after sag. This tolerance is suggested in the Eurocode where the tolerance length should not be less than the contact point under the most unfavourable characteristic combination of actions and the sag effects [3]. The tolerance can be represented in the model by assigning the saddle spring along a tolerance length. Gap distances in the spring correspond to the distance between the saddle and the cable perpendicular to the saddle perimeter.

Once the saddle nodes and springs are established, the free cable geometry is determined by defining the nodes along the linear length with an inclination angle  $\alpha$  as shown in Figure 7.6 and running the analysis.



(a) Actual setup.



(b) As modelled.

Figure 7.6: Actual case schematic and as modelled parametrised inclined saddled cable in an extradosed bridge cable setting.

The loadcase is defined as the pretension of the beam elements under self-weight, and the model is solved using geometric nonlinear analysis, consistent with previous cases. The modelling framework for the extradosed cable has been extensively detailed in the author's published Master thesis [135].

This model proves useful for determining force distribution along the saddle under various load

cases, including the capacity to account for differential pretensioning induced by incoming traffic loads. Differential tension forces on either side of the cable lead to an increased effect of friction between the cable and the saddle, which lead to investigating the cable slip with the saddle and the eccentric pressure that generates secondary moments on the pylon.

## 7.4 Parametrisation of the SPW cable model

The previous sections discuss the applicability of the saddled cable model on several cable setups, where cable contact with the saddle has implications on the static and dynamic behaviour. In these local interactions, the contact is shown to be significantly affected by the rigidity of the cable, especially the bending stiffness. Here, the focus is set on the detailed modelling of cable cross section to identify the effects of inter-wire friction on the rigidity of the cross section under bending.

The model provided in this thesis focuses on the development of detailed SPW cable models that balance efficiency with comprehensive results. The presented framework provides a detailed understanding of wire interactions. In comparison to other detailed models employing 3D meshed elements and contact algorithms, the efficiency of this model and its versatility lay in the ability to conduct analyses in most commercial software solvers.

The construction of the model hinges on assigning parameters that define the cable's cross sectional geometry and material properties. These parameters have interdependence in between; for example, the geometric construction relies on cable parameters (e.g., lay angle, cable length, number of wire layers), and the numerical formulation parameters (e.g., discretisation, number of elements, number of springs, slice rotation) utilise these geometric parameters for constructing the numerical model.

The user specifies the cable wire diameter and the number of wire layers, denoted as  $n_{\text{layer}}$ . The cross section is systematically generated with a compact hexagonal arrangement, where the distance between each pair of nodes equals the wire diameter. Node numbers are assigned based on their radial position and layer number to facilitate the connection of these nodes with beam elements, creating a helical wire. Slices along the cable are defined using geometric relationships involving the total length, lay length, and required discretisation.

Coupling springs are then assigned based on the final geometry of the model, connecting each pair of adjacent nodes. Each wire has six contact points with other wires. A node connecting a wire to another in a different layer is termed a radial contact (in the radial direction), while the spring coupling two wires in the same layer is termed a circumferential layer. Springs are labelled according to each layer to differentiate their stored cohesion force. An illustrative example of the final section after assigning  $n_{\text{layer}}$  is depicted in Figure 7.7.

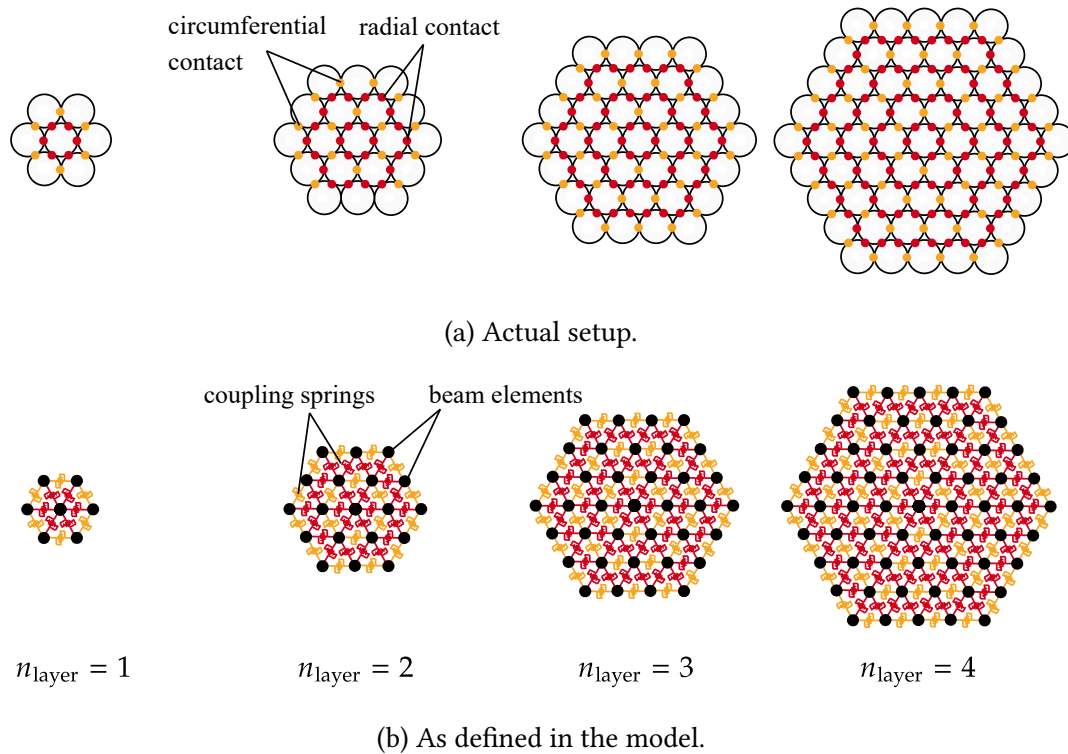


Figure 7.7: Parametrised cross section of a SPW cable. In the framework  $n_{\text{layer}}$  specifies the number of layers of a given cross section, which assigns a compact cross section with a  $n_{\text{layer}}$ .

The tension force can be applied in a load case as nodal forces at the end nodes of each beam element forming a helical wire, with displacement degree of freedom at the boundary in the direction of tension set free. Another approach involves assigning the end nodes as pinned. The tension force is then introduced as a negative strain or a pre-tension force in all elements. Bending loads are imposed in successive load case as distributed transverse loads on specific nodes on the outer wires or on the nodes of the core wire.

This framework proves valuable for practical applications that require detailed cable modelling, especially in scenarios where the cable experiences high curvatures and bending moments, such as near supports or at cable hanger clamps. The model is also valuable in studying maximum stresses on individual wires and analysing tension force redistribution in case of wire breaks.

# Chapter 8

## Summary, conclusions and outline

### 8.1 Summary and conclusions

Motivated by the need to enhance assessment models, this work aims at enhancing the systematisation of cable analysis by focusing on modelling and system identification of cables with physical-mechanical interactions with deviating supports and interwire friction. The work employs a modelling framework approach using FE analysis tools, and utilises inverse analyses and tailored application of the FE method for cable behaviour evaluation.

Chapter 1 opens by underlining the significance of cables, particularly in bridges and long span structures. Incidents of structural collapse stemming from cable system failure persist. Consequently, their incorporation into structures requires periodic monitoring. This in turn, directs attention toward vibration-based monitoring and inverse analysis techniques. The emergence of limitations of inaccuracies due to linearising simplifications of analytical equations, or significant computational cost of large computational models, highlights that advanced cable model development should not only prioritise sophistication, but also consider practicality and balance precision with efficiency.

Chapter 2 delves into cable systems and explores their mechanical and physical properties. This chapter aims to gain a comprehensive insight into cable components. It provides a detailed overview of multiwire cable types, anchorages, and vibration control devices, laying the foundational understanding of how cable systems differ in aspects such as the transfer of forces, resisting bending stresses, and interactions with supporting structures at the boundary. The emphasis on the composition of the cross section and load transfer mechanisms in this chapter is particularly central, as it directly informs effective FE analysis modelling.

Chapter 3 discusses the theoretical and numerical methodologies used in cable modelling. This chapter provides a comprehensive discussion on existing cable models by exploring assumptions, and discussing model applications and limitations. The chapter starts by a focus on the methodologies used for static and dynamic analyses using the FEM, especially the importance of including the nonlinear effects of the geometrical stiffness when cables undergo large displacements. Then, existing cable models are thoroughly examined with an aim to reach a systematic classification of existing cable models by first understanding their

assumptions, limitations, and applications, and then proposing a classification system. Key findings include insights into the assumptions (e.g. sag effects, bending stiffness, boundary conditions, assumed self weight, cable cross section representation), and the principles governing model parameters. The classification table of existing cable models is then included to provide a cable model guide for researchers and practitioners.

Chapter 4 provides a quantitative comparison between common cable models. Specifically, it focuses on cable force identification from vibration measurements, employing a comparative analysis between common simplified methods and more intricate nonlinear models, presented through two case studies of relatively long stay-cables. Cable tension forces are obtained by comparing predicted natural frequencies with those identified through field tests. Some of the challenges include selecting suitable optimisation methods and addressing assumptions affecting the model accuracy. Consistently in both case studies, the sagged bar model outperforms other models in predicting natural frequencies and tension forces, however with an increased computational cost. The trade-off between model complexity and computational cost is also highlighted.

This chapter contributes valuable insights into cable force identification, underscoring the importance of model selection and parameter optimisation. Additionally, it highlights that overestimation of cable length is influenced by the effects of sagged geometry, loading and bending stiffness on the cable contact point within supports.

Chapter 5 introduces the novel saddled cable model, emphasising its ability in addressing cable interaction with deviating saddles. First, the chapter evaluates four cable models for form-finding under self-weight and large displacement, assessing their accuracy in predicting static equilibrium. Models include a straight cable, a modified version considering increased weight, an initially sagged cable with a parabolic profile, and an extended cable with sliding supports. Model performance is assessed based on analytical solutions to highlight the differences between the models. Subsequently, the chapter introduces a numerical method attributing for the effects of geometric supports. Comparative analysis with the catenary analytical solution revealed nearly identical results, and the nonlinear radial springs are found to effectively model the contact between the curved deviating support and the cable. The incorporation of flexural rigidity underscored the substantial influence of bending stiffness on the contact point. The evaluation of various saddle models is based on parameters such as contact length, cable length, tension forces, and bending stiffness. Furthermore, the chapter demonstrates using the saddled cable model in cable force identification from on-site vibration measurements, emphasising its accuracy in predicting inverse analysis. The subsequent exploration includes the dynamic behaviour, underscoring the impact of saddles on dynamic response.

The applicability of the saddled cable model considerably influences static and dynamic

behaviour, with local interactions significantly affected by cable rigidity, especially bending stiffness. The complex nature of multiwire cable composition necessitates a deeper understanding of the interactions between cable wires that give an overall bending stiffness.

Chapter 6 provides insights into detailed cable cross section modelling, focusing on inter-wire friction effects on the bending stiffness. It investigates stick–slip behaviour in SPW cables, emphasising wire slippage mechanics and its impact on cable bending. This chapter begins with a literature review, highlighting the bending studies for structural cables and how only few studies exist on modelling the SPW cables. A novel FE model is then presented to simulate a bending test on a large diameter SPW cable, using surrogate GP models for cost effective predictions. The modelling results along with a parametric study show the notable impact of residual interlock on bending behaviour, with an interlock cohesion model exhibiting higher accuracy.

The FE model, with optimised parameters, investigates inter-wire slip, influenced by bending curvature and cross sectional orientation. A comparison with a calibrated bending stiffness beam model reveals wire slipping in regions with the largest curvature, spreading to lower curvature areas. Cyclic loading shows small hysteresis loops due to cable pretensioning's second-order effects, but inter-wire friction leads to residual displacement, affecting wire slip and bending stiffness.

Finally, Chapter 7 discusses the practical application of the presented cable models as system identification models. The chapter begins by discussing the sagged bar model. The parametric formulation of this model within FE solvers allows for broad applications, considering actors like cable inclination effects and internal support dampers. The chapter then sheds light on the saddled cable model, discussing its application in suspension bridges, external tendons, and extradosed bridges, demonstrating its applicability to different cases. The model's adaptability to different scenarios is highlighted. The parametric framework enables the efficient modelling of complex cable setups, considering factors like sag, cable inclination, and spring/ damper discretisation. Lastly, the chapter explores into the parametric formulation of the FE cable model, offering a detailed understanding of wire interactions in helically twisted wire cables. The model considers factors like wire diameter, lay length, and material properties, which provides an efficient and versatile framework for studying cable behaviour under bending.

In summary, the chapter emphasises the practical applicability of these cable models as a parametric toolbox for various scenarios in cable analysis, signifying the versatility and adaptability of the models in real-world applications.

## 8.2 Scope for further work

The findings presented in this thesis contribute to advancements in cable modelling and also shed light on the limitations inherent in numerical frameworks, providing valuable insights for future developments and improvements in cable modelling.

The saddled cable model, as shown in this study, shows a high accuracy when compared with experimental results, particularly in the evaluation of modal properties. Extending the validation process to include static equilibrium conditions, non-contact geometry experimental measurement methods such as laser scanning can be employed to capture precise cable profiles on-site. Subsequent comparisons with the numerical model further enhance the validation of the saddled cable model.

A noteworthy aspect is the local modelling of an SPW cable or any helically twisted cable on a saddle support—a novel implementation not previously achieved to the author's knowledge. This breakthrough, facilitated by the parametric models introduced in this thesis, allows for comprehensive investigations into the contact problem at the saddle, stick–slip of wires under geometric constraints, and cable stress identification under varying load cases.

Additionally, experimental studies on cable bending could offer valuable data for calibrating and refining the model. For instance, displacement measurements along the cable length can be used to study the effects of wire slip on geometric form under varying load amplitudes. Testing different loading positions along the cable axis can help identifying stick–slip behaviour relative to loading positions. Similarly, hysteresis testing on slack and tensioned cables can reveal the impact of wire slip on cable damping characteristics.

Moreover, leveraging the SPW model enables exploration into additional phenomena, including the effects of wire cuts, load redistribution between wires, and the influence of friction and cohesive interlock between wires on recovery length.

In a practical sense, the culmination of these advancements allows for the realisation of a FE toolbox tailored to cover a broad spectrum of cases outlined in the classification table (Table 3.2). This toolbox, compatible with various commercial software, facilitates practical applications and further extends the utility of the models developed in research for practical uses.

# Appendix A

## The Catenary Solution

The analytical solution for the catenary problem is explained as follows,

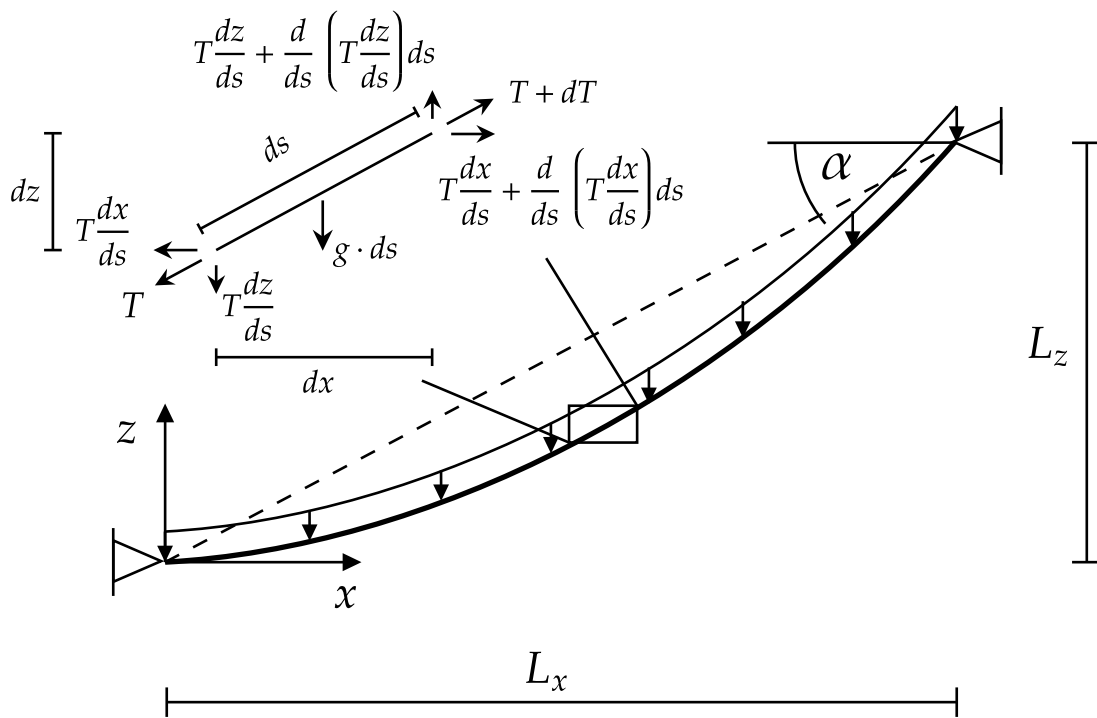


Figure A.1: Equilibrium of an infinitesimal element of a zero flexural stiffness member under its self weight.

where  $\sin \alpha = \frac{dz}{ds}$ ,  $\cos \alpha = \frac{dx}{ds}$ ,  $\tan \alpha = \frac{dz}{dx}$ .

The infinitesimal element infers that vertical equilibrium:

$$\frac{d}{ds} \left( T \frac{dz}{ds} \right) = g \quad (\text{A.1})$$

where  $T$  is the tension force and  $g$  the weight per unit length.

---

Horizontal equilibrium implies

$$\frac{d}{ds} \left( T \frac{dx}{ds} \right) = 0 \quad (\text{A.2})$$

Substituting  $T = T_h \frac{ds}{dx}$  (where  $T_h = T \frac{dx}{ds}$  as the horizontal tension component) and a subsequent multiplication by  $\frac{ds}{dx}$  into equation A.1 give

$$T_h \frac{d^2 z}{dx^2} = g \frac{ds}{dx} \quad (\text{A.3})$$

Using the Pythagorean equation of  $(ds)^2 = (dx)^2 + (dz)^2$  in equation A.3 gives

$$T_h \frac{d^2 z}{dx^2} = g \sqrt{1 + \left( \frac{dz}{dx} \right)^2} \quad (\text{A.4})$$

to simplify,  $a = \frac{dz}{dx}$  is introduced into equation A.4 such that  $\frac{da}{dx} = \frac{g}{T_h} \sqrt{1 + a^2}$ , which gives:

$$\frac{da}{\sqrt{1 + a^2}} = \frac{g}{T_h} dx \quad (\text{A.5})$$

By integrating both sides we get at:

$$\ln \left( a + \sqrt{1 + a^2} \right) = \frac{g}{T_h} x + K_1 \quad (\text{A.6})$$

Substitution of  $b = \frac{g}{T_h} x + K_1$  gives

$$a + \sqrt{1 + a^2} = e^b \Rightarrow a = \frac{e^b - e^{-b}}{2} = \sinh b \quad (\text{A.7})$$

thereby reaches to

$$\frac{dz}{dx} = \sinh \frac{g}{T_h} x + K_1 \quad (\text{A.8})$$

Integrating this expression solves the differential equation analytically leaving the two integration constants  $K_1$  and  $K_2$ , which are then solved by evaluating the boundary conditions at  $x = 0, y = 0$  and  $x = L_x, z = L_z$  ( $L_c$  being the chord length between the two supports).

$$z(x) = \frac{T_h}{g} \cosh \left( \frac{g}{T_h} x + K_1 \right) + K_2 \quad (\text{A.9})$$

$$K_1 = \sinh^{-1} \left( \frac{gL_z}{2T_h \sinh \frac{gL_c}{2T_h}} \right) - \frac{gL_c}{2T_h} \quad (\text{A.10})$$

$$K_2 = -\frac{T_h}{g} \cosh(K_1) \quad (\text{A.11})$$

This analytical solution is obtained from [17].

# Appendix B

## Computational benchmarking

The computer system used to run the FE simulations has the following specifications:

Table B.1: Computational power of the device used for nonlinear FE analysis.

CPU	Intel(R) Core(TM) i7-8700 CPU @ 3.20GHz 3.19 GHz
RAM	32.0 GB (31.7 GB usable)
GPU	Intel(R) UHD Graphics 630
System	Windows 10 64-bit

### B.1 Computations of the sagged bar model and the saddled cable model

The computational time required to solve each model is outlined in Tables B.2 to B.5, with details on the specific timeframes for each computation. The simulations were executed using the commercial FE solver, SOFiSTiK. Mechanical and geometric parameters can be found in the relevant chapters for reference.

These computational details are integral as benchmarking cases, offering a basis for future references and utilisation of the models.

In the context of residual forces, iteration tolerances are set at 0.001 kN. Notably, due to the substantial displacements experienced by the models in Chapter 4 and Chapter 5, the stiffness matrix  $\mathbf{K}$  undergoes updates after each iteration. While this necessitates additional computational time, it significantly contributes to the convergence stability of the models.

The computational time details provided in the tables offer estimates for the required computational demand. However, it's important to note that due to the numerical iterative nature of these computations, repeating the analyses may yield values that differ from those initially outlined in the tables, especially when using a different solver.

Table B.2: **Chapter 4**, computational cost for FE analysis of the cables for a single run and the optimisation requirements (opt.). *Mentioned details are collected along the following operations: geometry generation, a nonlinear form finding analysis, a subsequent Eigenvalue analysis, and results export in text formats.*

Model	no. nodes	no. elements	time per run [sec]	no. iterations	no. opt. parameters	no. opt. iterations
Øresund (ES-1)	532	531	14	141	3	1377
Øresund (ES-5)	349	348	12	196	3	2041
Øresund (EN-1)	529	528	13	122	3	1407
Queensferry C4	344	343	18	420	2	994

Table B.3: **Chapter 5**, Computational costs of FE analyses applied for self-weight comparison between models (without saddle springs). *The computational time involves: geometry generation, a nonlinear form finding analysis, and results export in text formats.*

Model	no. nodes	no. elements	time per run [sec]	iterations
Straight	1001	1000	58	97
Modified	1001	1000	56	97
Int. sagged	1001	1000	12	96
Extended	1001	1000	554	11560

Table B.4: **Chapter 5**, computational costs of FE analyses applied for determination of the contact point and the contact length (with saddle springs). *The computational time involves: geometry generation, a nonlinear form finding analysis, and results export in text formats.*

Model	no. nodes	no. elements	no. springs	time per run [sec]	iterations
Straight	1701	1700	802	197	642
Modified	1701	1700	802	148	511
Int. sagged	1701	1700	802	146	1175
Extended	1727	1726	802	1452	11284

Table B.5: **Chapter 5**, computational cost of FE analyses applied for cable force identification from vibration measurement of an external tendon. *The computational time involves: geometry generation, a nonlinear form finding analysis, an Eigenvalue analysis, and results export in text formats.*

Model	no. nodes	no. elements	no. springs	time per run [sec]	iterations	no. opt. parameters	no. opt. iterations
Saddled model for Extr. Tendon	250	249	7	75	44	4	2478

## B.2 Computational costs for the SPW cable model

The substantial size of the SPW cable model, coupled with its relatively small transverse displacements, led to the decision to update the stiffness matrix after every 4 iterations. This choice minimises the magnitude of updates required for the stiffness matrix, resulting in a potential reduction in the overall computational time.

With a small sag-to-span ratio (max.  $1/40$ ), the anticipated minimal impact of displacements on the cable form eliminates the need for subsequent updates of internal forces. Consequently, the analysis conducted is a nonlinear second-order analysis.

The table presented herein (Table B.6) offer detailed insights into the primary model featured in Model 02b. Notably, the displacements are dependent upon the magnitude of the vertical force, introducing a force-dependent computational time. The table provides a breakdown of computational time corresponding to each vertical load. As mentioned in the chapter, the model comprises 5063 nodes, encompassing a total of 5002 beam elements and 12948 inter-wire springs.

Table B.6: **Chapter 6**, computational cost of FE analyses applied for SPW detailed cable model.  
*The computational time involves: geometry generation, a nonlinear form finding analysis, and results export in text formats.*

Vertical Force [kN]	No. Itr. until convergence	Time per run [sec]
0	87	61
2	571	261
4	776	272
6	1432	301
8	990	272
10	1181	284
12	1006	277
14	596	243
16	1236	293
18	1425	301

# Bibliography

- [1] Morgese, M., Ansari, F., Domaneschi, M., and Cimellaro, G. P. Post-collapse analysis of morandi's polcevera viaduct in genoa italy. *Journal of Civil Structural Health Monitoring*, 10:69–85, 2020.
- [2] Clemente, P. Monitoring and evaluation of bridges: Lessons from the polcevera viaduct collapse in italy. *Journal of civil structural health monitoring*, 10(2):177–182, 2020.
- [3] 1993-1-11:2024-02, D. E. Eurocode 3 - Design of steel structures - Part 1-11: Tension components; German and English version prEN 1993-1-11:2024. Technical report, 2024.
- [4] Svensson, H. *Cable-Stayed Bridges: 40 Years of Experience Worldwide*. Wilhelm Ernst and Sohn, Berlin, Germany, 2013. ISBN 9783433601044. doi: 10.1002/9783433601044.
- [5] Gimsing, N. J. and Georgakis, C. T. *Cable Supported Bridges*. Wiley; 3rd edition, 2011. ISBN 9780470666289. doi: 10.1002/9781119978237.
- [6] Gläser, C., Theryo, T., Weiher, H., Chandoga, M., Kuilboer, C., Piekarski, J., Windisch, A., Ganz, H.-r., Krauser, L., and Ramirez, G. *FIB BULLETIN NO. 97 - External Tendons for Bridges*. 2020. ISBN 978-2-88394-146-5. doi: 10.35789/fib.BULL.0097.
- [7] Prato, C. A. and Ceballos, M. A. Dynamic bending stresses near the ends of parallel-bundle stay cables. *Structural Engineering International: Journal of the International Association for Bridge and Structural Engineering (IABSE)*, 13(1):64–68, 2003. ISSN 10168664. doi: 10.2749/101686603777965008.
- [8] Ceballos, M. A. and Prato, C. A. Determination of the axial force on stay cables accounting for their bending stiffness and rotational end restraints by free vibration tests. *Journal of Sound and Vibration*, 317(1-2):127–141, 2008. ISSN 0022460X. doi: 10.1016/j.jsv.2008.02.048.
- [9] of Transportation, U. D. Replaceable Grouted External Post-Tensioned Tendons. Technical Report October, 2019.
- [10] Wilczek, F. *A Beautiful Question: Finding Nature's Deep Design*. Penguin Books, New York, 2016. ISBN 978-0143109365.
- [11] Hunt, F. V. *Origins in Acoustics: The Science of Sound from Antiquity to the Age of Newton*. Yale University Press; First Edition, 1978. ISBN 978-0300022209.
- [12] Triantafyllou, M. S. Linear Dynamics of Cables and Chains. *Shock and Vibration Digest*, 16(3):9–17, 1984. ISSN 05831024. doi: 10.1177/058310248401600305.
- [13] Block, P., Gengnagel, C., and Peters, S. *Faustformel Tragwerksentwurf*. Dt. Verlag-Anst., 2013. ISBN 9783421039040.
- [14] Allen, E. and Zalewski, W. *Form and Forces: Designing Efficient, Expressive Structures*.

- Wiley, 2012. ISBN 9781118174258.
- [15] Ernst, H.-J. Der E-modul von seilen unter berucksichtigung des durchhanges. *Der Bauingenieur*, 40(2):52–55, 1965.
- [16] Ernst, H.-J. *Beitrag zur Beurteilung der behördlichen Vorschriften für die Seile von Personenschwebbahnen*. PhD thesis, Technischen Hochschule der Freien Stadt Danzig, 1933.
- [17] Kumarasena, S., Jones, N., Irwin, P., and Taylor, P. Wind induced vibration of stay cables. *Washington, DC: US Department of Transportation, Federal Highway Administration*, 2007.
- [18] Bathe, K. J. Finite element procedures, Englewood Cliffs, NJ: Prentice-Hall. 1996.
- [19] Yuan, X. and Dong, S. Nonlinear analysis and optimum design of cable domes. *Engineering Structures*, 24(7):965–977, jul 2002. ISSN 01410296. doi: 10.1016/S0141-0296(02)00017-2. URL <https://linkinghub.elsevier.com/retrieve/pii/S0141029602000172>.
- [20] Yuan, X., Chen, L., and Dong, S. Prestress design of cable domes with new forms. *International Journal of Solids and Structures*, 44(9):2773–2782, 2007. ISSN 00207683. doi: 10.1016/j.ijsolstr.2006.08.026.
- [21] Guo, J. and Jiang, J. An algorithm for calculating the feasible pre-stress of cable-struts structure. *Engineering Structures*, 118:228–239, 2016. ISSN 18737323. doi: 10.1016/j.engstruct.2016.03.058. URL <http://dx.doi.org/10.1016/j.engstruct.2016.03.058>.
- [22] Zhang, T., Zhang, Y., and Zhang, H. A three-stage criterion method for extracting local vibration modes of tensioned cables in beam string structures. *Frontiers in Materials*, (October):1–12, 2022. doi: <https://doi.org/10.3389/fmats.2022.1055635>.
- [23] Chawdhury, S. and Morgenthal, G. Numerical simulations of aeroelastic instabilities to optimize the performance of flutter-based electromagnetic energy harvesters. 29(4): 479–495, 2018. doi: 10.1177/1045389X17711784.
- [24] Chawdhury, S. and Morgenthal, G. A partitioned solver to simulate large-displacement fluid – structure interaction of thin plate systems for vibration energy harvesting. *Computers and Structures*, 224:106110, 2019. ISSN 0045-7949. doi: 10.1016/j.compstruc.2019.106110. URL <https://doi.org/10.1016/j.compstruc.2019.106110>.
- [25] Lepidi, M. Catenary configuration and geometric stiffness matrix of inextensible cables: Analytical high-order asymptotic solutions for parametric design. *Applied Mathematical Modelling*, 128:1–25, apr 2024. ISSN 0307904X. doi: 10.1016/j.apm.2023.12.019. URL <https://linkinghub.elsevier.com/retrieve/pii/S0307904X23005723>.
- [26] Block, P. and J., S. Structural design i: Lecture 3: Cables, 2023. URL <https://block.arch.ethz.ch/eq/course/4>.

- [27] Zui, H., Shinke, T., and Namita, Y. Practical Formulas for Estimation of Cable Tension Using the Vibration Method. *Journal of Structural Engineering*, 122(June):651–656, 1996. ISSN 0733-9445/96/0006-0651-0656.
- [28] Irvin, H. and Caughey, T. The linear theory of free vibrations of a suspended cable. *Proceedings of the Royal Society of London. A. Mathematical and Physical Sciences*, 341(1626):299–315, dec 1974. ISSN 0080-4630. doi: 10.1098/rspa.1974.0189. URL <https://royalsocietypublishing.org/doi/10.1098/rspa.1974.0189>.
- [29] Morse, P. M., Ingard, K. U., and Stumpf, F. B. *Theoretical Acoustics*. Number 5. Princeton University Press, 1986. ISBN 978-0691024011.
- [30] Ren, W. X., Chen, G., and Hu, W. H. Empirical formulas to estimate cable tension by cable fundamental frequency. *Structural Engineering and Mechanics*, 20(3):363–380, 2005. ISSN 12254568. doi: 10.12989/sem.2005.20.3.363.
- [31] Fang, Z. and Wang, J.-q. Practical Formula for Cable Tension Estimation by Vibration Method. *Journal of Bridge Engineering*, 17(1):161–164, 2012. ISSN 1084-0702. doi: 10.1061/(asce)be.1943-5592.0000200.
- [32] Mehrabi, A. B. and Tabatabai, H. Unified Finite Difference Formulation for Free Vibration of Cables. *Journal of Structural Engineering*, 124(11):1313–1322, 1998. ISSN 0733-9445. doi: 10.1061/(asce)0733-9445(1998)124:11(1313).
- [33] Ni, Y. Q., Ko, J. M., and Zheng, G. Dynamic analysis of large-diameter sagged cables taking into account flexural rigidity. *Journal of Sound and Vibration*, 2002. ISSN 0022460X. doi: 10.1006/jsvi.2002.5060.
- [34] Yan, B., Yu, J., and Soliman, M. Estimation of cable tension force independent of complex boundary conditions. *Journal of Engineering Mechanics*, 141(1), 2015. ISSN 07339399. doi: 10.1061/(ASCE)EM.1943-7889.0000836.
- [35] Ricciardi, G. and Saitta, F. A continuous vibration analysis model for cables with sag and bending stiffness. *Engineering Structures*, pages 1459–1472, 2008. ISSN 01410296. doi: 10.1016/j.engstruct.2007.08.008.
- [36] Rinaldi, C., Lepidi, M., Potenza, F., and Gattulli, V. Identification of cable tension through physical models and non-contact measurements Identification of cable tension through physical models and non-contact measurements. *Mechanical Systems and Signal Processing*, 205(November):110867, 2023. ISSN 0888-3270. doi: 10.1016/j.ymsp.2023.110867. URL <https://doi.org/10.1016/j.ymsp.2023.110867>.
- [37] Yan, B., Li, D., Chen, W., Deng, L., and Jiang, X. Mode shape-aided cable force determination using digital image correlation. *Structural Health Monitoring*, 20(5): 2430–2445, sep 2021. ISSN 1475-9217. doi: 10.1177/1475921720952163. URL <http://journals.sagepub.com/doi/10.1177/1475921720952163>.
- [38] Zhang, S., Shen, R., Wang, Y., De Roeck, G., Lombaert, G., and Dai, K. A two-step methodology for cable force identification. *Journal of Sound and Vibration*, 2020. ISSN

10958568. doi: 10.1016/j.jsv.2020.115201.
- [39] Lacarbonara, W. and Pacitti, A. Nonlinear modeling of cables with flexural stiffness. *Mathematical Problems in Engineering*, 2008. ISSN 1024123X. doi: 10.1155/2008/370767.
- [40] Chen, Y. and Feng, J. Efficient Method for Moore-Penrose Inverse Problems Involving Symmetric Structures Based on Group Theory. *Journal of Computing in Civil Engineering*, 28(2):182–190, 2014. ISSN 0887-3801. doi: 10.1061/(asce)cp.1943-5487.0000266.
- [41] Chen, Y. and Feng, J. Generalized Eigenvalue Analysis of Symmetric Prestressed Structures Using Group Theory. *Journal of Computing in Civil Engineering*, 26(4): 488–497, 2012. ISSN 0887-3801. doi: 10.1061/(asce)cp.1943-5487.0000151.
- [42] Zhang, W.-m. and Wang, Z.-w. Frequency-Based Cable Tension Identification Using a Nonlinear Model with Complex Boundary Constraints. *Shock and Vibration*, 2023(1): 1–19, feb 2023. ISSN 1875-9203. doi: 10.1155/2023/7795452. URL <https://www.hindawi.com/journals/sv/2023/7795452/>.
- [43] Haji Agha Mohammad Zarbaf, S. E., Norouzi, M., Allemang, R., Hunt, V., Helmicki, A., and Venkatesh, C. Vibration-based cable condition assessment: A novel application of neural networks. *Engineering Structures*, 177(September):291–305, 2018. ISSN 18737323. doi: 10.1016/j.engstruct.2018.09.060. URL <https://doi.org/10.1016/j.engstruct.2018.09.060>.
- [44] Jeong, S., Kim, H., Lee, J., and Sim, S.-h. Automated wireless monitoring system for cable tension forces using deep learning. *Structural Health Monitoring*, pages 1–17, 2021. doi: 10.1177/1475921720935837.
- [45] Wu, W.-h., Chen, C.-c., Lin, S.-l., and Lai, G. A Real-Time Monitoring System for Cable Tension with Vibration Signals Based on an Automated Algorithm to Sieve Out Reliable Modal Frequencies. *Structural Control and Health Monitoring*, 2023, 2023.
- [46] Le, L. X., Katsuchi, H., To, L. G., Zarbaf, S. E. H. A. M., and Thanh, C.-L. Estimation of Cable Tension with Unknown Parameters Using Artificial Neural Networks. In *Structural Control and Health Monitoring*, pages 77–88. 2021. ISBN 9789811609459. doi: 10.1007/978-981-16-0945-9\_6. URL [https://link.springer.com/10.1007/978-981-16-0945-9\\_6](https://link.springer.com/10.1007/978-981-16-0945-9_6).
- [47] Le, L. X., Katsuchi, H., and Kawai, S. Damping in stay cable with damper: Practical universal damping curve and full-scale measurement. *Journal of Sound and Vibration*, 569:118090, jan 2024. ISSN 0022460X. doi: 10.1016/j.jsv.2023.118090. URL <https://linkinghub.elsevier.com/retrieve/pii/S0022460X23005394>.
- [48] Spak, K., Agnes, G., and Inman, D. Parameters for Modeling Stranded Cables as Structural Beams. *Experimental Mechanics*, 54(9):1613–1626, 2014. ISSN 17412765. doi: 10.1007/s11340-014-9941-8.
- [49] Irvin, H. *Cable Structures*. MIT Press, Cambridge, MA, 1981. ISBN 0-262-09023-3.
- [50] Du, H., Liu, D. Y., Huang, F. W., and Liao, J. B. Method of Bending Stiffness Parameter

- Identification of Stay Cable. *Applied Mechanics and Materials*, 777:52–58, 2015. doi: 10.4028/www.scientific.net/amm.777.52.
- [51] Cho, S., Yim, J., Shin, S. W., Jung, H. J., Yun, C. B., and Wang, M. L. Comparative field study of cable tension measurement for a cable-stayed bridge. *Journal of Bridge Engineering*, 2013. ISSN 10840702. doi: 10.1061/(ASCE)BE.1943-5592.0000421.
- [52] Bellino, A., Marchesiello, S., Fasana, A., and Garibaldi, L. Cable tension estimation by means of vibration response and moving mass technique. *Mecanique et Industries*, 11(6):505–512, 2010. ISSN 12962139. doi: 10.1051/meca/2010058.
- [53] Li, S., Wang, L., Wang, H., Shi, P., Lan, R., Wu, C., and Wang, X. An Accurate Measurement Method for Tension Force of Short Cable by Additional Mass Block. *Advances in Materials Science and Engineering*, 2021. doi: <https://doi.org/10.1155/2021/6622628>.
- [54] Caetano, E. Cables. In *Innovative Bridge Design Handbook*, pages 555–596. Elsevier, 2016. ISBN 978-0-12-800487-6. doi: 10.1016/B978-0-12-800058-8.00021-9. URL <https://linkinghub.elsevier.com/retrieve/pii/B9780128000588000219>.
- [55] Geier, R., De Roeck, G., and Petz, J. Cable force determination for the danube channel bridge in Vienna. *Structural Engineering International: Journal of the International Association for Bridge and Structural Engineering (IABSE)*, 15(3):181–185, 2005. ISSN 10168664. doi: 10.2749/101686605777962991.
- [56] Peeters, B., Couvreur, G., Razinkov, O., Kündig, C., van der Auweraer, H., and de Roeck, G. Continuous monitoring of the Øresund Bridge: System and data analysis. *Structure and Infrastructure Engineering*, 5(5):395–405, 2009. ISSN 15732479. doi: 10.1080/15732470701478362.
- [57] Geier, R., De Roeck, G., and Flesch, R. Accurate cable force determination using ambient vibration measurements. *Structure and Infrastructure Engineering*, 2(1):43–52, 2006. ISSN 1573-2479. doi: 10.1080/15732470500253123.
- [58] Russell, J. C. and Lardner, T. J. Experimental Determination of Frequencies and Tension for Elastic Cables. *Journal of Engineering Mechanics*, 124(10):1067–1072, 1998. ISSN 0733-9399. doi: 10.1061/(asce)0733-9399(1998)124:10(1067).
- [59] Nam, H. and Nghia, N. T. Estimation of Cable Tension Using Measured Natural Frequencies. *Procedia Engineering*, 14:1510–1517, 2011. ISSN 1877-7058. doi: 10.1016/j.proeng.2011.07.190. URL <http://dx.doi.org/10.1016/j.proeng.2011.07.190>.
- [60] Liu, M., Zheng, L., Zhou, P., and Xiao, H. Stability and Dynamics Analysis of In-Plane Parametric Vibration of Stay Cables in a Cable-Stayed Bridge with Superlong Spans Subjected to Axial Excitation. *Journal of Aerospace Engineering*, 2020. ISSN 08931321. doi: 10.1061/(ASCE)AS.1943-5525.0001104.
- [61] Gong, J., Zhi, X., Fan, F., and Shen, S. Static and dynamic stiffness in the modeling of

- inclined suspended cables. *Journal of Constructional Steel Research*, 172:106210, 2020. ISSN 0143974X. doi: 10.1016/j.jcsr.2020.106210. URL <https://doi.org/10.1016/j.jcsr.2020.106210>.
- [62] Liao, W., Ni, Y., and Zheng, G. Tension force and structural parameter identification of bridge cables. *Advances in Structural Engineering*, 2012. ISSN 13694332. doi: 10.1260/1369-4332.15.6.983.
- [63] He, W.-y., Meng, F.-c., and Ren, W.-x. Cable force estimation of cables with small sag considering inclination angle effect. *Advances in Bridge Engineering*, 2021. doi: <https://doi.org/10.1186/s43251-021-00037-8>(2021).
- [64] Papailiou, K. O. Bending of helically twisted cables under variable bending stiffness due to internal friction, tensile force and cable curvature. *Doctor of Technical Sciences thesis, No. 11057, ETH, Zürich, Switzerland*, 1995.
- [65] Papailiou, K. O. On the bending stiffness of transmission line conductors. *IEEE Transactions on Power Delivery*, 12(4):1576–1583, 1997. ISSN 08858977. doi: 10.1109/61.634178.
- [66] Foti, F. and Martinelli, L. Mechanical modeling of metallic strands subjected to tension, torsion and bending. *International Journal of Solids and Structures*, 2016. ISSN 00207683. doi: 10.1016/j.ijsolstr.2016.04.034.
- [67] Yu, Y., Chen, Z., and Liu, H. Advanced approaches to calculate recovery length and force redistribution in semi-parallel wire cables with broken wires. *Engineering Structures*, 131:44–56, 2017. ISSN 18737323. doi: 10.1016/j.engstruct.2016.10.017. URL <http://dx.doi.org/10.1016/j.engstruct.2016.10.017>.
- [68] Dastous, J. B. Nonlinear finite-element analysis of stranded conductors with variable bending stiffness using the tangent stiffness method. *IEEE Transactions on Power Delivery*, 20(1):328–338, 2005. ISSN 08858977. doi: 10.1109/TPWRD.2004.835420.
- [69] Foti, F. and Martinelli, L. An analytical approach to model the hysteretic bending behavior of spiral strands. *Applied Mathematical Modelling*, 40(13-14):6451–6467, 2016. ISSN 0307904X. doi: 10.1016/j.apm.2016.01.063.
- [70] Bendalla, A. S. K., Tondo, G. R., and Morgenthal, G. A nonlinear finite element framework and Gaussian process-based prediction of stick/slip behaviour in semi-parallel wire cables. *International Journal of Solids and Structures*, 284(May):112522, 2023. doi: 10.1016/j.ijsolstr.2023.112522.
- [71] Bendalla, A. S. K. and Morgenthal, G. A nonlinear finite element framework for static and dynamic analysis of structural cables with deviating supports. *Engineering Structures*, 291(June):116363, sep 2023. ISSN 01410296. doi: 10.1016/j.engstruct.2023.116363.
- [72] Geier, R. *Systemidentifikation seilgestützter Tragwerke: Die dynamische Strukturantwort von Schrägseilen*. PhD thesis, Technische Universität (TU) Wien, 2004. URL <https://publik.tuwien.ac.at/showentry.php?ID=144709&lang=2>.

- [73] Clerc, M. *Particle Swarm Optimization*. 2006. ISBN 9780470612163. doi: 10.1002/9780470612163.
- [74] Haji Agha Mohammad Zarbaf, S. E., Norouzi, M., Allemang, R. J., Hunt, V. J., and Helmicki, A. Stay Cable Tension Estimation of Cable-Stayed Bridges Using Genetic Algorithm and Particle Swarm Optimization. *Journal of Bridge Engineering*, 22(10), oct 2017. ISSN 1084-0702. doi: 10.1061/(ASCE)BE.1943-5592.0001130. URL [https://doi.org/10.1061/\(ASCE\)BE.1943-5592.0001130](https://doi.org/10.1061/(ASCE)BE.1943-5592.0001130).
- [75] Morgenthal, G., Rau, S., Taraben, J., and Abbas, T. Determination of Stay-Cable Forces Using Highly Mobile Vibration Measurement Devices. *Journal of Bridge Engineering*, 23(2):1–13, 2018. ISSN 10840702. doi: 10.1061/(ASCE)BE.1943-5592.0001166.
- [76] Shuang-rui, C. and Quan-sheng, Y. A method of measuring the cable tension force with the application of smart phones. *Computer Modelling & New Technologies*, 17:11–18, 2013.
- [77] Yu, Y., Han, R., Zhao, X., Mao, X., Hu, W., Jiao, D., Li, M., and Ou, J. Initial validation of mobile-structural health monitoring method using smartphones. *International Journal of Distributed Sensor Networks*, 2015, 2015. ISSN 15501477. doi: 10.1155/2015/274391.
- [78] Geffen, V. V. A study of friction models and friction Compensation. *A study of friction models and friction Compensation*, pages 1–24, 2009. URL <http://www.mate.tue.nl/mate/pdfs/11194.pdf>.
- [79] Spak, K., Agnes, G., and Inman, D. Cable modeling and internal damping developments. *Applied Mechanics Reviews*, 65(1):1–18, 2013. ISSN 00036900. doi: 10.1115/1.4023489.
- [80] Wu, W. H., Chen, C. C., Leu, M. R., and Lai, G. Determination of stay cable force based on multiple vibration measurements to consider the effects of unsymmetrical boundary constraints. *Proceedings of the 6th European Workshop - Structural Health Monitoring 2012, EWSHM 2012*, 2(123):1219–1226, 2012.
- [81] Chen, C.-c., Wu, W.-h., Huang, C.-h., and Lai, G. Determination of stay cable force based on effective vibration length accurately estimated from multiple measurements. *Smart Structures and Systems*, 11(4):411–433, 2013.
- [82] Chen, C.-c., Wu, W.-h., Leu, M.-r., and Lai, G. Tension determination of stay cable or external tendon with complicated constraints using multiple vibration measurements. *MEASUREMENT*, 86:182–195, 2016. ISSN 0263-2241. doi: 10.1016/j.measurement.2016.02.053. URL <http://dx.doi.org/10.1016/j.measurement.2016.02.053>.
- [83] Wu, W.-h., Chen, C.-c., Chen, Y.-c., Lai, G., and Huang, C.-m. Tension determination for suspenders of arch bridge based on multiple vibration measurements concentrated at one end. *Measurement*, 123(April 2017):254–269, 2018. ISSN 0263-2241. doi: 10.1016/j.measurement.2018.03.077. URL <https://doi.org/10.1016/j.measurement.2018.03.077>.
- [84] Waisman, H., Montoya, A., Betti, R., and Noyan, I. C. Load Transfer and Recovery Length

- in Parallel Wires of Suspension Bridge Cables. *Journal of Engineering Mechanics*, 137(4): 227–237, 2011. ISSN 0733-9399. doi: 10.1061/(asce)em.1943-7889.0000220.
- [85] Montoya, A., Waisman, H., and Betti, R. A simplified contact-friction methodology for modeling wire breaks in parallel wire strands. *Computers & Structures*, 100-101(June): 39–53, 2012. ISSN 00457949. doi: 10.1016/j.compstruc.2012.03.003.
- [86] Ranzi, G., Gara, F., and Ansourian, P. General method of analysis for composite beams with longitudinal and transverse partial interaction. *Computers & Structures*, 84(31-32): 2373–2384, 2006. ISSN 00457949. doi: 10.1016/j.compstruc.2006.07.002.
- [87] Liang, B., Zhao, Z., Wu, X., and Liu, H. The establishment of a numerical model for structural cables including friction. *Journal of Constructional Steel Research*, 139: 424–436, 2017. ISSN 0143974X. doi: 10.1016/j.jcsr.2017.09.031. URL <https://doi.org/10.1016/j.jcsr.2017.09.031>.
- [88] DYWIDAG-Systems International GmbH. Drahtspannsystem SUSPA-Draht EX für externe Vorspannung mit 30 bis 84 Spannstahldrähten nach DIN EN 1992-1-1 und DIN EN 1992-2. Technical report, Deutsches Institut für Bautechnik, 2018. URL <https://www.dibt.de/de/service/zulassungsdownload/detail/z-133-139>.
- [89] MATLAB. *MATLAB (R2019b)*. The MathWorks Inc., Natick, Massachusetts, 2010.
- [90] Chen, Z., Yu, Y., Wang, X., Wu, X., and Liu, H. Experimental research on bending performance of structural cable. *Construction and Building Materials*, 2015. ISSN 09500618. doi: 10.1016/j.conbuildmat.2015.08.026.
- [91] Zheng, X., Hu, Y., Zhou, B., and Li, J. Modelling of the hysteretic bending behavior for helical strands under multi-axial loads. *Applied Mathematical Modelling*, 97:536–558, 2021. ISSN 0307904X. doi: 10.1016/j.apm.2021.04.004. URL <https://doi.org/10.1016/j.apm.2021.04.004>.
- [92] Saltelli, A., Ratto, M., Andres, T., Campolongo, F., Cariboni, J., Gatelli, D., Saisana, M., and Tarantola, S. *Global sensitivity analysis: The primer*, volume 76. John Wiley and Sons, Ltd, 2008. ISBN 9780470725184. doi: 10.1002/9780470725184.
- [93] Lee, W. An insight into wire rope geometry. *International Journal of Solids and Structures*, 28(4):471–490, 1991. ISSN 00207683. doi: 10.1016/0020-7683(91)90060-S. URL <https://linkinghub.elsevier.com/retrieve/pii/002076839190060S>.
- [94] Caetano, E. Characterisation and assessment of damage in cable structures. *Journal of Civil Structural Health Monitoring*, 12(6):1267–1283, 2022. ISSN 21905479. doi: 10.1007/s13349-022-00614-z. URL <https://doi.org/10.1007/s13349-022-00614-z>.
- [95] Di, F., Sun, L., and Chen, L. In-plane dynamic behaviors of two-cable networks with a pretensioned cross-tie. *Structural Control and Health Monitoring*, 28(7):8–12, 2021. ISSN 15452263. doi: 10.1002/stc.2755.

- [96] Cardou, A. and Jolicoeur, C. Mechanical models of helical strands. *Applied Mechanics Reviews*, 50(1):1–14, 1997. ISSN 00036900. doi: 10.1115/1.3101684.
- [97] Han, Y., Yong, H., Zhang, X., and Zhou, Y. Optimal designs of the multilevel chiral helical structures with local contact and fretting wear. *International Journal of Solids and Structures*, 273:112265, jun 2023. ISSN 00207683. doi: 10.1016/j.ijsolstr.2023.112265. URL <https://linkinghub.elsevier.com/retrieve/pii/S0020768323001622>.
- [98] Tondo, G. R., Rau, S., Kavrakov, I., and Morgenthal, G. Stochastic stiffness identification and response estimation of Timoshenko beams via physics-informed Gaussian processes. *Probabilistic Engineering Mechanics*, 74(May):103534, 2023. ISSN 0266-8920. doi: 10.1016/j.probengmech.2023.103534. URL <https://doi.org/10.1016/j.probengmech.2023.103534>.
- [99] Tondo, G. R., Kavrakov, I., and Morgenthal, G. A physics-informed machine learning model for reconstruction of dynamic loads. *IABSE Symposium, Istanbul 2023: Long Span Bridges*, 119(Istbr):315–322, 2023. doi: 10.2749/istanbul.2023.0315.
- [100] Raj, T. M. and Parthasarathy, N. S. A complete review of friction models of composite cables. 2007. URL <https://www.researchgate.net/publication/267232490Acompletreviewoffrictionmodelsofcompositecables>.
- [101] Raoof, M. and Hobbs, R. E. Analysis of Multilayered Structural Strands. *Journal of Engineering Mechanics*, 114(7):1166–1182, jul 1988. ISSN 0733-9399. doi: 10.1061/(ASCE)0733-9399(1988)114:7(1166). URL [https://doi.org/10.1061/\(ASCE\)0733-9399\(1988\)114:7\(1166\)](https://doi.org/10.1061/(ASCE)0733-9399(1988)114:7(1166)).
- [102] Raoof, M. Wire recovery length in a helical strand under axial-fatigue loading. *International Journal of Fatigue*, 13(2):127–132, 1991. ISSN 01421123. doi: 10.1016/0142-1123(91)90004-I.
- [103] Huang, X. and Vinogradov, O. G. Dry friction losses in axially loaded cables. *Structural Engineering and Mechanics*, 4(3):330–344, 1996. ISSN 12254568. doi: 10.12989/sem.1996.4.3.330.
- [104] Sun, H., Xu, J., Chen, W., and Yang, J. Time-Dependent Effect of Corrosion on the Mechanical Characteristics of Stay Cable. *Journal of Bridge Engineering*, 23(5):1–13, 2018. ISSN 1084-0702. doi: 10.1061/(asce)be.1943-5592.0001229.
- [105] Xu, J., Sun, H., and Cai, S. Effect of symmetrical broken wires damage on mechanical characteristics of stay cable. *Journal of Sound and Vibration*, 461:114920, 2019. ISSN 10958568. doi: 10.1016/j.jsv.2019.114920. URL <https://doi.org/10.1016/j.jsv.2019.114920>.
- [106] Vemula, S. S., Ji, M., Headings, L. M., Gargesh, K., Soghtrati, S., and Dapino, M. J. Analytical model for large deflection bending of helically stranded electrical wires. *International Journal of Mechanical Sciences*, 170(November 2019):105355, 2020. ISSN

00207403. doi: 10.1016/j.ijmecsci.2019.105355. URL <https://doi.org/10.1016/j.ijmecsci.2019.105355>.
- [107] Guo, L., Liu, H., and Chen, Z. Experimental research on the bending performance of locked coil wire rope and Galfan strand. *Construction and Building Materials*, 304 (September):124667, 2021. ISSN 09500618. doi: 10.1016/j.conbuildmat.2021.124667. URL <https://doi.org/10.1016/j.conbuildmat.2021.124667>.
- [108] Oliveto, N. D. and Sivaselvan, M. V. Nonlinear finite element analysis of three-dimensional free and harmonically forced vibrations of stranded conductor cables. *Earthquake Engineering and Structural Dynamics*, 43(14):2199–2216, nov 2014. ISSN 00988847. doi: 10.1002/eqe.2449. URL <https://onlinelibrary.wiley.com/doi/10.1002/eqe.2449>.
- [109] Karathanasopoulos, N. and Kress, G. Mechanical response of a helical body to axial, torsional and radial strain. *International Journal of Mechanical Sciences*, 94-95:260–265, 2015. ISSN 00207403. doi: 10.1016/j.ijmecsci.2015.02.022. URL <http://dx.doi.org/10.1016/j.ijmecsci.2015.02.022>.
- [110] Cao, X. and Wu, W. The establishment of a mechanics model of multi-strand wire rope subjected to bending load with finite element simulation and experimental verification. *International Journal of Mechanical Sciences*, 142-143:289–303, jul 2018. ISSN 00207403. doi: 10.1016/j.ijmecsci.2018.04.051. URL <https://linkinghub.elsevier.com/retrieve/pii/S0020740318309111>.
- [111] Ménard, F. and Cartraud, P. Solid and 3D beam finite element models for the nonlinear elastic analysis of helical strands within a computational homogenization framework. *Computers & Structures*, 257:106675, dec 2021. ISSN 00457949. doi: 10.1016/j.compstruc.2021.106675. URL <https://linkinghub.elsevier.com/retrieve/pii/S0045794921001978>.
- [112] Zhou, B., Hu, Y., Zheng, X., and Zhu, H. Bending Behavior of a Frictional Single-Layered Spiral Strand Subjected to Multi-Axial Loads: Numerical and Experimental Investigation. *Applied Sciences*, 12(9):4792, may 2022. ISSN 2076-3417. doi: 10.3390/app12094792. URL <https://www.mdpi.com/2076-3417/12/9/4792>.
- [113] Alkharisi, M. K. and Heyliger, P. R. Free Vibration of Inclined Twisted Cables. *Structures*, 50:1879–1896, apr 2023. ISSN 23520124. doi: 10.1016/j.istruc.2023.03.015. URL <https://linkinghub.elsevier.com/retrieve/pii/S2352012423003016>.
- [114] Yu, Y., Wang, X., and Chen, Z. A simplified finite element model for structural cable bending mechanism. *International Journal of Mechanical Sciences*, 113:196–210, 2016. ISSN 00207403. doi: 10.1016/j.ijmecsci.2016.05.004. URL <http://dx.doi.org/10.1016/j.ijmecsci.2016.05.004>.
- [115] Gara, F., Ranzi, G., and Leoni, G. Displacement-based formulations for composite beams

- with longitudinal slip and vertical uplift. *International Journal for Numerical Methods in Engineering*, 65(8):1197–1220, 2006. ISSN 00295981. doi: 10.1002/nme.1484.
- [116] Hanaor, D. A., Gan, Y., and Einav, I. Contact mechanics of fractal surfaces by spline assisted discretisation. *International Journal of Solids and Structures*, 59:121–131, 2015. ISSN 00207683. doi: 10.1016/j.ijsolstr.2015.01.021. URL <http://dx.doi.org/10.1016/j.ijsolstr.2015.01.021>.
- [117] Alarcón, H., Salez, T., Poulard, C., Bloch, J.-F., Raphaël, É., Dalnoki-Veress, K., and Restagno, F. Self-Amplification of Solid Friction in Interleaved Assemblies. *Physical Review Letters*, 116(1):015502, jan 2016. ISSN 0031-9007. doi: 10.1103/PhysRevLett.116.015502.
- [118] Karathanasopoulos, N. and Angelikopoulos, P. Optimal structural arrangements of multilayer helical assemblies. *International Journal of Solids and Structures*, 78-79: 1–8, jan 2016. ISSN 00207683. doi: 10.1016/j.ijsolstr.2015.09.023. URL <https://linkinghub.elsevier.com/retrieve/pii/S0020768315004084>.
- [119] Feyrer, K. *Wire Ropes*. Springer Berlin Heidelberg, Berlin, Heidelberg, 2007. ISBN 978-3-540-33821-5. doi: 10.1007/978-3-540-33831-4. URL <http://link.springer.com/10.1007/978-3-540-33831-4>.
- [120] Furst, A., Marti, P., and Gans, H. R. Bending of Stay Cables. *Structural Engineering International*, pages 42–46, 2000.
- [121] Caetano, E. D. S. *Cable Vibrations in Cable-Stayed Bridges*. 2007. ISBN 978-3-85748-115-4.
- [122] Zhang, Y., Wang, J., Ye, G., and Xu, R. Bending Stiffness of Parallel Wire Cables Including Interfacial Slips among Wires. *Journal of Structural Engineering*, 144(10):04018164, 2018. ISSN 0733-9445. doi: 10.1061/(asce)st.1943-541x.0002171.
- [123] Zhang, Y., Feng, Q., Wang, G., and Xu, R. Analytical model for the bending of parallel wire cables considering interactions among wires. *International Journal of Mechanical Sciences*, 194:106192, mar 2021. ISSN 00207403. doi: 10.1016/j.ijmecsci.2020.106192. URL <https://linkinghub.elsevier.com/retrieve/pii/S0020740320342971>.
- [124] Brügger, A., Lee, S. Y., Robinson, J., Morgantini, M., Betti, R., and Noyan, I. C. Internal Contact Mechanics of 61-Wire Cable Strands. *Experimental Mechanics*, 62(8):1475–1488, 2022. ISSN 17412765. doi: 10.1007/s11340-022-00896-w. URL <https://doi.org/10.1007/s11340-022-00896-w>.
- [125] Yang, J., Fei, H., Sun, Q., and Hao, X. W. Analysis of Contact Friction Behavior in the Bending Process of Semi-Parallel Steel Wire Cable. *Civil Engineering Journal*, 31(3): 456–466, 2022. ISSN 1805-2576. doi: 10.14311/CEJ.2022.03.0034.
- [126] Belkhabbaz, A., Gueguin, M., Hafid, F., Yang, C., Allix, O., and Ghidaglia, J. M. Surrogate model based approach to predict fatigue stress field in multi-stranded cables. *International Journal of Solids and Structures*, 230-231:111168, 2021. ISSN 00207683. doi: 10.1016/j.ijsolstr.2021.111168. URL <https://doi.org/10.1016/>

- j.ijsoistr.2021.111168.
- [127] Filotto, F. M., Runkel, F., and Kress, G. Cross section shape optimization of wire strands subjected to purely tensile loads using a reduced helical model. *Advanced Modeling and Simulation in Engineering Sciences*, 7(1), 2020. ISSN 22137467. doi: 10.1186/s40323-020-00159-0. URL <https://doi.org/10.1186/s40323-020-00159-0>.
- [128] Rasmussen, C. E. and Williams, C. K. I. *Gaussian Processes for Machine Learning*. The MIT Press, 2006. ISBN 0-262-18253-X.
- [129] Neal, R. M. Priors for Infinite Networks. pages 29–53. 1996. doi: 10.1007/978-1-4612-0745-0\_2. URL [http://link.springer.com/10.1007/978-1-4612-0745-0\\_2](http://link.springer.com/10.1007/978-1-4612-0745-0_2).
- [130] MacKay, D. J. Introduction to Gaussian processes. *NATO ASI series F computer and systems sciences*, 168:133–166, 1998.
- [131] Murphy, K. P. *Machine learning: a probabilistic perspective*. MIT press, 2012.
- [132] Metwally, M. Nonlinear Numerical Analysis of Stay Cable Vibrations by Declaration of Authorship. (September), 2012.
- [133] Mohareb, S., Goldack, A., Schlaich, M., and Walbridge, S. Fretting fatigue analysis of bridge stay cables at saddle supports using multiaxial stress-based approaches. In *IABSE Conference, Vancouver 2017: Engineering the Future - Report*, 2017. ISBN 9783857481536.
- [134] Han, S., Zhang, Q., Bao, Y., Cheng, Z., Jia, D., and Bu, Y. Frictional Resistance Between Main Cable and Saddle for Suspension Bridges. II: Interlayer Slip of Strands. *Journal of Bridge Engineering*, 25(8):04020043, 2020. ISSN 1084-0702. doi: 10.1061/(asce)be.1943-5592.0001547.
- [135] Bendalla, A. S. K. Nonlinear Numerical Modelling of Cable Elements in Bridges for Dynamic Analysis. *Bauhaus-University Weimar*, page 107, 2019. doi: <https://doi.org/10.25643/bauhaus-universitaet.3994>.
- [136] Tauscher, M., Bendalla, A. S. K., and Chayeb, G. Fault Identification in Wireless Structural Health Monitoring Systems based on Fault Patterns. In *Forum Bauinformatik*, pages 365–373, Bochum, 2023. doi: 10.13154/294-10112.

# Publications by the Author

[70] Bendalla, A. S. K., Tondo, G. R., and Morgenthal, G. A nonlinear finite element framework and Gaussian process-based prediction of stick/slip behaviour in semi-parallel wire cables. *International Journal of Solids and Structures*, 284(May):112522, 2023. doi: 10.1016/j.ijsolstr.2023.112522

[71] Bendalla, A. S. K. and Morgenthal, G. A nonlinear finite element framework for static and dynamic analysis of structural cables with deviating supports. *Engineering Structures*, 291(June):116363, sep 2023. ISSN 01410296. doi: 10.1016/j.engstruct.2023.116363

[135] Bendalla, A. S. K. Nonlinear Numerical Modelling of Cable Elements in Bridges for Dynamic Analysis. *Bauhaus-University Weimar*, page 107, 2019. doi: <https://doi.org/10.25643/bauhaus-universitaet.3994>

[136] Tauscher, M., Bendalla, A. S. K., and Chayeb, G. Fault Identification in Wireless Structural Health Monitoring Systems based on Fault Patterns. In *Forum Bauinformatik*, pages 365–373, Bochum, 2023. doi: 10.13154/294-10112